

NI

NATIONAL AERONAUTICS AND SPACE ADMINISTRATION

Technical Memorandum 33-354

Summary of Turbine Erosion Meeting

Held at the Jet Propulsion Laboratory, December 29-30, 1966

*Edited by
Lance G. Hays*

GPO PRICE \$ _____
CFSTI PRICE(S) \$ _____
Hard copy (HC) 2.00
Microfiche (MF) .50
653 July 65

FACILITY FORM 602

N67-37102	(THRU)
(ACCESSION NUMBER)	
221	(CODE)
(PAGES)	03
C1-88487	(CATEGORY)
(NASA CR OR TMX OR AD NUMBER)	

JET PROPULSION LABORATORY
CALIFORNIA INSTITUTE OF TECHNOLOGY
PASADENA, CALIFORNIA

June 15, 1967

Rg/47258

NATIONAL AERONAUTICS AND SPACE ADMINISTRATION

Technical Memorandum 33-354

Summary of Turbine Erosion Meeting

Held at the Jet Propulsion Laboratory, December 29-30, 1966

*Edited by
Lance G. Hays*

Approved by:

A handwritten signature in dark ink, appearing to read "D. R. Bartz", is written over a horizontal line.

D. R. Bartz, Manager
Research and Advanced Concepts Section

JET PROPULSION LABORATORY
CALIFORNIA INSTITUTE OF TECHNOLOGY
PASADENA, CALIFORNIA

June 15, 1967

Technical Memorandum 33-354

**Copyright © 1967
Jet Propulsion Laboratory
California Institute of Technology**

**Prepared Under Contract No. NAS 7-100
National Aeronautics & Space Administration**

CONTENTS

Preface	iv
Lance G. Hays	
List of Participants	v
1. Experiments on Turbine Erosion and Internal Flow	1
R. Spies	
2. Analytical Investigation of Turbine Erosion Phenomena	13
W. D. Pouchot, W. K. Fentress, and R. E. Kothmann	
3. Limited Impact Erosion and Metal Losses in Two-Stage Potassium Turbines	41
W. F. Zimmerman and R. J. Rossbach	
4. Potassium Erosion and Turbine Experiments	65
Lloyd V. Wilson	
5. Potassium Turbine Experiments	79
J. Rebeske	
6. Refractory Metal Potassium Turbine Experiments	83
J. P. Davis	
7. Mercury Erosion and Turbine Experiments	91
H. Derow	
8. Turbine Erosion During Mercury Rankine Turbo-Alternator Endurance Tests	99
C. Winder	
9. Potassium Turbine Erosion Experiments	115
Hans D. Lindhardt	
10. A Model for Multiple-Drop-Impact Erosion of Brittle Solids	129
Olive Engel	
11. Some Remarks on the Wet Vapor Turbine	145
G. Gyarmathy	
12. Experimental Investigations of Internal Flow in Turbines	159
D. G. Christie	
13. Liquid Impact and Material Removal Phenomena	173
J. H. Brunton	
14. Theory of Erosion	193
A. Thiruvengadam	

PREFACE

This document is a summary of the proceedings of an informal meeting on the subject of turbine erosion. The meeting was held at the Jet Propulsion Laboratory on December 29-30, 1966. The purpose of the meeting was to review two research programs being directed for the Office of Advanced Research and Technology, NASA, by the Jet Propulsion Laboratory and to provide an opportunity for workers in this field to exchange their views and information.

Because of the informal nature of the program, no papers were required. Instead, most participants have provided abstracts of their talks and copies of their visual material, for reproduction herein. In some cases, the notes taken during the conference which emphasize important issues or questions raised during the discussions are included. Although by no means complete, it is hoped this summary will provide a stimulus for further contact between participants in the meeting and other interested parties.

Lance G. Hays

LIST OF PARTICIPANTS
(* indicates authors of papers included in Summary)

D. Bartz Jet Propulsion Laboratory	*R. E. Kothmann Westinghouse, Steam Division
J. Baughman North American Aviation, Inc. Rocketdyne Division	J. Lafferty University of Michigan
*J. H. Brunton Cambridge University (England)	G. S. Leighton AEC (Germantown)
G. Cherry Aerojet-General Corp.	*H. D. Lindhardt Philco-Aeronutronic
F. Cheslak Philco-Aeronutronic	S. V. Manson NASA Office of Advanced Research and Technology
*D. G. Christie Central Electricity Research Laboratory (England)	W. Meyers Livermore Radiation Laboratory
*J. P. Davis Jet Propulsion Laboratory	E. Miller General Electric (Schenectady)
*H. Derow Aerojet-General Corp.	*W. D. Pouchot Westinghouse Astronuclear Laboratory
D. Dougherty Mechanical Technology, Inc.	*J. Rebeske AiResearch Corp.
D. Elliott Jet Propulsion Laboratory	*R. J. Rossbach General Electric (Evansdale)
*O. Engel General Electric (Evandale)	E. Schnetzer General Electric (Evansdale)
*W. K. Fentress Westinghouse, Steam Division	R. Smisek Philco-Aeronutronic
*G. Gyarmathy USAF, Wright-Patterson AFB	*R. Spies North American Aviation, Inc. Rocketdyne Division
L. Hays Jet Propulsion Laboratory	*A. Thiruvengadam Hydronautics, Inc.
D. Hirsch NASA, SNAP 8 Office (Azusa)	P. Thys North American Aviation, Inc. Rocketdyne Division
J. Joyce NASA Lewis Research Center	

LIST OF PARTICIPANTS (contd)

C. Walter
Livermore Radiation Laboratory

R. Werner
Livermore Radiation Laboratory

*L. V. Wilson
Oak Ridge National Laboratory

*C. Winder
Thompson Ramo-Woolridge
(Cleveland)

H. Young
Oak Ridge National Laboratory

1. EXPERIMENTS ON TURBINE EROSION AND INTERNAL FLOW

R. Spies
North American Aviation, Inc.
Rocketdyne Division
Canoga Park, California

Rocketdyne is currently conducting a program on investigating variables in turbine erosion. The investigation uses steam to observe the erosion effects.

Objectives and tasks of the program are:

- (1) Investigate effects of following on erosion.
 - (a) Vapor quality.
 - (b) Droplet size.
 - (c) Droplet velocity.
 - (d) Turbine geometry.
- (2) Design steam loop task.
- (3) Develop measurement apparatus task.
 - (a) Nozzle tests.
 - (b) Turbine tests.
- (4) Fabricate turbine wheels and housing task.
 - (a) Demountable blades.
 - (b) More than one material.
- (5) Test turbine task.
 - (a) Vary tip speed.
 - (b) Vary spacing.
- (6) Evaluation task.
- (7) Laser pulsing system development task.

A brief review of results obtained last year is shown in Figs. 1-1 and 1-2. Tests made with the nozzle block showed only areas where water collected and subsequently the water was re-entrained in the vapor flow. Puddles appeared on the

trailing edge and on the suction surface. Slow-moving drops were observed on the suction surface. Position of the drops was observed during high-speed photography and the velocity was calculated.

A number of equations exist for predicting critical droplet size. In Fig. 1-3 the calculated size for steam and potassium drops is given for four sets of correlation criteria. Measured droplet size is compared to predictions in Fig. 1-2. In Fig. 1-3, it is of interest to note that, regardless of criterion chosen, the drop size for steam and potassium is nearly the same. This drop-size sameness lends validity to the idea that results in potassium may be predictable in steam. Experimental results will be required to confirm this assumption.

In turbine tests, the movement of water through the turbine stage is recorded on high-speed film. (Films of some typical tests were shown. Large quantities of water can be observed to flow over the stator walls.)

The turbine was operated with four types of blade materials: pure copper, soft aluminum, Tens-50 aluminum, and stainless steel. To obtain uniformly wet steam, steam is expanded through a separate expansion turbine and a first test turbine stage. A line diagram of the loop is shown in Fig. 1-4. Figure 1-5 shows a typical expansion curve.

The range of conditions (wetness and speed) over which the turbine was operated is shown in Fig. 1-6. Four separate test periods are noted. Certain blades were changed between each of the tests to observe the erosion. Therefore, some blades were included for the complete test time, some for each of the tests, and some for various combinations. The measured weight change for the various materials is shown in Fig. 1-7. Aluminum suffered severe loss, while copper and stainless steel showed no loss during the first three tests, and stainless steel showed a slight loss only during the last, high-speed test. (The small weight gain during the initial test is attributed to oxidation.) Copper was not used at the high speed because of stress limitations.

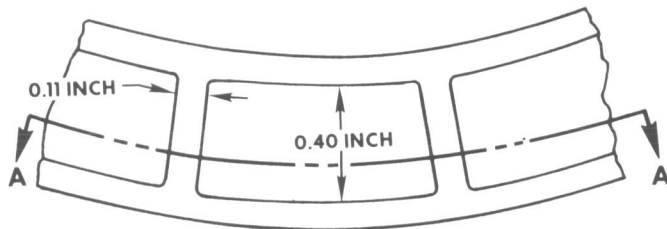
Figures 1-8 through 1-11 show the blades at various test times. Damage to the aluminum blades is very evident.

Work is continuing. More detailed tests to observe droplet information and propagation are planned.

DISCUSSION

Hans Linhardt made a comment that the leading edges of the Rocketdyne stator blades were not of conventional design. Comparison was made with leading edges of the nozzle blades on General Electric turbine, and the Rocketdyne blades were found to be bulbous in comparison. Dr. Olive Engel pointed out that the sudden increase in velocity of droplets (noted in the Rocketdyne pictures) may be due to breakup and atomization of the droplets. This effect has been noted elsewhere. D. G. Christie stated that their observation of droplet breakup showed that the droplets start to break up when the droplets move across the wake region into the main stream. A critical Weber number of about 20 appears to describe the breakup process; the value of velocity is chosen where the droplets start breaking up. S. V. Manson pointed out that there was a size effect in turbines which had not been considered in the Rocketdyne presentation, namely the channel and cord length, Reynolds numbers, and the radial dimensions. The statement was made that there should be a size effect on erosion between cases, such as the Westinghouse large steam turbine and the Rocketdyne small steam turbine, and this size effect could be expressed in terms of macroscopic flow parameters, such as the Reynolds number.

EROSION TEST NOZZLE DIMENSIONS



RADIAL VIEW

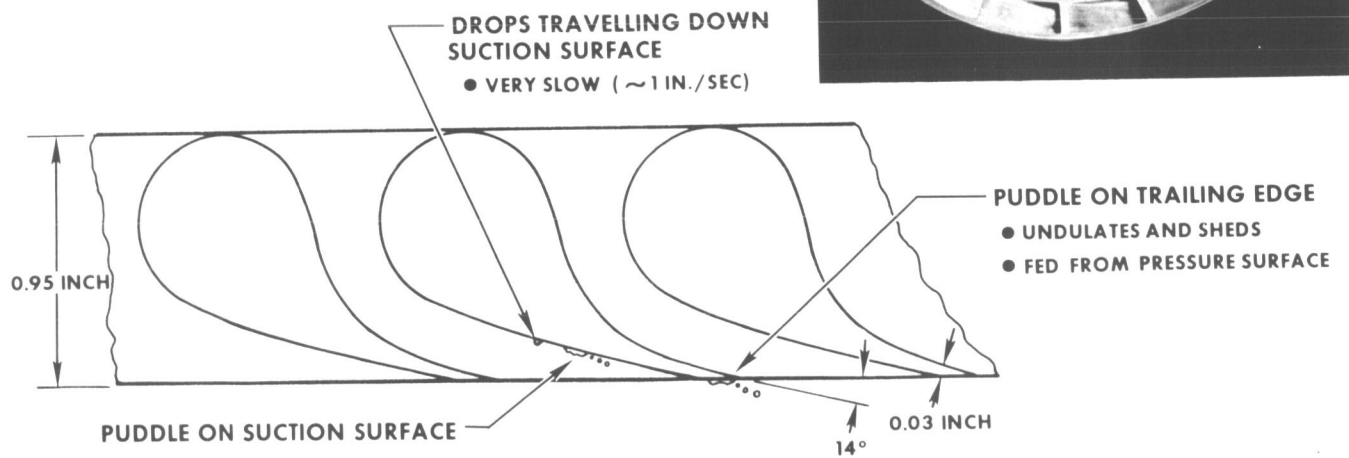
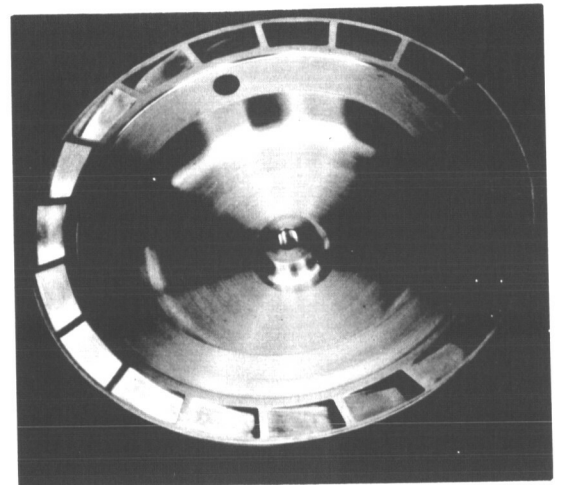
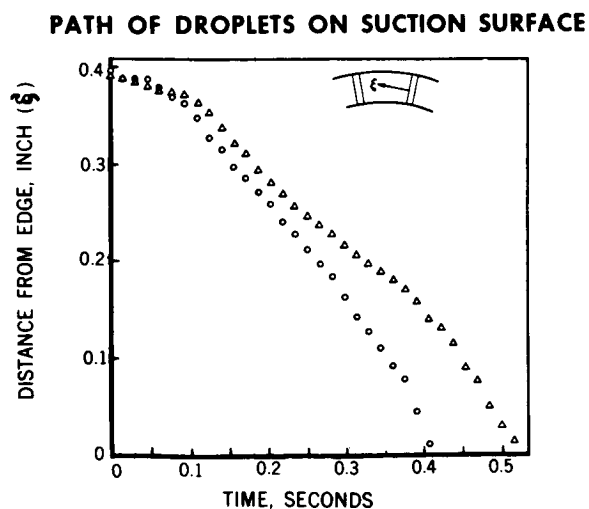
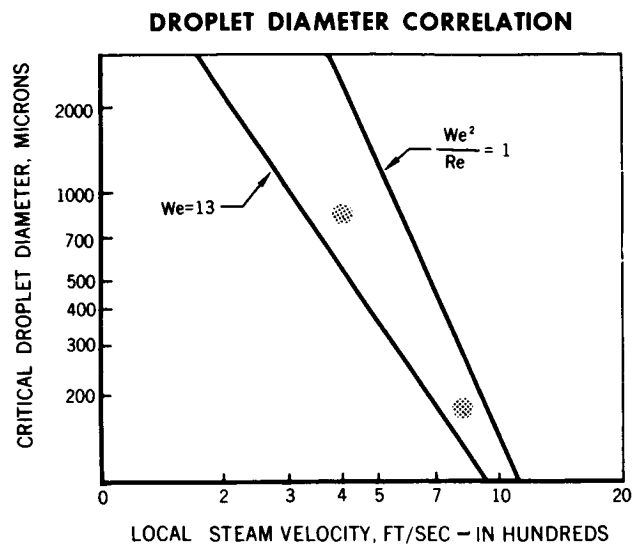
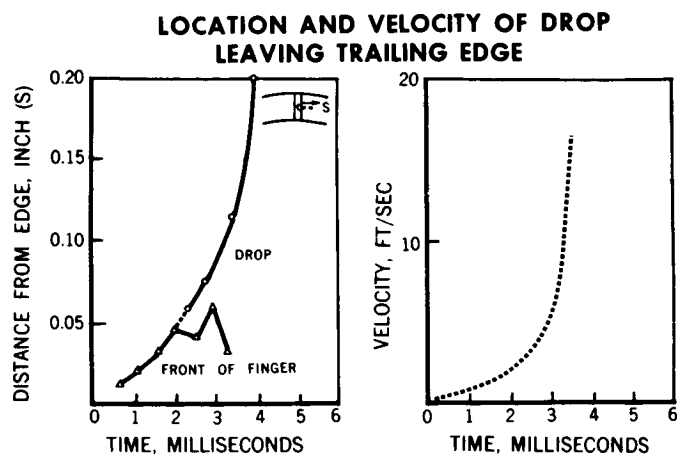


Fig. 1-1. Observations of turbine erosion in nozzle tests



EROSION TEST NOZZLE DIMENSIONS

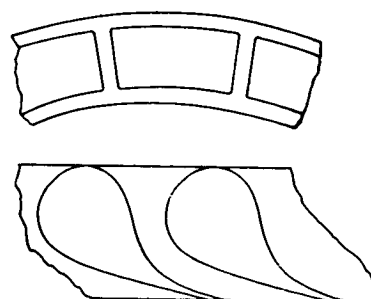


Fig. 1-2. Nozzle test results

PARAMETER

$$We = \frac{\text{DYNAMIC PRESSURE}}{\text{SURFACE TENSION PRESSURE}} = \frac{\text{DRAG FORCE}}{\text{SURFACE TENSION}} = \frac{\rho U^2 d_c}{\sigma_L} = 13$$

$$\frac{We^2}{Re} = \frac{\text{DRAG FORCE}}{\text{SURFACE TENSION}} \times \frac{\text{VISCIOUS FORCE}}{\text{SURFACE TENSION}} = \frac{\rho U^3 d_c \mu}{\sigma_L^2} = 1$$

$$WeRe = \frac{\text{DRAG FORCE}}{\text{SURFACE TENSION}} \times \frac{\text{DRAG FORCE}}{\text{VISCIOUS FORCE}} = \frac{\rho^2 U^3 d_c^2}{\sigma_L \mu} = 4000$$

$$= 2000$$

CRITICAL DROP SIZE AT 1000 FT/SEC	
STEAM AT 130 F	POTASSIUM AT 1160 F
92 μ	82 μ
188 μ	108 μ
95 μ	85 μ
67 μ	60 μ

Fig. 1-3. Modeling considerations of steam and potassium drop size

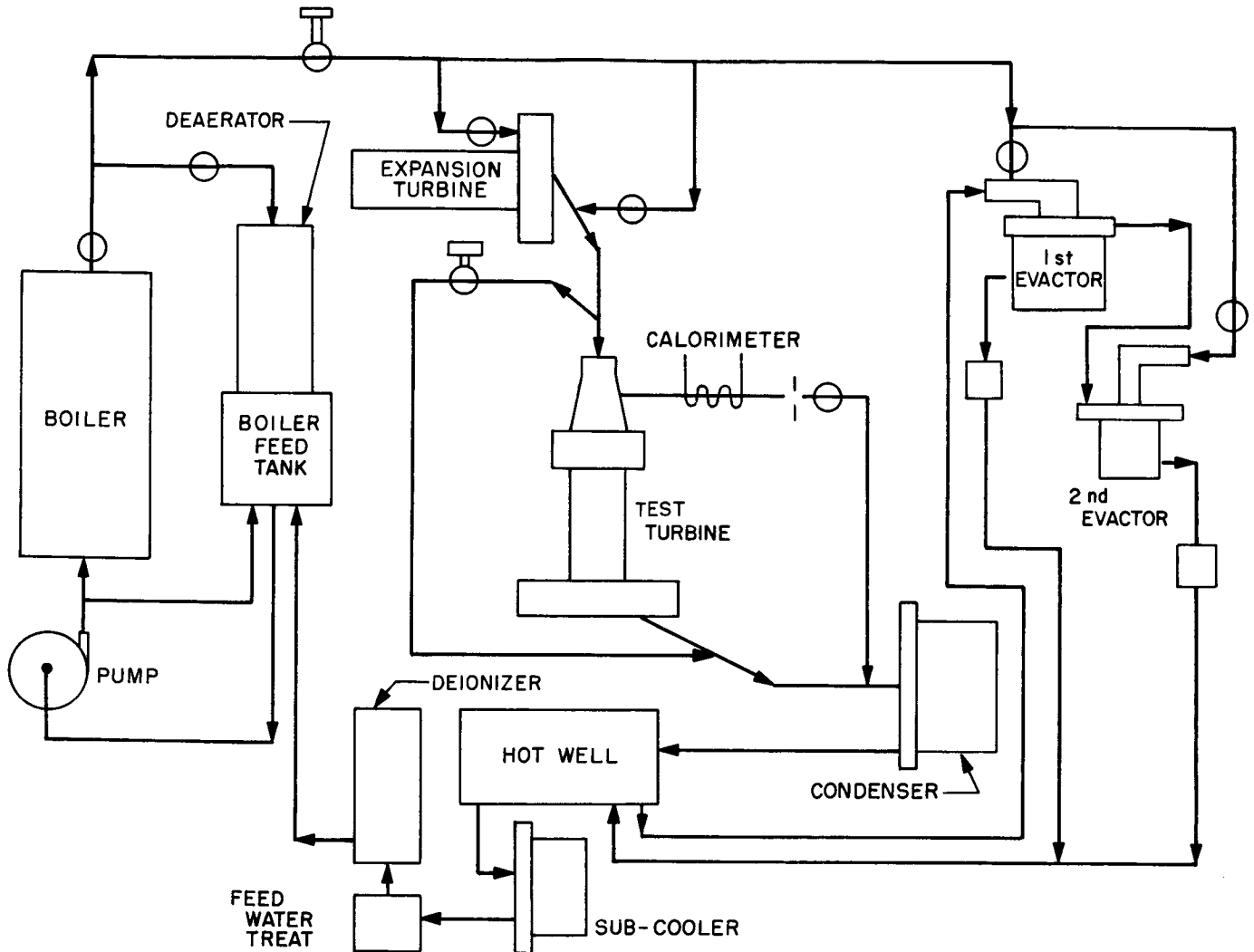


Fig. 1-4. Turbine erosion test loop diagram

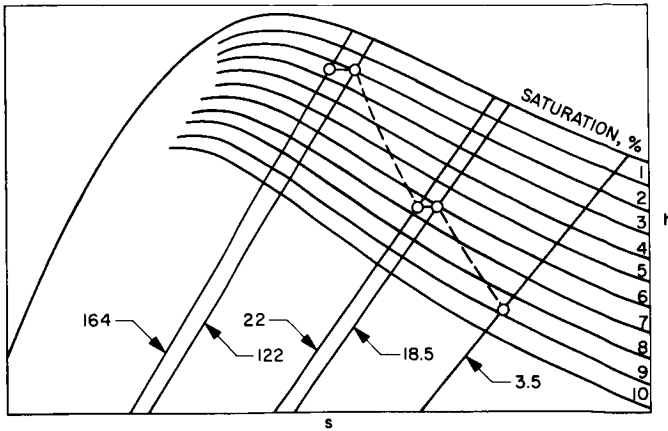


Fig. 1-5. Typical condition line of steam erosion tests

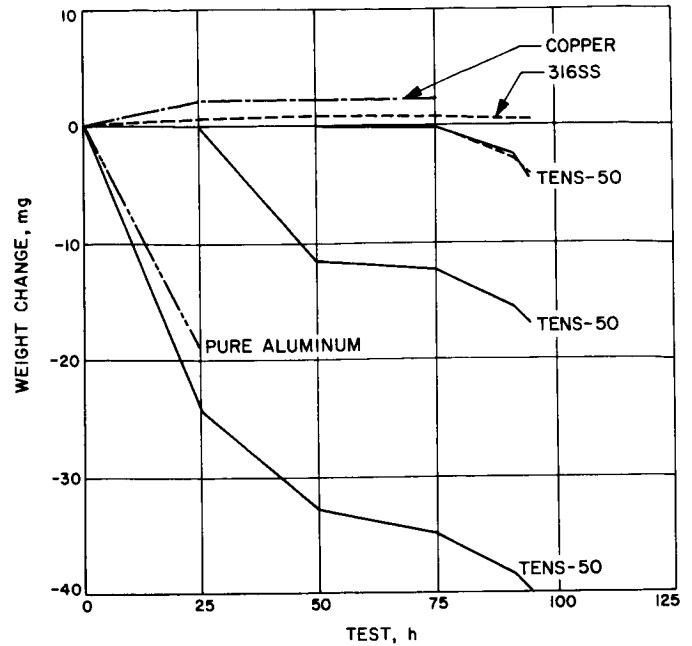


Fig. 1-7. Material weight change versus time

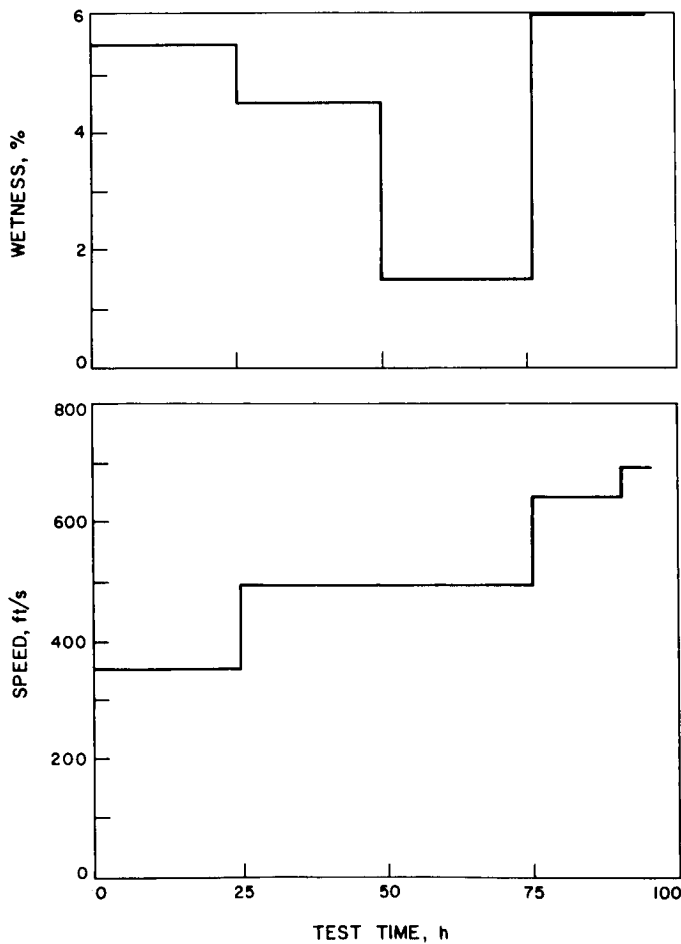


Fig. 1-6. Wetness and speed versus time

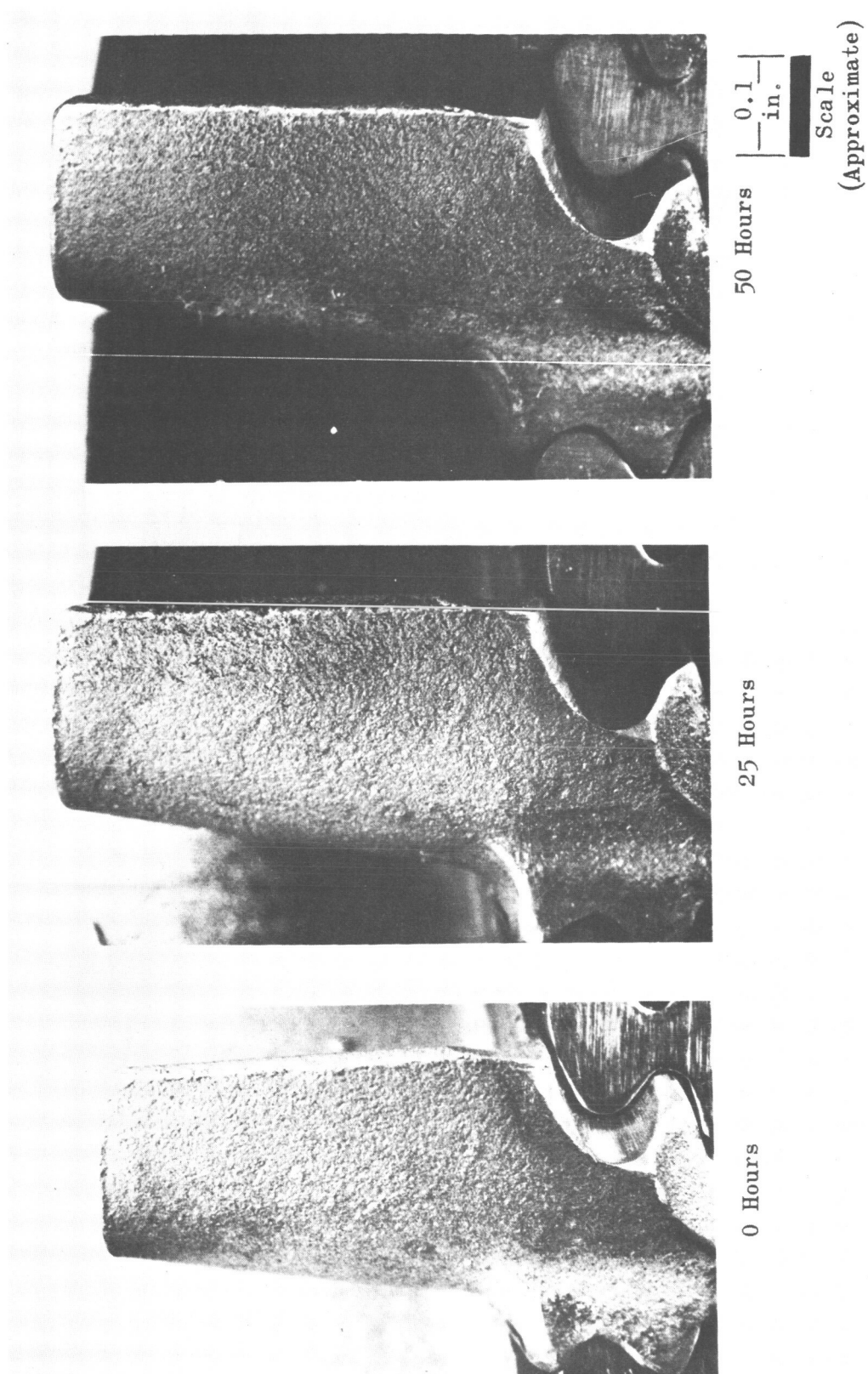


Fig. 1-8. Stainless steel blade, No. 103

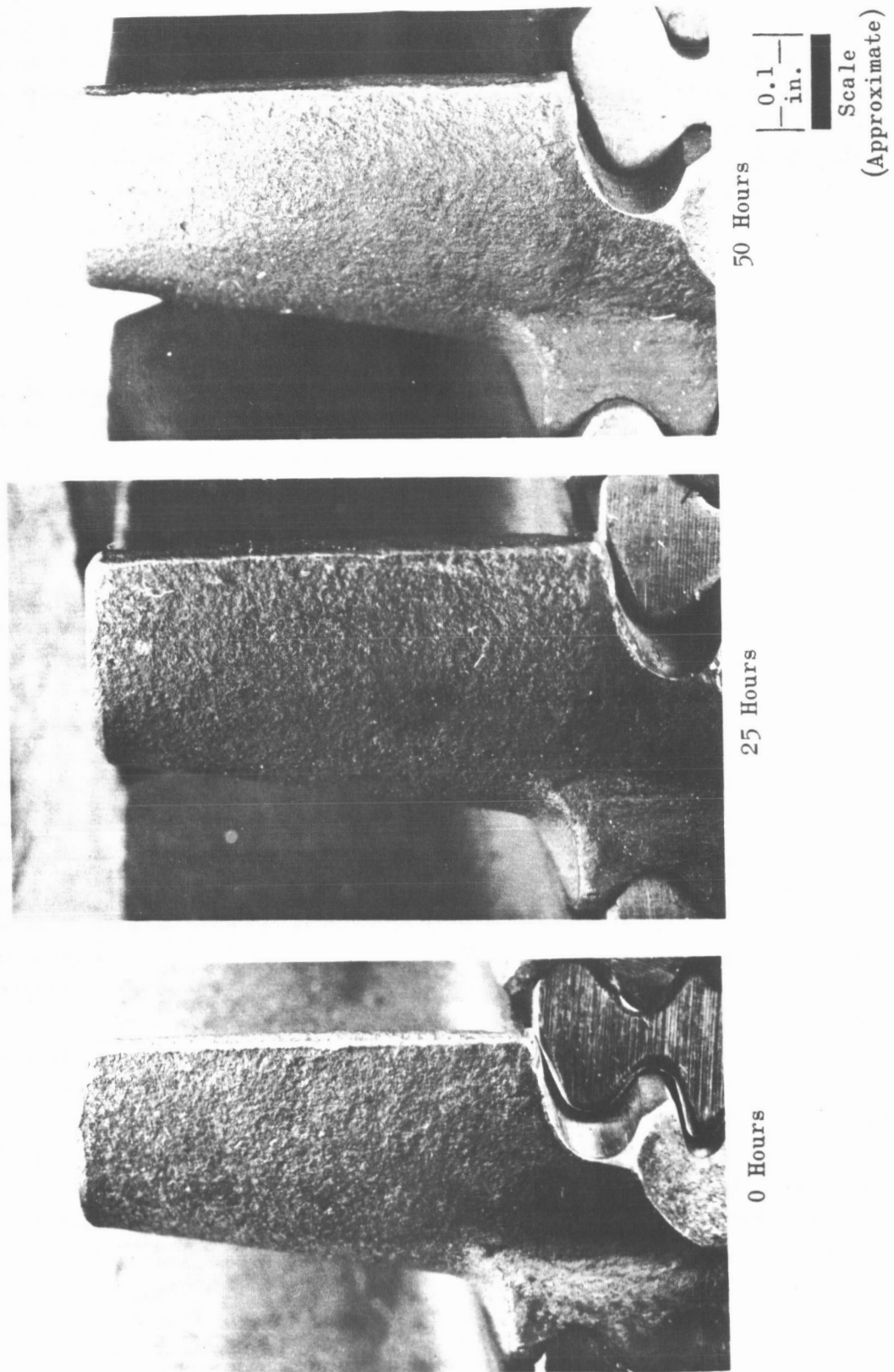
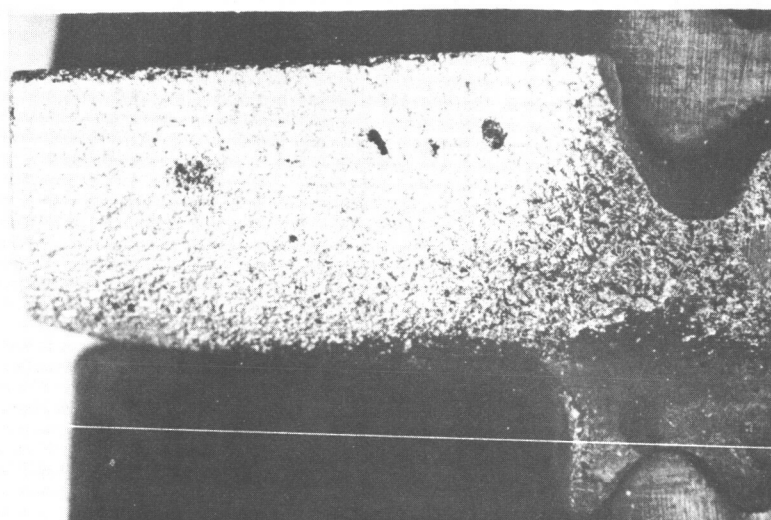
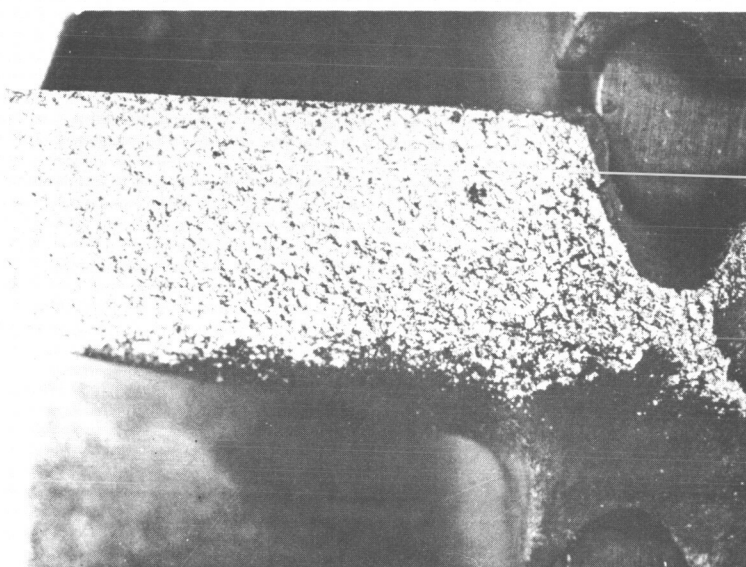


Fig. 1-9. Tens-50 aluminum blade, No. 140



50 Hours



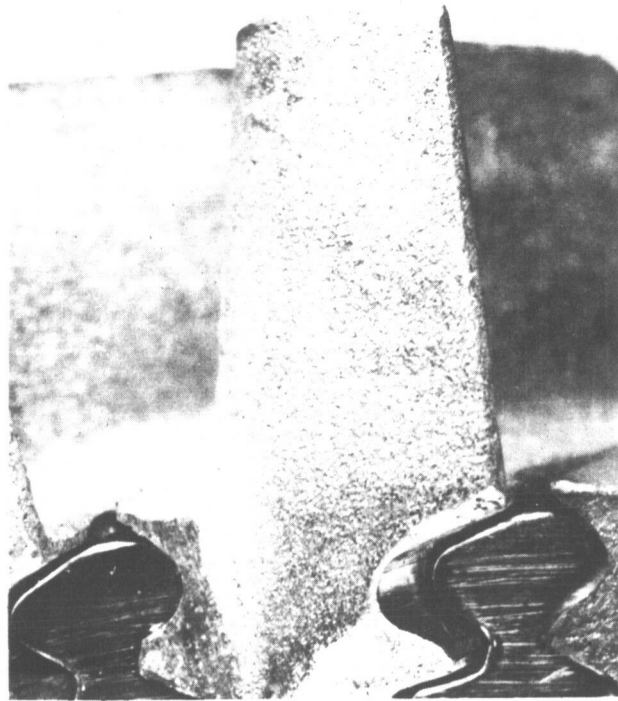
25 Hours



0 Hours

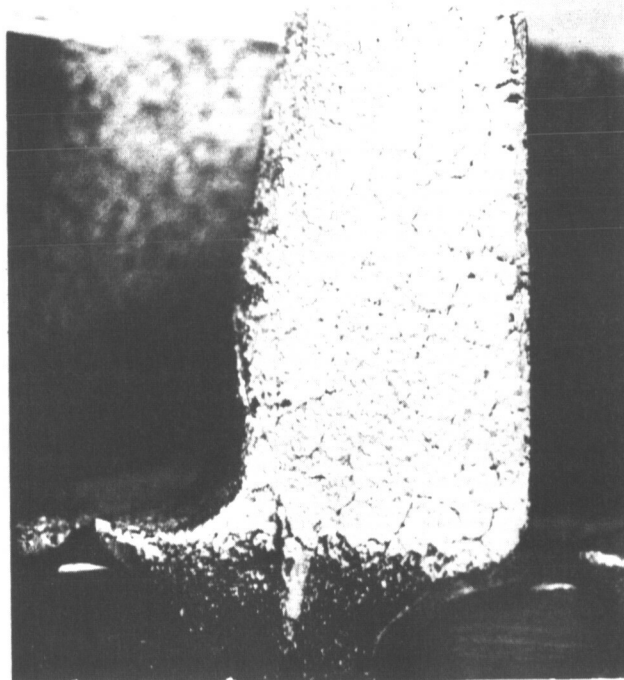
0.1 in.
Scale
(Approximate)

Fig. 1-10. Copper blade, No. 110



0 Hours

0.1
in.
Scale
(Approximate)



25 Hours

Fig. 1-11. Aluminum blade, No. 125

2. ANALYTICAL INVESTIGATION OF TURBINE EROSION PHENOMENA

W. D. Pouchot
Westinghouse Astronuclear Laboratory
Pittsburgh, Pennsylvania

W. K. Fentress and R. E. Kothmann
Westinghouse Steam Division
Lester, Pennsylvania

Presented hereafter are some of the detailed results and theory from a study done under Contract NAS 7-390 to develop an analytical-empirical model of turbine erosion to fit and explain experience in both steam and metal vapor turbines. As the study is continuing, this presentation is in the nature of a progress report.

The qualitative aspects of the model follow, to a large extent, opinions on the erosion process in wet vapor steam turbines that are widely held within the steam turbine community at the present time. In respect to the quantitative aspects, the study is indebted to excellent previous studies by Gyarmathy (Ref. 2-1) and Gardner (Ref. 2-2). The study is a refinement and extension of these two previous works (more the former than the latter) and based on later experience and substantial additional component process theory and computation. In general, the approach to obtaining quantitative answers for the various processes that lead to erosion was to use well-known theoretical or empirical methods wherever possible and to inject novelty only as a last resort. Some of the objectives of this study are:

- (1) Provide analytical-empirical model of turbine erosion.
- (2) Provide useful model for preliminary erosion estimates.
- (3) Provide guidance to experimental programs.
- (4) Make design suggestions to minimize turbine erosion.

The model is concerned with the erosion on the nose and leading edge of rotor blades of turbines operated in wet vapor. While other regions of erosion have been observed, the chief area of erosion in well ordered flow turbines operated at or near their design conditions is on the inlet edge of the rotor blades.

As the vapor expands in a set vapor turbine, the temperature of the vapor is reduced below the saturation point until supersaturation becomes sufficient to cause

spontaneous condensation. The thermodynamic condition at initiation of the rapid spontaneous condensation is called the Wilson line, and its location is a function of the particular vapor properties and of the rate that the vapor is expanding. For a vapor such as steam or potassium, the location of the Wilson line generally corresponds to a degree of supersaturation equivalent to an equilibrium moisture content of less than 4.5%. At the Wilson line, condensation takes place rapidly, and the moisture content quickly approaches equilibrium. Thereafter, in the turbines examined, the expansion process is close to an equilibrium expansion.

The original spontaneous nucleation creates sufficient surface area to allow further condensation to occur with minimal supersaturation. As originally formed, the condensation nuclei are extremely small ($0.01 \mu\text{m}$ diameter) and are of relatively uniform size because of the short time period involved. The nuclei grow quite rapidly to about $0.2 \mu\text{m}$ diameter as the supersaturation potential created by the expansion in advance of spontaneous condensation is exhausted. Thereafter, a slower growth takes place as the droplets progress through the turbine. The final size attained may approach $1 \mu\text{m}$ in diameter.

Because of their small size, the condensate particles are essentially locked to the vapor and most of them remain with the stream tube of their birth until turbine exit. However, a small percentage of the condensate fog collects on surfaces because of the curvature of the passages and rotation of the moving blades. By calculation, the percentage collected per turbine row (even in the wettest rows) is 5% or less of the total fog present; generally the percentage is less. The collected moisture causes the erosion. The fog particles cause no erosion since they follow the vapor flow as it slices cleanly over the blading surfaces.

The small percentage of fog particles collected form into rivulets, films, and drops on the blading surfaces. The predominant force on the rotating blading is the centrifugal field of the blades. Under this force, the liquid collected on the rotors flows nearly radially upwards and is thrown from the tips of the blades. The particle flow, thereafter, is essentially in the tangential direction, and the initial flow velocity is approximately the same as the peripheral speed of the blades. The tangential distance of travel in large turbines is around 5 inches.

Due to the high peripheral velocity of the turbine blade tips, the liquid flung from the tips is well atomized. However, the atomized drops are still large in size compared to the fog particles. Most of these atomized drops proceed in an almost

undisturbed trajectory to impact the turbine casing at a very shallow angle. Even with a 5-in. path length, the time of flight is less than 0.5 ms at 1200 ft/s tip velocity. This time is too short for the vapor drag forces to produce any appreciable deceleration or acceleration of most of the flung liquid. A small percentage of the liquid is undoubtedly in the form of small drops (of sufficiently high surface to mass ratio) that are turned into the succeeding stator by the vapor stream. However, such drops will slice cleanly along the stators and cause no damage. For these reasons, erosion at the inlet of stators is seldom encountered in practice where the moisture impinging on the casing is removed through suitable slots.

On the stator blades, the primary force acting on the collected liquid is the drag force of the mainstream flow. Under this force the liquid flows to the rear of the stator where it collects until torn from the stator as rather large particles. In the model used the collected liquid is assumed to follow the bulk flow streamlines, and, on a time average basis, to be uniformly distributed along a stator from hub to tip. Although the first assumption is of doubtful validity because of the secondary flows at blade hub and tip; the second assumption is still reasonable, since the liquid displaced from the pressure surface of a particular stator will flow over the casing or rotor hub and will terminate on the suction surface of a companion stator.

The liquid which is torn from the back of stator vanes causes the erosion that this model seeks to explain in a quantitative manner. Most of the large liquid drops torn from the stators undergo further breakup, and all drops undergo acceleration between stator and rotor. However, in the time available, the drops attain only a fraction of vapor stream velocity, and because of the vector velocity difference, the drops strike the nose and convex surfaces of the rotating blades. Due to the high velocity of the liquid drops relative to the rotor blades, some of the larger drops strike with sufficient intensity to cause material removal by repetitive impact. The erosion of the rotor blades is confined to the nose and leading edge of the convex surface because of shadow effect of companion blades. Because the blade speed is highest at the tip and, hence, the incident drop velocities are highest, the greatest degree of erosion occurs at the blade tips.

The overall erosion model is composed of a number of component processes. A breakdown by related grouping of the detail processes is as follows:

- (1) Nucleation and growth of condensate drops.
- (2) Boundary layers, blade wakes, and moisture deposition.
- (3) Atomization and trajectories of damaging liquid.
- (4) Material removal.

Numerical results of calculations for each of the processes are illustrated through the examination of two very different turbines. The first one is a very large steam turbine with 48-in.-long blades, and is the design used in the Yankee Nuclear Power Station. The second one is a relatively small conceptual-designed turbine with 2-1/4-in.-long blades for use in a space Rankine cycle power plant. This turbine is referred to as the Six-Stage Potassium Turbine. Further information on both turbines is shown in Figs. 2-1 through 2-3.

Figures 2-4 through 2-11 explore the detailed process of spontaneous condensation in a supersaturated flowing vapor. The analysis used for steam follows the same general method of solution which was first described by Oswatitish (Ref. 2-3), but uses improvements introduced by Gyarmathy. Further modification for use with metal vapor was carried out along the lines of Katz, Saltzburg, and Reiss (Ref. 2-4).

Figures 2-4 through 2-6 illustrate the process in the diverging portion of a converging-diverging nozzle. Figures 2-7 and 2-8 give the nucleation rate and flow equations used in the calculations. The last figures (Figs. 2-9 through 2-13) in this group give results for both steam and potassium turbines. The mean drop size calculated for the six-stage potassium turbine is believed to be about twice the actual size because the input value of surface tension was about 15% above actually observed values.

Figures 2-14 through 2-17 cover the component flow processes of the vapor and condensate flow program which had the following objectives:

- (1) Vapor flow.
 - (a) Axisymmetric flow downstream of the blade.
 - (b) Boundary layer on surface of blades.
 - (c) Blade wake calculations.
- (2) Deposition of moisture on blades.

- (a) Deposition on inlet edge.
- (b) Deposition on concave surface.
- (3) Movement of moisture on blades.
 - (a) Stator blades.
 - (b) Rotor blades.

Examples of axisymmetric flow downstream of the blades are given in Figs. 2-14 and 2-15. Figure 2-16 gives an example of boundary layer properties calculated by the method of Truckenbrodt (Ref. 2-5). A portion of a blade wake calculated by the method of NACA-TN-3771 (Ref. 2-6) is given in Fig. 2-17. Figures 2-18 and 2-19 show stator blade nose and concave-side moisture collection calculated essentially by the method of Gyarmathy (Ref. 2-1). Typical values of moisture movement on a stator blade are shown in Fig. 2-20. The calculation is based on viscous flow in a liquid film. A summary of the conclusions and recommendations on these component flow processes are:

- (1) Calculations define:
 - (a) Axisymmetric flow downstream of blade rows.
 - (b) Vapor boundary layer on surface of blades.
 - (c) Wakes downstream of blade rows.
 - (d) Deposition of moisture on surface of blades.
 - (e) Viscous film movement of moisture on blades.
- (2) Additional work required:
 - (a) Downstream wakes.
 - (b) Deposition of moisture; inertial impaction by detailed calculation, deposition by secondary flows in blade tips region, and deposition by particle diffusion.
- (3) Movement of moisture - nature of retained moisture on blade surfaces needs further investigation.

The next series of figures (Figs. 2-21 through 2-30) illustrate the processes of atomization of the liquid collected by the stator blades after this liquid departs the stators, the acceleration of the liquid in the intervening space between stator and

rotor, and the resulting impact with the succeeding rotor blades. The objectives of this series of calculations are:

- (1) Provide calculational procedure for obtaining:
 - (a) Drop-size distribution impacting turbine rotors.
 - (b) Velocities of impact.
- (2) Check against available experimental information.

Figures 2-21 through 2-23 give the basis of the calculations. Figures 2-24 through 2-27 give results for the large steam turbine. Figures 2-28 through 2-30 give results for the small six-stage potassium turbine. It should be noted that a major difference exists in the value of the Secondary Atomization Weber Number criteria used between the large and the small turbines.

Figure 2-31 gives empirical information on the resistance of stellite, a common steam turbine erosion shield material, as a function of a reduced velocity, i. e., the normal impact velocity minus a threshold velocity below which erosion can be considered negligible. This velocity has been found to vary with drop size (Ref. 2-7). Figure 2-32 shows the result of a correlation wherein the variation was given by

$$V_{cd} \propto (1/D)$$

The ultimate objective of the material removal portion of this study is the deduction of empirical relationships between erosion rates and the controlling external variables, such as velocity, angle of impingement, size, shape, and fluid properties of impinging drops. To date, however, attention has been focused on water drops.

The last three figures (Figs. 2-33 through 2-35) summarize the impacting liquid rates for the two turbines, and give calculated erosion for the Yankee Steam Turbine. The impact rates given in Fig. 2-34 for the six-stage potassium turbine are believed to be high by about a factor of two. This is because the calculated diameters of potassium condensation nuclei are believed to be larger than those which would actually occur (as stated previously).

Some overall conclusions about the status of this study are as follows:

- (1) A continuous analytical model of rotor blade erosion in wet vapor turbines has been constructed.
- (2) Calculated depth of rotor blade erosion, using the model, for the Yankee low-pressure steam turbine is in reasonable agreement with actual operational experience.
- (3) Calculations using the fluid dynamic portion of the erosion model have been carried out on a six-stage conceptual design of potassium space turbine.
- (4) The amounts of blade-surface-collected condensate are substantially higher in the space turbine examined than in the Yankee steam turbine. The sub-division of the collected moisture as it strikes the rotor blades is substantially finer in the potassium turbine than in the Yankee steam turbine.

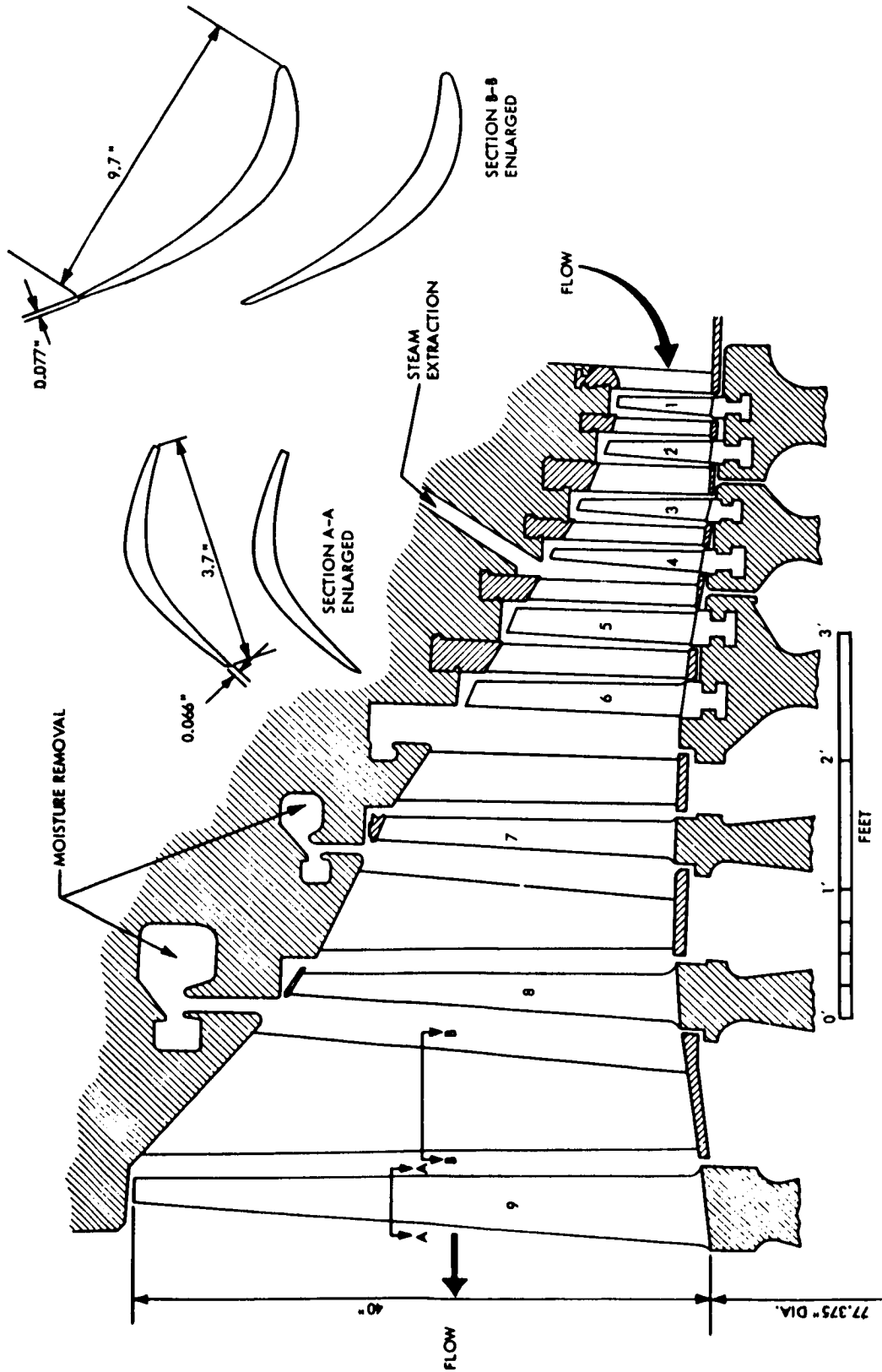


Fig. 2-1. Yankee steam turbine

JPL Technical Memorandum 33-354

ROW NO.	9TH ROTOR	9TH STATOR	8TH ROTOR	1ST ROTOR	INLET
EFFECTIVE BLADE HEIGHT (IN.)	40.00	37.44	27.23	6.49	7.55
EFFECTIVE MEAN DIAMETER (IN.)	117.50	118.40	110.64	88.35	89.35
STATIC PRESSURE (PSIA)	0.88	1.515	2.313	45.345	59.2
MOISTURE CONTENT	0.152	0.140	0.130	0.0240	0.0100
TEMPERATURE (°F)	97.5	115.9	131.5	274.9	292.0
JET VELOCITY (FPS)	1133.	1057.	1016.	699.0	-----
MEAN WHEEL SPEED (FPS*)	922.8	929.9	869.0	693.9	-----
TIP WHEEL SPEED (FPS*)	1237.0	1224.0	1082.8	744.9	-----
STEAM FLOW (PPH × 10 ⁻³)				904.9	904.9
AXIAL SPACE STATOR EXIT TO ROTOR INLET (IN.)	1.9	1.9	1.7	0.5	
TRAILING EDGE THICKNESS (IN.)	0.066	0.077	0.065	0.033	
BLADING MATERIAL	← 12% CHROMIUM STEEL →				
STELLITE SHIELDS	YES		YES	NO	NO

* STATOR BLADE "WHEEL SPEED" IS THAT SPEED EQUIVALENT TO A ROTOR OF THE SAME DIAMETER.

Fig. 2-2. Yankee steam turbine, row by row mean diameter data

ROW NO.	6R	6S	5R	1R	INLET
EFFECTIVE BLADE HEIGHT (IN.)	2.25	1.87	1.62	.49	.45
EFFECTIVE MEAN DIAMETER (IN.)	6.85	6.75	6.66	5.80	5.70
STATIC PRESSURE (PSIA)	16.90	19.69	22.04	123.4	178.6
MOISTURE CONTENT	.154	.146	.139	.016	-----
TEMPERATURE (°F)	1422.	1454.	1477.	1930.	2100.
JET VELOCITY (FPS)	822.	815.	1075.	937.	-----
MEAN WHEEL SPEED (FPS)	717.	707.	697.	607.	-----
TIP WHEEL SPEED (FPS)	955.	905.	869.	-----	-----
FLOW (PPS)	5.76	5.76	5.76	5.76	5.76

Fig. 2-3. Potassium turbine, row by row mean diameter data

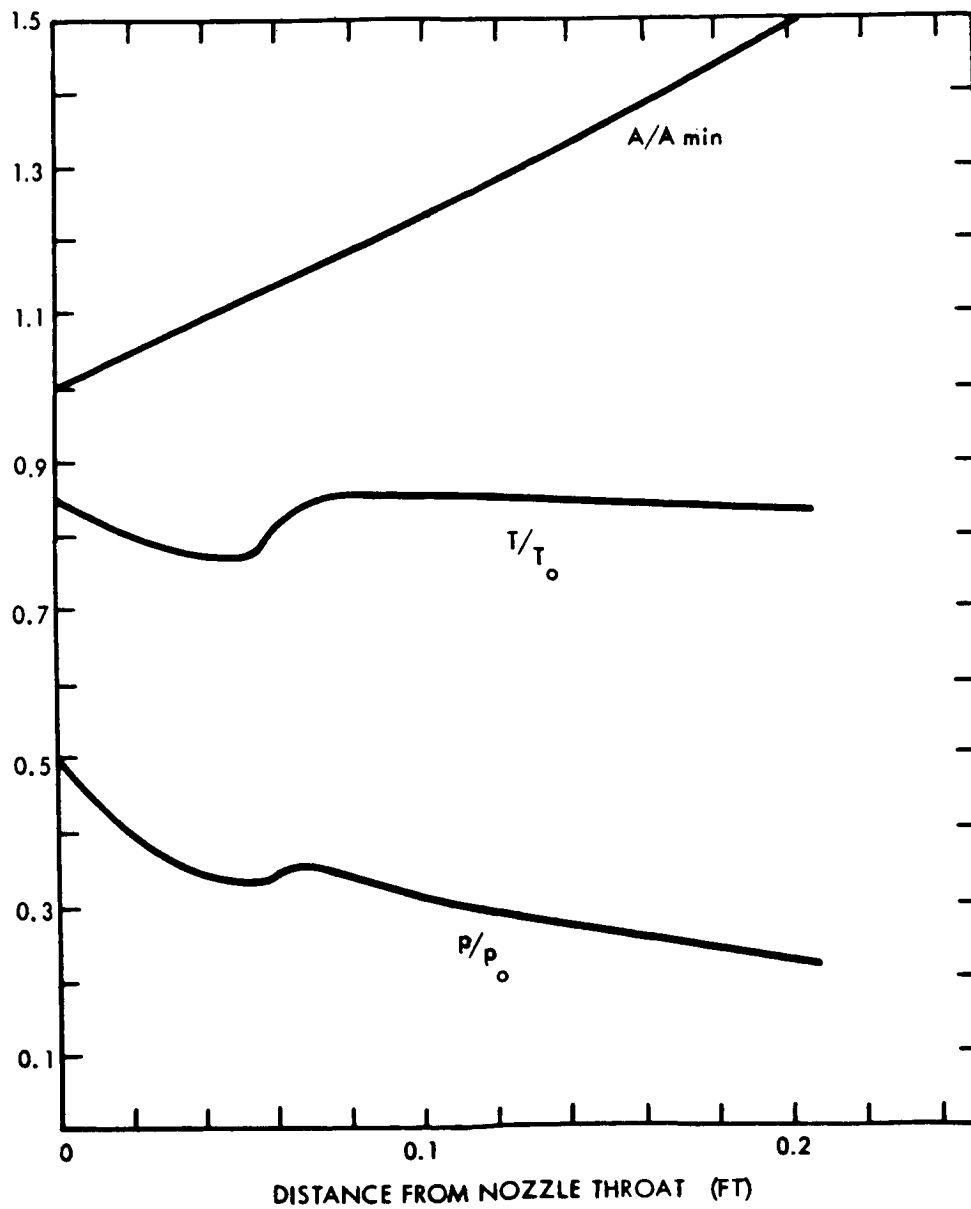


Fig. 2-4. Area, temperature, and pressure ratios for divergent portion of a nozzle with condensing flow

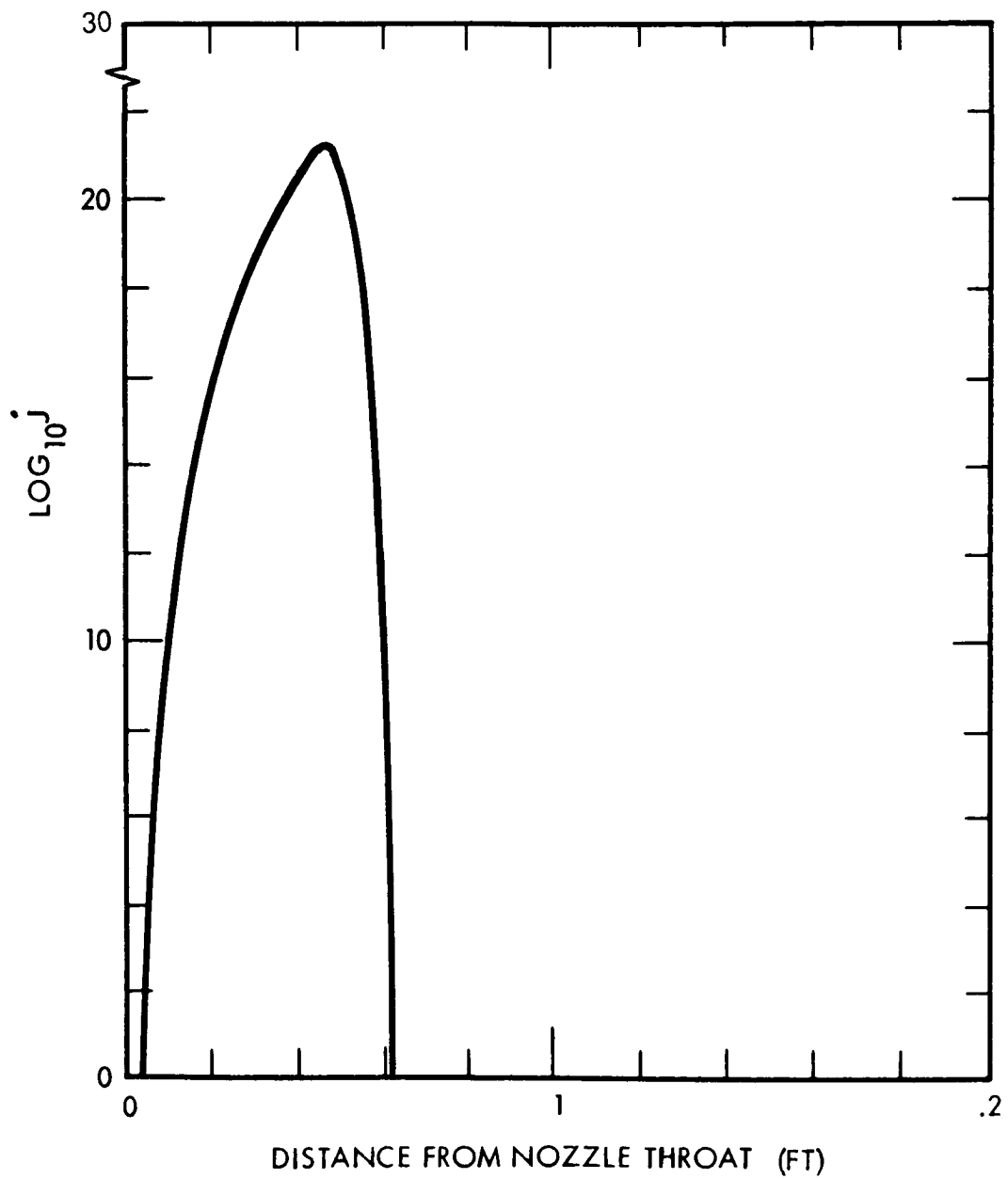


Fig. 2-5. Nucleation rate in divergent portion of nozzle

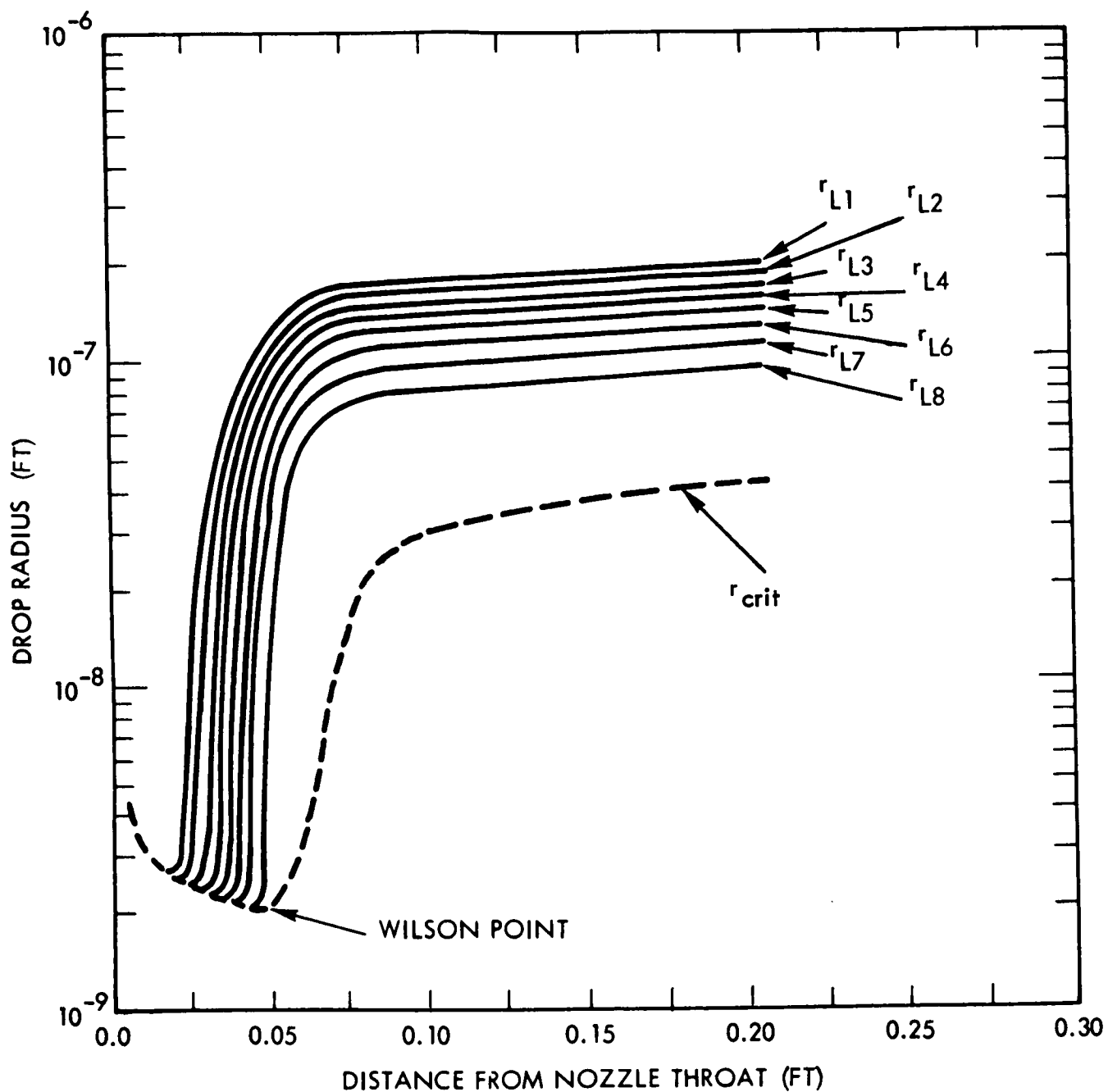


Fig. 2-6. Droplet growth in divergent portion of nozzle

$$r_{\text{crit}} = \frac{2\sigma M}{\rho_L R_0 T \Delta_1}$$

$$j = \frac{N_0 P P_{\text{eff}}}{\rho_L (R_0 T)^2} \sqrt{\frac{2 M g \sigma N_0}{\pi}} \exp(-Z_1 / \Delta_1^2)$$

$$Z_1 = \frac{16 \pi N_0 M^2}{3 \rho_L^2} \left(\frac{\sigma}{R_0 T} \right)^3$$

$$\Delta_1 = \ln(P_1 / P_{1s})$$

$$P_{\text{eff}} = \sum_{i=1}^n i^{3/2} P_i$$

Fig. 2-7. Nucleation rate

$$\frac{1}{A} \frac{dA}{dz} + \frac{1}{W} \frac{dW}{dz} - \frac{1}{v} \frac{dv}{dz} + \frac{1}{X} \frac{dy}{dz} = 0$$

$$\frac{1}{W} \frac{dW}{dz} + \frac{P x v g \eta_p}{W^2} - \frac{1}{P} \frac{dP}{dz} = 0$$

$$\frac{W^2}{J g} \frac{1}{W} \frac{dW}{dz} + x \frac{d}{dz} (h(V, T)) - h_{fg} \frac{dy}{dz} + y c_{pL} \frac{dT_L}{dz} = 0$$

$$\frac{1}{P} \frac{dP}{dz} + \frac{1}{v} \frac{dv}{dz} - \frac{1}{T} \frac{dT}{dz} - \frac{1}{Z_c} \left(\frac{\partial Z_c}{\partial v} \frac{dv}{dz} + \frac{\partial Z_c}{\partial T} \frac{dT}{dz} \right) = 0$$

Fig. 2-8. Flow equations

	Condensation-Performance Program Polytropic Efficiency $\eta_p = 1.0$				Steam Division Program Equilibrium Moisture			
	Pressure (PSIA)	Axial Velocity (FPS)	Temperature (°F)	Moisture	Pressure (PSIA)	Axial Velocity (FPS)	Temperature (°F)	Moisture
Inlet	57.5	119.7	269		59.2		292	0.010
Stator No. 1	50.7	165.8	247		51.9	165	283	0.017
Rotor No. 1	44.4	183.3	258	0.0165	45.3	180	274.9	0.0240
Stator No. 2	39.0	196.1	264	0.0303	39.7	192	267	0.0310
Rotor No. 2	34.3	199.8	257	0.0374	34.9	198	259	0.0380
Stator No. 3	30.6	192	250.5	0.0438	30.5	196	251.3	0.0440
Rotor No. 3	27.0	195	243	0.04997	26.5	202	243.2	0.0500

Fig. 2-9. Comparison of condensation, performance program results for Yankee turbine

	$\eta_p = 1.0$	$\eta_p = 0.85$
	Mean Diameter (Microns)	Mean Diameter (Microns)
1st Stator	--	--
1st Rotor	--	--
2nd Stator	--	--
2nd Rotor	0.470	0.568
9th Stator	0.730	0.877
9th Rotor	0.755	0.908

Fig. 2-10. Mean droplet diameter for Yankee turbine

	CONDENSATION PROGRAM				EQUILIBRIUM CALCULATION		
	P, (ATM)	T (°R)	U _a (FPS)	ΔT (°F)	P (ATM)	T (°R)	U _a (FPS)
Inlet	2.6	2060	-	24	2.6	2060	-
1-S	1.81	1892	370	83	1.905	1987	346
1-R	1.47	1818	424	112	1.54	1940	408
2-S	1.03	1705	402	153	1.08	1869	398
2-R	0.77	1623	534	180	0.81	1811	542

Fig. 2-11. Two-stage potassium turbine results

	P (LB/IN. ²)	T (°R)	γ_e	γ
STATIC, INLET	171	2543	SUPER-HEATED	-
1-R	121	2344	0.0146	0
5-S	28	1774	0.135	0.0117
6-S	15.4	1811	0.154	0.134
6-R	11.2	1754	0.175	0.156

Fig. 2-12. Six-stage potassium turbine

GROUP	NUMBER (DROPS/LB)	AT EXIT 5-S		AT EXIT 6-S	
		r_1 (MICRONS)	γ_1 (MICRONS)	r_1 (MICRONS)	γ_1 (MICRONS)
1	7.26×10^{11}	0.564	0.0007	0.795	0.002
2	1.7×10^{12}	0.545	0.0015	0.783	0.0045
3	3.8×10^{13}	0.363	0.0102	0.66	0.0604
4	6.2×10^{13}	0.22	0.0036	0.58	0.0672
		$N_{TOTAL} = 1.02 \times 10^{14}$ $\bar{r} = 0.304$		$N_{TOTAL} = 1.02 \times 10^{14}$ $\bar{r} = 0.62$	

Fig. 2-13. Drop size distribution in six-stage potassium turbine

	9TH ROTOR INLET					9TH STATOR EXIT					9TH STATOR INLET	
	HUB	1/4	MEAN DIA.	3/4	TIP	HUB	1/4	MEAN DIA.	3/4	TIP	MEAN DIA.	
DIAMETER (IN.)	78.63	98.63	118.63	138.63	158.63	78.4	98.4	118.4	138.4	158.4		
EXIT FLOW ANGLE (DEG.)	26.3	24.4	24.2	24.7	25.6	27.6	25.8	25.6	26.1	26.9		
STATIC PRESSURE (PSIA)	1.011	1.285	1.487	1.637	1.751	1.021	1.289	1.487	1.635	1.746	2.263	
TEMPERATURE (°F)			115.6					115.6			130.4	
SPECIFIC VOLUME (CFPP)	282.0	226.0	197.5	181.0	170.2	280.0	226.0	197.5	181.0	170.5	134.0	
JET VELOCITY (FPS)	1390.1	1192.5	1051.2	945.0	862.9	1383.0	1190.0	1051.0	947.0	866.0		
WHEEL SPEED (FPS)	617.6	774.6	931.7	1088.8	1245.9							
INLET VELOCITY TO NEXT ROW (FPS)	880.0	583.6	433.0	458.0	597.4	884.6	597.6	454.7	479.1	613.3		

Fig. 2-14. Yankee turbine, fluid properties along height of blade

ROW	6 ROTOR INLET				6 STATOR EXIT				6 STATOR INLET	
	1/4	M	3/4	T	H	1/4	M	3/4	T	M
DIAMETER (IN.)	5.82	6.82	7.82	8.82	4.75	5.75	6.75	7.75	8.75	
GAUGING										
EXIT FLOW ANGLE (DEG.)	28.57	30.60	32.64	34.64	28.28	30.30	32.43	34.57	36.62	
STATIC PRESSURE (PSIA)	18.76	19.69	20.35	20.83	17.43	18.79	19.69	20.33	20.80	22.04
TEMPERATURE (°F)							1454.			1477.
SPECIFIC VOLUME (CFPP)	21.70	20.81	20.23	19.82	23.13	21.67	20.81	20.25	19.85	
JET VELOCITY (FPS)	900.6	811.7	744.5	692.5	1021.0	898.3	811.7	746.5	696.2	
AXIAL VELOCITY (FPS)										
WHEEL SPEED (FPS)	609.5	714.2	818.9	923.6						
INLET FLOW ANGLE TO NEXT ROW (DEG.)										
INLET VELOCITY TO NEXT ROW (FPS)										

Fig. 2-15. Potassium turbine fluid properties along height of blade, sixth stage

		δ / l	δ / l	δ / l	δ -IN.	C_f	τ -PPSF
EIGHT ROTOR BLADE AT 3/4 BLADE HEIGHT WHERE $D = 125.3"$, $l = 3.15$ AND $Re_l = 2.49 \times 10^5$	PRESSURE SIDE	0.001180		0.001664	0.0308	0.00606	0.677
	SUCTION SIDE	0.003831		0.005938	0.0865	0.00348	0.390
	TOTAL	0.005011		0.007602	0.1173		
NINTH STATOR BLADE AT 3/4 BLADE HEIGHT WHERE $D = 137.0"$, $l = 11.1"$ AND $Re_l = 6.1 \times 10^5$	PRESSURE SIDE	0.000829		0.001168	0.0761	0.00504	0.392
	SUCTION SIDE	0.002705		0.004085	0.2234	0.00317	0.246
	TOTAL	0.003534		0.005253	0.2995		

Fig. 2-16. Yankee turbine calculated boundary layer properties

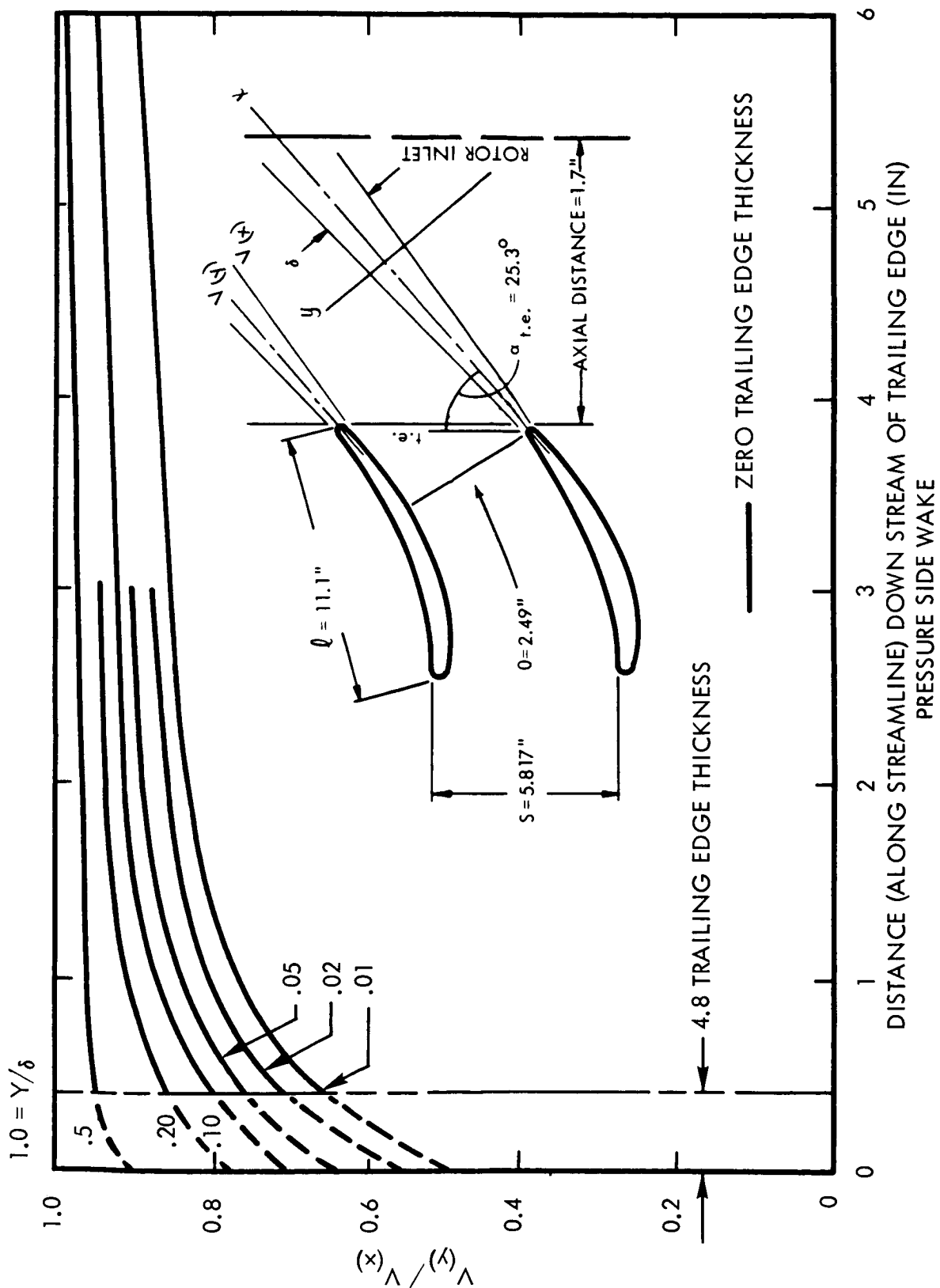


Fig. 2-17. Wake pressure side velocities, ninth Yankee turbine stator

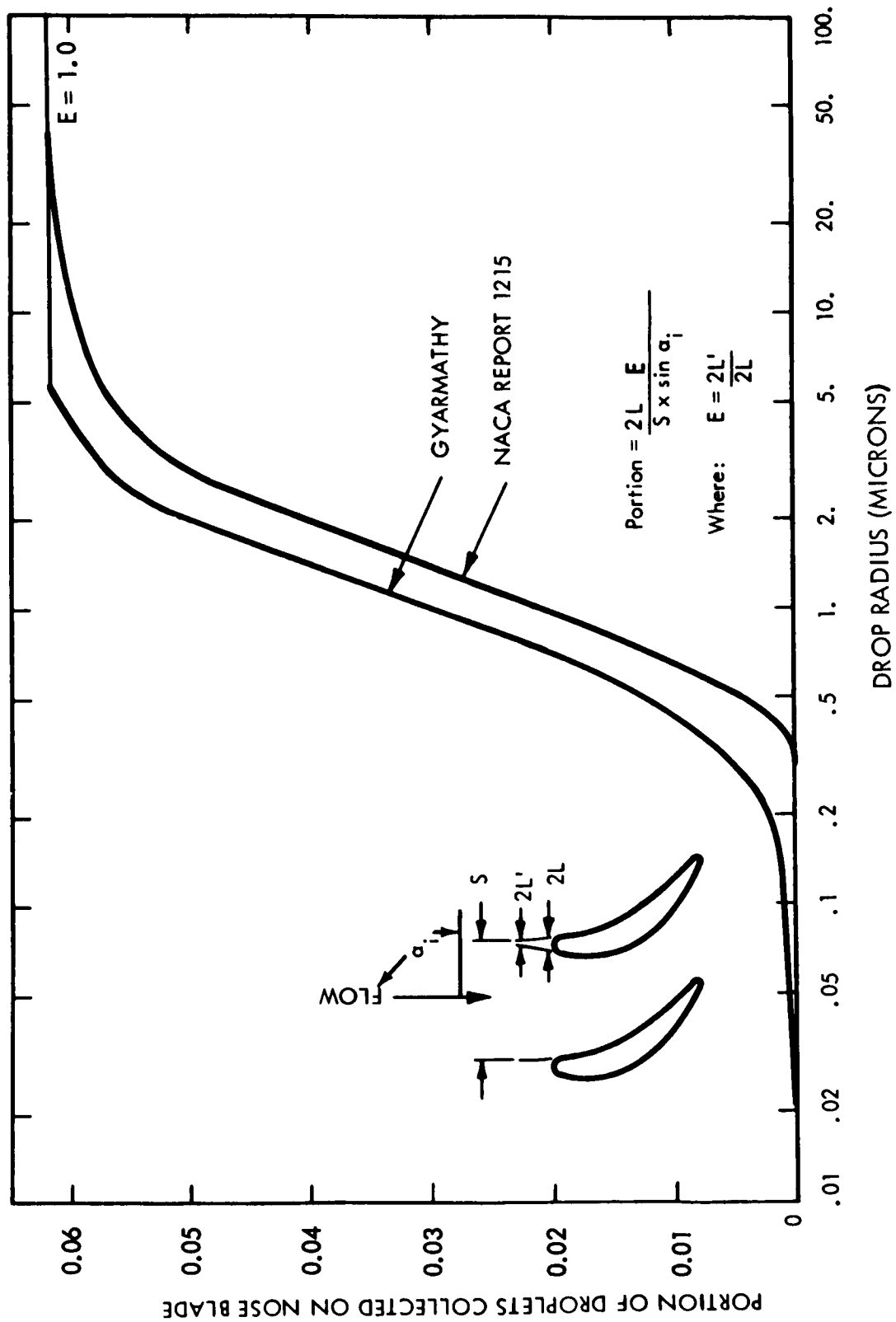


Fig. 2-18. Portion collected on nose, ninth Yankee turbine stator

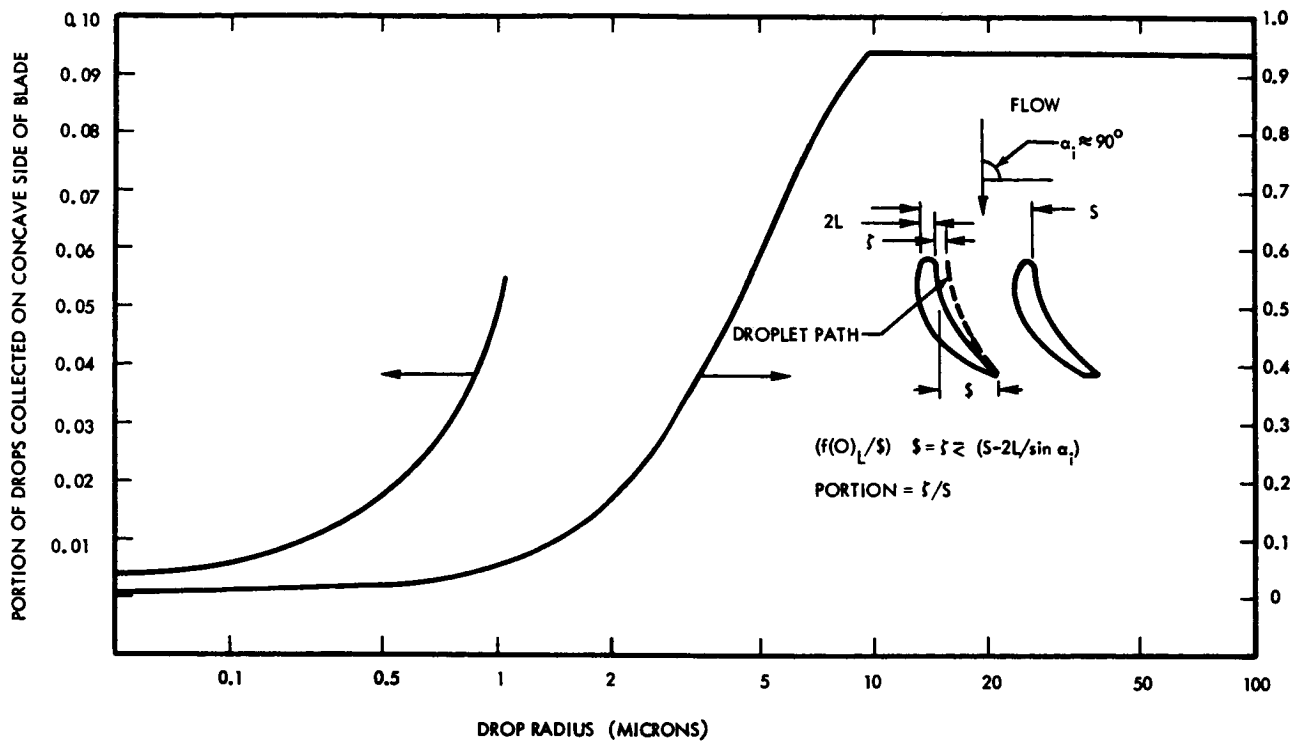


Fig. 2-19. Portion collected, concave side, ninth Yankee turbine stator

ϵ	$\dot{m}_L \times 10^6$ slugs/sec	$\delta \times 10^6$ (f)	$\bar{\mu}$ (fps)	Re_L
0.005	2.67	4.31	3.10	6.6
0.01	5.34	5.94	4.51	13.1
0.02	10.68	8.01	6.67	26.2
0.05	26.7	11.23	11.90	65.6
0.10	53.4	13.60	19.60	131.0

Fig. 2-20. Potassium turbine moisture transport on sixth stator blade

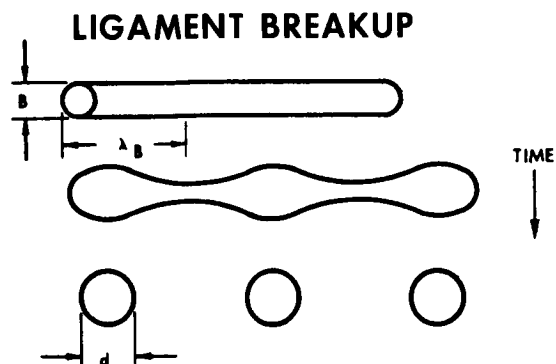
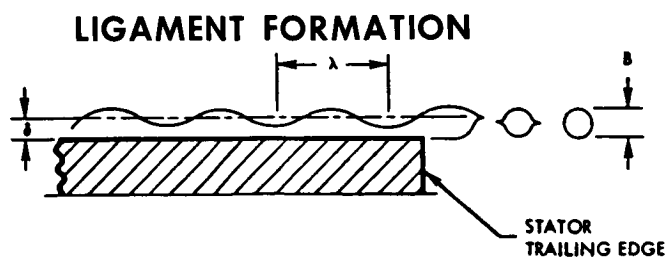


Fig. 2-21. Sheet atomization model

AVERAGE PRIMARY DROP SIZE EQUATIONS

$$\bar{d} = 17.0 \left(\frac{\dot{m}_L \mu_L}{\rho_L \left(r_s + \frac{\dot{m}_L U_s}{X} \right)} \right)^{1/4} \left(\frac{\mu_L}{r_s} \sqrt{\frac{\sigma_L}{\rho_L}} \right)^{1/3}$$

Fig. 2-22. Primary atomization equations

$$\bar{d} = 17.0 \left(\frac{\mu_L X}{\rho_L U_s} \right)^{1/4} \left(\frac{\mu_L}{r_s} \sqrt{\frac{\sigma_L}{\rho_L}} \right)^{1/3}$$

PRIMARY DISTRIBUTION EQUATION

$$\frac{dN}{dz} = a z^2 e^{-b z^n}$$

YANKEE TURBINE $n=1$.6 STAGE POTASSIUM TURBINE $n=1/4$.

ONE-DIMENSIONAL TRAJECTORY
EQUATION

$$\frac{d^2 x}{dt^2} = \frac{dV_d}{dt} = 0.75 C_D \frac{\rho_g}{\rho_d} \frac{(V_{rel})^2}{D_d}$$

TIME TO COMPLETION
OF BREAKUP

$$t = 2.4 \left(\frac{D_d}{V_{rel}} \right) \sqrt{\frac{\epsilon_d}{\epsilon_g}}$$

SECONDARY BREAKUP CRITERION

$$We_d = \frac{\rho_g (V_{rel})^2 D_d}{g \sigma_d}$$

MASS MEAN DIAMETER
OF SECONDARY DROPS

$$D_{3-0} = \left[\frac{136 g^{3/2} \mu_d \sigma_d^{3/2} D_d^{1/2}}{\rho_g^2 \rho_d^{1/2} V_{rel}^4} \right]^{1/3}$$

TIME TO START OF BREAKUP

$$t' = 1.1 \left(\frac{D_d}{V_{rel}} \right) \sqrt{\frac{\rho_d}{\rho_g}}$$

SECONDARY DROP SIZE
DISTRIBUTION

$$\frac{dV}{dz} = \frac{\pi a}{6} z^5 e^{-bz^n}$$

Fig. 2-23. Secondary atomization equations

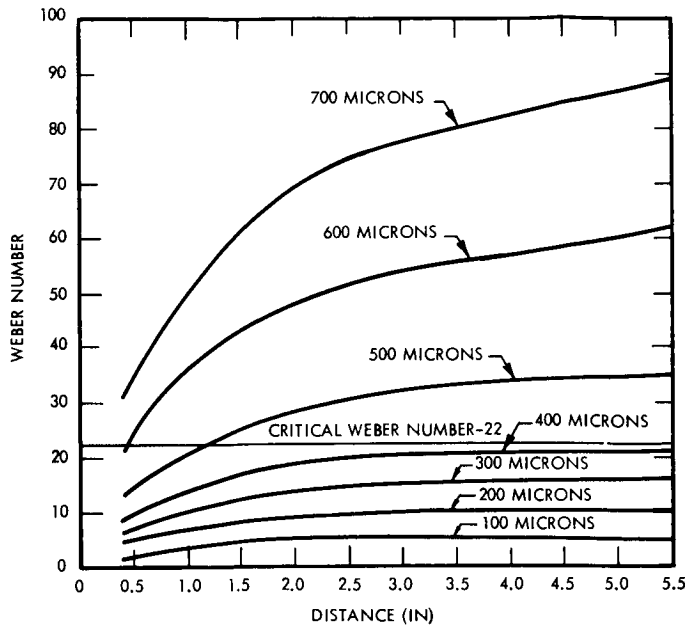


Fig. 2-24. Ninth Yankee stator wake, Weber number versus distance at $y/y_0 = 0.01$ suction side

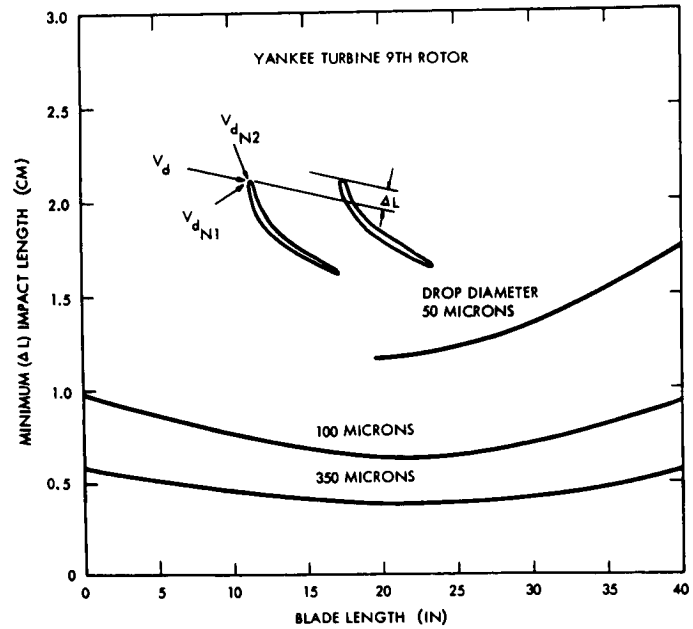


Fig. 2-25. Axial length impacted (minimum), Yankee turbine

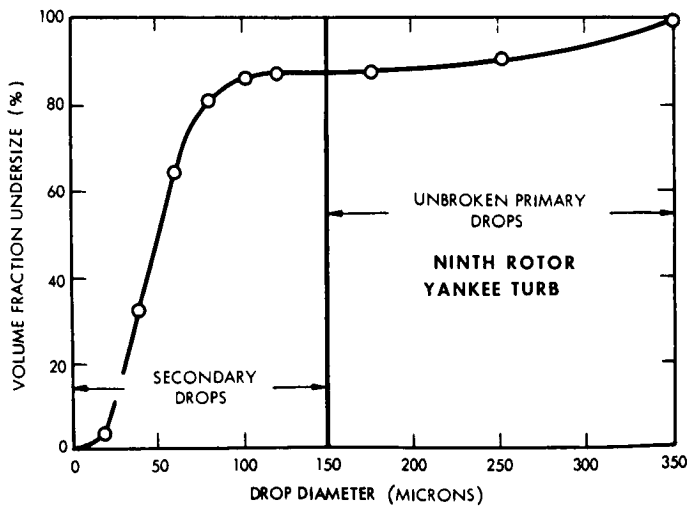


Fig. 2-26. Impacting drop size distribution, Yankee turbine ninth rotor blade

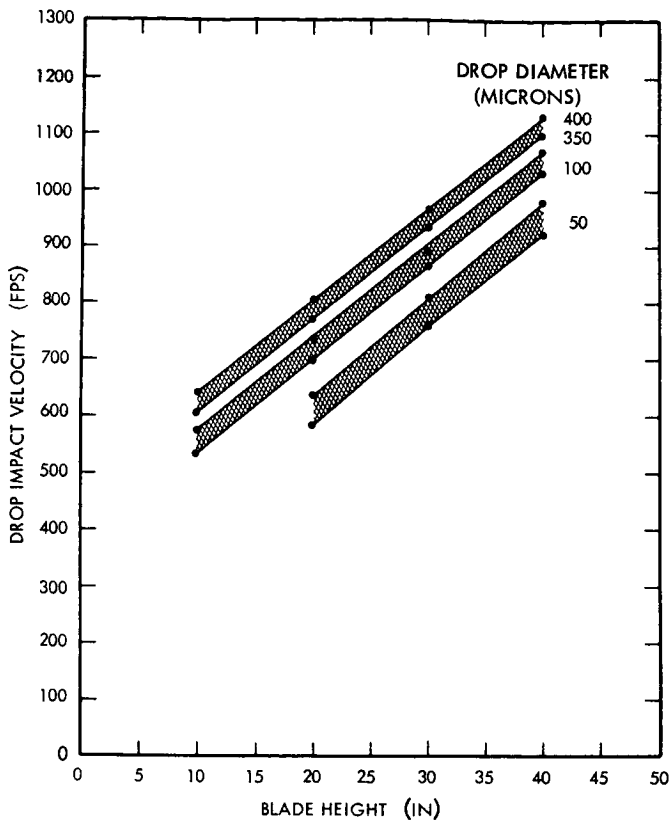


Fig. 2-27. Drop impact velocities, ninth rotor blade of Yankee turbine

DROP DIAMETER (MICRONS)	VOLUME (% UNDERSIZE)
10	4
20	16
$41 = \bar{d}$	45
60	62
90	80
120	89
180	96
240	98
420	99.8

Fig. 2-28. Primary atomization in six-stage potassium turbine

DOWNSTREAM DISTANCE (IN)	TIME (SEC)	VELOCITY (FPS)	WEBER NUMBER	REMARKS
0	-	-	-	STATOR TRAILING EDGE
0.072	0	0	12.7	4.8 TRAILING EDGE THICKNESSES
0.125	$0.075 (10^{-3})$	108	10.3	
0.250	$0.148 (10^{-3})$	177	10.0	
0.289	$0.165 (10^{-3})$	190	9.9	ROTOR INLET

SIXTH STATOR, SUCTION SIDE WAKE, $Y/\delta = .01$, $3/4$ BLADE HEIGHT, 75μ DIA. DROP

CALCULATED TIME OF FRACTURE - $.05 (10^{-3})$ SEC.

SMD - 40μ (NUKIYAMA - TANASAWA EQ.)

Fig. 2-29. Secondary atomization in six-stage potassium turbine

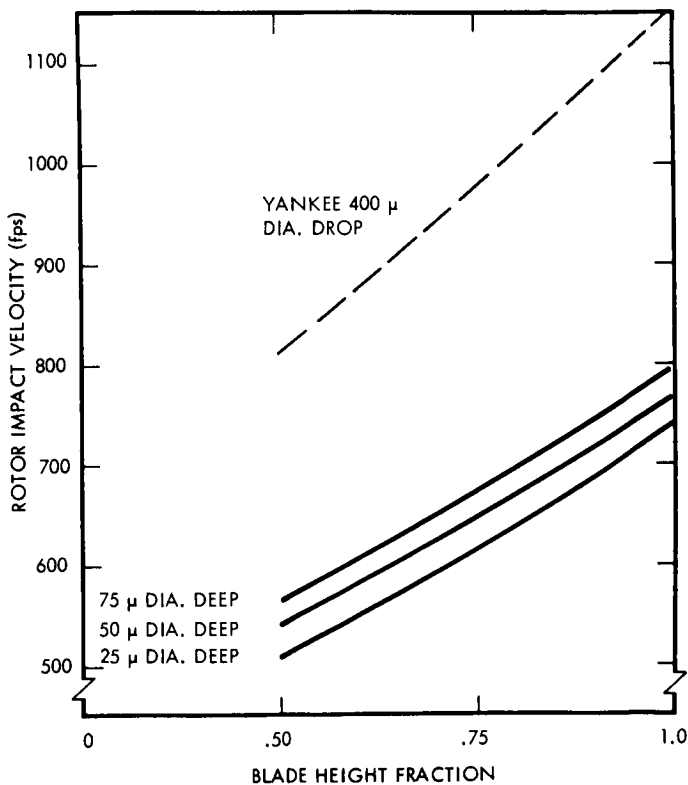


Fig. 2-30. Maximum impact velocities on six-stage potassium turbine

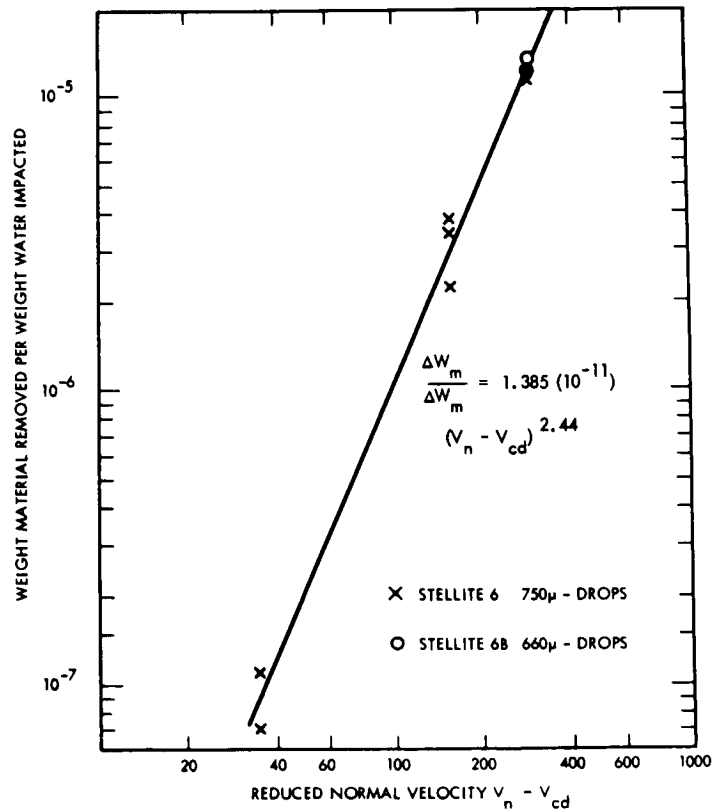


Fig. 2-31. Stellite erosion rates, data from Pearson; reduced normal velocity ($V_n - V_{cd}$)

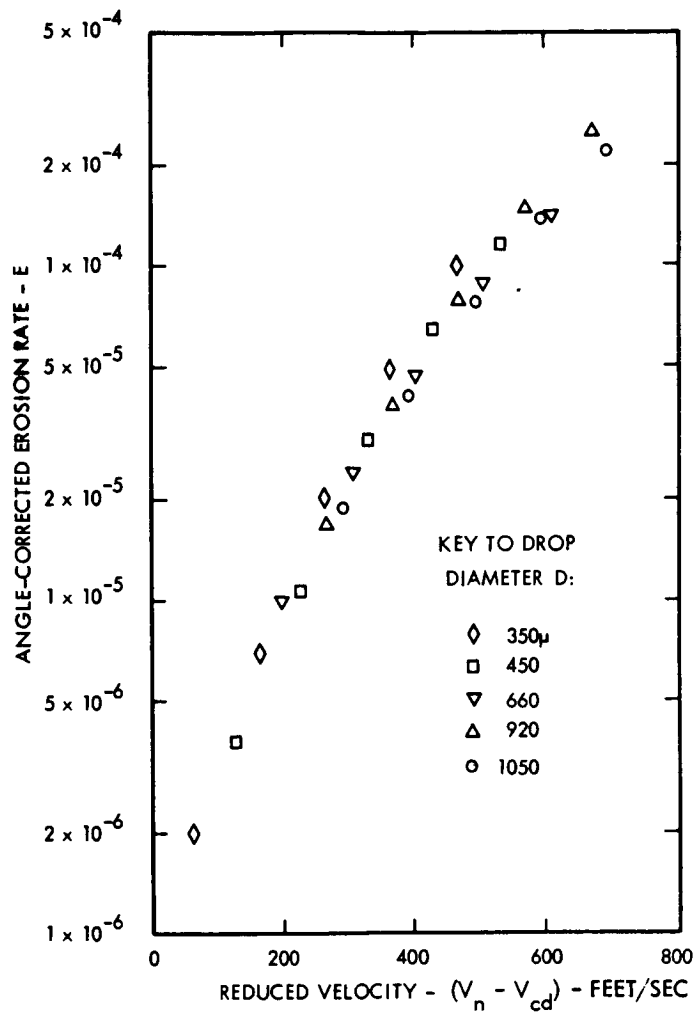


Fig. 2-32. Correlation of data of Pearson by use of critical velocity

FLOW (STEAM PLUS WATER)	364,000 KG/HR
BULK MOISTURE AT NINTH STATOR	13.5%
BULK MOISTURE AVERAGE PARTICLE RADIUS	0.44 μ
PORTION OF BULK MOISTURE COLLECTED NINTH STATOR	2.5%
COLLECTED MOISTURE IMPACTING NINTH ROTOR	1230 KG/HR
AVERAGE LOCAL RATE OF IMPACTING OF MOISTURE	62 GM/CM/HR
AVERAGE LOCAL RATE PER 13,000 HOURS	802 KG/CM

Fig. 2-33. Yankee turbine ninth rotor liquid impact rates

FLOW (VAPOR PLUS LIQUID)	9100 KG/HR
BULK MOISTURE SIXTH STATOR	14.3 %
BULK MOISTURE AVERAGE PARTICLE RADIUS	0.55 μ
PORTION OF BULK MOISTURE COLLECTED SIXTH STATOR	6 %
COLLECTED MOISTURE IMPACTING SIXTH STATOR	78 KG/HR
AVERAGE LOCAL RATE OF IMPACTING OF MOISTURE	382 GM/CM/HR
AVERAGE LOCAL RATE/10,000 HOURS	3820 KG/CM

Fig. 2-34. Sixth rotor impact rates for six-stage potassium turbine

	DROP SIZE INTERVAL (MICRONS)	BLADE LENGTH FROM HUB (IN.)	EROSION RATE (GM/CM ² /HR)	AVERAGE DEPTH EROSION IN 13,000 HRS (MILS)
PRESSURE SIDE WAKE	350 - 275	40	0.45 (10^{-5})	2.8
	350 - 300	38	0.17 (10^{-5})	1.0
	350 - 320	36	0.05 (10^{-5})	0.2
SUCTION SIDE WAKE	400 - 275	40	2.5 (10^{-5})	15.5
	400 - 300	38	1.4 (10^{-5})	8.6
	400 - 320	36	0.9 (10^{-5})	5.5

Fig. 2-35. Calculated erosion Yankee turbine ninth rotor, maximum stable drop size criterion, $W_e = 22$

REFERENCES

- 2-1. Gyarmathy, G., The Bases for a Theory of the Wet Steam Turbine. Juris-Verlag, Zurich, 1962
- 2-2. Gardner, G. C., "Events Leading to Erosion in the Steam Turbine," Proc. Inst. Mech. Eng., 178, Pt. 1, No. 23, pp. 593--623, 1963-64.
- 2-3. Oswatitish, K. Z., Ver. dent Ing., 86, p. 702, 1942.
- 2-4. Katz, J. L., Saltsburg, H., and Reiss, H., Nucleation in Associated Vapors, SCPP-65-32. North American Aviation Science Center, May 18, 1965.
- 2-5. Truckenbrodt, E., A Method of Quadrature for Calculations on the Laminar Boundary Layer in Case of Plane and Rotationally Symmetrical Flow, NACA-TM-1379. National Advisory Committee for Aeronautics, Washington, May 1955.
- 2-6. Lieblein, S., and Roudebush, W. H., Low-Speed Wake Characteristics of Two-Dimensional Cascade and Isolated Airfoil Sections, NACA-TN-3771. National Advisory Committee for Aeronautics, Washington, Oct. 1956.
- 2-7. Pearson, D., A Summary of the M. E. L. Experimental Data on Erosion, CEGB, RID Dept. (Gr. Brit.), Marchwood Engrg. Labs., RDD/M/M18, Job No. 30023, Nov. 1964.

3. LIMITED IMPACT EROSION AND METAL LOSSES IN
TWO-STAGE POTASSIUM TURBINES

W. F. Zimmerman and R. J. Rossbach
General Electric
Evandale, Ohio

(Presented by R. J. Rossbach)

Under NASA Contract NAS 5-1143 the General Electric Company designed, fabricated, and tested a two-stage 200-horsepower turbine (Fig. 3-1) for operation in wet potassium vapor to determine its performance and to study impact erosion and chemical corrosion of materials for Rankine-cycle space-power turbines. The tested materials (limited impact erosion and metal losses) in the two-stage potassium turbine were (Figs. 3-2 through 3-5):

- (1) Blades (slight corrosion only).
- (2) Erosion inserts (eroded).
- (3) Blade clips (eroded).
- (4) Honeycomb tip shroud (eroded).

During the 5000 hours of endurance testing, certain turbine parts were exposed for the entire time, while others were exposed for only 2000 or 3000 hours. The erosion and corrosion results obtained are presented herein. During endurance testing the following conditions were held: inlet vapor temperature, 1500°F; second-stage inlet vapor temperature, 1425°F; exit vapor temperature, 1240°F; rotative speed, 18,250 rpm; first-stage inlet vapor quality, 99.5%; second-stage inlet vapor quality, 97%; exit vapor quality, 92%; and second-stage tip speed, 770 ft/s.

Stationary erosion inserts of aged U-700, stress-relieved and recrystallized TZM molybdenum alloy, stress-relieved TZC molybdenum alloy, and AS-30 columbium alloy were installed behind the second-stage rotor blades in the path of droplets leaving the blade tips. The highest velocity attained by the droplets was the second-stage tip speed of 770 ft/s. Of these various materials, impact erosion was observed in only the U-700 inserts. The yield strength, fatigue strength, and strain energy properties of U-700 indicated it might be more resistant to impact erosion than the other materials which were not eroded. However, the presence of a diffusion zone of composition dissimilar to U-700 at the surface of the erosion pits indicated that

the basic properties of the U-700 might have changed ahead of the advancing impact erosion front.

Other evidences of impact erosion occurred only in the 3000-hour test at (1) the edges of the Type 316 stainless steel honeycomb tip shroud to a minor extent, and at (2) the advancing edges of the Rene' 41 blade clips on the aft side of the first- and second-stage wheels. Impact erosion was much less severe on the first-stage blade clips. No impact erosion was observed on the leading edges of the turbine blades. The following is a brief summary of the impact erosion observations:

- (1) Impact eroded.
 - (a) U-700 (erosion inserts).
 - (b) Rene' 41 (blade clips).
 - (c) Type 316 stainless steel (honeycomb tip shroud).
- (2) Not impact eroded.
 - (a) Blades: U-700, TZM, and TZC.
 - (b) Erosion inserts: TZM, TZC, and AS-30.

Minor blade-metal weight losses occurred as the result of liquid metal chemical corrosion which may have been accelerated by temporary increases in oxygen content in the potassium during startup of the system. Since the turbine and the 8-inch inlet vapor duct had been exposed to air prior to the 2000-hour test, this surface contamination was picked up by the distilled potassium coming from the boiler. In cleaning the turbine facility, the initial potassium condensate reached an oxygen level of 69 ppm or higher during the first two hours of the 2000-hour endurance test. However, in the next three hours the oxygen content dropped to below 15 ppm where it stayed for the remainder of the 2000-hour test. Since no contamination of the 8-inch inlet vapor duct occurred prior to the 3000-hour endurance test, the potassium oxygen content remained below 16 ppm for that entire test.

A brief summary of the 2000-hour and 3000-hour tests results (Fig. 3-6) is given in the following list.

- (1) 2000-hour test.
 - (a) No component impact erosion.
 - (b) No impact erosion of refractory alloy inserts.

- (c) Impact erosion of U-700 inserts.
 - (d) Minor blade corrosion (probably a function of system cleanliness and aerodynamic effects).
- (2) 3000-hour test.
- (a) No blade impact erosion.
 - (b) No impact erosion of refractory alloys (up to 5000 hours).
 - (c) Continued impact erosion of U-700 inserts.
 - (d) Blade clips impact erosion (worse in the second-stage).
 - (e) Minor honeycomb shroud impact erosion.
 - (f) Very limited blade corrosion.

The turbine and its components performed in a highly reliable manner, and were in very good condition after the total test period of 5000 hours. The absence of impact erosion on the rotating blades was particularly encouraging.

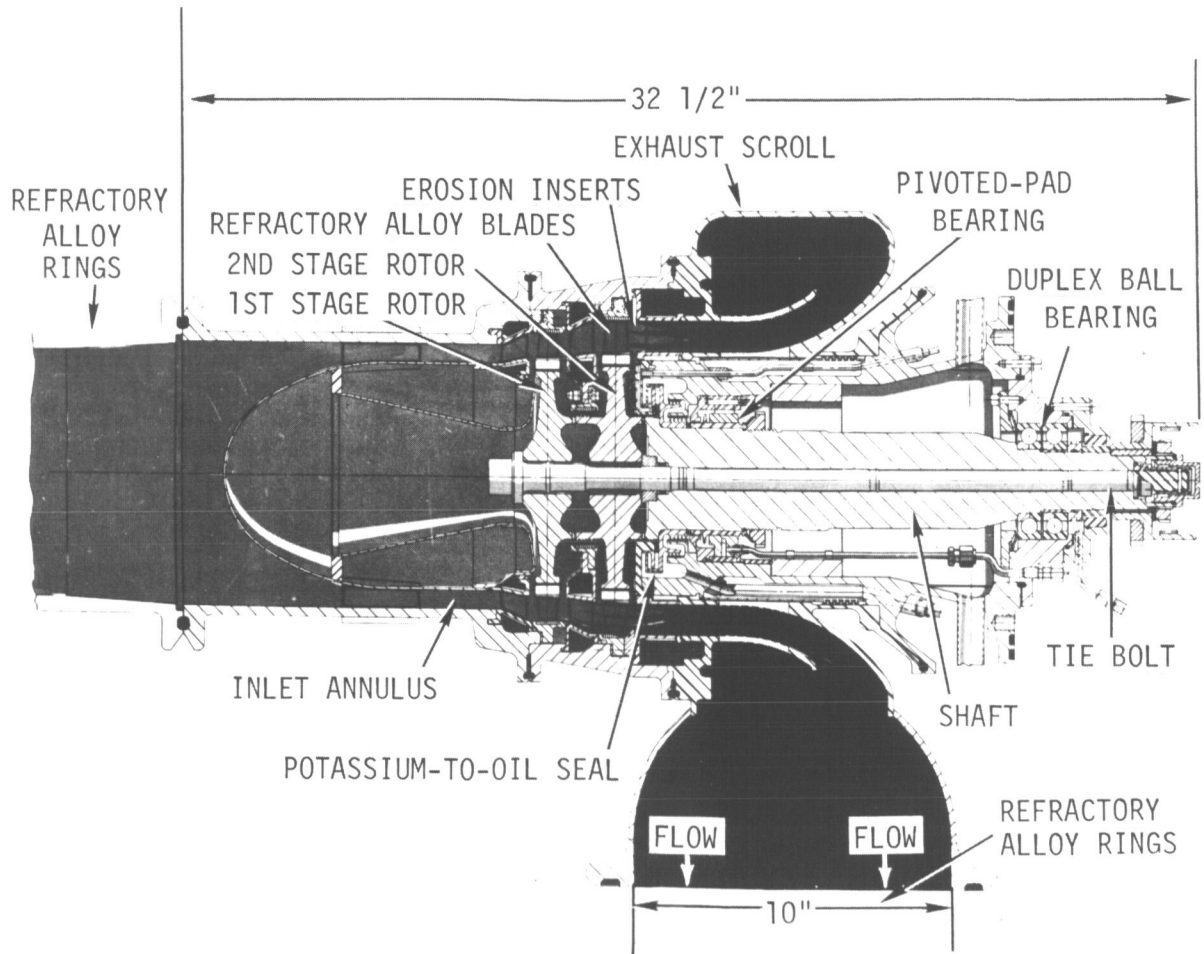


Fig. 3-1. Two-stage potassium turbine

SECOND STAGE TURBINE WHEEL AFTER 2000 HOUR ENDURANCE TEST (FORWARD FACE)

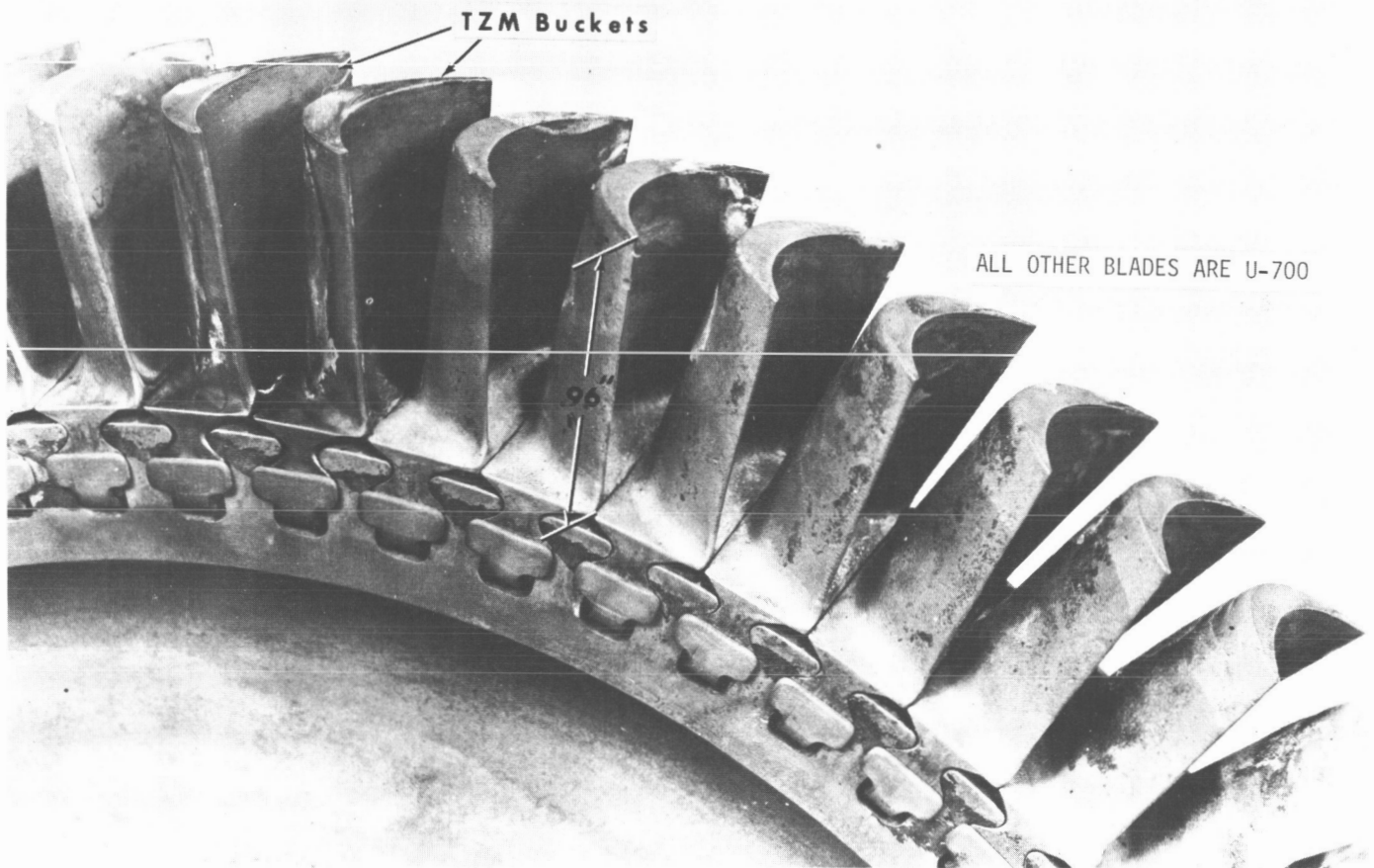


Fig. 3-2. Blade corrosion and lack of blade erosion

SECOND STAGE TURBINE WHEEL AFTER 2000 HOUR ENDURANCE TEST AND VAPOR BLASTING (FORWARD FACE)

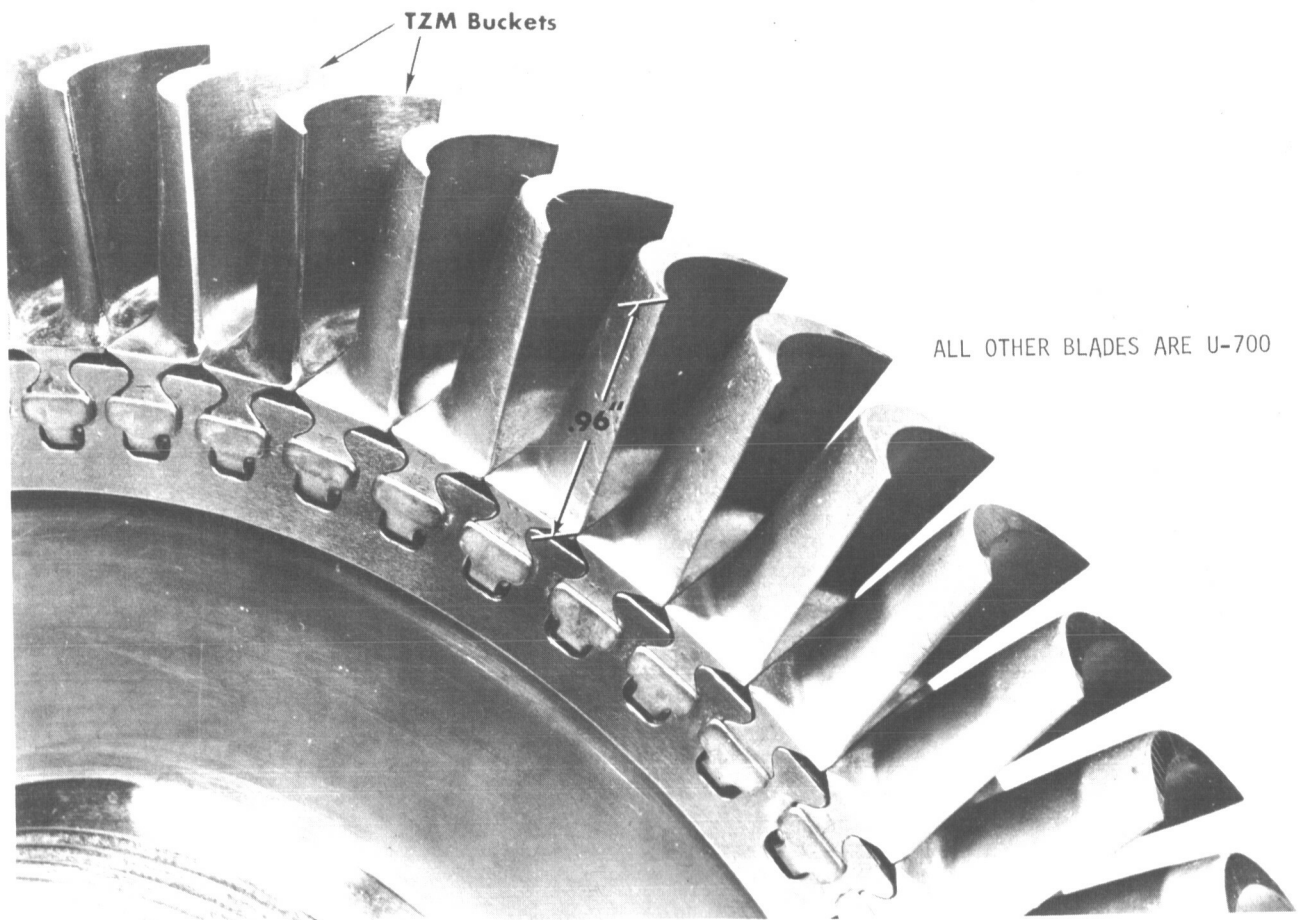


Fig. 3-2 (contd)

**SECOND STAGE TURBINE WHEEL
AFTER 5000 HOUR ENDURANCE TEST (FORWARD FACE)**



Fig. 3-2 (contd)

Convex Blade Surfaces After Potassium Turbine Test

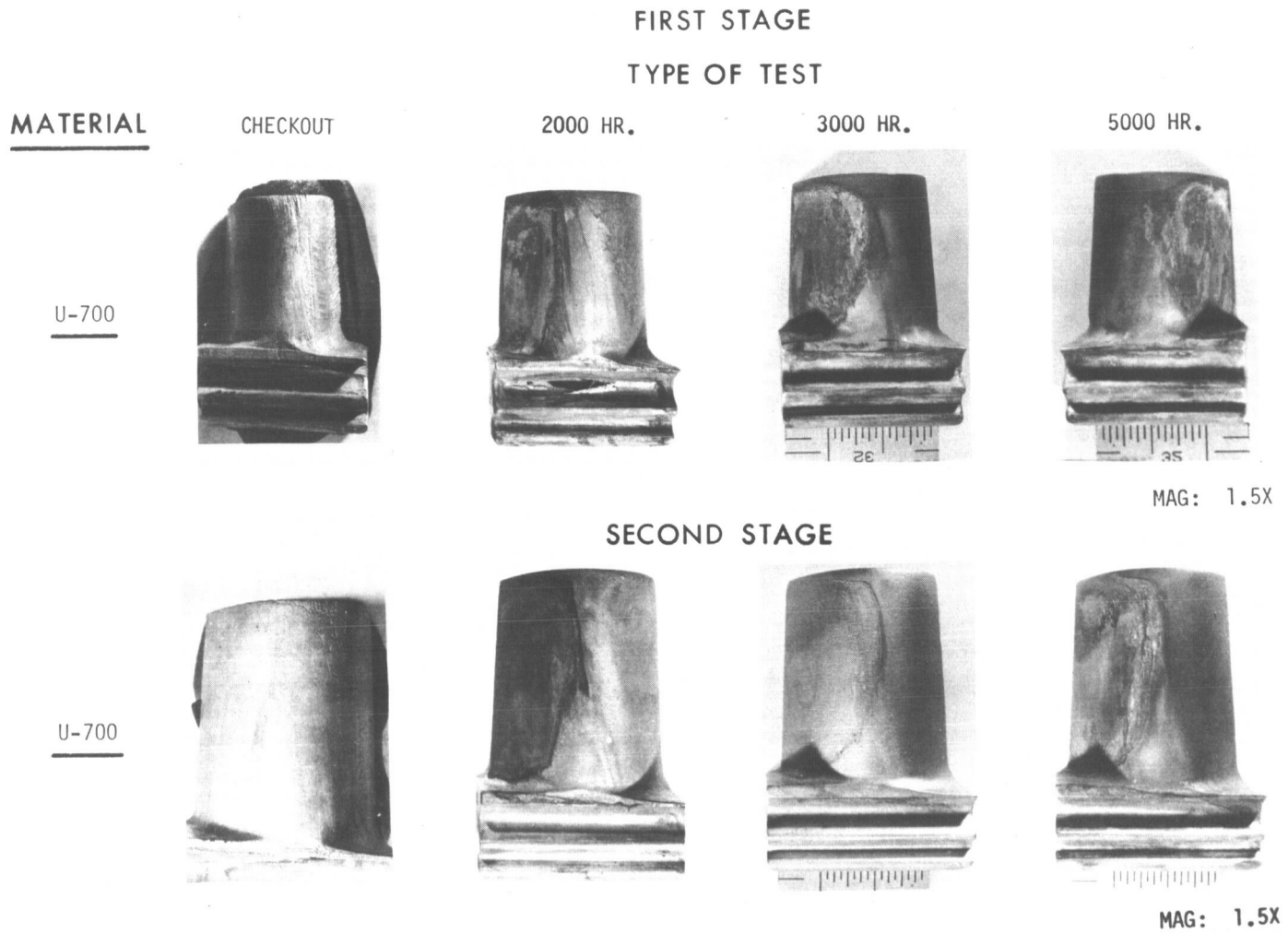


Fig. 3-2 (contd)

Convex Blade Surfaces After Potassium Turbine Test

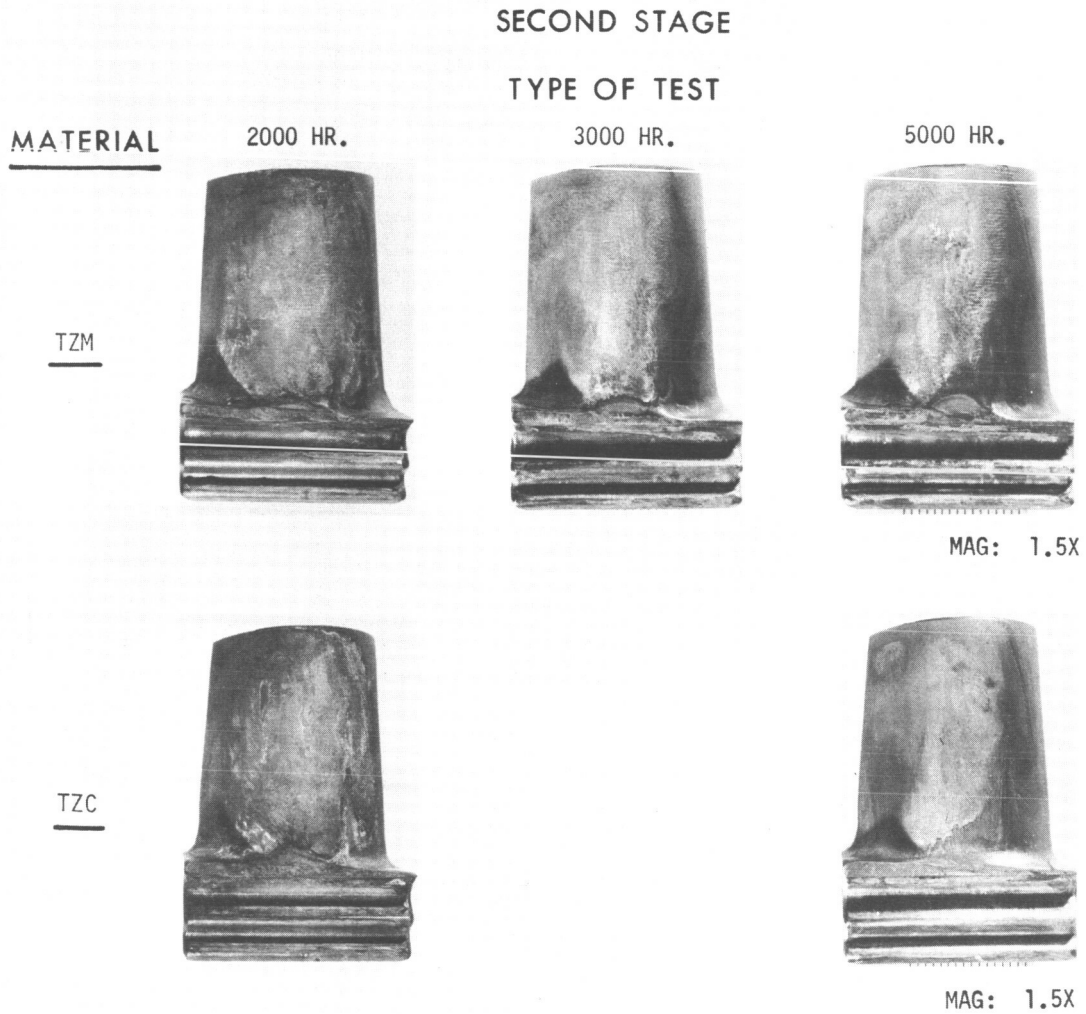


Fig. 3-2 (contd)

TZM Second Stage Leading And Trailing Edge Blade Effects (After 2000-Hour Test)

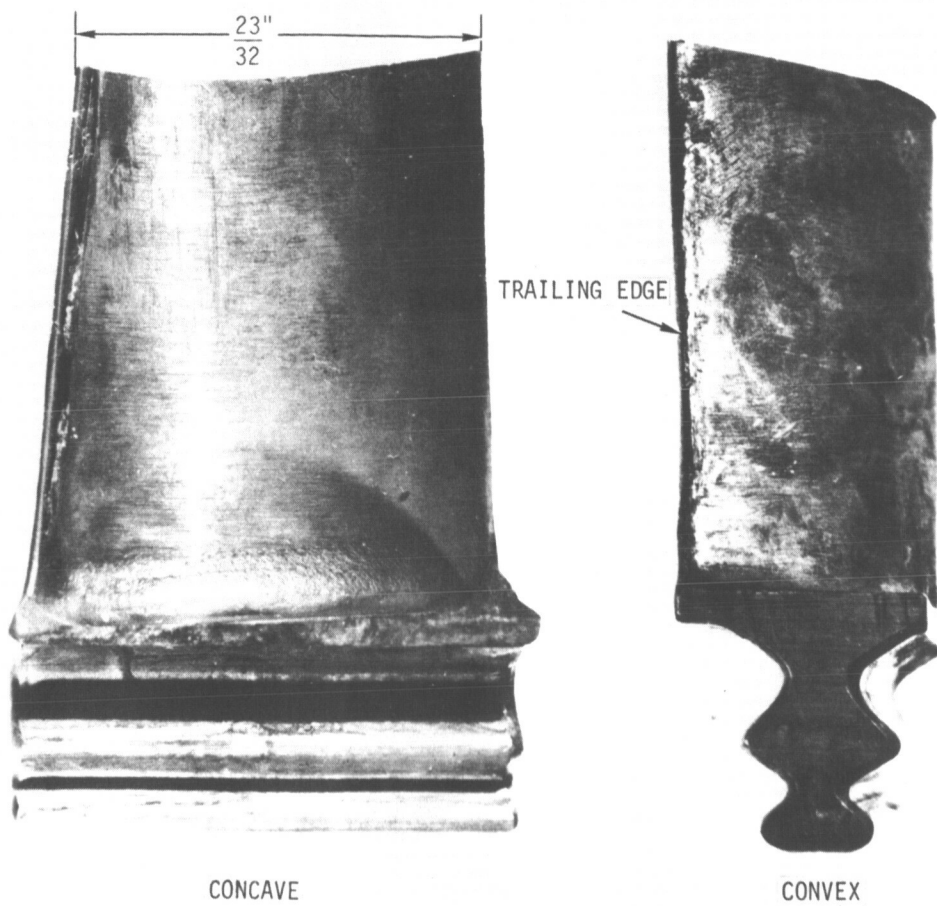
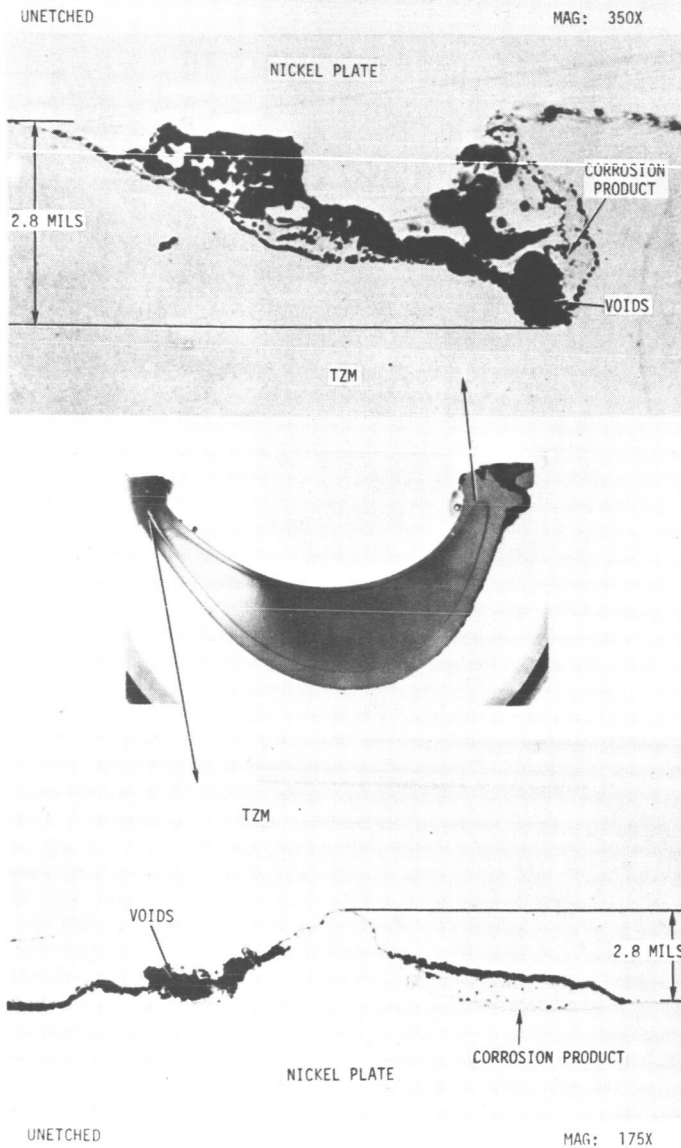


Fig. 3-2 (contd)

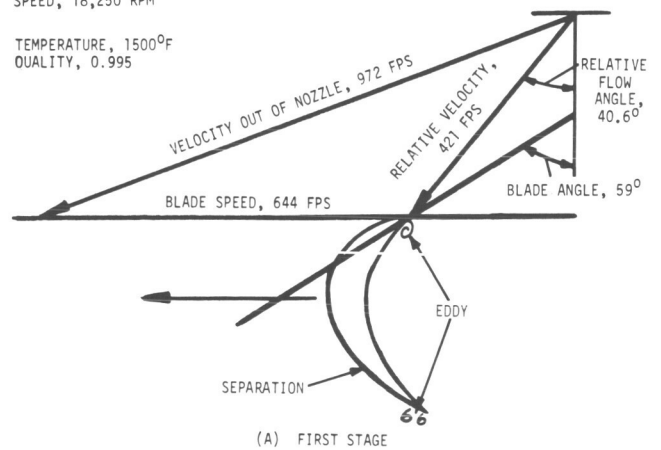
TZC BLADE SECTION (After 2000-Hour Test)



Flow Vector Diagrams For 2000-Hour Test

SPEED, 18,250 RPM

TEMPERATURE, 1500°F
QUALITY, 0.995



TEMPERATURE, 1390°F
QUALITY, 0.967

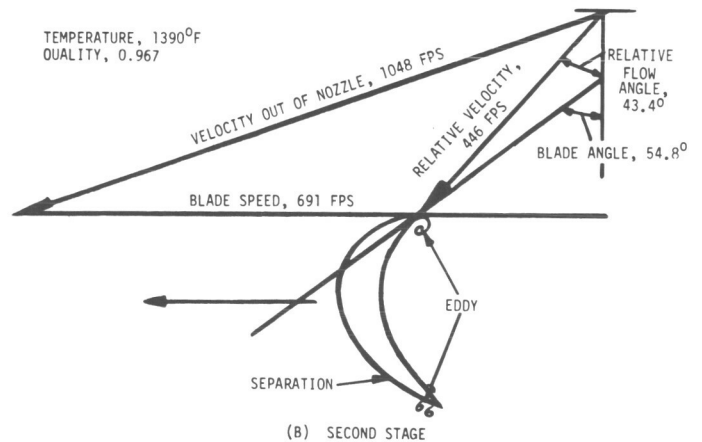
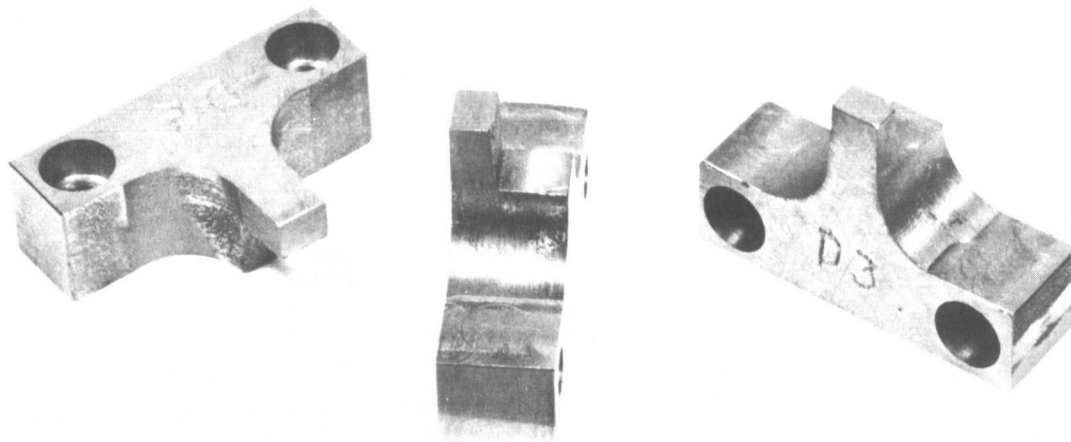


Fig. 3-2 (contd)

EROSION INSERTS



EROSION INSERTS INSTALLED IN SECOND STAGE SHROUD

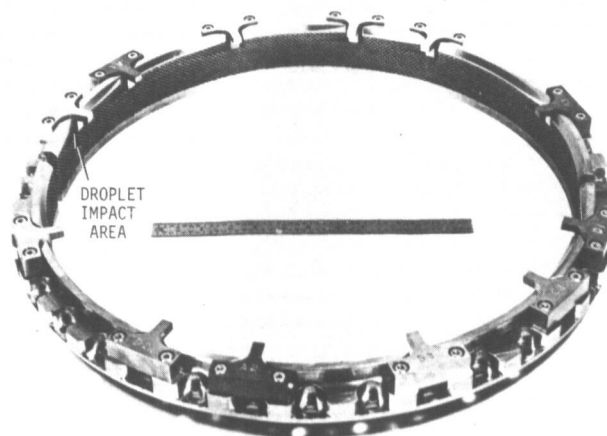


Fig. 3-3. Erosion inserts

Erosion Insert Tested In The Potassium Turbine

MATERIAL	COMPOSITION	CONDITION	SPECIMENS TESTED		
			2000-HOURS	3000-HOURS	5000-HOURS
U-700	0.06 C, 18.7 Co, 15.1 Cr, 4.48 Al, 3.40 Ti, 0.029 B, 5.15 Mo, Bal. Ni	2125°F - 2 HRS. A.C. 1975°F - 2 HRS. A.C. 1550°F - 2 HRS. A.C. 1400°F - 2 HRS. A.C.	A-1, A-2, A-3	A-1, A-2, A-4*, A-5*, A-6*	A-1, A-2
TZM	0.55 Ti, 0.09 Zr, 0.019 C, BAL. Mo	RECRYSTALLIZED; 2850°F - 1 HR.	B-1, B-2, B-3	NONE	NONE
TZM	0.55 Ti, 0.09 Zr, 0.19 C, BAL. Mo	STRESS RELIEVED 2200°F - 1 HR.	C-1, C-2, C-3	C-1, C-2	C-1, C-3
TZC	1.1 Ti, 0.13 Zr, 0.13 C, BAL. Mo	AS-ROLLED: 3092°F	D-1, D-2, D-3	D-1, D-3	D-1, D-3
AS-30	17.4 W, 0.98 Zr, 0.087 C, BAL. Co	STRESS RELIEVED 1900°F - 1 HR.	NONE	E-1*, E-2*, E-3*	NONE

* NEWLY INSTALLED FOR 3000-HOUR TEST

LIQUID POTASSIUM IMPACT SURFACE OF U-700 EROSION INSERTS (After 2000 Hr. Test)

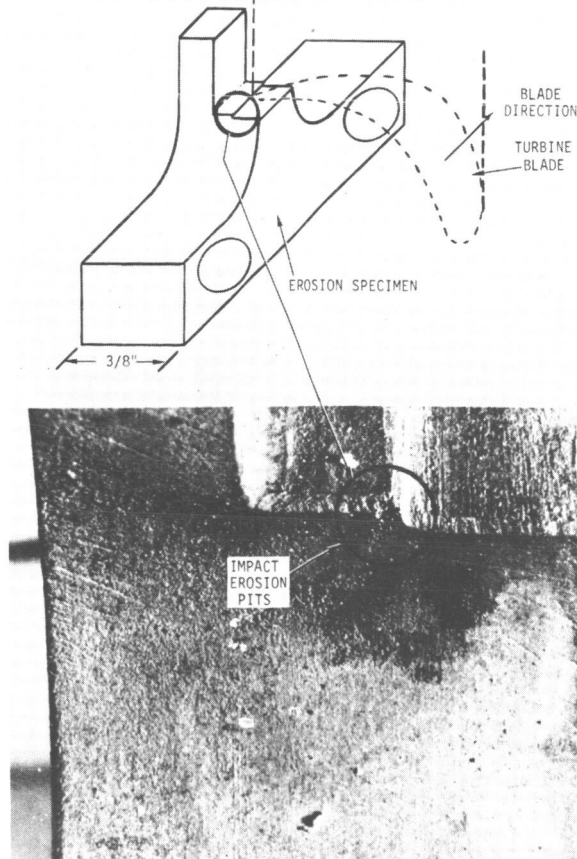


Fig. 3-3 (contd)

Comparison Of Impact Erosion On Various Materials After Turbine Test For 2000-, 3000- And 5000-Hours

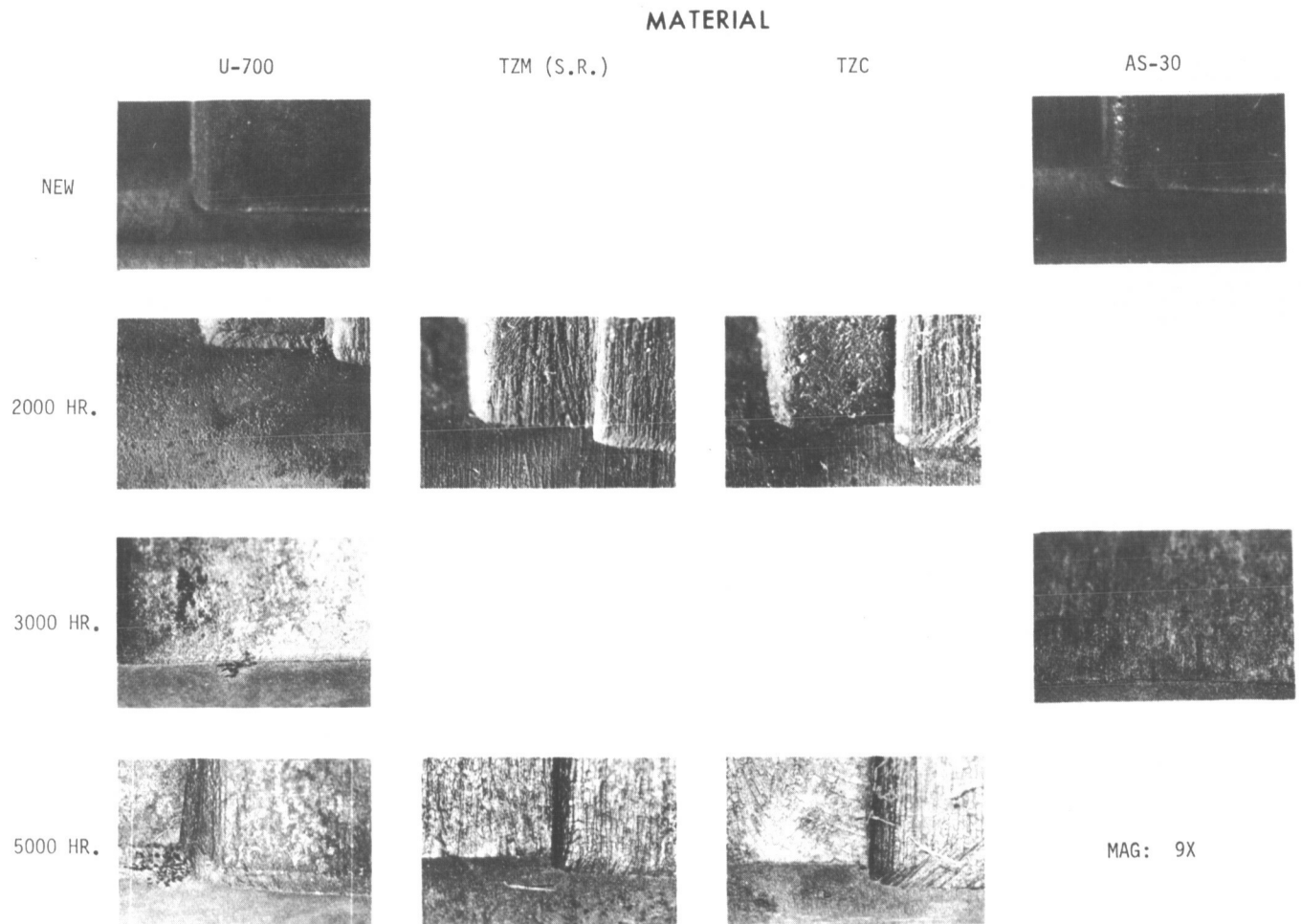
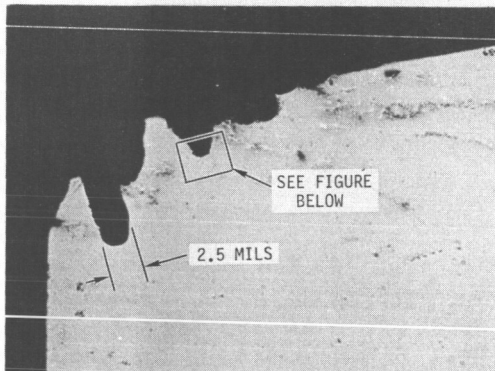


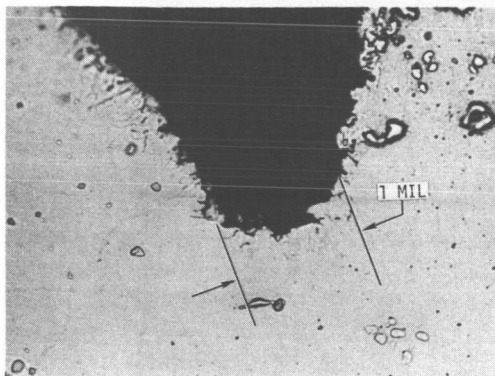
Fig. 3-3 (contd)

Impact Erosion Pits In U-700 Erosion Insert A-3 After 2000-Hour Test



ETCHANT: UNETCHED

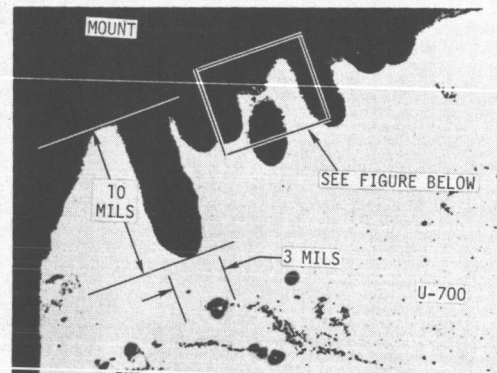
MAG: 100X



ETCHANT: UNETCHED

MAG: 1000X

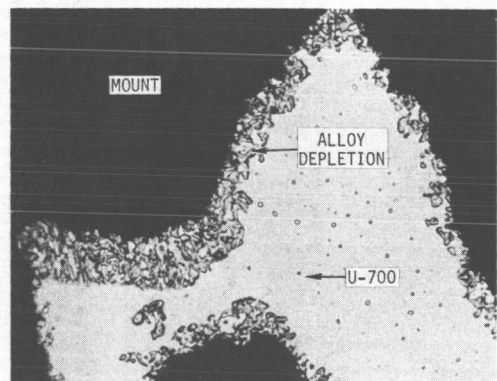
Impact Erosion Pits In U-700 Insert A-3



AT A SECOND PLANAR POSITION

ETCHANT: UNETCHED

MAG.: 100X



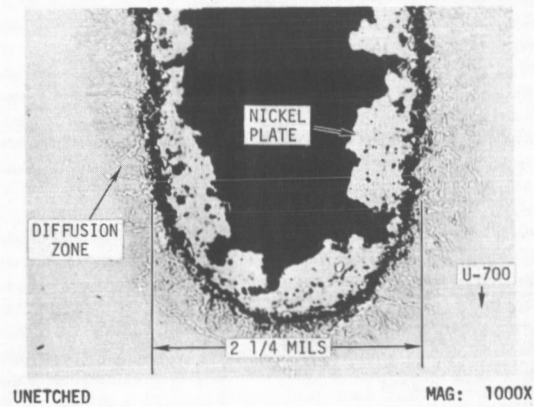
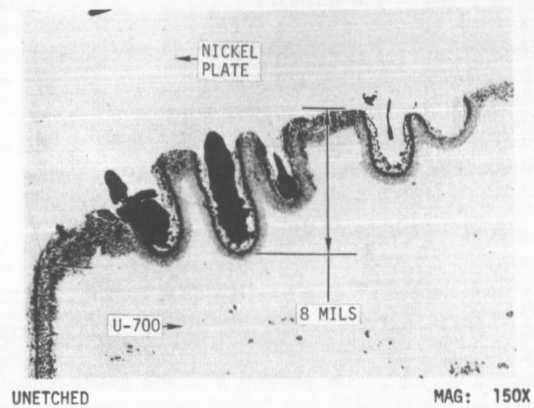
SEE ABOVE FIGURE

ETCHANT: 3% NITROL

MAG.: 1000X

Fig. 3-3 (contd)

U-700 EROSION INSERT (After 5000-Hour Test)



Impact Erosion On Stellite 6B Steam Turbine Blade Insert

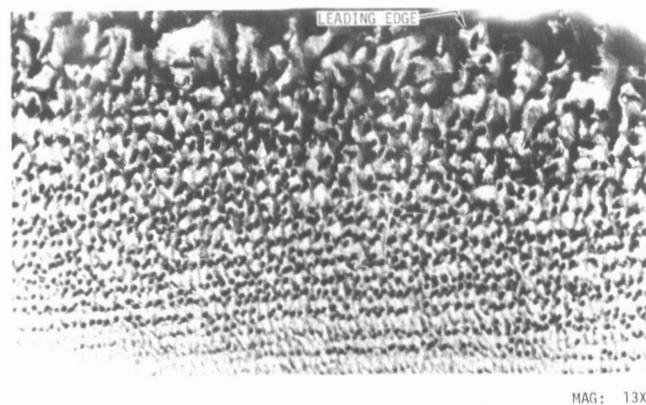
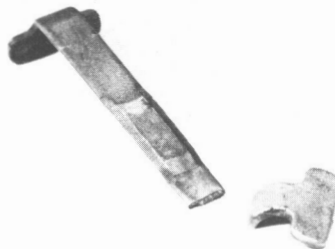


Fig. 3-3 (contd)



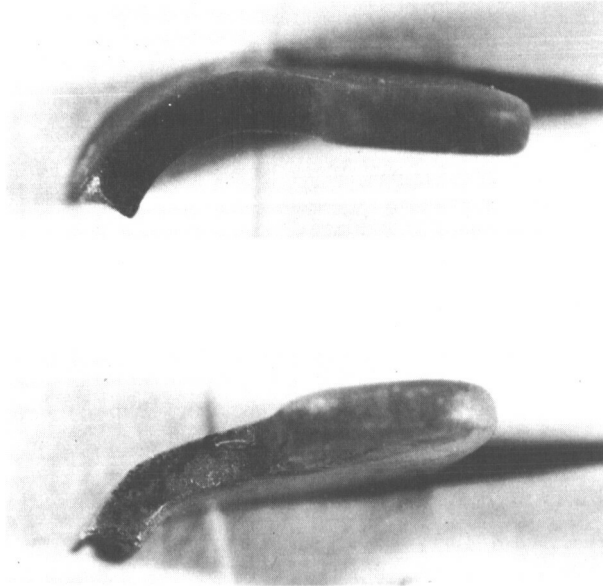
ERODED 2nd STAGE BLADE CLIP



MAG: 2.5X

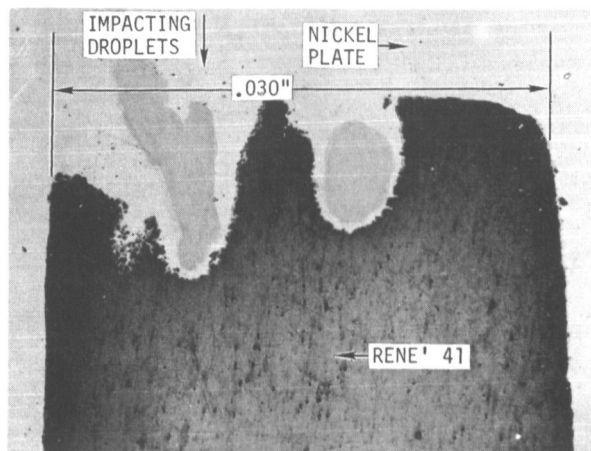
Fig. 3-4. Blade clips

**ERODED 2nd STAGE RENE' 41 BLADE CLIPS
(Aft Side)**



MAG: 14X

2nd STAGE RENE' 41 BLADE CLIP

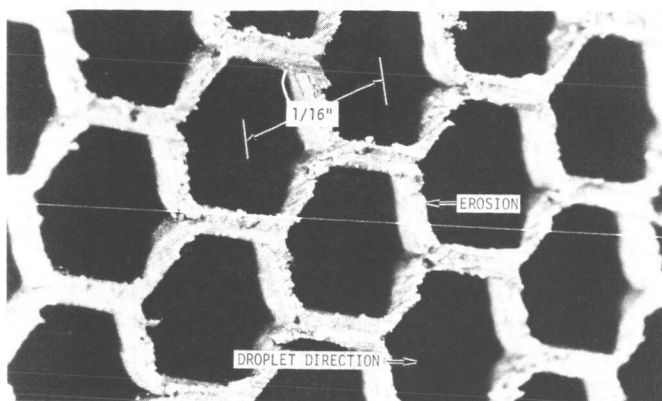


UNETCHED

MAG: 150X

Fig. 3-4 (contd)

Erosion Of Second Stage Honeycomb Tip Shroud



Yield And Fatigue Strength Of TZM And U-700

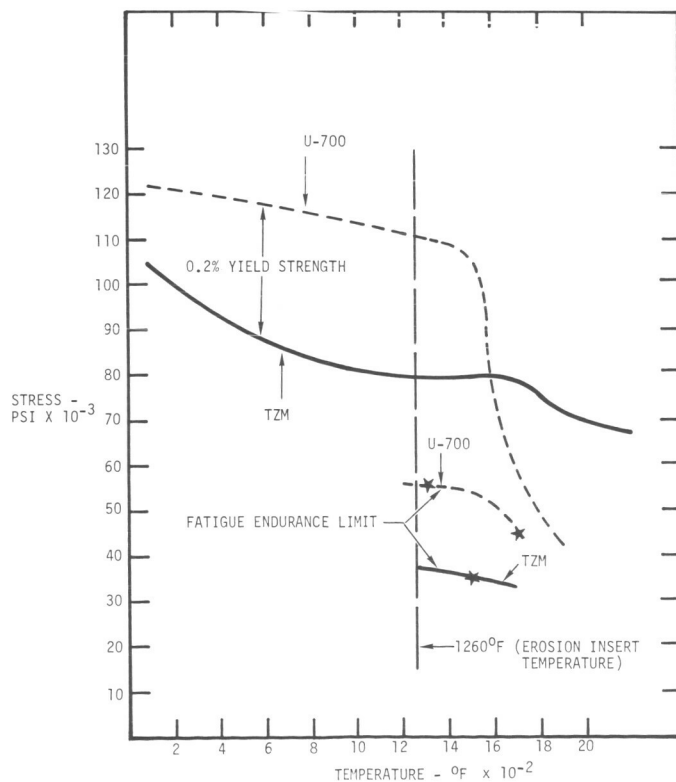


Fig. 3-5. Honeycomb tip shroud

Cavitation Damage Resistance vs Estimated Strain Energy

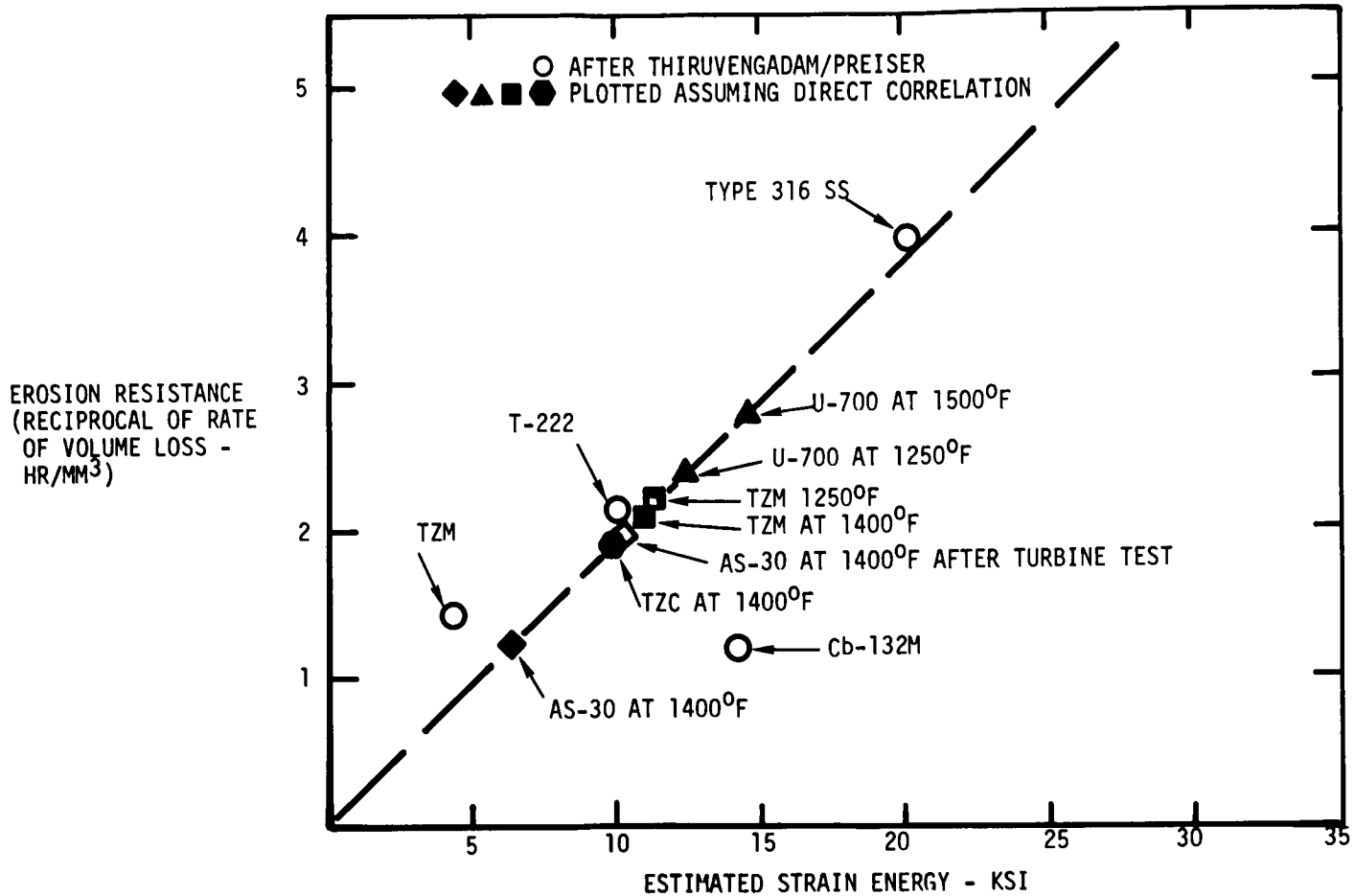


Fig. 3-5 (contd)

Blade Weight Changes After 2000-Hour And 3000-Hour Tests

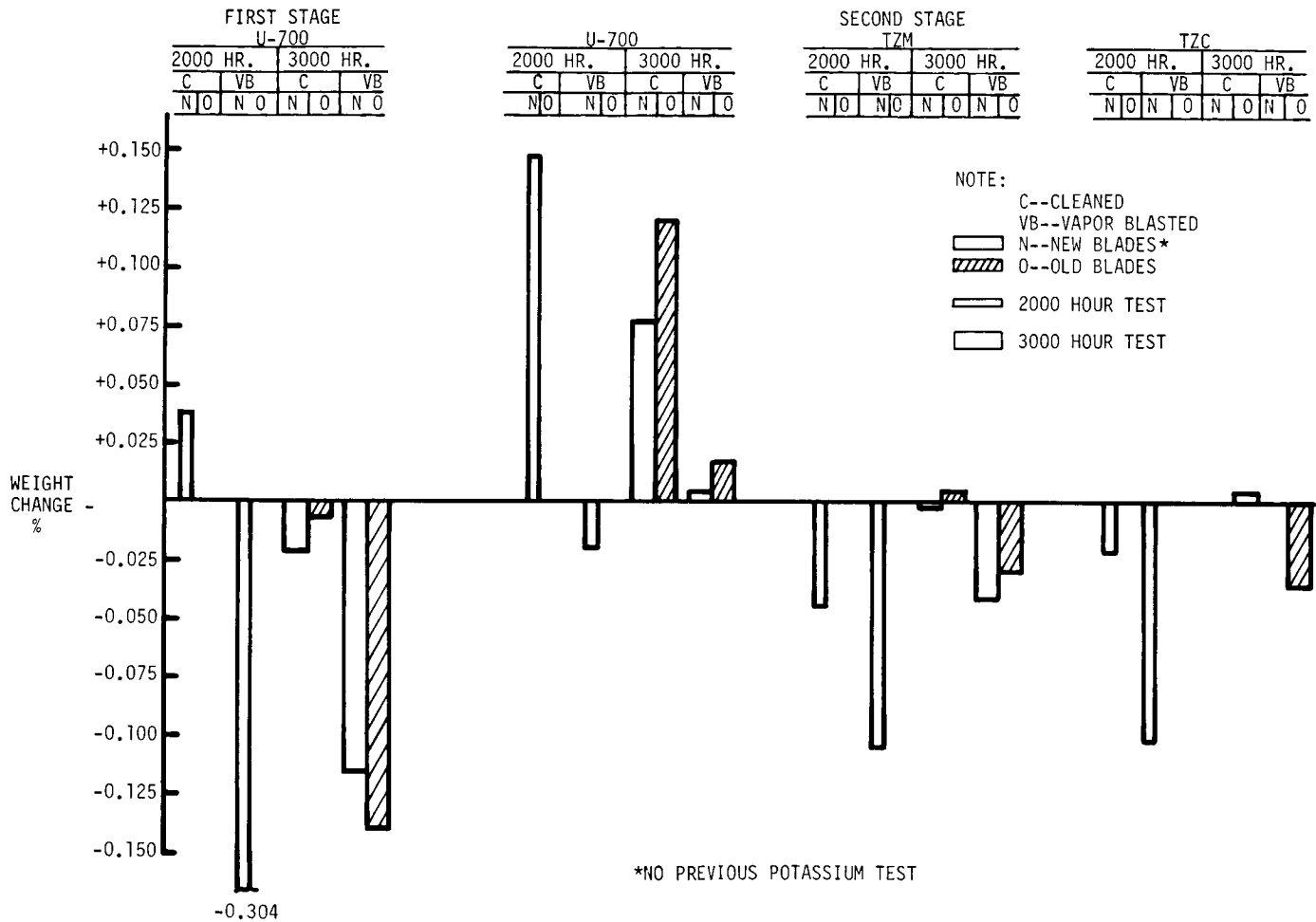


Fig. 3-6. Weight losses versus system cleanliness

Refractory Alloy Contamination Specimens

Average Blade Weight Changes After 2000-Hour
And 3000-Hour Endurance Tests

MATERIAL	TEST DURATION -HRS.	NO. OF BLADES*		CHANGE IN WEIGHT - %			
				AFTER CLEANING		AFTER VAPOR BLASTING	
		NEW	OLD	NEW	OLD	NEW	OLD
FIRST STAGE:							
U-700	2000	61**	0	+0.038	N.A.	-0.304	N.A.
	3000	7	55	-0.021	-0.006	-0.115	-0.139
SECOND STAGE:							
U-700	2000	52**	0	+0.147	N.A.	-0.019	N.A.
	3000	7	45	+0.077	+0.120	+0.003	+0.017
TZM	2000	4**	0	-0.044	N.A.	-0.105	N.A.
	3000	2	2	-0.002	+0.004	-0.042	-0.029
TZC	2000	4**	0	-0.033	N.A.	-0.102	N.A.
	3000	0	4	N.A.	+0.004	N.A.	-0.035

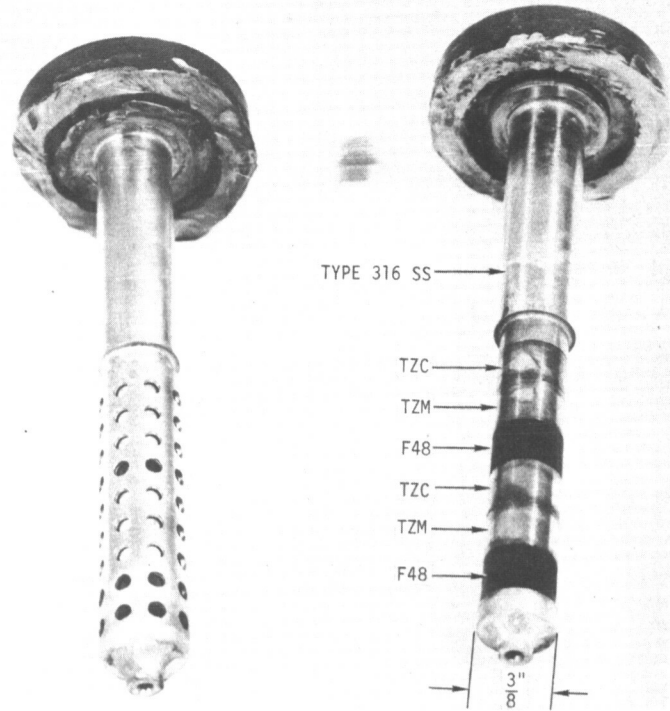
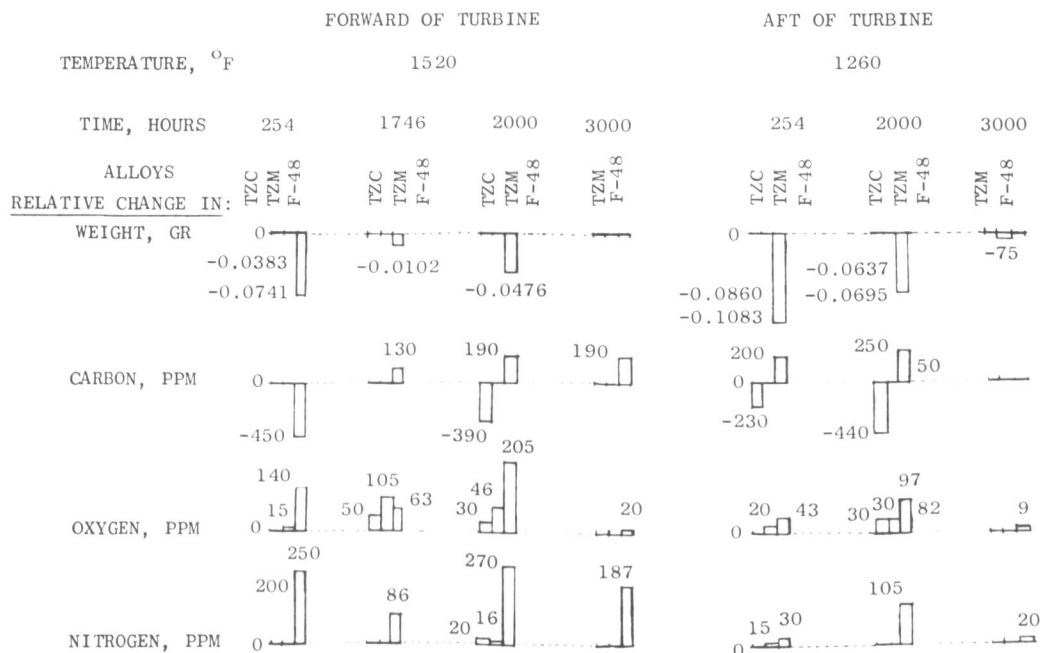
NOTES:

N.A. - NOT APPLICABLE

*NEW - NOT PREVIOUSLY USED IN ENDURANCE TESTING

*OLD - USED IN 2000-HOUR ENDURANCE TEST

**BRAND NEW AT BEGINNING OF 2000-HOUR TEST

Changes In Weight And In Carbon Oxygen And Nitrogen Content
Of Refractory Alloys During Turbine Testing

OXYGEN CONCENTRATION IN POTASSIUM DURING TURBINE ENDURANCE TESTING

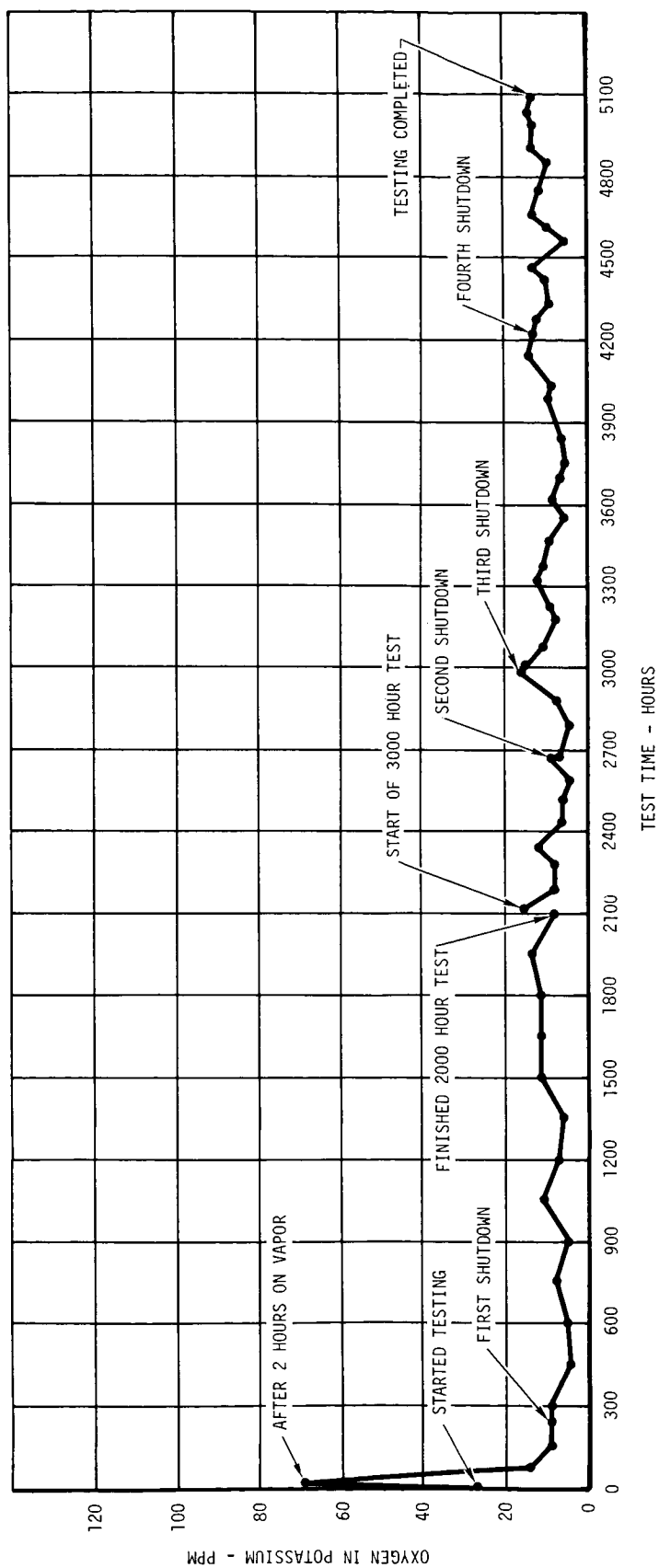


Fig. 3-6 (contd)

4. POTASSIUM EROSION AND TURBINE EXPERIMENTS

Loyd V. Wilson
Oak Ridge National Laboratory
Oak Ridge, Tennessee

A series of engineering scale tests has been conducted at Oak Ridge National Laboratory for the intended purpose of screening candidate materials for use as turbine nozzles and blades in high-temperature Rankine-cycle systems. The materials of interest have been:

- (1) Type 316 stainless steel.
- (2) Haynes alloy 25 (Co - 50%; Cr - 20%; W - 15%; Ni - 10%; Fe - 3%).
- (3) Columbium - 1% zirconium.
- (4) Molybdenum (TZM; Ti - 5%; Zr - 0.08%; C - 0.02%).
- (5) D-43 columbium (Zr - 1%; W - 10%; C - 0.1%).

These materials have been and are being subjected to a range of temperatures, vapor velocities, and vapor qualities in forced-convection boiling-potassium loops. Schematically the test loop is shown in Fig. 4-1. This loop consists basically of a boiler, nozzle and blade test section, air-cooled condenser, and electrodynamic pump.

At the inlet to the boiler, which is heated by electrical clamshell heaters, there is a preheater section containing two hot fingers to promote stable boiling. The vapor from the boiler still contains some moisture that is evaporated when it passes through the drier section, that is also heated by clamshell electrical heaters. The purpose of the drier section is to provide dry and saturated vapor at the inlet to the nozzle test section.

The nozzle and blade test section consists of three nozzles in series in which the flow in the first and third nozzles is subsonic and in the second nozzle is supersonic. The jet of each nozzle impinges upon a stationary blade specimen. After leaving the third nozzle and impingement surface, the vapor is condensed in an air-cooled condenser and subcooled approximately 50°F in the condenser hot well.

PRECEDING
PAGE BLANK

The liquid passes to the electrodynamic pump which is a rotating field electromagnetic pump. A flow control valve is provided at the pump discharge to decouple the boiler from the pump and to reduce flow fluctuations resulting from small fluctuations in the boiler pressure.

Two 316 stainless steel loops have been operated at a vapor temperature of 1600°F, and one columbium - 1% zirconium loop is presently operating at 2000°F. This latter loop, shown in Fig. 4-2, is different from the one just described in that it is operated in a vacuum facility and has a NaK-cooled condenser.

Figure 4-3 shows the nozzle test section of the loops with the operating conditions of the nozzles for both the stainless steel loop and the Cb-1% Zr loop. As previously mentioned the first and third nozzles are operating in the subsonic range with Mach numbers of 0.85 and 0.75, respectively, for the stainless steel loop, and 0.88 and 1.0 for the columbium loop. In both loops the supersonic nozzles are operated with Mach numbers a little over 2. These Mach numbers are calculated based on an equilibrium expansion, as are the vapor qualities indicated. For most of the tests the impingement was on flat specimens inclined at an angle of 45 deg.

Figure 4-4 shows the Mollier diagram for the expansion process through the nozzles. The wet vapor from the boiler comes into the drier section at some point along the indicated constant pressure line, and heat is added in the drier section to bring the vapor up to a point on the saturation line. The vapor passes through the first nozzle to its downstream pressure line where the kinetic energy of the jet is converted to enthalpy during and after impingement, but the heat loss between stages is sufficiently high that it is necessary to actually add heat to bring the vapor back up to the saturation line for the second-stage nozzle. The second-stage nozzle is a converging-diverging nozzle and expands the vapor through a pressure ratio of approximately 12 to an exit quality of approximately 82 to 83% based on an equilibrium expansion. Again heat must be added to bring the vapor back up to the saturation line for the third nozzle. After impingement the exhaust from the third nozzle passes into the air-cooled condenser.

Before discussing the test results, some of the difficulties encountered in accomplishing stable loop operation should be mentioned. Basically, the instabilities resulted in slugs of liquid being carried over to the test section. The loop was modified at various times by installing the throttle valve in the line between the

pump and the boiler, by increasing the boiler diameter to decrease the vapor velocity leaving the boiler, and by installing bubble nucleators, or hot fingers, in the preheater section of the boiler. These instabilities had their effect not only on the test specimens, as will be shown later, but on the loop itself. Figure 4-5 shows a section through the top of the drier of the Cb - 1% Zr loop after 3000 hours.

In addition to the damaging effects of loop instabilities, another phase of the erosion phenomena should be mentioned. In some of the earlier tests, oxides in the potassium were removed in a zirconium hot trap located in a bypass line from the pump discharge to the pump suction. This operation was performed only periodically until the oxide level was recognized to be apparently higher than anticipated. The bypass line was removed and a full-flow hot trap was placed in the preheater outlet.

The first test used Type 316 stainless steel nozzles and blades, and ran for 750 hours at design conditions in the stainless steel loop. No significant damage occurred to the specimens other than minor deposits on the nozzles and blades and a slight roughening of the impingement area of blade no. 2 where the supersonic jet hit.

Nozzle and blade specimens of Haynes alloy 25 were installed in the stainless steel loop. The first-stage impingement specimen (Fig. 4-6) was cratered by wet vapor during the initial 216 hours of unstable loop operation, but in a subsequent 1679 hours of stable operation with hot fingers, no further damage was done to any of the surfaces other than a slight buildup of deposits as shown in Fig. 4-7.

Four tests were then run with TZM molybdenum specimens at a maximum temperature of 1600°F. The first two tests were thought to be compromised by leaks and the tests were terminated after 504 hours and 2067 hours, respectively. The specimens were badly attacked and covered with a reaction layer of metallic oxides. The third test with TZM was terminated on schedule after 1000 hours, and examination revealed the same kind of attack and deposition buildup. Figure 4-8 shows this deposition on the second-stage impingement specimen and the low-pressure side of the nozzle.

At this time, a full-flow hot trap was installed in the preheater outlet, and the fourth test with TZM specimens was run for 1000 hours after which the specimens were in excellent shape.

From this result, one can conclude that for the earlier runs the prerun cleaning procedures were inadequate or that there was a leak in the system. The impurities in the liquid droplet carryover attacked the specimens both by erosion and corrosion plus considerable deposition of debris. Prerun cleaning plus a full-flow hot trap gave excellent control of the impurities.

Only one test has been completed in the Cb - 1% Zr loop. During this test, nozzle and impingement specimens of Cb - 1% Zr were subjected to potassium vapor at 2000°F inlet temperature to the three stages for 3000 hours. Post-test examination showed no significant damage to the specimens. The impingement specimens in this test were different from those used in previous tests, and the impingement specimen that was exposed to the supersonic jet is shown in Fig. 4-9. At the point of impingement, there was an attack of about 1 mil and there was a metallic deposition of about 1 mil on the concave portion of the specimen. Analysis of this layer showed large amounts of chromium which presumably came from some of the stainless steel components in the loop. This mass transfer resulted in a reduction in the throat diameter of from 1 to 4 mils, except that the exit of the divergent portion of the second-stage nozzle increased by about 5 mils. Weight measurements of the impingement specimens showed weight increases of from 3 to 8 mg from the original weight of 30 g.

It must be realized that the more meaningful aspect of turbine erosion could not be explored in a system of this type, i. e., one without any rotating parts in the potassium system. We had hoped to obtain information of a relative nature by subjecting various candidate materials to supersonic velocities and relatively wet vapor. We realize that the velocity of the supersonic nozzle is not a realistic velocity in the present state of potassium vapor turbines, nor is the flat impingement specimen typical of the geometry where erosion is expected in the turbine.

However, some things happened that are of interest:

- (1) The presence of oxides and other impurities in the system make their own contribution to erosion.
- (2) Mass transfer effects are felt both upon the impingement specimen and in the nozzle. The effects on the impingement specimen can mask measured weight losses by erosion. Mass transfer in the nozzle can result in a change in the nozzle geometry resulting in

decreased mass flow rates, and in the case of a convergent-divergent nozzle, an increase in the nozzle velocity.

Also, we have run a potassium vapor turbine driving a boiler feed pump in a Rankine-cycle system. Figure 4-10 shows the turbo-pump which was operated at speeds up to 700 rpm and at vapor temperatures of approximately 1500°F. The nozzle velocity was over 2000 ft/s and the tip speed of the wheel was approximately 200 ft/s. After approximately 2700 hours of turbine operation, there was no visual evidence of damage to the TZM molybdenum turbine wheel.

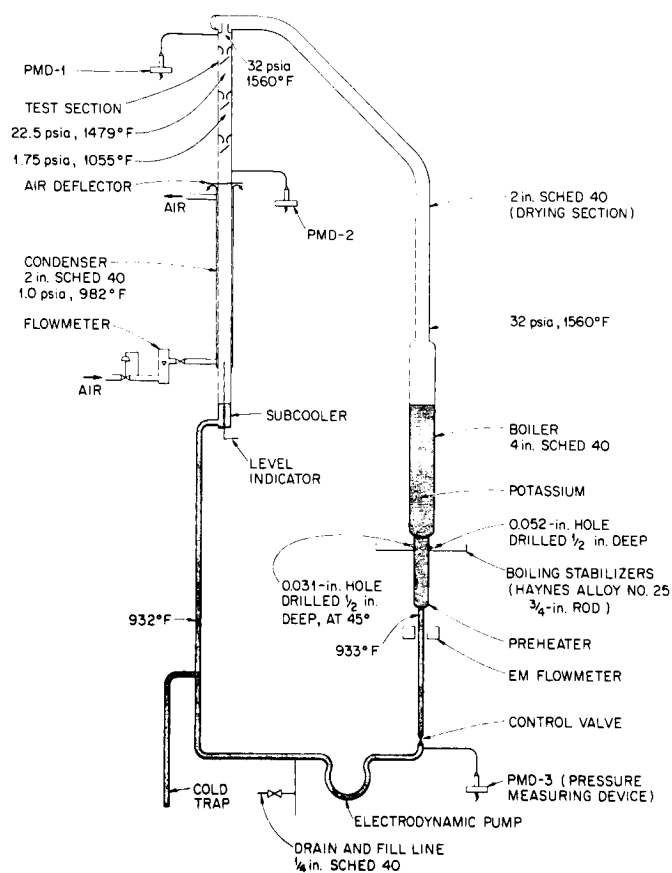


Fig. 4-1. Type 316 stainless steel forced-circulation boiling-potassium corrosion loop

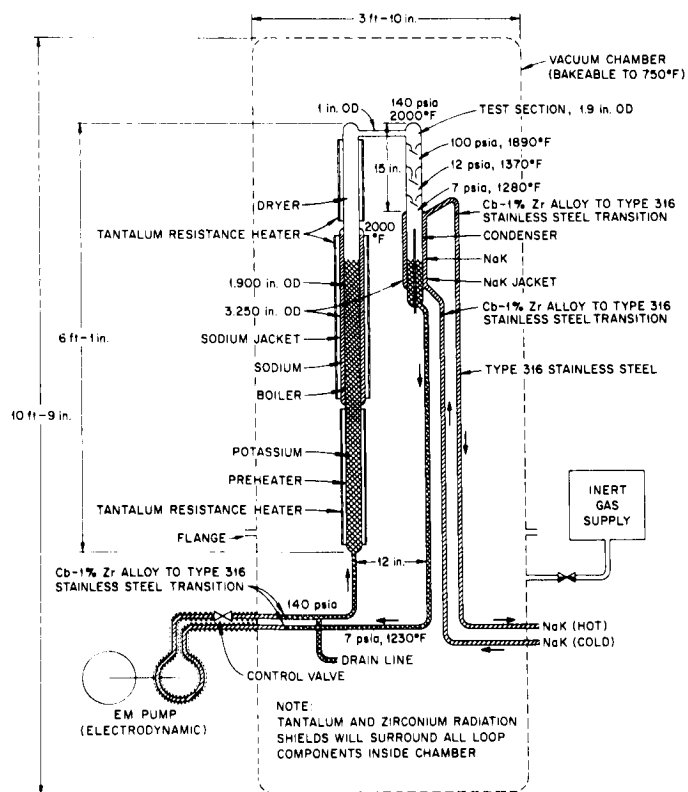


Fig. 4-2. Cb-1% Zr forced circulation boiling potassium corrosion loop

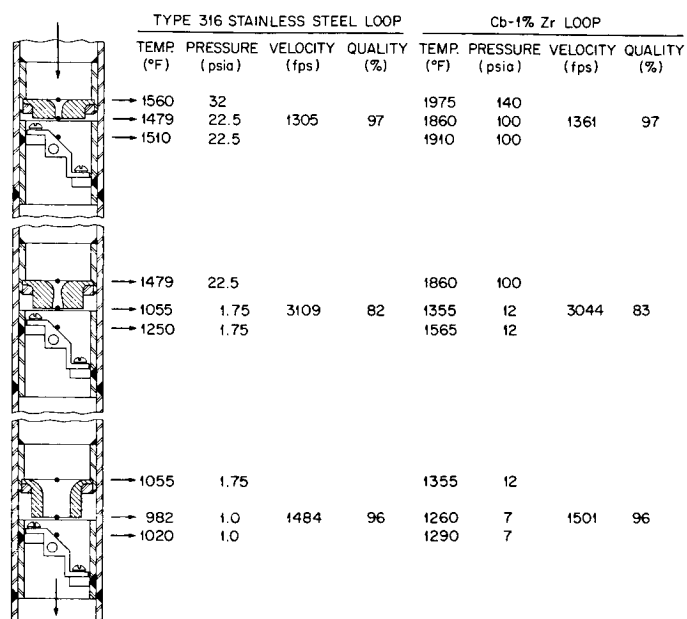


Fig. 4-3. Nozzle and turbine blade test section of boiling potassium corrosion loop

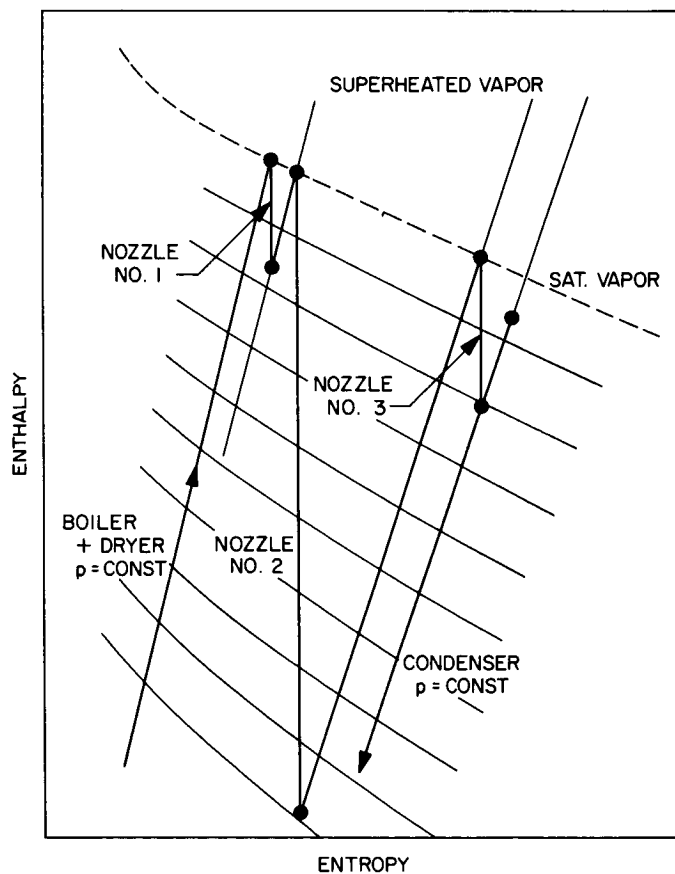


Fig. 4-4. Mollier diagram

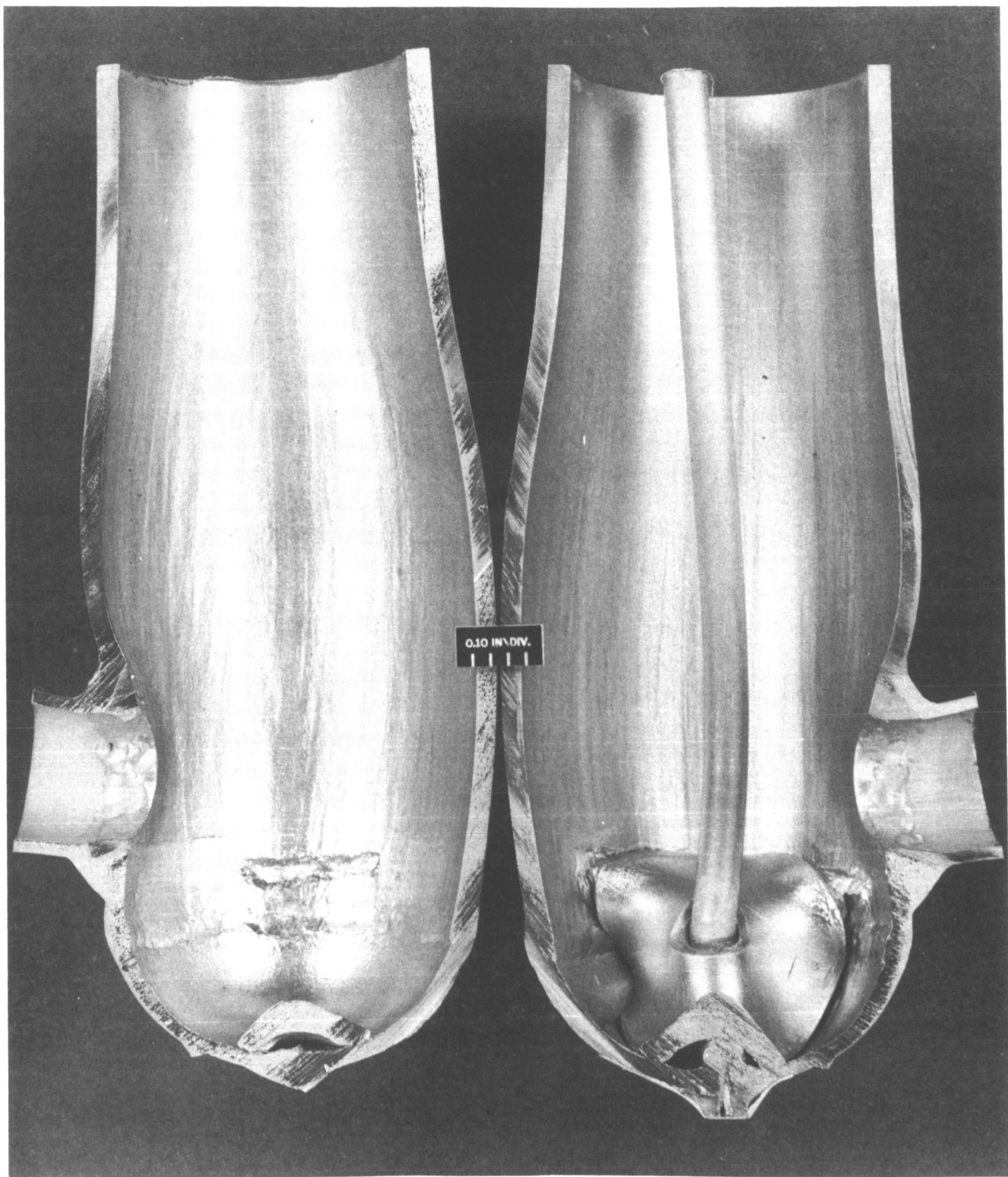


Fig. 4-5. Top of dryer section of Cb-1% Zr loop after 3000 hours of operation

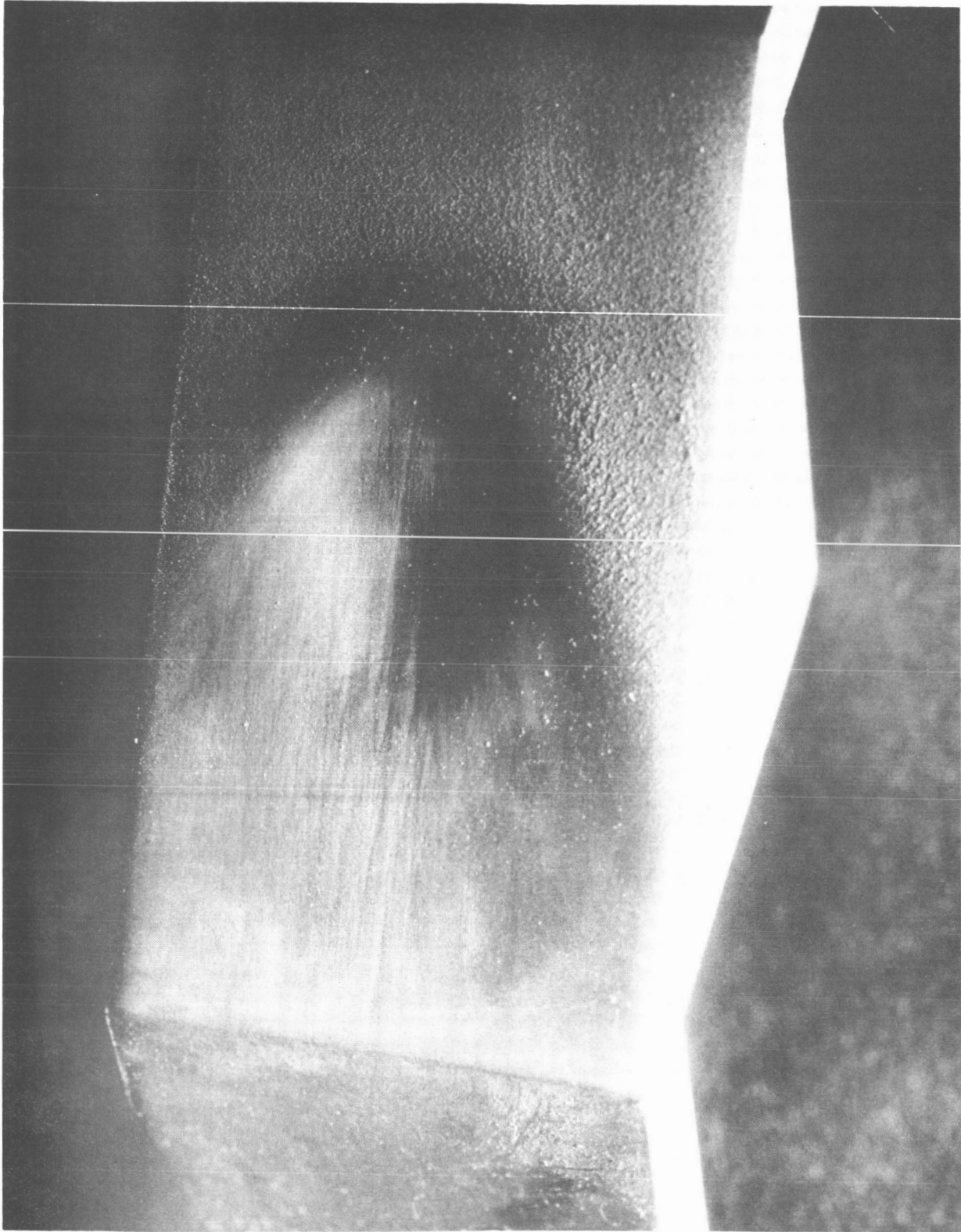


Fig. 4-6. Haynes alloy No. 25 impingement specimen after 216 hours of unstable loop operation



Fig. 4-7. Haynes alloy No. 25 specimen after an additional 1679 hours of stable operation

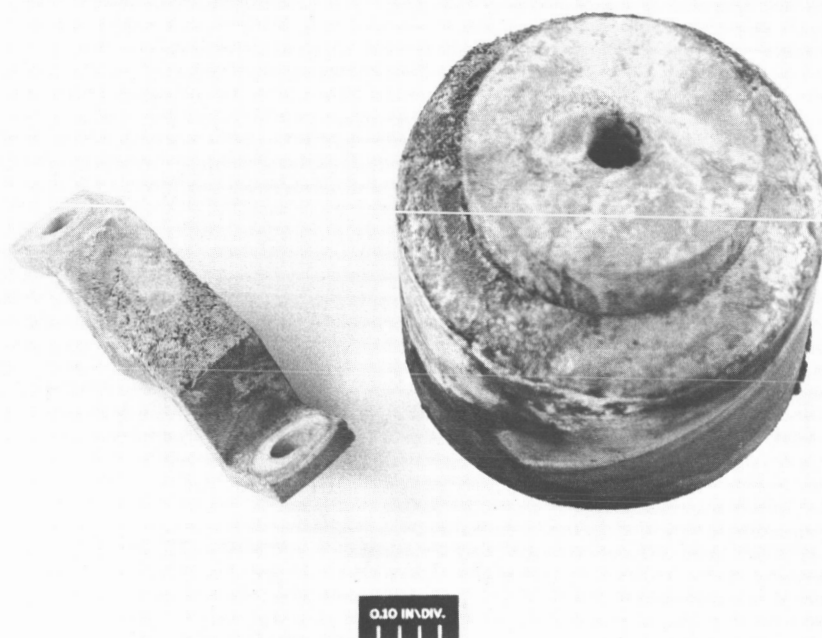
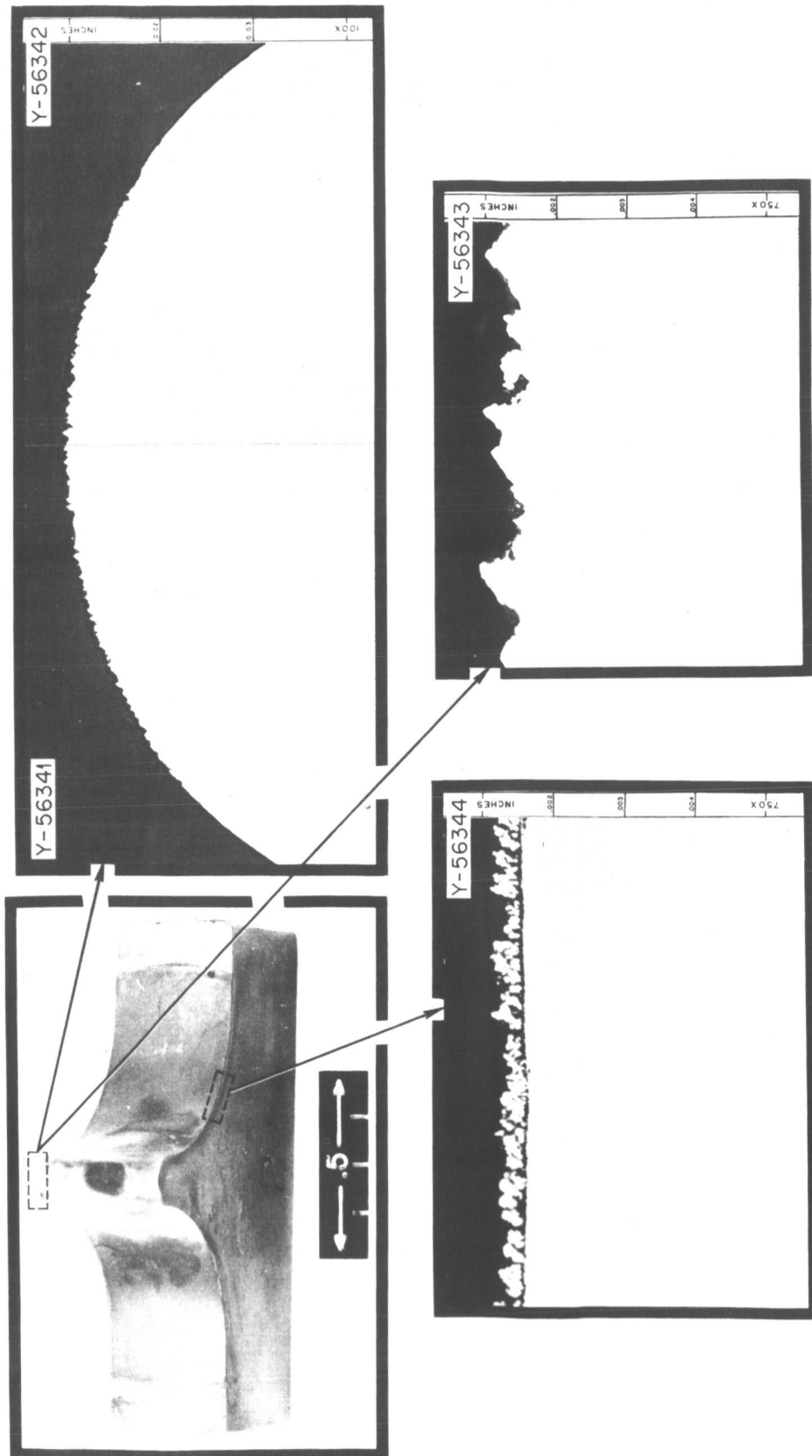


Fig. 4-8. Specimen and nozzle from third TZM test after 1000 hours



SPECIMENS ARE IN AS-POLISHED CONDITION

TEST CONDITIONS

VAPOR TEMPERATURE: 743°C

VAPOR QUALITY: 83%

VAPOR VELOCITY: 3080 fps

TEST DURATION: 3000 hr

Fig. 4-9. Cb-1% Zr blade specimen from second stage of boiling potassium pumped loop

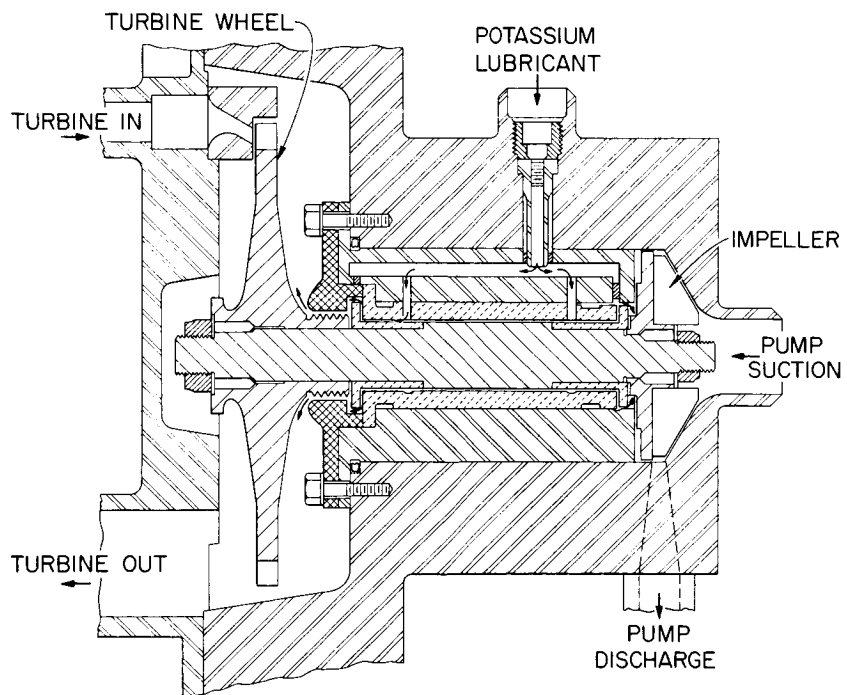


Fig. 4-10. Aeronutronic Mark I turbine pump

5. POTASSIUM TURBINE EXPERIMENTS

J. Rebeske
AiResearch Corporation
Phoenix, Arizona

The first slide* showed an overall view of the turbine test facility and bearing test facility. The turbine test facility was said to be very similar in design to General Electric's facility. The second slide showed a picture of an erosion test rig which was operated with potassium at 1400°F. Geometrically similar blades were run with water at relative velocities of 200 ft/s. Haynes-Stellite 6B showed a slight amount of erosion after 75 hours in water, but no erosion was measured after 25 hours in potassium. The next slide showed a tabulation of the results obtained in erosion testing. Haynes-Stellite 6B, TZM, TZC, and Mo-1/2Ti showed very low-weight loss compared with the other candidate materials tested. Pictures were then shown for the turbo-dynamic test rig that was fabricated to test bearings, and for the layout of the bearing test and the turbine, which was used to drive the bearings. The turbine rotated at 24,000 rpm.

Three photographs of the turbine which was used for driving a potassium bearing rig are shown herein. This turbine wheel (Fig. 5-1) was fabricated from Inconel-X by conventional milling procedures. The inlet vapor quality to the turbine was not measured, but it is believed to be very dry because the boiler does have a drying section consisting of a column packed with stainless mesh. The turbine was operated for 2700 hours with most of this time at an inlet temperature of 1350°F. The mean blade speed was 760 ft/s at 24,000 rpm, and the design spouting velocity of the two partial-admission nozzle bank was 2413 ft/s at a 16-deg angle to the plane of rotation. The other two photos (Figs. 5-1 and 5-2) show the nozzle banks and the exhaust housing accumulated mass-transfer products, respectively. These products were diffusion-bonded to the structural material during the 2000-hour test run. These deposits, when removed, had a portion of the structural wall attached. Thus, when chemically analyzed, the deposits showed an analysis close to that of Type 316 stainless steel. The mass-transfer material is suspected to be nickel, however this assumption was not verified due to the termination of our contract.

*All slides were not available for publication.

The last slide presented during the talk showed a schematic of the large 300-kW turbine which was operated in the large turbine test facility. The turbine was operated a total of 15 hours at 24,000 rpm. The test was terminated at that time because of a failure in the shaft between the turbine and the generator due to a proximity probe. The tip speed of the turbine was 800 ft/s, and the rotor material was Inconel-X.

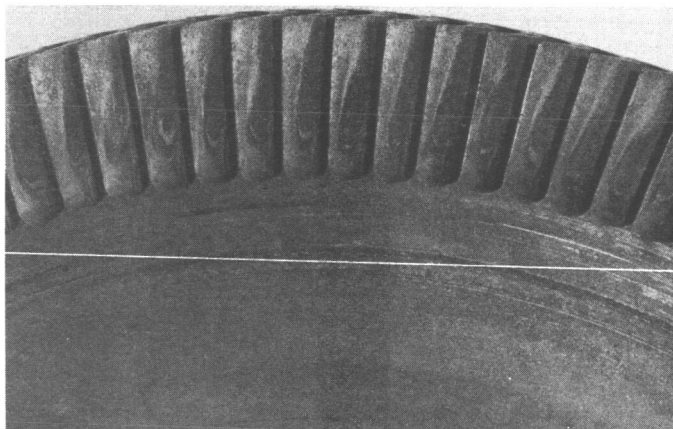


Fig. 5-1. Turbine wheel blades

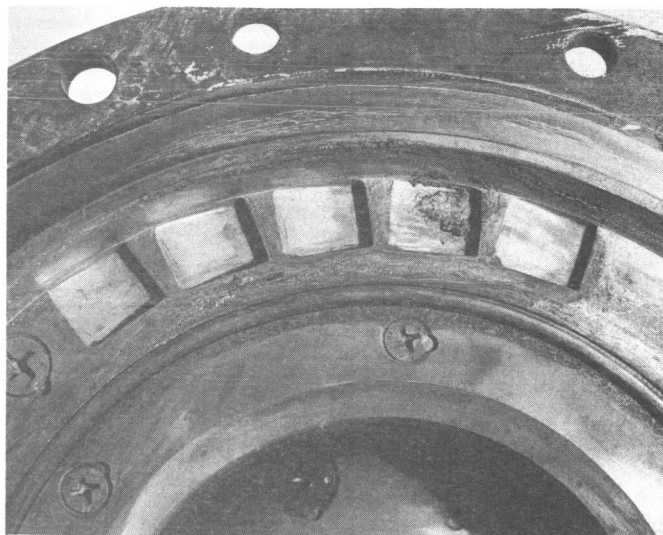


Fig. 5-2. Accumulated mass-transfer products on nozzle banks

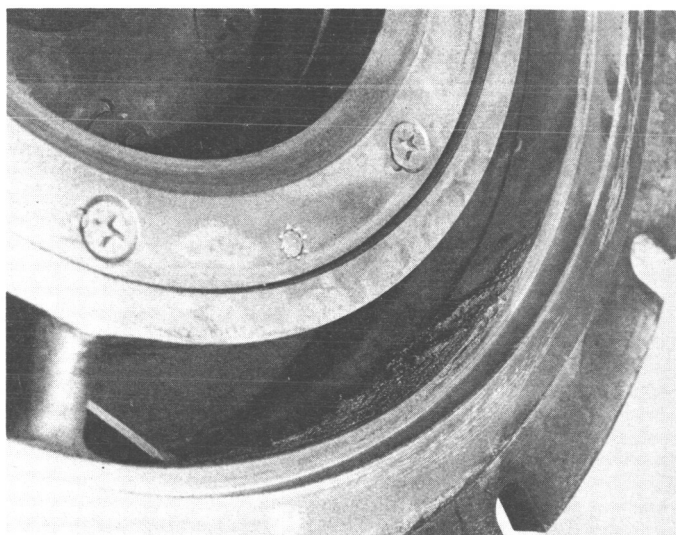


Fig. 5-3. Accumulated mass-transfer products on exhaust housing

6. REFRACTORY METAL POTASSIUM TURBINE EXPERIMENTS

J. P. Davis
Jet Propulsion Laboratory
Pasadena, California

High-temperature alkali-metal nuclear Rankine-cycle systems are prime contenders as power sources for potential electric propulsion application. These systems generally maintain a distinct weight advantage when compared to alternate possibilities, such as thermionic and Brayton-cycle nuclear systems in the power range of 100--1000 kWe, using equivalent design constraints and engineering optimism. As is the case with most conceptual systems early in the design evaluation, many fundamental problem areas do not influence the weight estimates or the steady-state full-power equations. Comparing the Rankine, Brayton, and thermionic modes of power conversion, it is apparent that the Rankine system is, in a hydraulic sense, the most complex and least understood of the three as a direct consequence of its two-phase fluid characteristics. Of particular interest to us are problems of boiling and condensing stability and overall system response. These problems are not unique to space nuclear applications. The problems have been encountered and handled, often empirically, in nuclear and conventional steam power plants for many years. Existing theoretical stability models have not been developed to the degree that they can be confidently applied to predict behavior even in water systems. Alkali-metal systems, using boiler concepts of straight-through non-recirculating negligible-inventory type designed to operate in zero gravity environment, pose additional unknowns not usually encountered in land-based power plants. Additional complexity is introduced by the nature of alkali metals being much more sensitive than water to geometry and bubble nucleation sites, and prone to large degrees of liquid superheat.

As a consequence of these and other areas of uncertainty involving Rankine-cycle systems, JPL decided in 1961 to construct a two-loop lithium boiling potassium test facility to study these problem areas. Actual loop construction commenced in 1963, and the initial phases of operation were begun in late 1965.

The loop is constructed of columbium-1% zirconium alloy and designed to operate at temperatures up to 2100°F. The primary purpose of this facility is to investigate overall transient and steady-state characteristics of a two-loop Rankine-cycle pilot plant which contains all the essential components of a Rankine space power plant and which approximately simulates velocities, temperatures, pressures,

transit times, and heat fluxes in the range of actual system interest. Transient investigations include start-up, load perturbations, shut-down, and the effects of various control concepts on system performance. The primary heat source is by direct resistance heat generation in a section of tube wall and liquid metal. This type of source lends itself to programming of reactor kinetic equations for simulation of reactor power response to various system perturbations. The system is instrumented to the extent that steady-state local-boiling heat-transfer coefficients and two-phase pressure-drop data will be determined for a variety of operating parameters. Performance of individual components are also being evaluated for potential application to actual systems. The loop is not intended as a corrosion or component life test facility.

Rather than discuss any specific data gained to date, except for one rather exciting transient, I think the most useful information would be a description of the various components and some of my comments on operating experience for those of you who will ultimately be planning high-temperature liquid-metal refractory-metal experiments, specifically involving turbine studies.

Figures 6-1 and 6-2 show a flow isometric and schematic of the system, respectively, and Table 6-1 shows the loop operating conditions. A photograph of the uninsulated loop is shown in Fig. 6-3. The primary-side lithium flow enters a direct current resistance-heated helical coil to which reactor kinetic equations may be programmed for simulation of power response to various system perturbations. The lithium then enters a centrifugal pump which employs a combination recirculation and liquid level indicator sump, then flows through an electromagnetic flowmeter, boiler, and returns to the heater inlet. About 10% of the flow is bypassed to an yttrium hot trap which is located in the coolest part of the system to minimize mass transfer effects. The pump was placed downstream of the heater for arrangement considerations and, therefore, operates at the highest system temperature.

The secondary-side potassium enters a countercurrent annular-flow boiler, exits through a flow orifice to the turbine, and condenses in a radiating condenser. The condenser is surrounded by an array of rotatable radiation shields to vary the effective condenser area. The potassium exits from the condenser subcooled; flows through an electromagnetic pump, electromagnetic flowmeter, preheater, zirconium-gettered hot trap, and liquid throttle valve; and returns to the boiler inlet.

The loop is contained in a 5-ft diameter by 7-ft long main enclosure with auxiliary enclosures for the condensing radiator and fill/dump system, as shown in Fig. 6-3. The system is run in a recirculating argon atmosphere slightly above atmospheric pressure. Make-up argon has an oxygen and water vapor content of about 1 ppm each.

The loop is foil-wrapped with two layers of tantalum and one layer of zirconium, and is insulated with about 3 in. of glass-rock-foamed high-purity silica.

All material that comes in contact with fluids above 1500°F is Cb-1% Zr with the exception of tungsten valve facings, hot trap getters, and the turbine wheel. The fill and dump system is constructed of Types 304 and 321 stainless steel.

An attempt has been made in the loop design to permit variation of operational parameters to study various regimes of stable and unstable operation, particularly when the primary heater is programmed to simulate a nuclear reactor of varying negative temperature coefficients and utilizing different system control techniques.

The lithium pump is a variable speed dc unit permitting change in primary coolant flow rate. The potassium system I²R preheater permits variation in boiler inlet subcooling from several hundred degrees to a few degrees below saturation. The boiler inlet throttle valve allows liquid pressure drop (from the variable power EM dc conduction pump to boiler inlet) to be varied from less than 1 psi to full pump head.

It is therefore possible to simulate a broad range of potential system operating conditions and study their quantitative effects on system performance.

Table 6-1. 30 kW-2100°F loop operating conditions

Item	Operating conditions	Supplier and type
Lithium (liquid) Flow rate Temperature Pressure	1 to 10 gal/min 2100°F Up to 20 psig	Foot Mineral Company
Potassium (liquid) Flow rate Temperature Pressure	0 to 1 gal/min 1500 to 2000°F Up to 200 psig	MSA Research
Centrifugal pump (lithium)	Up to 10 gpm at 100 ft 2100°F service	Byron-Jackson
EM pump, dc (potassium) Temperature Head-flow, nominal	1500°F 90 psi-150 lb/h	MSA Research Cb-1Zr
Swing gate valves (bellows seal) Lithium Potassium	2100°F lithium service 2000°F boiling potassium service	Valcor Engineering 5/8 in. OD 3/4 in. Schedule 80
EM flowmeters Lithium	2100°F service	MSA flowmeter FM-4 5/8 in. OD 1/16 in. wall Cb-1Zr duct
Potassium	1500°F service	3/8 in. OD Cb-1Zr duct Cb-1Zr
Diaphragm	Lithium and potassium pressure measurements Loop design conditions	JPL Aeronutronic
Potassium boiler Turboalternator Inlet temperature Exhaust temperature Weight flowrate Design speed Electrical output	1900°F 1500°F 0.0324 lb/s 12,000 rpm 1.0 kW	Cb-1Zr case Molybdenum turbine wheel, shaft, alternator rotor SS 316 alternator housing
Dump tanks and valves (Argon, vacuum and fill)	500°F service	Material SS 304 and 321

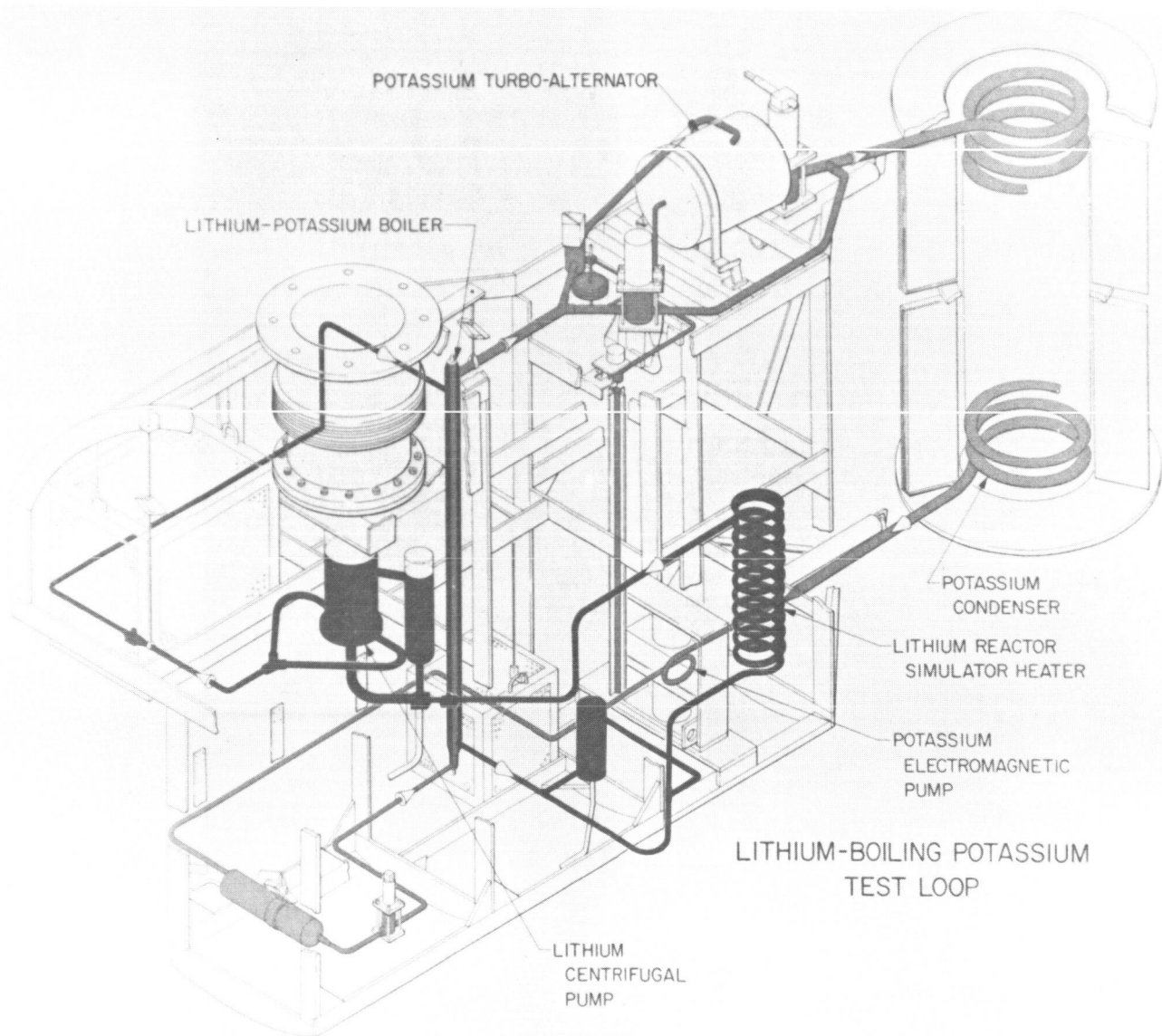
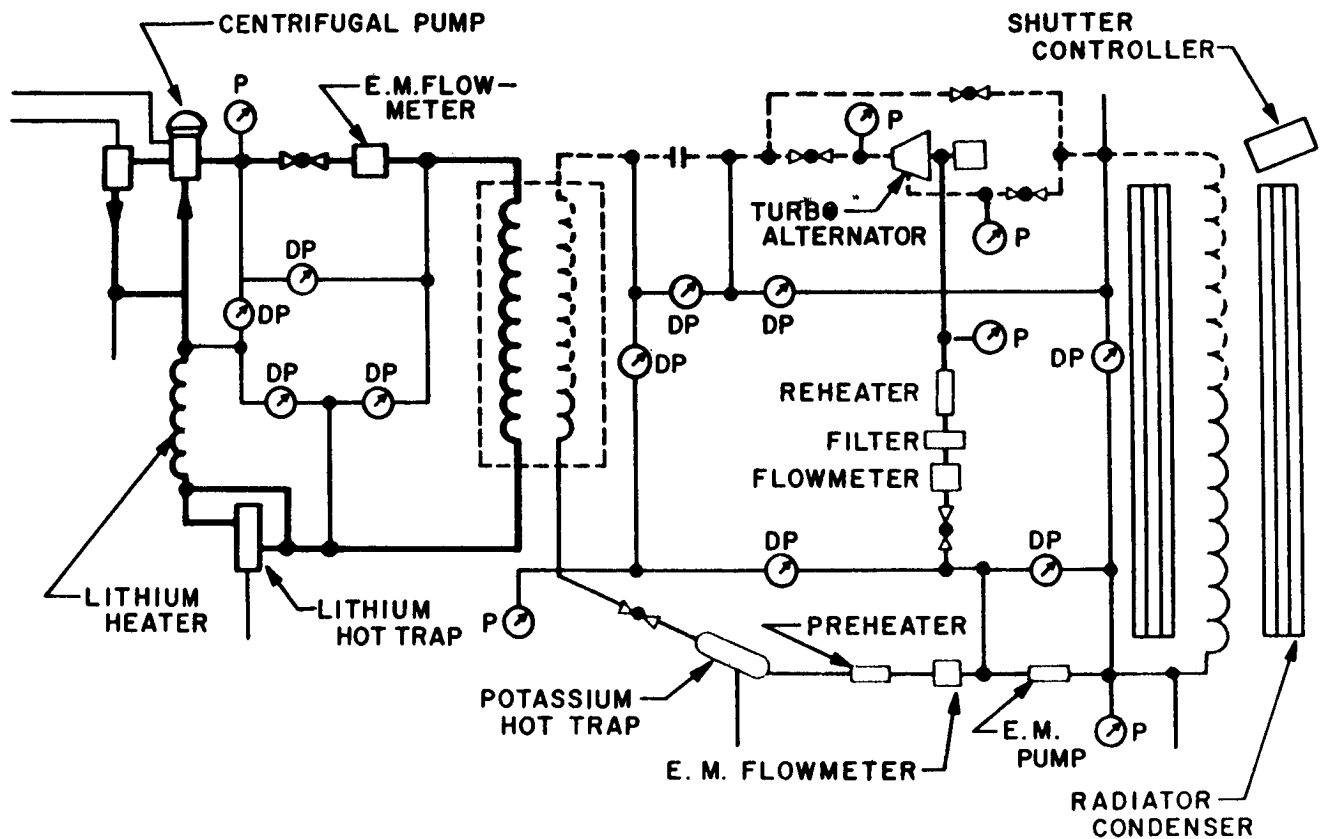


Fig. 6-1. Lithium-boiling potassium test loop



LITHIUM BOILING POTASSIUM FLOW DIAGRAM

Fig. 6-2. Lithium-boiling potassium loop flow diagram

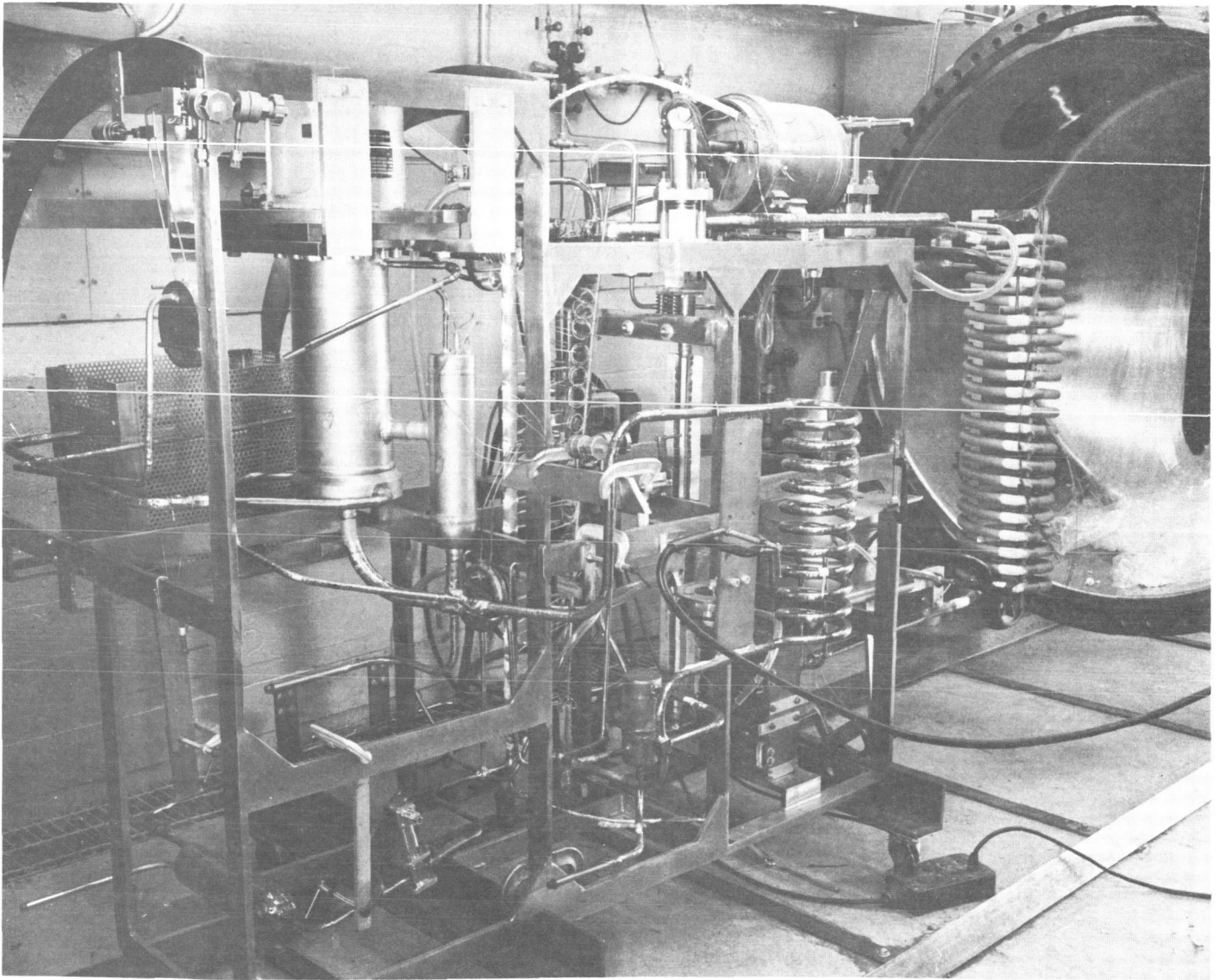


Fig. 6-3. Uninsulated loop of lithium-potassium system

7. MERCURY EROSION AND TURBINE EXPERIMENTS

H. Derow
Aerojet-General Corporation
Azusa, California

The results discussed were performed under the auspices of NASA Lewis Research Center under contract to develop SNAP 8 (Refs. 7-1 and 7-2). Aerojet-General has the responsibility for the power conversion system and Atomics International has the responsibility for the reactor system. This system is a mercury Rankine cycle system and is presented in the first slide. * The second slide shows a picture of the mercury turbine used in the system. The turbine is a four-stage machine that rotates at 12,000 rpm. The first two stages are 38% partial admission, and the last two stages are 100% admission. The vapor velocity at the exit is a maximum of 640 ft/s. The velocity of the vapor relative to the rotors is 350 to 400 ft/s. The calculated quality to the last stage of the turbine is 93%. The wheel uses Stellite 6B as the construction material.

Erosion tests were started in late 1961 in a low-power mercury loop. The first test specimens were blades which were installed stationary in the test loop. After 300 hours of operation the blades were metallurgically examined. The materials which were run included 347 stainless steel, Haynes 25, Stellite 6B, the 400 series of stainless steel, and others. A difference in erosion was detected between the 300 and 400 stainless series, and the Stellite 6B and Haynes 25 on the other hand. The Stellite 6B and Haynes 25 alloys did not appear to be changed metallurgically whereas definite effects were noted on the stainless steels.

A second test series was inaugurated to provide more accelerated erosion conditions. Pin specimens were used and high velocity wet mercury vapor was impinged directly on them. In the next slide, the test loop that was used for these erosion tests was described. Figures 7-1 and 7-2 are schematics of the pin specimens and test arrangement used in these tests, respectively. The test conditions for this experiment were 1000 ft/s mercury vapor velocity, 82 to 88% vapor quality, and a test specimen temperature of approximately 640°F. Figure 7-3 summarizes the results of the testing and the time of exposure which ranged from about 5 to 15 hours. Several different hardnesses of Dynacut steel were tested in an

* All slides were not available for publication.

attempt to determine the effect of hardness. Stellite 6B exhibited the greatest resistance to erosion. It is significant to note that the two molybdenum alloys tested, TZM and Mo-1/2Ti, exhibited the least resistance to erosion. The hardest specimens of Dynacut tool steel were as erosion resistant as the Stellite 6B; however, a decrease in hardness, which would have been necessary for turbine wheel fabrication, resulted in much poorer erosion resistance. Figure 7-4 is a photograph of the test specimens after exposure to the mercury.

As a result of the erosion test, Stellite 6B was chosen as the material for the turbine. However, after operation of the turbine, this alloy was found to undergo a crystallographic transformation at the operating temperatures of the system, resulting in a severe loss of ductility.

A chart was given which summarized the results of the turbine testing to date. A total of 816 hours were logged by the first unit. This unit underwent a massive failure which was not necessarily related to the ductility loss of the Stellite 6B. The first- and second-stage wheels shattered, whereas, the third and fourth were intact when the unit was removed. Three other units were tested with the Stellite 6B wheels pretransformed to avoid the volume change which would occur during operation of the turbine. These units operated satisfactorily. The only differences noted on the wheels after operation was a slight roughening of the surface similar to a vapor hone finish. Metallurgical examination revealed nothing which gave any definite indication of erosion.

Pictures were shown of the turbine wheels after operation. The statement was made that one area where the Aerojet results differ appreciably from other results was that the refractory metal alloys TZM and Mo-1/2Ti were not found to be very erosion resistant, whereas, other people have found that these alloys are very erosion resistant. No explanation was offered for this result.

DISCUSSION

It was pointed out by L. Hays that the appearance of alloys which contained elements soluble in the mercury was quite different than the erosion patterns occurring on the materials which did not contain such elements. Specifically, these materials were the TZM alloy which contains zirconium, and the Mo-1/2Ti alloy. It was suggested that the predominant-material-removable mechanisms might be

accelerated corrosion, resulting from the high liquid flow velocities over the surface, rather than mechanical erosion. The question was raised as to whether such smoothed erosion patterns have ever been observed in steam. The comment was subsequently made by E. Miller that similar types of washing erosion or accelerated corrosion had been seen with high-velocity oxygenated steam. A. Thiruvengadam pointed out that, in cavitation testing, differences in surface appearance, such as those shown in these tests, were obtained with mercury. He stated that he believed that the chemical effects played a role in material removal with liquid metals under these conditions.

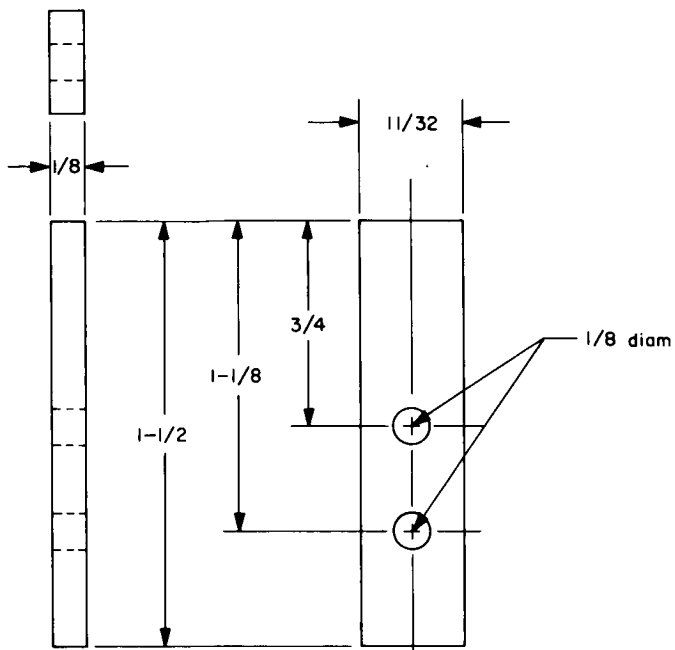


Fig. 7-1. Pin type accelerated erosion test specimen used in low-power loop

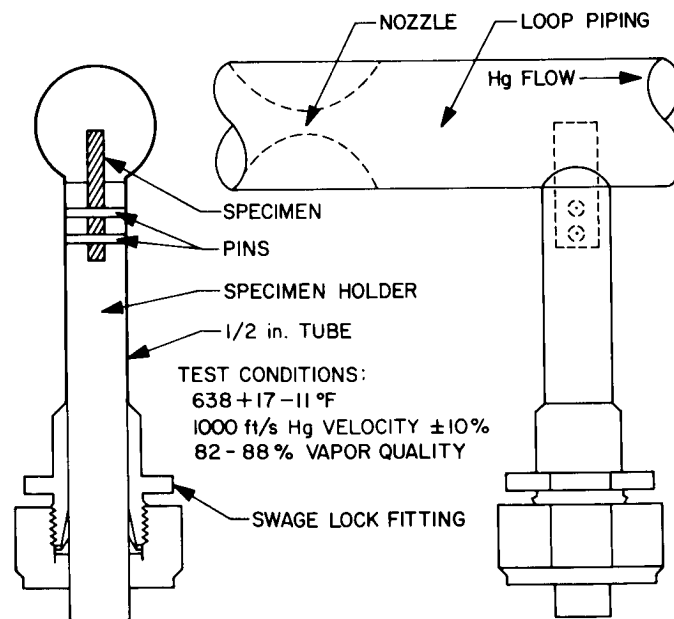


Fig. 7-2. Erosion test specimen location in low-power loop

<u>MATERIAL</u>	<u>DENSITY (LB/IN³)</u>	<u>ORIGINAL WT. GMS.</u>	<u>TEST TEMP. °F</u>	<u>EXPOSURE TIME-HRS.</u>	<u>WEIGHT LOSS-GMS</u>	<u>CALCULATED VOLUME LOSS (IN³ X 10⁵)</u>
Mo-TZM	.369	9.8613	637	5	.8023	479.0
Mo- $\frac{1}{2}$ Ti	.369	10.6385	653	5	.7061	421.6
Mo- $\frac{1}{2}$ Ti	.369	9.7699	627	5	.6707	400.1
Cb-752	.326	7.1344	620	3.5	.5867	396.4
17-4PH	.281	7.9403	620	5	.1448	113.5
Lapelloy	.281	7.9118	620	5	.1483	116.3
Lapelloy	.281	7.9022	620	5	.1403	110.0
Lapelloy	.281	8.0322	620	4	.1329	104.2
AISI 347	.286	7.7620	628	5	.1145	88.3
AISI 410	.280	7.7548	629	5	.0749	58.9
PH15-7Mo	.271	7.5480	615	5	.0393	31.25
18-4-1 Tool Steel	.290	8.8753	620	5	.0173	13.14
Dynacut Tool Steel	.284	7.8966	620	5	.0369	28.62
Dynacut Tool Steel	.284	8.0063	620	5	.0216	16.75
Dynacut Tool Steel	.284	8.2336	639	14	.0070	5.42
Dynacut Tool Steel	.284	8.2336	655	5	.0045	3.49
Stellite 6B	.303	8.4745	636	15	.0091	6.61
Stellite 6B	.303	8.4770	625	15	.0088	6.40
Stellite 6B	.303	8.4745	650	5	.0059	4.29
Stellite 6B	.303	8.6966	620	5	.0055	4.00
Stellite 6B	.303	8.4770	637	5	.0046	3.34

Fig. 7-3. Test condition and results of material specimens exposure to erosive environment

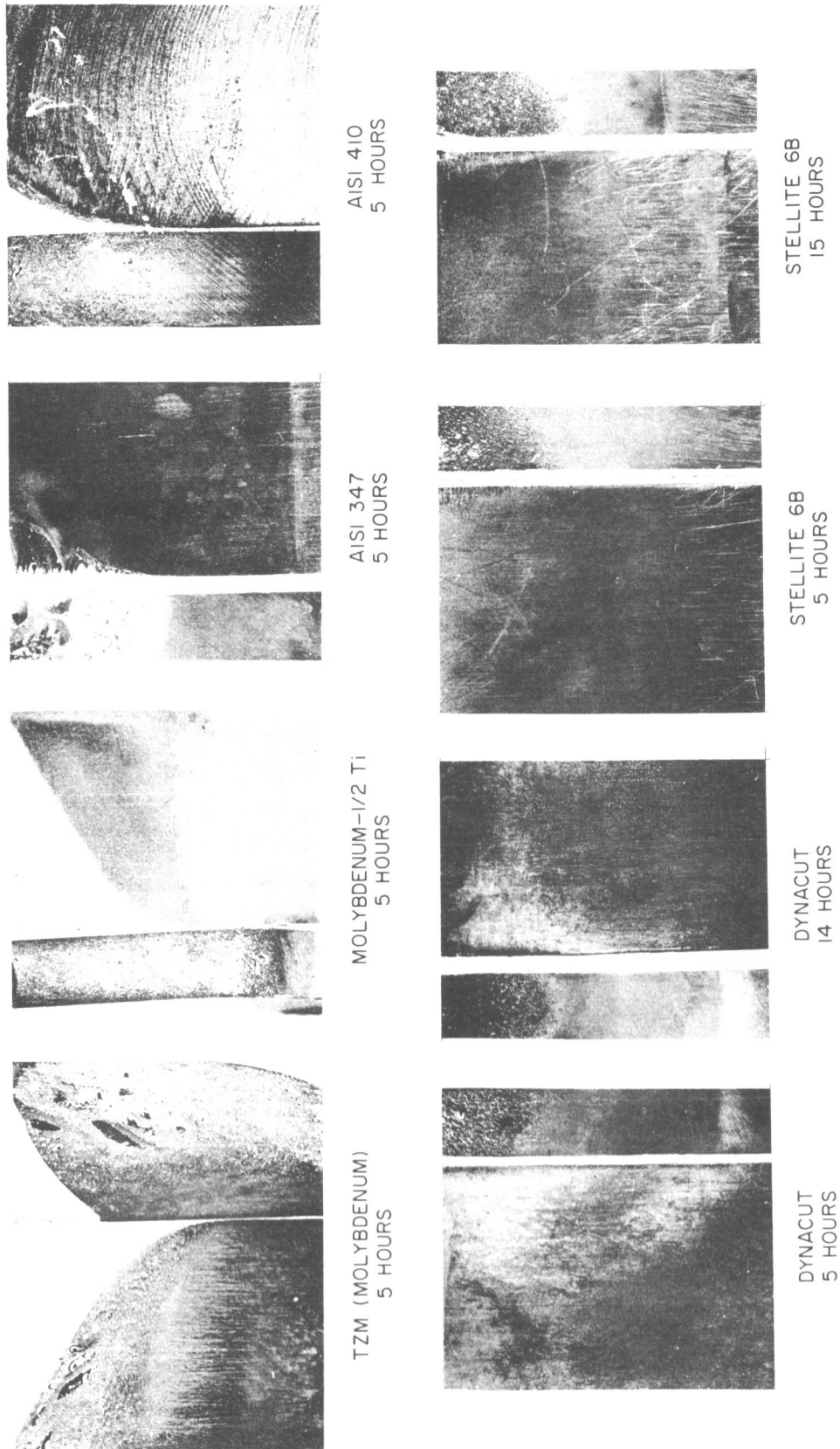


Fig. 7-4. Pin type erosion specimens after exposure to accelerated erosion conditions in low-power loop for exposure times (hours) indicated, side view and impact surface of specimen shown in each case

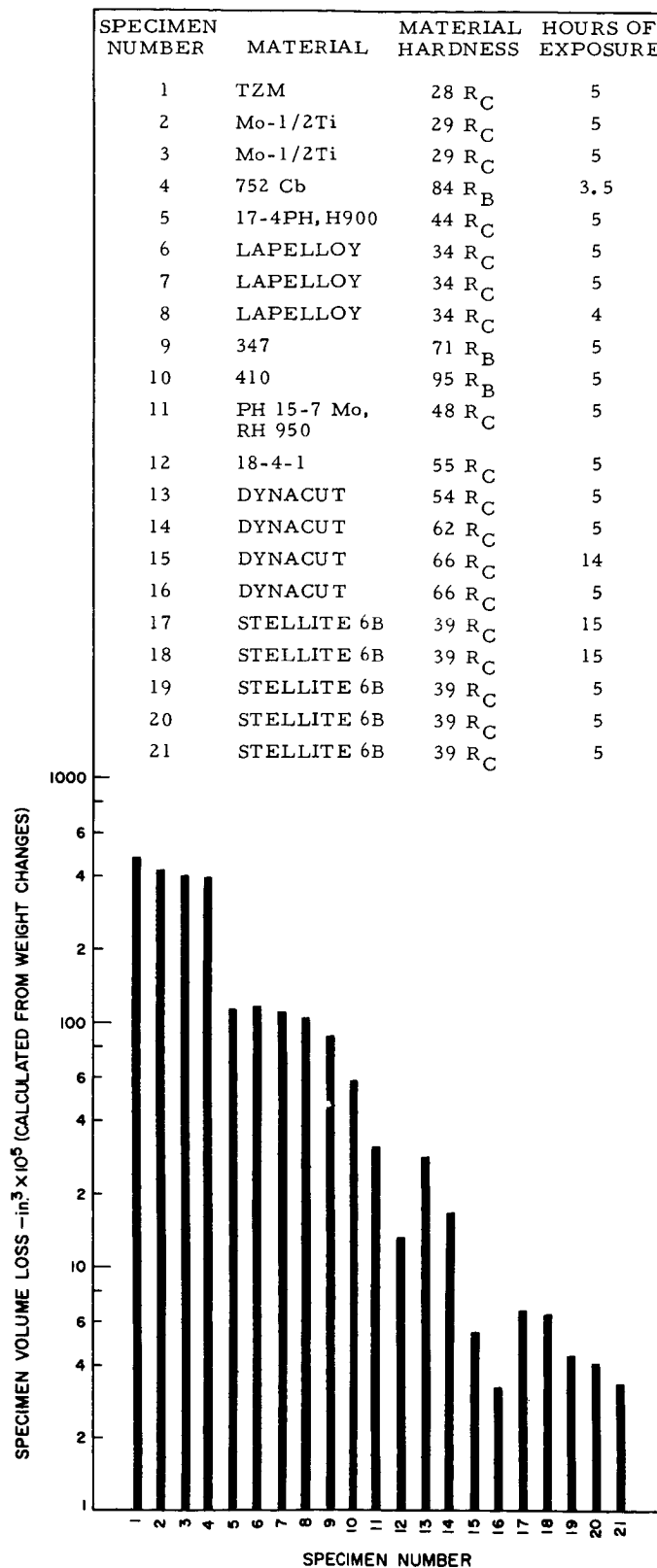


Fig. 7-5. Volume loss of specimens accelerated mercury erosion tests

REFERENCES

- 7-1. Beil, H. E. , Selection of Accelerated Mercury Erosion Test Method, Technical Memorandum No. 390:63-4-137. Aerojet-General Corp. , Azusa, Calif. , Sept. 1963.
- 7-2. Beil, H. E. , Accelerated Erosion Testing of Candidate SNAP-8 Turbine Rotor and Nozzle Materials, Technical Memorandum No. 390:64-4-207. Aerojet-General Corp. , Azusa, Calif. , Feb. 1964.

8. TURBINE EROSION DURING MERCURY RANKINE TURBO-ALTERNATOR ENDURANCE TESTS

C. Winder
Thompson Ramo-Woolridge
Cleveland, Ohio

The history of the reduction of mercury turbine erosion is discussed starting with the endurance tests conducted on the Sunflower Program, a NASA-funded solar space power system. The turbine erosion experienced by two turbo-alternators that were developed by the AEC Mercury Rankine Program (MRP, previously SNAP 2) at TRW is also discussed. The latest design, the CRU V, is shown to have negligible turbine erosion after 7182 hours of design point operation.

The presentation will discuss the turbine erosion experience of three different turbo-alternators: two machines (CRU V and the earlier CRU IVM) from the AEC MRP program, and one machine (CSU I) from the NASA Sunflower Program. The presentation will lead from the rather high damage of the earlier days to the almost non-existent damage of the current CRU V.

The Sunflower CSU 1-3 was operated for 4329 hours, or about one-half year. Figure 8-1 shows the Sunflower turbo-alternator design point and a cross-sectional view. Sunflower was a solar mercury Rankine power plant designed for earth orbit. The machine was a three-stage impulse turbine with the first and second stages having partial admission and the third stage full admission. The turbine wheels were constructed of separate buckets held in place by a heavy shrink-fitted shroud ring. Materials were predominantly PH15-7 Mo, 17-4 PH, and Haynes 25.

Shaft power output of the turbine was about 5000 W at an overall efficiency of 50%. The features important to turbine erosion on this unit are:

- (1) Wheel-tip speed was 314 ft/s.
- (2) Heavy-walled 360°-inlet collector, which had high heat loss and tended to collect liquid.
- (3) Turbine bucket material was PH15-7 Mo.
- (4) Heavy turbine casing sections were used for the whole length of turbine.
- (5) Recessed wheel shroud-anulli were used to trap liquid, and were undrained.

- (6) Boiler-carryover and vapor-inlet-line condensations were present.
- (7) Nozzle mismatch (25% oversize third-stage nozzle on the 2348-hour test) encouraged liquid to collect at trailing edge of nozzle and to drip off into third-stage wheel.
- (8) Partial-admission turbine encouraged liquid particles to reenter exit side of second-stage wheel.

Figure 8-2 shows the third-stage turbine wheel from Sunflower CSU I-3 after 2348 hours. Figure 8-3 shows a different wheel which ran for 4329 hours with less damage (after twice the operating time) than the wheel shown in Fig. 8-2. This improvement is due to better matched nozzles, better turbine inlet vapor quality, and heaters on the inlet collector.

The AEC Mercury Rankine Program produced six turbo-alternator designs (I, II, III, IV, IVM, and CRU V). Figure 8-4 shows the design point for CRU IVM which was run for 6300 hours. This machine was a two-stage impulse turbine with equal stage pressure ratios. The construction was of separate vanes and buckets. The turbine wheel shroud had an interference fit to hold the blades in position. Materials were PH15-7 Mo (first stage) and 17-4 PH (second stage). Shaft power was 7000 W at about 0.58 efficiency. Early expectations of high erosion rates dictated certain compromises of design, such as separate special blade materials and lower than optimum wheel tip speeds. However, the low turbine erosion rates experienced by CRU IVM encouraged the CRU V turbine design selection.

The erosion experienced in 6300 hours by this unit is shown in Fig. 8-5. This figure shows the first-stage turbine wheel inlet side. The darkened markings on the turbine bucket leading edge represent the damage which was relatively superficial.

Figure 8-6 is a magnified view of the inlet of the second-stage wheel showing damage closer to the root. The interesting point is that the damage to the second-stage wheel was significantly less than the first-stage wheel. The explanation for this latter condition is the poor quality vapor provided by the boiler during the major portion of the test.

The boiler used for the CRU IVM endurance tests was an early design prototype NaK to mercury boiler which was not used on later CRU V tests. The comparison of the boiler inlet flow to turbine inlet vapor flow (using a turbine nozzle calibration) showed the vapor quality to be usually 80 to 90%. The liquid separating and

collection tendency of the turbine inlet collector encouraged the formation of large drops of liquid which entered the turbine through the last nozzle throat.

The most recent MRP turbo-alternator is the CRU V. The first unit built has now accumulated about 7200 hours of operation, and the fifth unit has approximately 6200 hours. The other three units have been used in shorter performance and development tests.

Figure 8-7 shows the design point for the CRU V. The exhaust pressure of 9.2 psia for this unit is slightly higher than the pressures (6.0 to 7.5 psia) used for previous CRU designs. This pressure increase is used for condenser stability and weight reduction.

Figure 8-8 is a CRU V cross-section. Other CRU V information pertinent to turbine erosion is as follows:

- (1) Partial admission first-stage nozzle.
 - (a) Early units had single 66° arc of admission.
 - (b) Nozzle vanes are Nivco 10 milled and ground to shape.
 - (c) Nozzle vane trailing edges are 0.003-in. thick.
- (2) Turbine wheels (first stage is Nivco 10 and second stage is PH15-7 Mo) are single piece EDM (electrical discharge machining) integral blades (LE of 0.010-in. diameter; TE of 0.003-in. diameter). The wheels are unshrouded, and have a rough surface from EDM.
 - (a) First stage is impulse with tip speed of 350 ft/s and wheel inlet relative velocity is Mach No. 0.75.
 - (b) Second-stage wheel tip speed is 376 ft/s. Second stage is mostly impulse with only 1.3 psia drop to maintain constant velocity in the vanes. Wheel inlet Mach No. is +1.12 at 576 ft/s.
 - (c) Second-stage wheel inlet equilibrium quality is 89.5%.
- (3) The second-stage nozzle vanes are EDM integral with an inner ring of 17-4 PH. The nozzle is completed by welding an outer ring over the vanes.

Figure 8-9 shows the turbine hardware after 6500 hours of operation. Figure 8-10 shows the second-stage wheel inlet side after 7182 hours of operation (the first stage is in the foreground). As can be seen in these figures, the damage is slight. Under 40- to 50-power magnification, some damage can be seen on the blade convex side downstream of the leading edge and directly on the leading edge. This damage is limited to the upper portion of the blade.

The first-stage nozzle, as shown in Fig. 8-11, has unique damage to the trailing edges of the vanes. When new, the trailing edges are 0.003-in. thick. The nozzle shown has 7182 hours of operation. The exact cause of the damage is not known; however, other machines have not had the problem. The nozzle has not yet been disassembled and sectioned. Metallurgical analysis may reveal the cause. The damage does not appear to be typical impingement erosion, and the first-stage wheel is practically unmarked which is not consistent with nozzle liquid damage.

The operating conditions and a cross-sectional view of the SCAP (silent compact auxiliary power) turbo-alternator are shown in Fig. 8-12. The SCAP was an Army research program.

The turbine velocities are quite high for this machine (Figs. 8-12 and 8-13) and, after approximately 200 hours of operation, no turbine erosion was detectable. There are no plans for endurance testing of this machine at the present time.

CONCLUSION

Turbine erosion experienced in 34,000 hours of total operation in these small MRP turbo-alternators has been minor in relation to the 10,000-hour life objective. Equilibrium moisture levels at design point were approximately 10% at the inlet to the last stage, except when poor boiler performance reduced inlet vapor quality. Under the latter conditions, the first-stage wheel usually suffered more damage than the second stage.

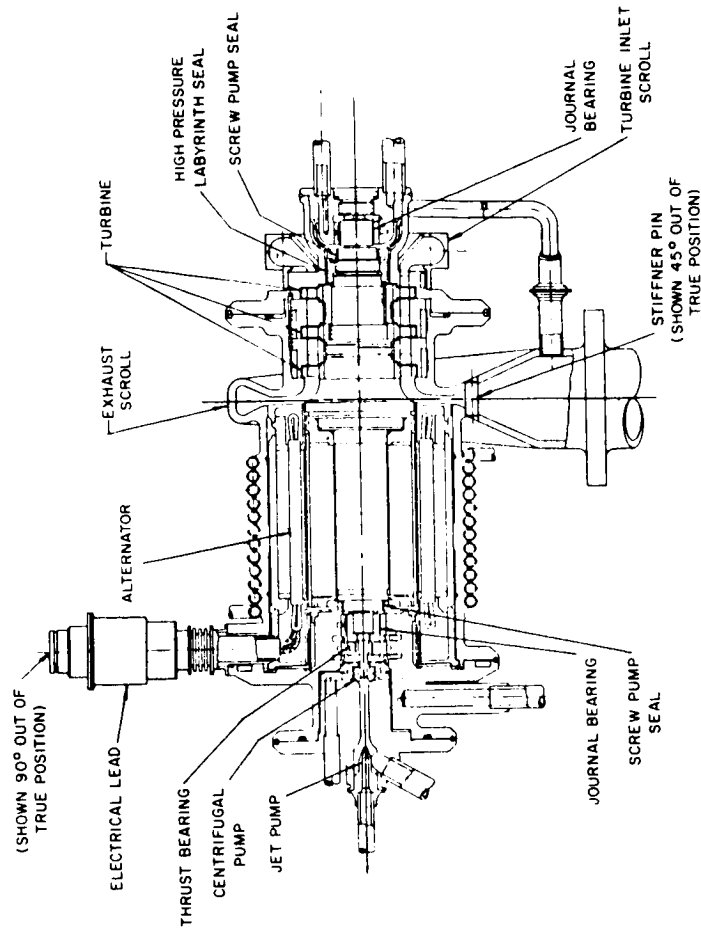
Detail design of the turbine hardware has helped to reduce wheel erosion by ensuring that separated liquid does not re-enter the wheel blades. Other conclusions are:

- (1) Continued MRP boiler improvement over the years has contributed strongly to reduction of turbine erosion.

- (2) Early concern (1957--1960) that dictated lower than optimum wheel tip speeds proved unfounded. Currently, turbine designs are based on best ratio of the tip speed to sonic velocity.
- (3) Supersaturation has not been found in the experience to date. Designs are based on saturated vapor. The earliest turbine designs assumed supersaturation and had bad performance. Correlation of temperatures, pressures, and turbine performances with predictions denied the existence of supersaturation in the systems operated to date.
- (4) Better attention to clean aerodynamic design of turbines to control condensate has resulted in reduction in erosion. Examples are: CRU V and CRU IVM. Full admission nozzles seemed to be a help in improving liquid distribution and reducing erosion.

Currently, it is planned to run two CRU V turbines for 10,000 hours with good pretest record of hardware conditions to provide further data. One CRU is currently operating.

The largest unknown in the data presented is the actual amount, size, and velocity distribution of moisture present in the turbine.



SHAFT SPEED 40,000 RPM

TURBINE INLET CONDITIONS
13.7 LB/MIN 240 PSIA 1250°F
TURBINE EXHAUST PRESSURE
7.0 PSIA
DEMONSTRATED POWER OUTPUT-DESIGN
3.5 KWe GROSS
DEMONSTRATED POWER OUTPUT-MAX.
3.76 KWe GROSS
DEMONSTRATED MACHINE EFF.-DESIGN
36%
DEMONSTRATED ENDURANCE
4329 HOURS

PRINCIPAL DESIGN FEATURES

WELDED CAST HOUSING
THREE STAGE TURBINE

Fig. 8-1. Sunflower CSU 1-3 turbo-alternator data

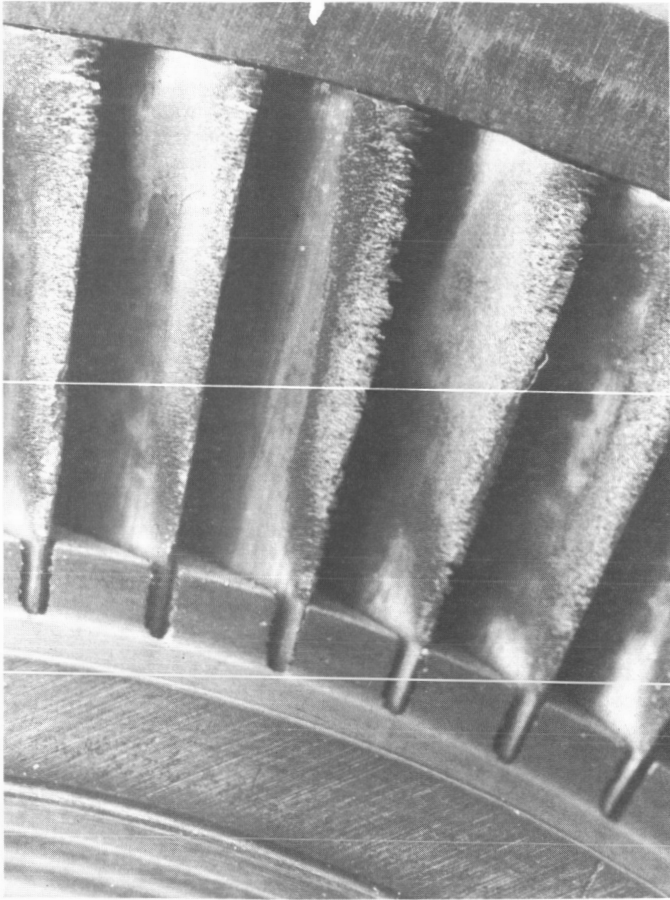


Fig. 8-2. Third-stage turbine wheel, inlet; Sunflower CRU 1-3 after 2344 hours

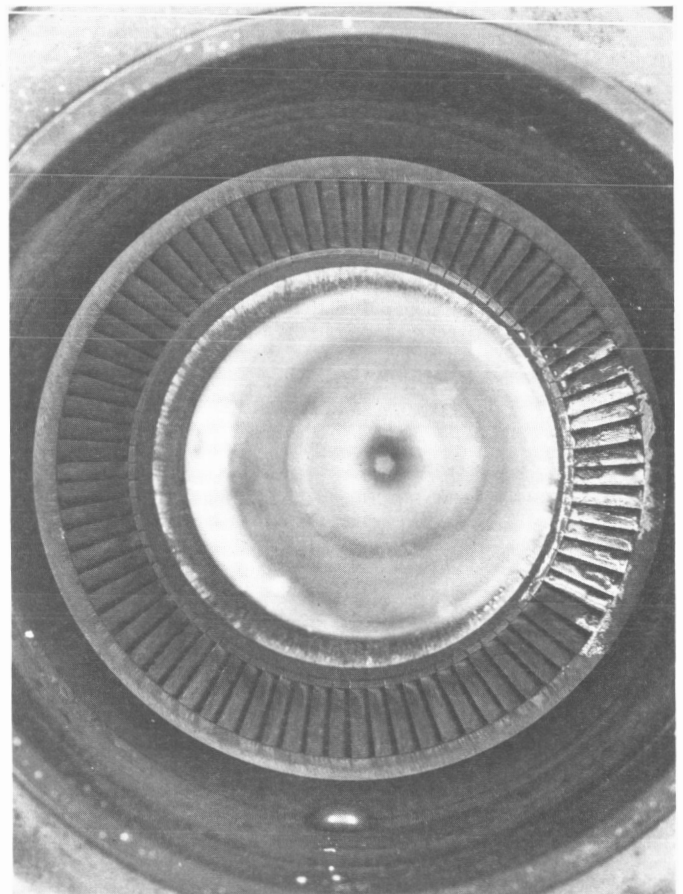
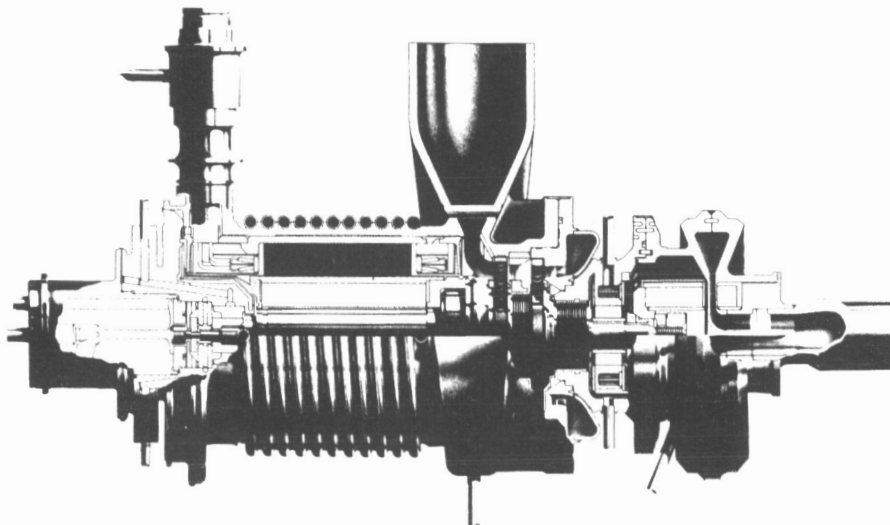


Fig. 8-3. Third-stage turbine wheel, inlet; Sunflower CSU 1-3A after 4329 hours



TURBINE INLET CONDITIONS
20.0 LB/MIN 115 PSIA 1150°F
TURBINE EXHAUST PRESSURE

7.5 PSIA

DEMONSTRATED POWER OUTPUT - DESIGN

4.1 KWe GROSS

DEMONSTRATED POWER OUTPUT - MAX.

6.5 KWe GROSS

DEMONSTRATED MACH. EFF. - DESIGN

40%

DEMONSTRATED ENDURANCE

6296 HOURS

SHAFT SPEED 36,000 RPM

PRINCIPAL DESIGN FEATURES:

WELDED CAST HOUSING

ISOLATION OF HIGH TEMPERATURE TURBINE INLET SCROLL

THERMOELASTIC SYMMETRY OF TURBINE BEARING SUPPORT

(NaK PUMP REMOVED FROM SHAFT - CAPACITANCE PROBES SUBSTITUTED)

Fig. 8-4. CRU IVM turbo-alternator data

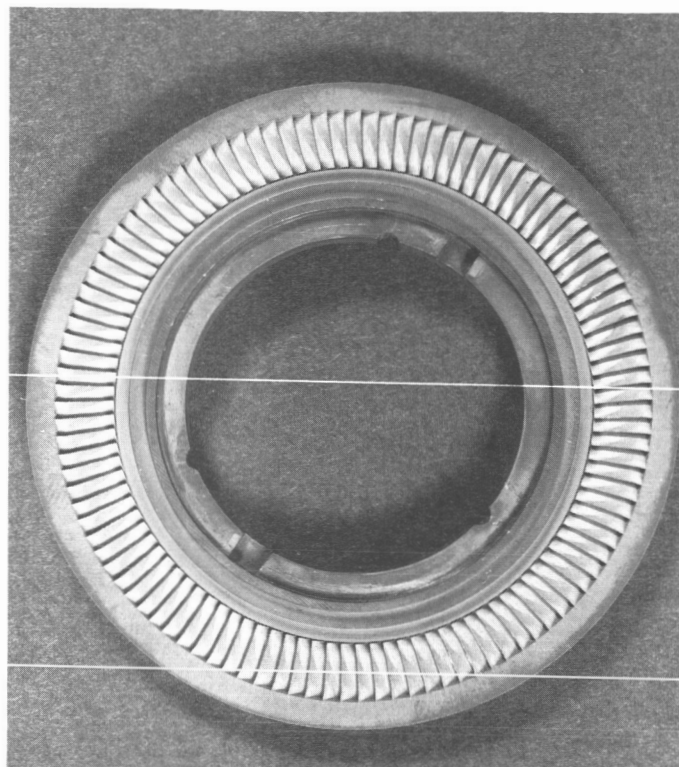
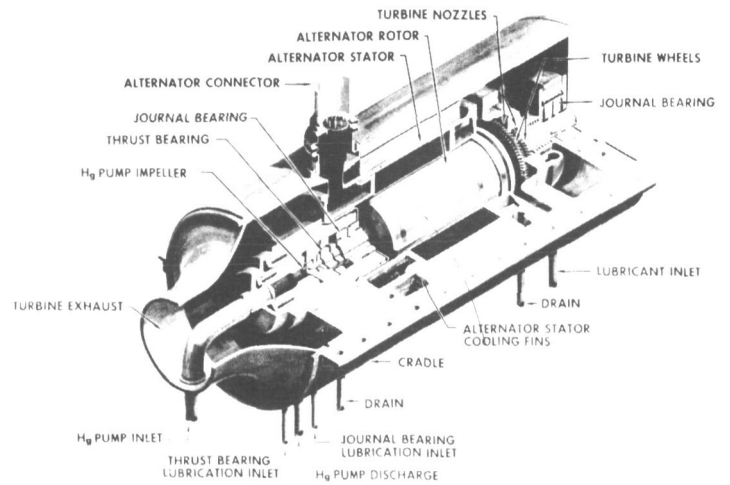


Fig. 8-5. First-stage turbine wheel, inlet; CRU IV M-3A after 6300 hours



Fig. 8-6. Second-stage turbine wheel, inlet; CRU IV M-3A after 6300 hours

TURBINE INLET CONDITIONS
20.0 LB/MIN 115 PSIA 1150°F
TURBINE EXHAUST PRESSURE
9.2 PSIA
DEMONSTRATED POWER OUTPUT-DESIGN
4.1 KWe GROSS
DEMONSTRATED POWER OUTPUT-MAX.
5.6 KWe GROSS
DEMONSTRATED MACH. EFF.-DESIGN
43%
DEMONSTRATED ENDURANCE
7182 HOURS



SHAFT SPEED 36,000 RPM

PRINCIPAL DESIGN FEATURES:

VAPOR COOLED, THREE PHASE ALTERNATOR
HIGH LEVEL OF COMPONENT INTERCHANGEABILITY
SEPARATION OF STRUCTURAL FUNCTIONS
AXIALLY SPLIT, MACHINED HOUSING

Fig. 8-7. CRU V turbo-alternator data

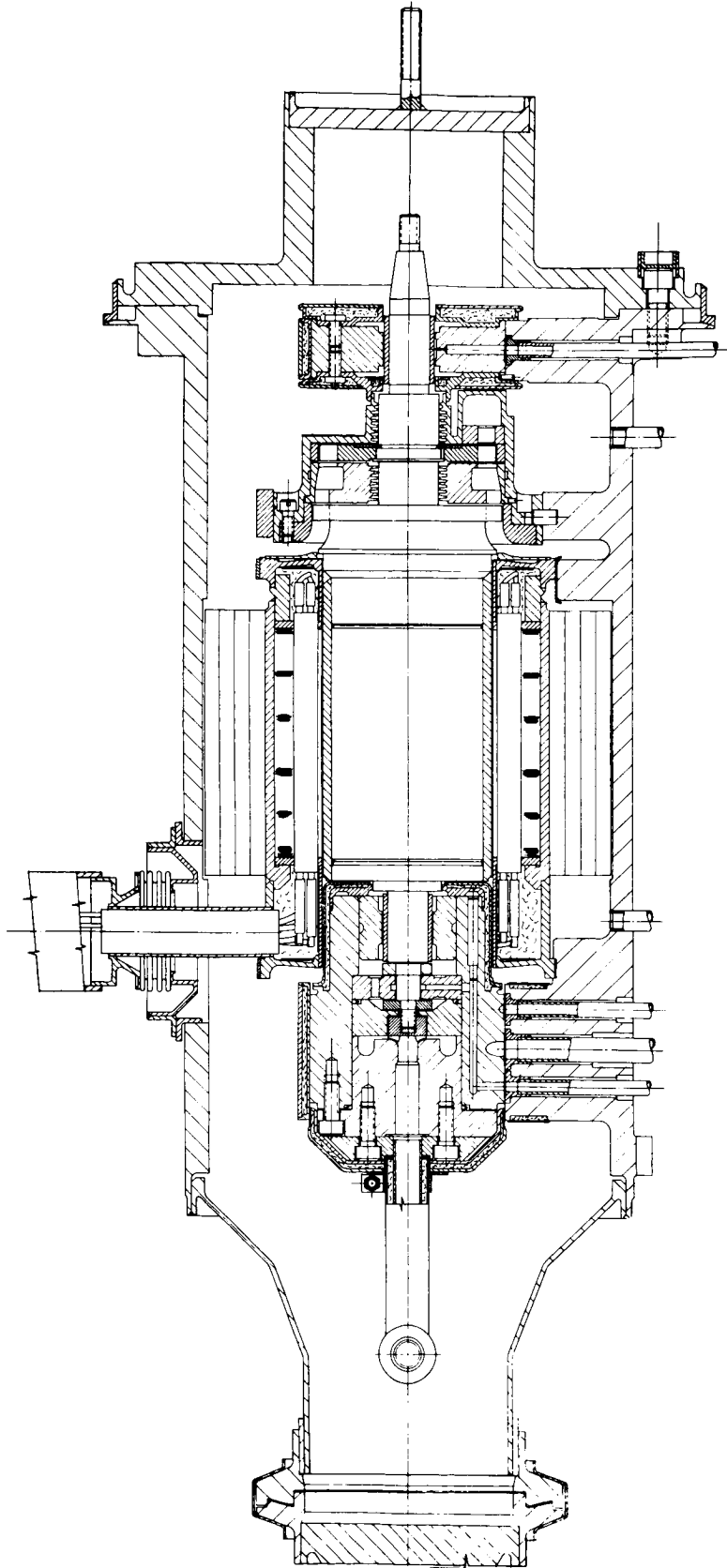
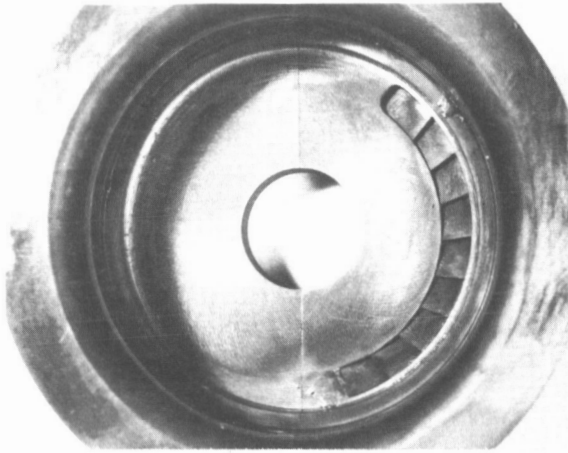
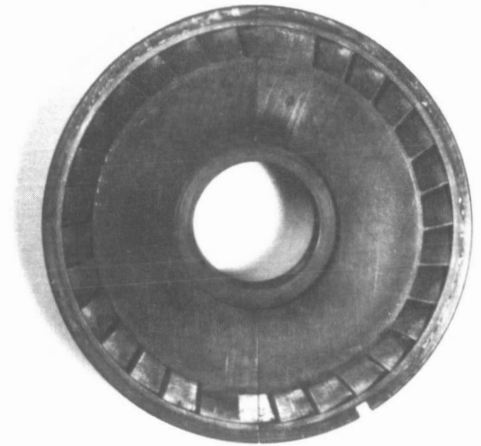


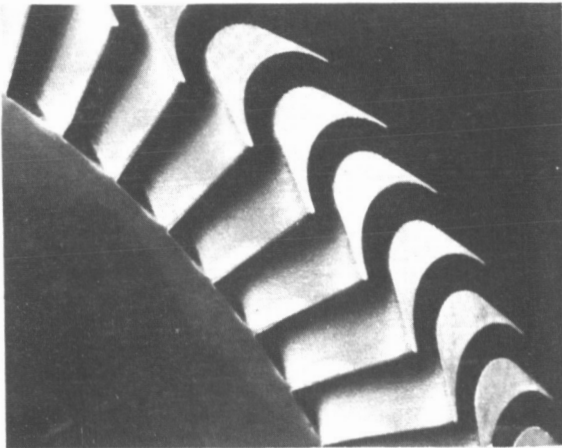
Fig. 8-8. CRU V turbo-alternator, sectional view



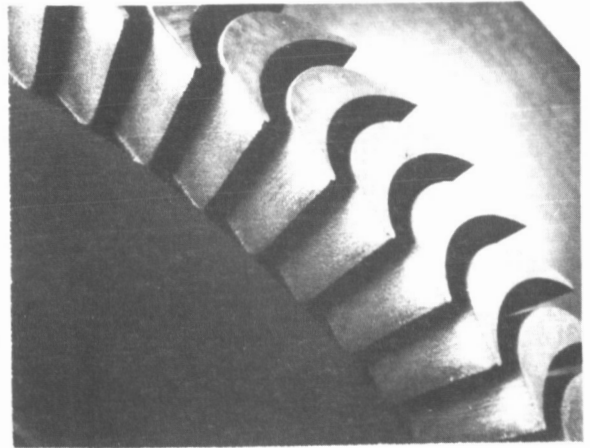
1ST STAGE NOZZLE



2ND STAGE NOZZLE



1ST STAGE ROTOR BLADES



2ND STAGE ROTOR BLADES

Fig. 8-9. CRU V turbine hardware after 6500 hours of operation (CRU V-1C)

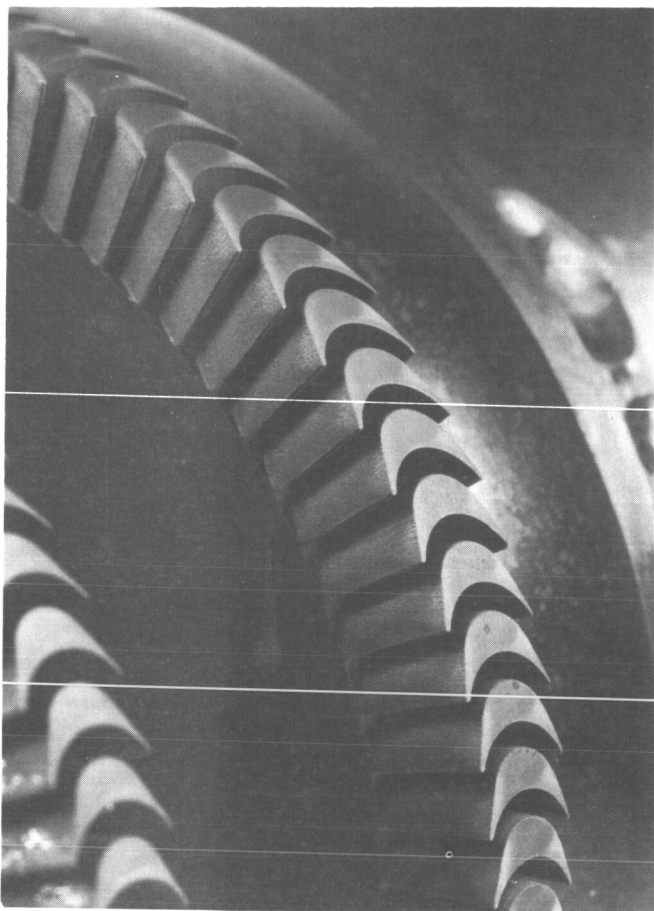


Fig. 8-10. Second-stage turbine wheel,
CRU V-1D after 7182 hours

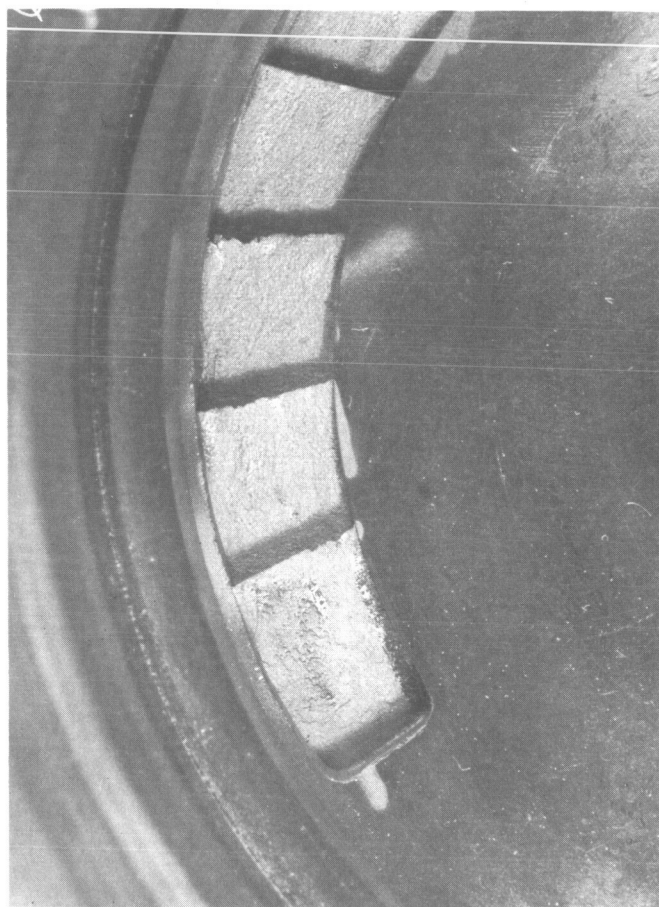
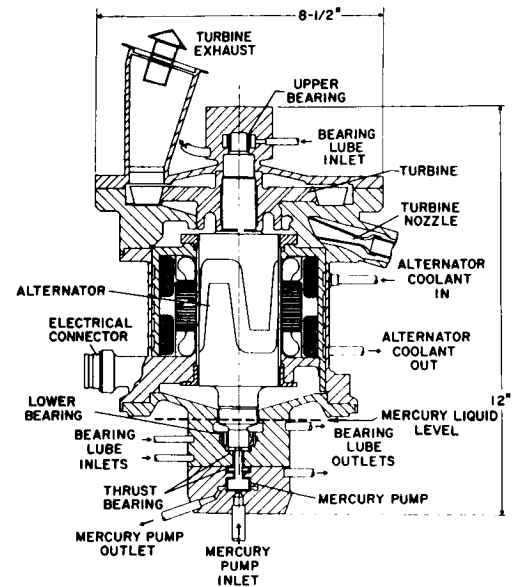


Fig. 8-11. First-stage nozzle discharge,
CRU V-5C after 7182 hours

TURBINE INLET CONDITIONS
10.75 LB/MIN 318 PSIA 1300°F
TURBINE EXHAUST PRESSURE
1.85 PSIA
DEMONSTRATED POWER OUTPUT-DESIGN
3.6 KWe GROSS*
DEMONSTRATED POWER OUTPUT-MAX.
4.0 KWe GROSS*
DEMONSTRATED MACHINE EFF.-DESIGN*
36.4%
DEMONSTRATED ENDURANCE
350 HOURS
DEMONSTRATED STARTUPS
OVER 200



SHAFT SPEED 24,000 RPM

PRINCIPAL DESIGN FEATURES

GRAPHITE BEARINGS
BRUSHLESS-ELECTRICALLY EXCITED ALTERNATOR
VERTICAL SHAFT
SINGLE STAGE SUPERSONIC TURBINE
SPOUTING VELOCITY $M = 3.60$ APPROACH VELOCITY $M = 2.36$
SIMPLIFIED MERCURY PUMP

***NOTE: 0.3 KW REQUIRED FOR ALTERNATOR FIELD EXCITATION SUBTRACTED**

Fig. 8-12. SCAP TAU 1 turbo-alternator data



Fig. 8-13. SCAP turbo-alternator rotor

9. POTASSIUM TURBINE EROSION EXPERIMENTS

Hans D. Linhardt
Philco-Aeronutronics
Newport Beach, California

PRECEDING
PAGE BLANK

This abstract summarizes the results of potassium experiments at Aeronutronic. The work is divided into two tasks: Task I to determine potassium condensate droplet sizes and Task II to test a turbine in a potassium vapor flow.

Task I was directed toward the experimental determination of potassium vapor condensate droplet sizes for typical thermodynamic expansion processes in the temperature range of $1500^{\circ}\text{F} < T < 1000^{\circ}\text{F}$ and theoretical exhaust quality conditions of $0.80 < x < 0.95$. For this purpose, a forced-convection boiling-condensing closed-loop potassium facility was developed. The potassium loop provided the specified potassium vapor conditions to the test section which consisted of various expansion nozzles and nickel-plated wedge specimens placed downstream of the nozzle. After performance of seven short duration (four to five hours) tests, the wedge erosion damage lengths were measured and correlated with the two-phase flow theory.

The analysis of the test data provided internally consistent, accurate, and reproducible information on free-stream droplet size as a function of theoretical vapor-nozzle-exhaust quality and saturation inlet temperature. The significant result of Task I was that the measured average free-stream droplet size was $0.50 \mu\text{m}$ which agreed reasonably well with Gyarmathy's recent analysis. In addition, the exploratory program has proved that the selected nozzle-wedge erosion method works and, therefore, should be used for future, more detailed, two-phase flow investigations.

Task II was directed toward the design, fabrication, and testing of a supersonic turbine within the previously described loop. The unit used in this study was a supersonic turbine that was run for 96 continuous hours at an average shaft speed of 17,800 rpm with average stagnation conditions of 1250°F , 5.6 psia, and theoretical nozzle exit vapor quality of $x = 0.85$.

The test turbine wheel, which was made of TZM material, had four different blade geometries with blade angle varying between 25 and 40 degrees. The most prominent feature evident on inspection of the turbine wheel was an erosion groove starting at the leading edge near the root of each blade, and then continuing

in a radial direction to the blade tip immediately behind the leading edge on the convex side of the blade. In addition, two of the three partial-admission turbine nozzles experienced a large amount of what appeared to be corrosion with large deposits visible on the nozzle walls. Due to flow separation, it is believed that a puddle of liquid potassium accumulated downstream of the corroded nozzle area, from which large liquid potassium droplets were shed. The impingement of these secondary droplets upon the turbine wheel would explain the erosion groove on each blade. The small amount of erosion visible on the concave and convex side of the blades near the leading edge is attributed to the impingement of primary, or free-stream, potassium droplets.

Figures 9-1 and 9-2 show the potassium loop layout. Figure 9-3 shows an assembly drawing of the nozzle-wedge test section. Figure 9-4 summarizes the nozzle wedge test conditions of the experiments. Figure 9-5 shows the resulting droplet size as a function of vapor exit quality. Figure 9-6 shows the result of the erosion on a wedge. Figure 9-7 shows the condition of the turbine wheel shaft, bearings, and counterbalance wheel after testing. Figures 9-8 and 9-9 show the appearance of the typical turbine section before and after testing. Figure 9-10 illustrates, by interpretive sketch, the erosion phenomena on a turbine blade. Figure 9-11 is a photograph of the nozzles used in the turbine study showing deposit accumulation and erosion damage.

Full details of the experiments and results can be found in these reports:

- (1) Linhardt, H. D., Potassium Condensate Droplet Size Determination, Publication No. U-3709 (SAN 595-1). Aeronutronic Division of Philco-Ford Corporation, Aug. 1, 1966.
- (2) Linhardt, H. D., et al., Potassium Turbine Erosion, Publication No. U-3904 (SAN 595-2). Aeronutronic Division of Philco-Ford Corporation, Dec. 15, 1966.

DISCUSSION

In response to questions, the author pointed out that the exit diameter of the nozzle was about 0.25 in. for the experiments measuring the size of condensation droplets. The wedges used had a different angle on the top side than the bottom side and, as a result, the difference in pressure caused a transverse flow of

potassium vapor. It was pointed out that the damage encountered by the potassium turbine during the 100-hour test could have been due to washing corrosion because of a high oxygen content in the potassium. Deposits were encountered on the nozzles after a 100 hours of testing; the deposits were determined to be stainless steel that was deposited by mass transfer from other parts of the loop. Dr. Linhardt said that they had experienced discoloration and possible pitting of the nozzles upstream of the throat, indicating that condensation had occurred at this location; this experience was in agreement with the theoretical predictions of Glassman. Dr. Gyarmathy stated that the boundary layer was super-heated which would tend to evaporate droplets in the boundary layer. Also, he pointed out that the natural motion of the vapor would be such that the droplets would tend to be thrown away from the wall rather than toward it.

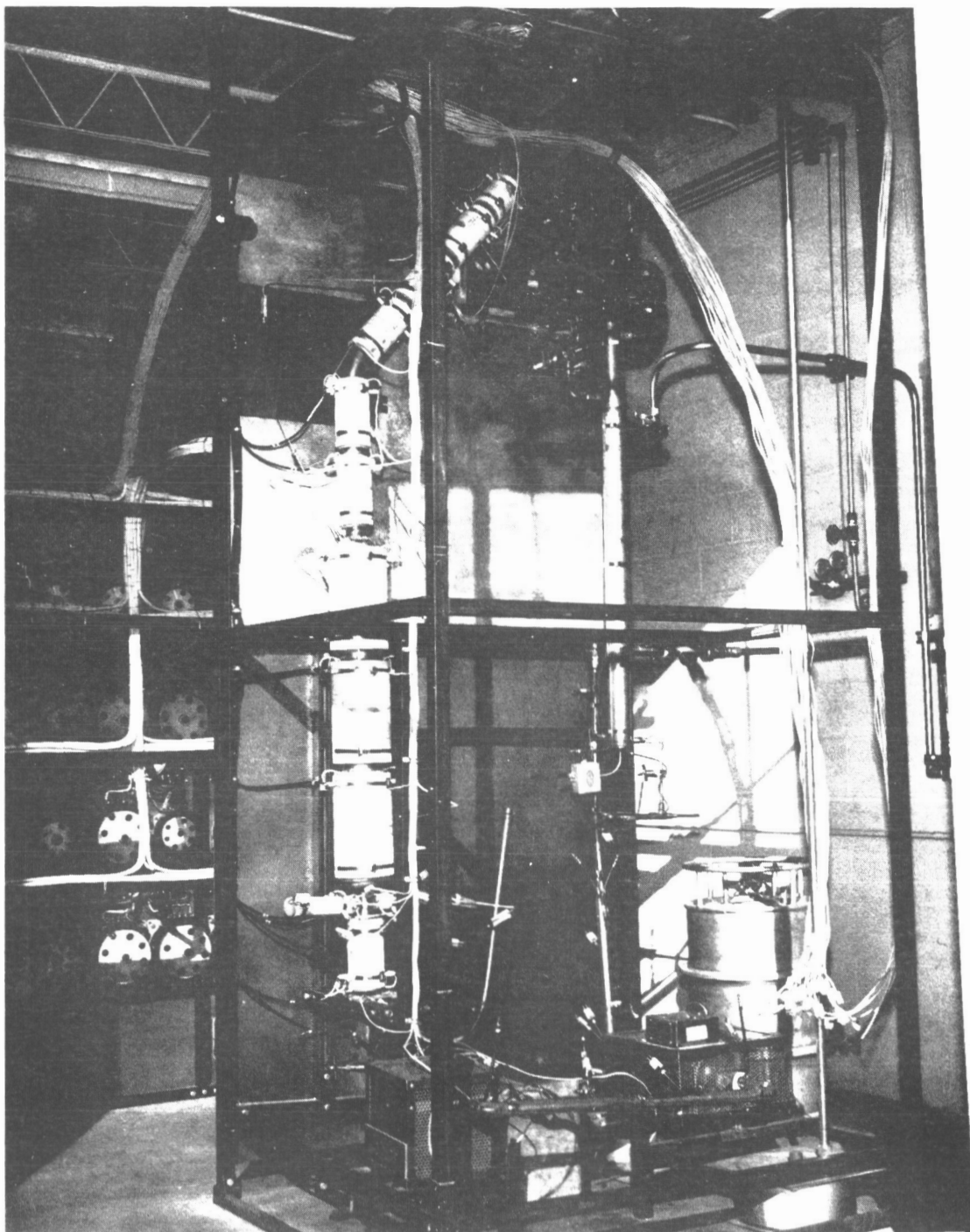


Fig. 9-1. Potassium loop prior to final insulation

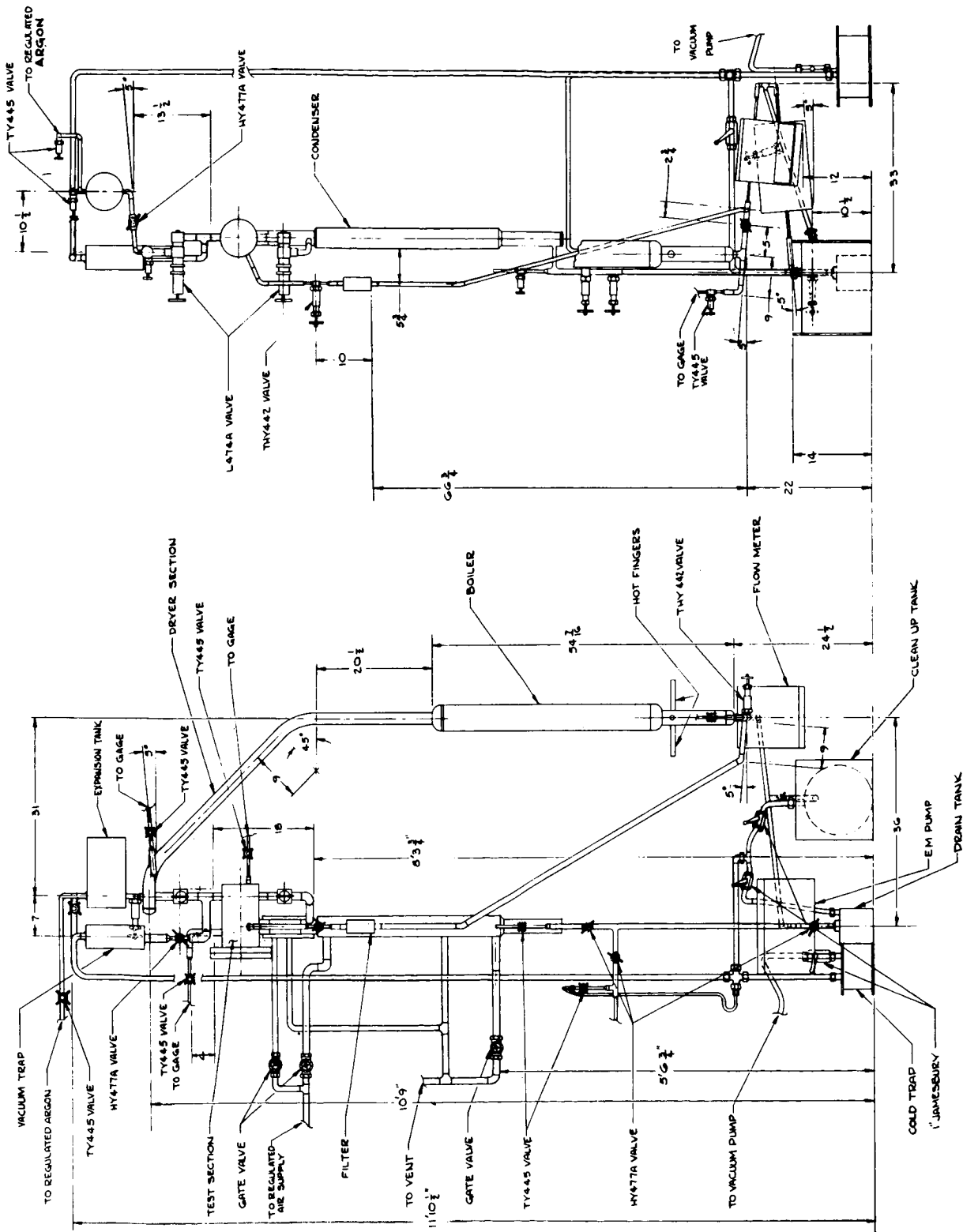


Fig. 9-2. Potassium loop installation drawing

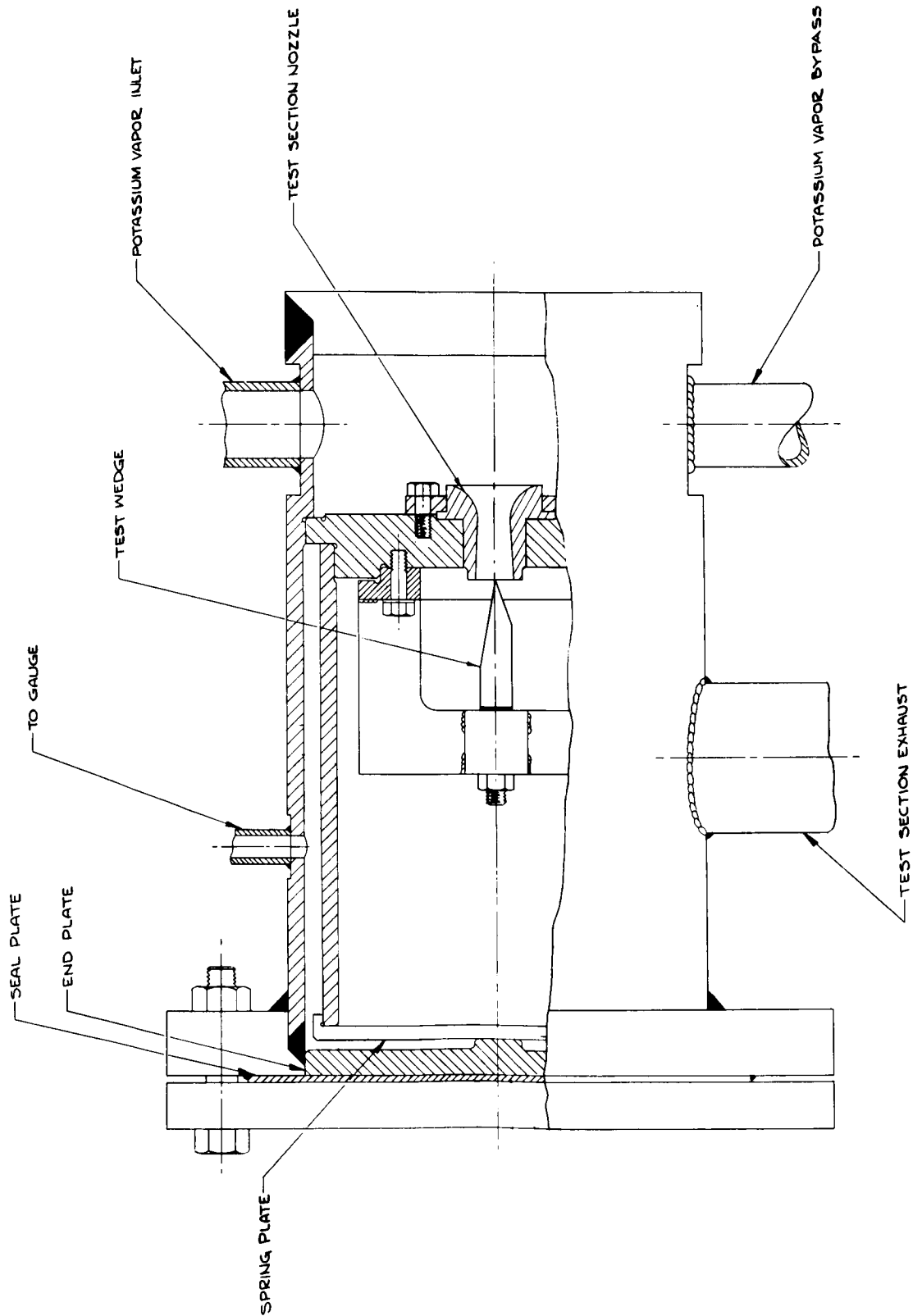


Fig. 9-3. Test section layout drawing with mounted nozzle-wedge specimen

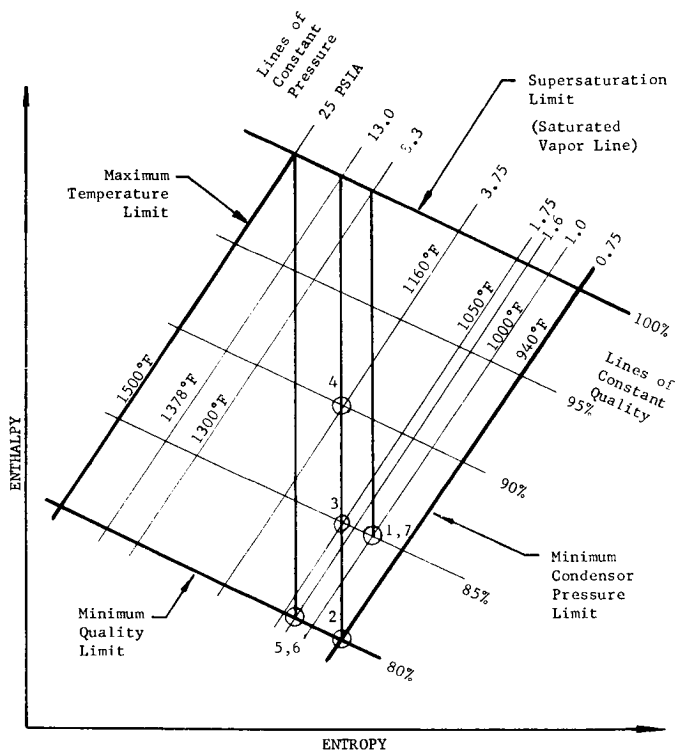


Fig. 9-4. Mollier chart for selected thermodynamic processes

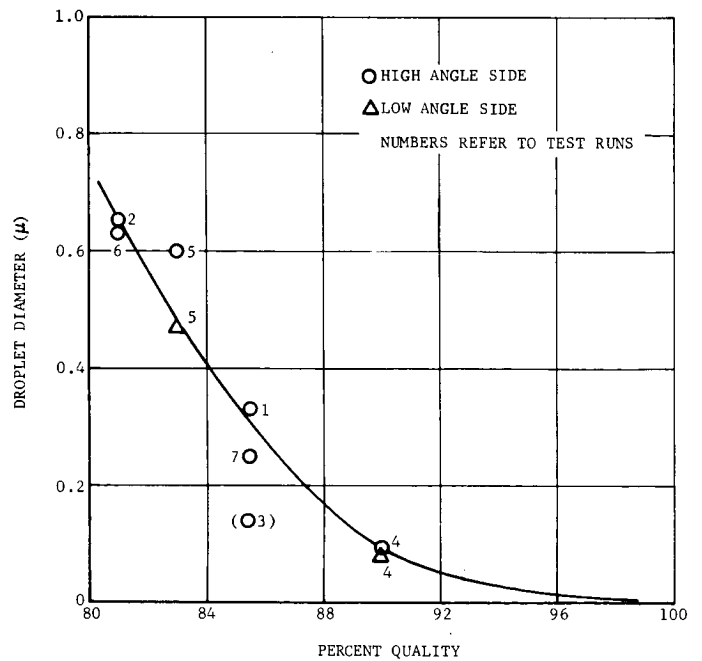


Fig. 9-5. Correlation of droplet size and vapor quality for potassium flow

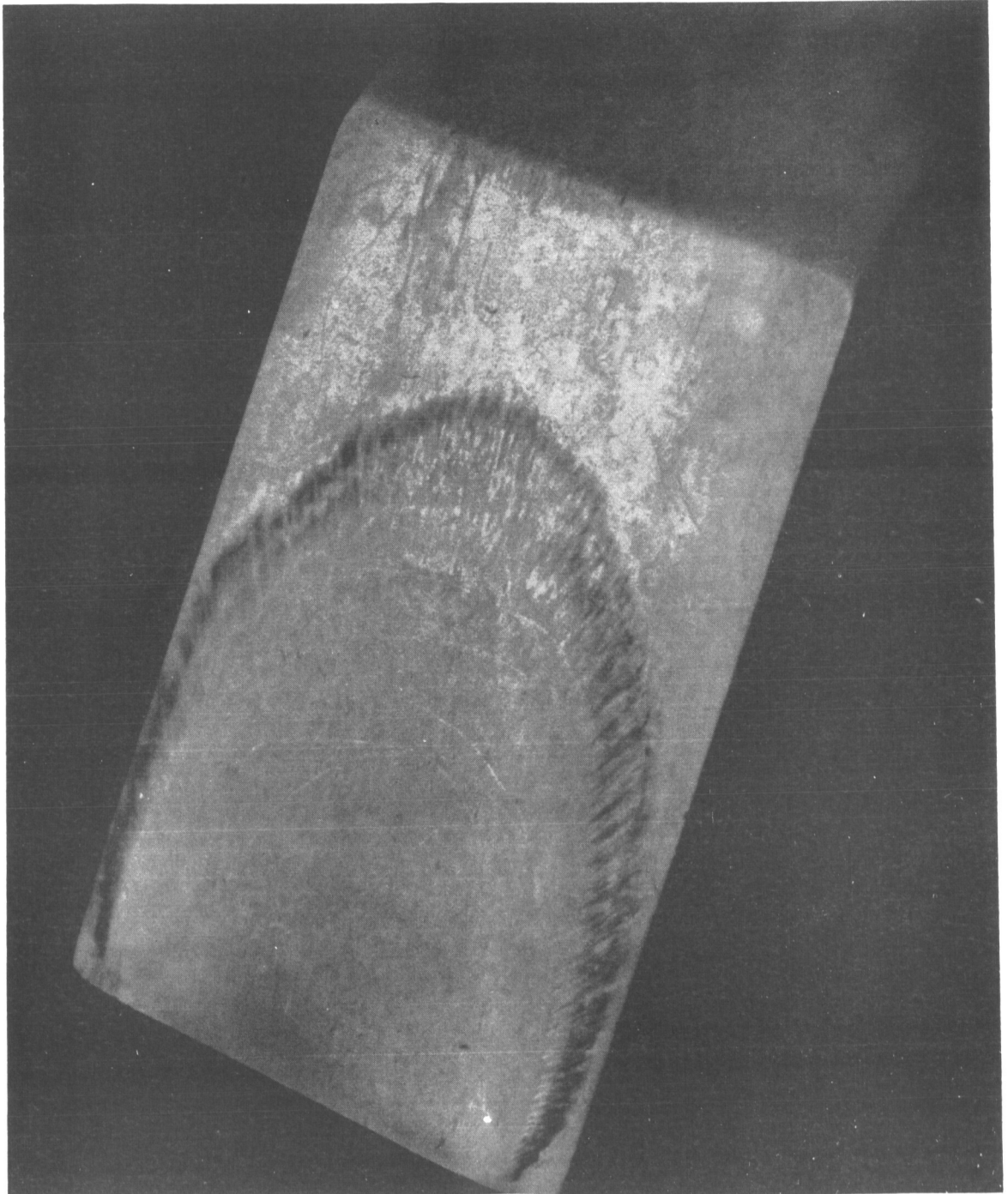


Fig. 9-6. Damage length of nickel wedge due to impingement of 0.60- μ m potassium droplets

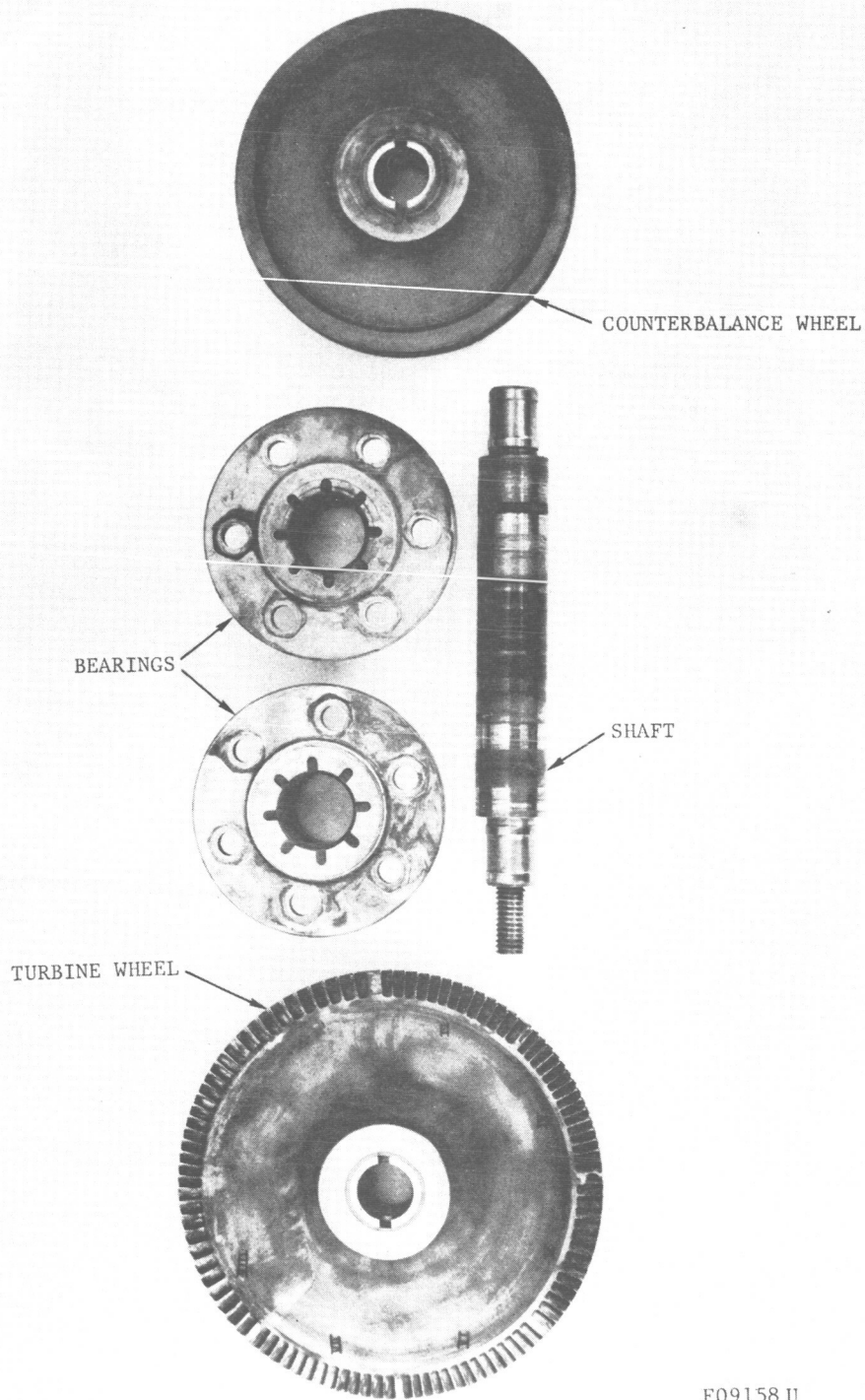


Fig. 9-7. Turbine wheel, shaft, bearings, and counterweight after endurance test



Fig. 9-8. Typical appearance of turbine blades before testing



Fig. 9-9. Turbine blades after endurance test,
25-degree blade angle, Section VIII

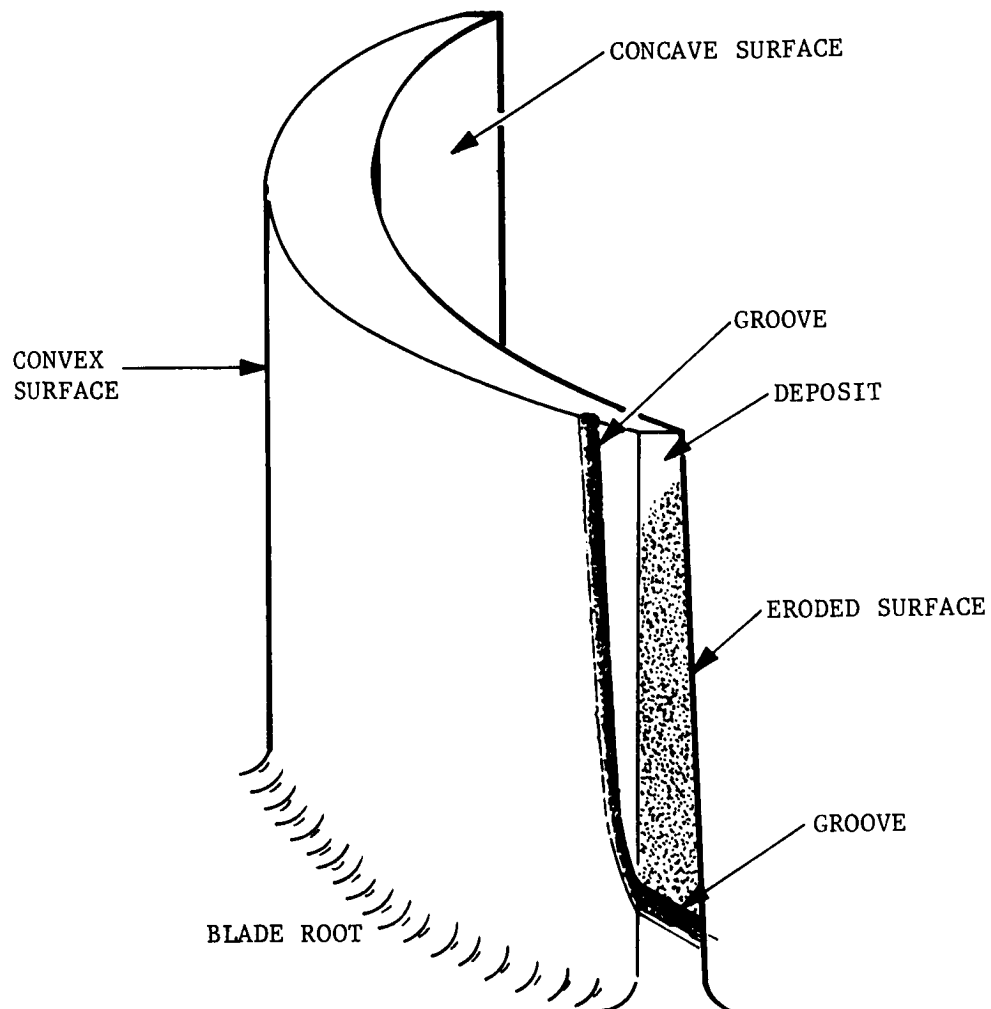


Fig. 9-10. Typical turbine blade erosion pattern

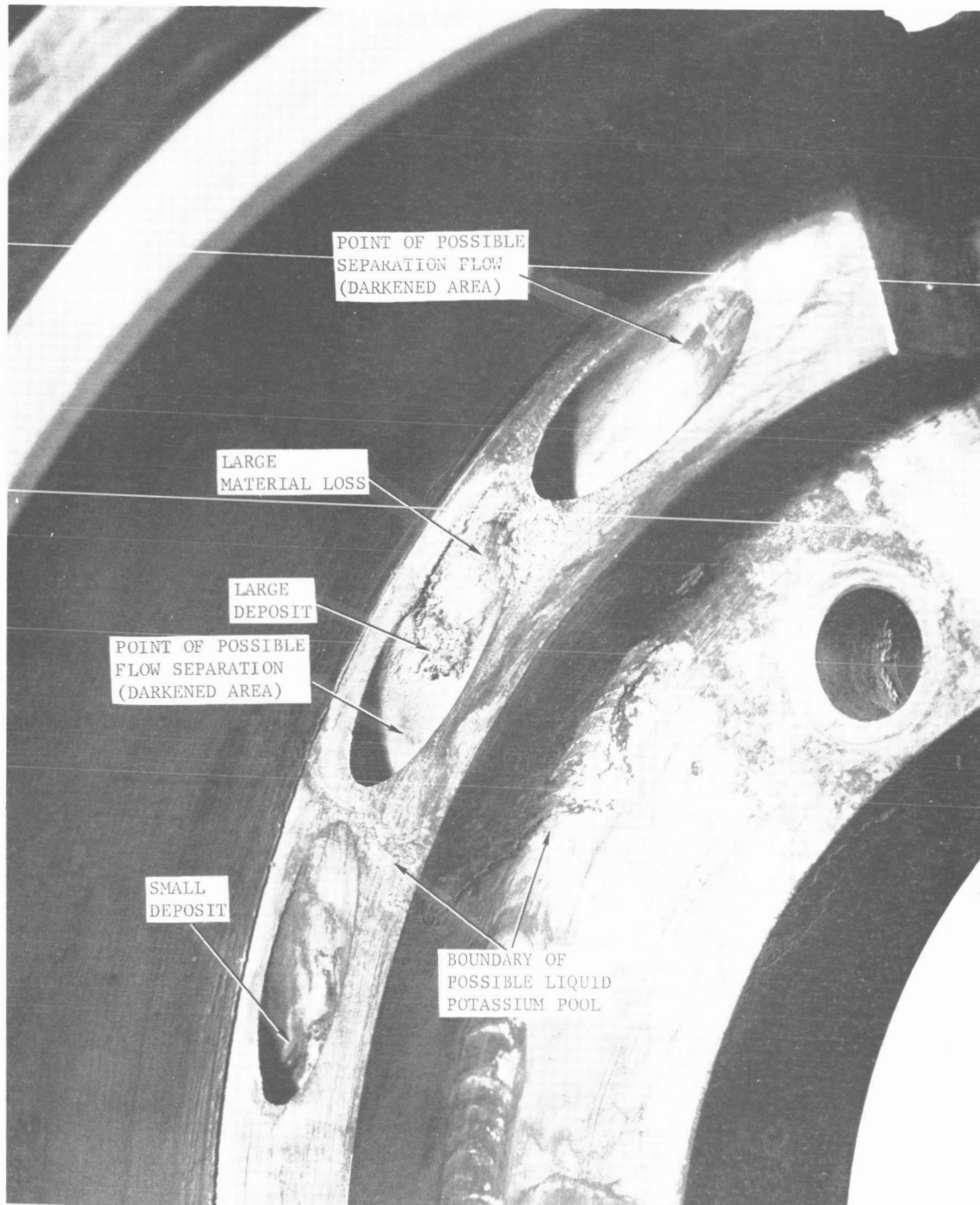


Fig. 9-11. Nozzle block No. 1 after endurance test

10. A MODEL FOR MULTIPLE-DROP-IMPACT EROSION OF BRITTLE SOLIDS

Olive Engel
General Electric
Evandale, Ohio

INTRODUCTION

When liquid drops impinge against the surface of a solid, high pressures and high fluid-flow velocities are produced. If the impingement process is continuous, as it is when turbine buckets intercept waterdrops present in a steam flow, even the strongest materials eventually fail. In attempting to deal with this problem, it is essential to understand every aspect of the problem: the forces that are involved, the manner in which failure is accomplished in different materials, and the rate at which the process progresses.

Forces Involved

An impinging drop has two damage-producing attributes. The drop exerts a localized pressure and flows out radially around the point of impact.

Figure 10-1 shows the stresses that develop as a result of the localized pressure. At the periphery of the compressed area, the principal stresses are tensile and compressive. The radial tensile stresses around the compressed area constitute one of the major damage-producing attributes of an impinging drop. Near the center of the compressed area below the impacted drop, the principal stresses are all compressive. Damage is not produced in this area because materials do not tend to fail under pressure.

If the impact occurs between a moving plate and a stationary drop, shear stresses exist around the plug of plate material that is slowed down as a result of the collision; shear stresses also exist in the plate material around the point of impact. At the convexity that develops on the trailing face of the plate when the compressional wave, initiated by the impact, reflects as a tension wave, the principal stresses are all tensile.

The pressure produced by the impact drives the drop liquid that is close to the solid surface radially outward around a central stagnation point. The radial flow velocity is much higher than the impact velocity and does constitute an important

damage-producing attribute of an impacted drop. This drop velocity is shown in Figure 10-2.

The radially flowing liquid exerts a shear stress on the surface of the solid over which it is running. This shear stress is able to produce a small amount of erosion even when the surface is smooth and polished. If the radially flowing liquid runs over a sizable surface protrusion, such as the raised edges of cracks that have been produced by the impact pressure, the liquid exerts forces against the protruding material and tends to break the material away. Pressure exerted against the protrusion results in a shear stress at the base of the protrusion and in a turning moment that tends to bend the protrusion over.

Failure Mechanisms

The mechanism by which multiple-drop-impact erosion occurs is not only a function of these impact properties of an impinging drop; it is also a function of the specific properties of the solid material against which the drop impinges. There are as many mechanisms of multiple-drop-impact erosion as there are broad groups of material properties. (I am indebted to Dr. Albrecht Herzog for this insight given during a conversation at the Wright Air Development Center, Wright-Patterson Air Force Base, Ohio, in 1953.) To understand the erosion mechanism for a specific material requires a detailed study of the response of this material to the stresses that result from the localized impact pressure and from the high-speed radial flow of an impinging drop.

Erosion Rate

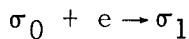
A knowledge of the rate at which erosion progresses on different kinds of materials is important in determining their usefulness in specific applications. In what follows, the rate of erosion of brittle materials is discussed in terms of the particular way in which the materials fail under liquid-drop impingement. The category of brittle materials includes metals and non-metals that are brittle at the time of exposure to drop impact, or that become brittle as the process of drop impingement continues. The yield strength and ultimate strength of brittle materials are almost the same. Consequently, the response of brittle materials to liquid-drop impact will be essentially elastic until energy sufficient to break the characteristic bonds of the material, at the weakest points at which they exist, is supplied. Cracks will then form at these points.

EROSION MODEL FOR BRITTLE SOLIDS

The basic picture of erosion of these materials can be seen best by considering the case of an ideal brittle material that has uniform bond strength and does not work harden. Let us suppose that liquid drops impinge in uniform density against the surface of a test plate of such a material and let the uniform density remain constant with elapsed time. Let the impinging drops have a relative impact velocity and a fixed angle of attack (Fig. 10-3) such that the energies delivered by the individual drop blows are sufficient to cause crack initiation and crack growth in the solid material to a depth σ below the surface. Let the surface of the test specimen be subdivided into unit cells of size σ .

Finally, let the condition for breaking away of a piece of the solid material be the intersection of at least three cracks (Fig. 10-4). A consequence of this condition is that there are at least three species of cells, which involve various stages of crack development in the surface layer of σ -cells. These three species may be defined as follows: the species σ_0 is a unit cell that contains no cracks: the species σ_1 is a unit cell that contains one crack; and the species σ_2 is a unit cell that contains two cracks which may or may not intersect. Of special interest is the species σ_2^* which contains two intersecting cracks. The species σ_2^* is a critical site in the sense that, if just one more intersecting crack should form in such a way as to complete crack formation around a tetrahedral piece of the solid, this piece will break away as an eroded fragment.

When drop impingement begins, the cells of the surface layer contain no cracks. It has been assumed that the impact energy delivered by a single drop is sufficient to initiate a crack to a depth σ in a surface cell. This event can be represented in the following way (Fig. 10-5).



where e is the energy per unit volume needed to form a crack in the material being considered.

As drop impact is continued, the density of σ_1 -cells in the surface layer will increase, and the chance that a σ_1 -cell will be struck by another drop and develop

a second crack will become increasingly more probable. This event can be described as

$$\sigma_1 + e \rightarrow \sigma_2$$

If the two cracks intersect in the formed σ_2 -cell, it becomes a σ_2^* -cell or a critical site.

If a σ_2^* -cell is struck by a drop and a third crack forms in such a way as to complete crack formation around a tetrahedral piece of the solid, the event can be represented in the following way

$$\sigma_2^* + e \rightarrow \sigma_0 + \text{eroded fragment}$$

The σ_0 -cell formed in this event is composed of the underlayer material that is exposed when the eroded fragment breaks away. Consequently, the ejection of an eroded fragment simultaneously regenerates starting material. The newly exposed cell of underlayer material is not exactly the same as a cell of the original surface material, however, because the angle that the newly exposed surface presents to the impinging drops differs from that presented by the original surface and the newly exposed material may contain residual crack ends.

The simplified picture of the erosion process presented so far is restricted to consideration of the cracking damage produced by the impact energy; it has not taken into account the damage that results from the radial flow of the liquid contained in the drops. It is applicable to an erosive environment in which flow is minimized, such as cavitation erosion produced with use of a magnetostriction oscillator. With a little reflection, however, it can be seen that even this simple model is able to interpret the characteristic features of curves of erosion rate plotted against time for data obtained with use of a magnetostriction oscillator.

No loss of material can occur until a minimum of three cracks intersect in such a way as to circumscribe a triangular pyramid. Consequently, there must be an initial period during which no erosion takes place (incubation period). During this period the density of σ_1 -cells, σ_2 -cells, and σ_2^* -cells in the surface layer will build up.

When the density of σ_2^* -cells becomes high enough so that the probability that one of them will be struck by a drop is substantial, a large number of cells will contain one or more cracks. The density of σ_2^* -cells will be greater at this time than at any later time, because up to this time no process has been operating that removed σ_2^* -cells. Consequently, this event will quite suddenly become a frequent occurrence, and the rate of erosion plotted against time will exhibit a sharp rise (accumulation period).

Concomitant with the process of destroying σ_2^* -cells by the loss of eroded fragments is the process of regeneration of σ_0 -cells as the underlayer material is exposed. The initial rapid rate of erosion contains a check against itself by slowing it down, since not only are the essential σ_2^* -cells being destroyed, but σ_0 -cells are being produced. These σ_0 -cells must be converted to σ_1 -cells, and then to σ_2^* -cells before they can again become sites of material loss. Consequently, after the first rapid rise, the rate of erosion will begin to fall off (attenuation period).

The state of a system that is subject to competing processes will pass through a maximum or a minimum. The rate of erosion plotted against time will pass through a maximum and then fall until the rate of producing σ_2^* -cells versus the rate of destroying them becomes equal. At this time the rate of erosion should be essentially constant (steady-state period; see Fig. 10-6).

If this model is applied to a ductile metal, which work hardens to the point of embrittlement and then cracks, the essential features are the same but there are some modifications. In the case of a ductile metal, the first drops that impinge produce craters (by plastic flow) rather than cracks. As the cratering process continues, the surface becomes covered with craters and new craters are superposed over old craters until the worked metal becomes brittle enough to crack. When this point is reached, the model that has been described will operate as for a brittle material until eroded fragments are broken loose. When the underlayer material is exposed, however, it will have to be work hardened to the point of embrittlement before cracks will form in it to produce σ_1 -cells, σ_2 -cells, and σ_2^* -cells. This new feature will result in an oscillation in the curve of erosion rate plotted against time.

Test of the Model

It is of interest to see to what degree the aspects of the erosion-rate curve, which is predicted by this simple model, are observed in actual erosion-rate-versus-time plots of experimental data. As noted previously, the model that has been presented applies to the case that fluid flow is absent. This is essentially the case in cavitation erosion that is produced with use of a magnetostriction oscillator. Thiruvengadam, Preiser, and co-workers have given erosion-rate-versus-time plots for cavitation erosion produced in this way on Stellite 6B, Cb-132 M, 316 stainless steel, TZM (SR), T-222, nickel 201, and 1100-aluminum. Their data are presented in Figs. 10-7 through 10-13 with the permission of Mr. James P. Couch, Nuclear Power Technology Branch, NAS 3-4172, NASA Lewis Research Center, Cleveland, Ohio.

The solid lines shown in these figures were drawn for these sets of data by the experimenters. These curves show the general trend. The dashed curves have been sketched in to show what may be the actual response of each metal. From a casual inspection of these plots, it can be seen that the features predicted by the model are present. There is an intercept on the time axis (incubation period) predicted by the model while the density of σ_2^* -cells builds up. There is a steep rise toward the maximum (accumulation period) predicted by the model for the time during which the density of σ_2^* -cells is the greatest. There is a decrease in rate (attenuation period) predicted by the model for the time during which σ_2^* -cells are being removed as eroded fragments, and σ_0 -cells in the underlayer material are being exposed.

There is a maximum value of erosion rate predicted by the model because competition exists between the rate of formation of critical sites (σ_2^* -cells) and the rate of formation of low-density crack sites (σ_0 -cells in the underlayer material). Finally, there is a decline in slope to a steady-state value predicted by the model for the time that the rate of formation of critical sites is equal to the rate of formation of low-density crack sites. All of the dashed curves exhibit oscillation about the solid curves of general trend after the maximum value has been passed. This oscillation is predicted by the model for metals that work harden to embrittlement rapidly.

Values of the length of the zero-erosion period (incubation period), maximum rate of erosion, and the slope of the rise to the maximum found for the dashed

curves in Figs. 10-7 through 10-13 are given in Table 10-1. Further information on the steady state erosion rate, hardness and lattice type is presented in Table 10-2. The metals are listed in the order of decreasing tensile strength with the exception that T-222 and TZM (SR) should occupy the second and third places in the list, respectively, on the basis of their tensile strengths, rather than the fourth and fifth places. From this tabulation, it can be seen that the trend in the length of the incubation period is opposite to that of the maximum rate of erosion and slope of rise to the maximum value.

DISCUSSION

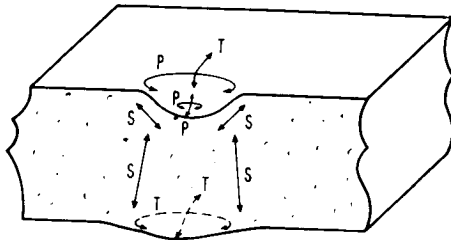
The question was raised as to whether Dr. Engel had considered the frequency of oscillations encountered in experimental curves shown during the talk. In response to the question, Dr. Engel replied that she had not attempted to correlate the frequency of oscillations nor the slope. However, she felt that the slope of the oscillations should be a measure of the rate of work hardening of the material, and that the area under each oscillation should be a measure of the capacity of the material to absorb work hardening. The question was asked as to whether the oscillations of the experimental data could just be due to the uncertainties in the weight measurements themselves. It was stated that oscillations were shown on several different sets of data and, therefore, the oscillations would not be expected to be due to the measurement uncertainties. Dr. Thiruvengadam stated that the measurement accuracies of the experiments that were discussed by Dr. Engel was approximately 1/10 of a milligram. The oscillations shown appeared to be a real effect, but he pointed out that they were not repeatable. Different specimens of the same material showed very little repeatability with respect to the oscillations. It was also said that the existence of the oscillations in the data was sufficient reason to accept that it was a real effect. Dr. Engel said that displacement of the oscillations from specimen to specimen could just be due to differences in the surface preparation for different specimens.

Table 10-1. Cavitation-erosion-rate data

Metal	Zero-erosion period, min	Maximum rate of erosion, mg/h	Slope of rise to maximum, mg/h ²
Stellite 6B	60	1	1
Cb-132 M	54	23	23
316 stainless steel	54	43	200
T-222	24	51	30
TZM (SR)	7	64	1200
Nickel 201	4	234	3600
1100-aluminum	1	240	9000

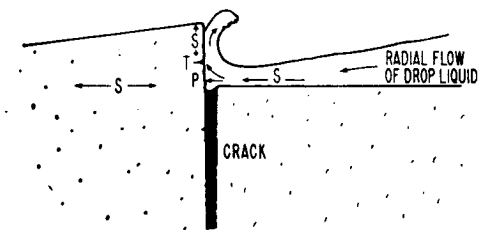
Table 10-2. Cavitation-erosion-rate, hardness and lattice-type data

Metal	Brinell hardness	Steady-state rate of erosion, mg/h	Frequency	Lattice type
Stellite 6B	379	0.5 ± 0.5	1 cycle/4 h	Hexagonal
Cb-132 M	273	9 ± 2	1 cycle/2.4 h	Body centered
316 stainless steel	154	16 ± 6	1 cycle/1.7 h	Face centered
T-222	274	22 ± 2	1 cycle/2 h	Body centered
TZM (SR)	294	19 ± 3	1 cycle/1 h	Body centered
Nickel 201	145	90 ± 12	1 cycle/40 min	Face centered
1100-aluminum	<45	99 ± 9	1 cycle/40 min	Face centered



P = pressure T = tension S = shear

Fig. 10-1. Stresses from localized pressure



P = pressure T = tension S = shear

Fig. 10-2. Radial flow velocity of drop liquid

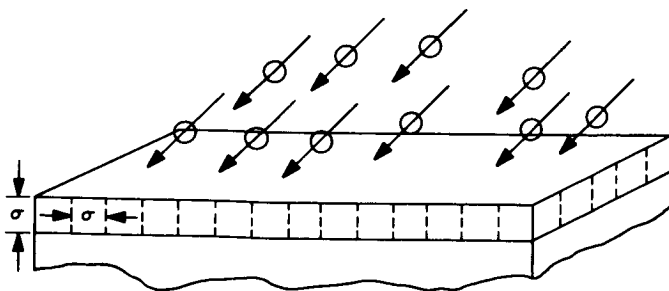
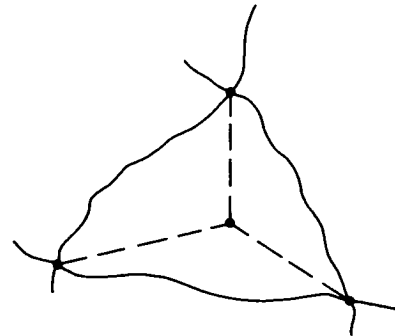


Fig. 10-3. Impact conditions of impinging drops



INTERSECTION OF THREE CRACKS

- σ_0 CELL - CELL CONTAINING NO CRACKS
- σ_1 CELL - CELL CONTAINING ONE CRACK
- σ_2 CELL - CELL CONTAINING TWO CRACKS
- σ_2^* CELL - CELL CONTAINING TWO INTERSECTING CRACKS

Fig. 10-4. Minimum conditions for erosion

IF e IS MINIMUM ENERGY REQUIRED FOR CRACK FORMATION,

$$\begin{aligned}
 \sigma_0 + e &\longrightarrow \sigma_1 \\
 \sigma_1 + e &\longrightarrow \sigma_2 \\
 \sigma_1 + e &\longrightarrow \sigma_2^* \\
 \sigma_2^* + e &\longrightarrow \sigma_0 + \text{ERODED FRAGMENT}
 \end{aligned}$$

Fig. 10-5. Depth σ increase from impact energy

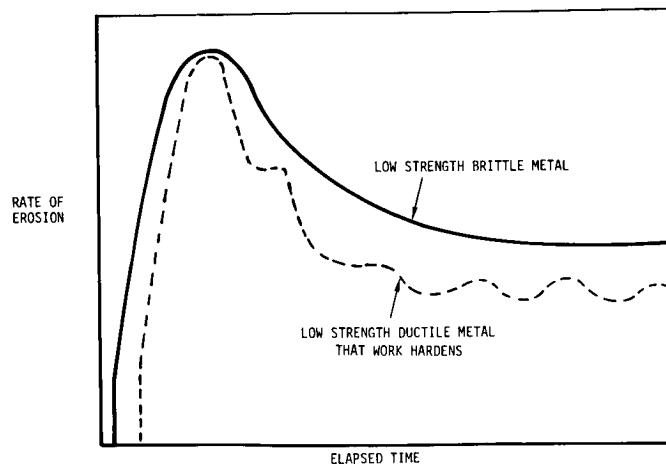


Fig. 10-6. Erosion rate curves

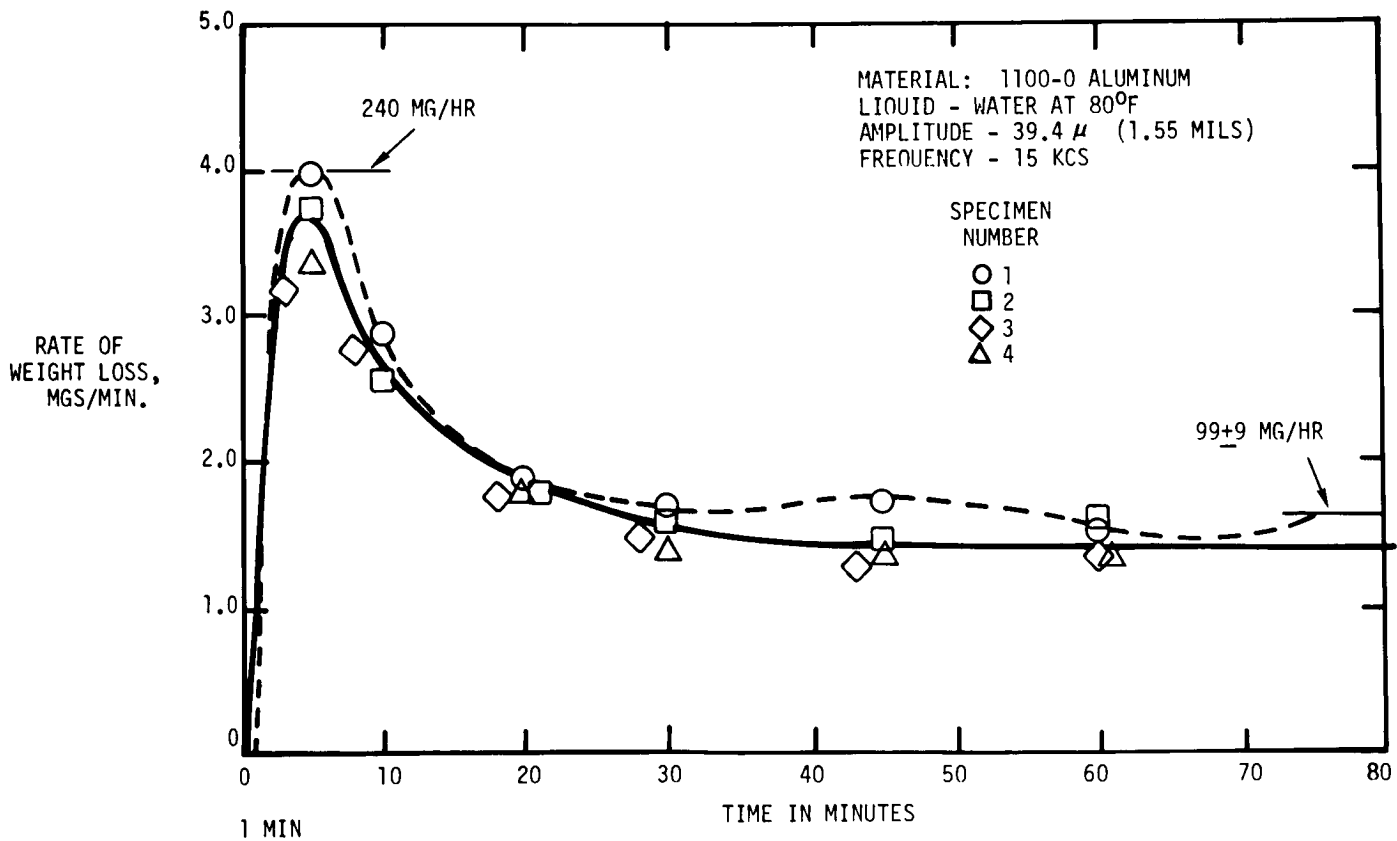


Fig. 10-7. Effect of testing time on rate of cavitation damage of 1100-0 Al

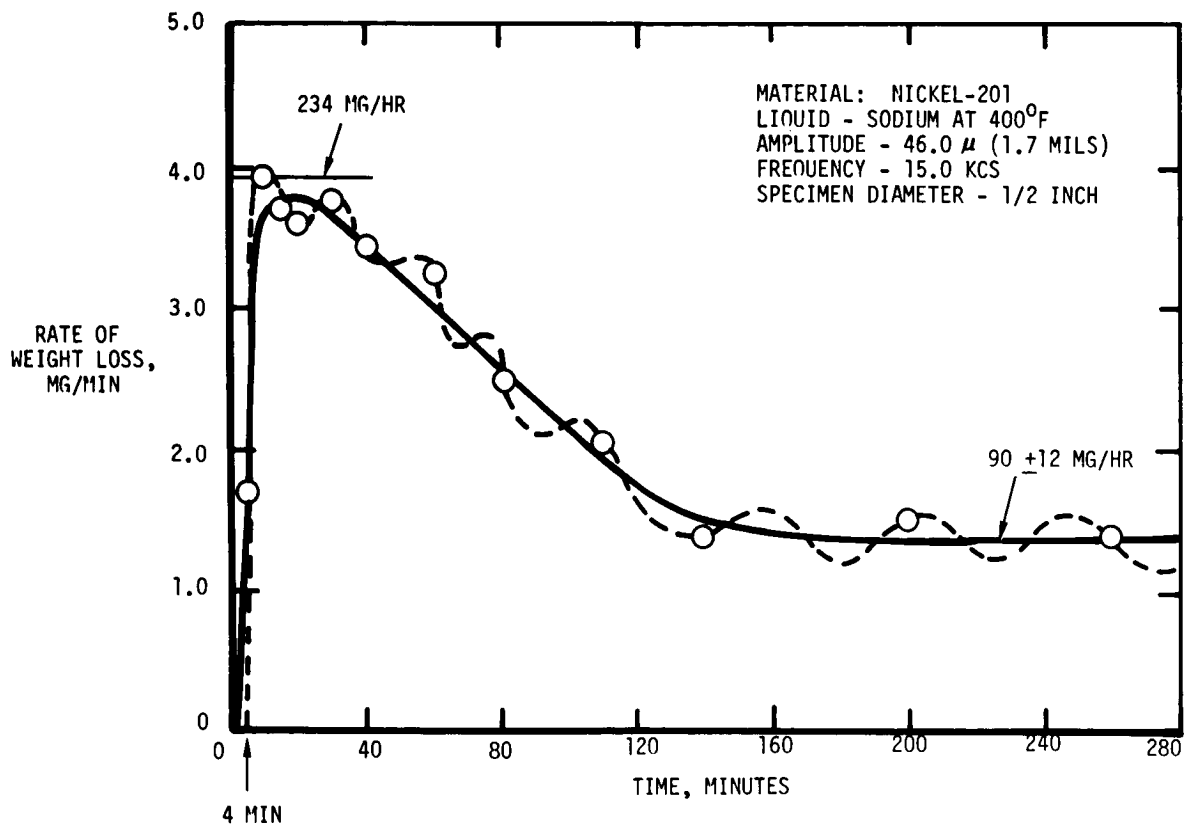


Fig. 10-8. Effect of testing time on rate of cavitation damage of Ni-201

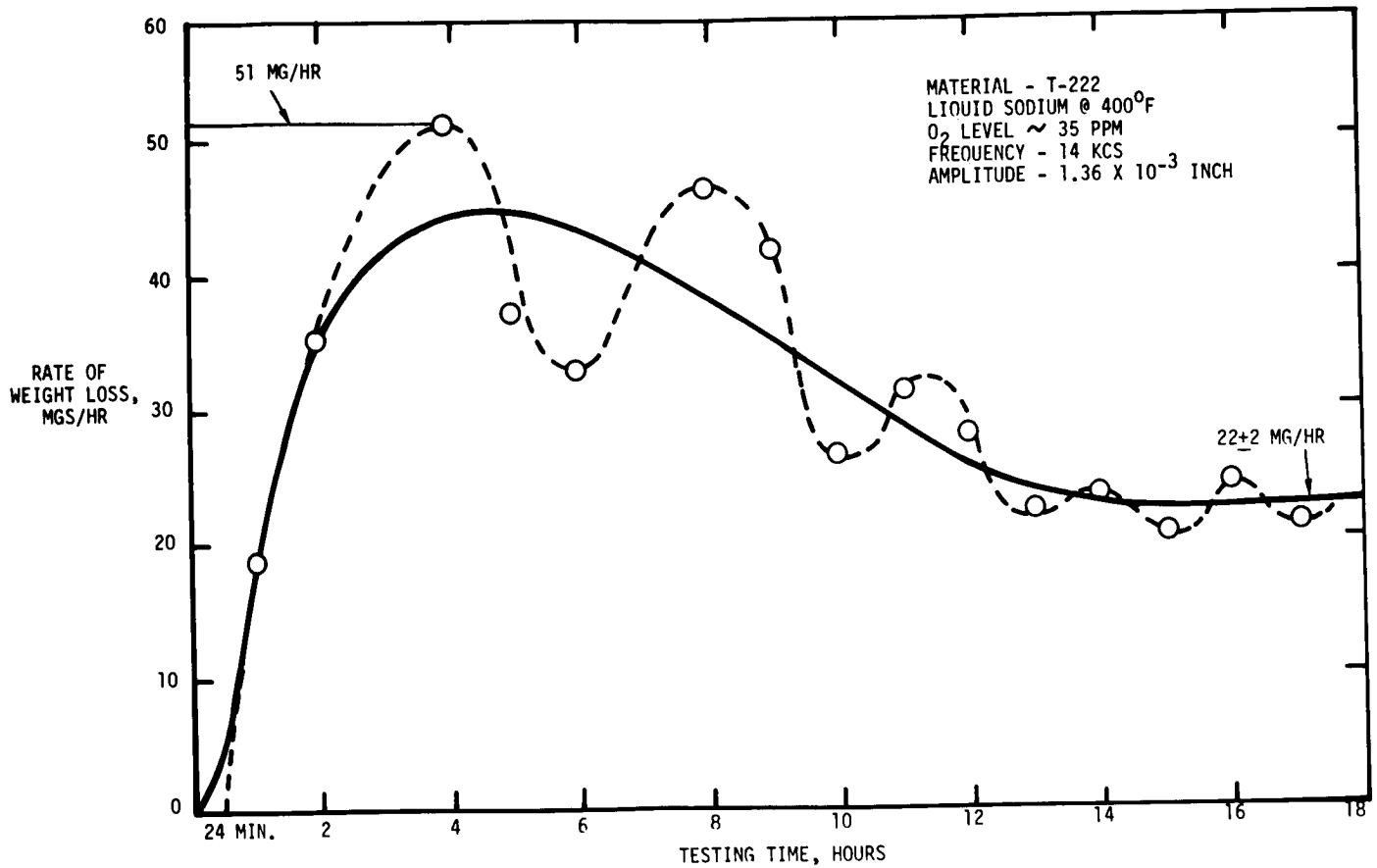


Fig. 10-9. Effect of testing time on rate of cavitation damage of T-222

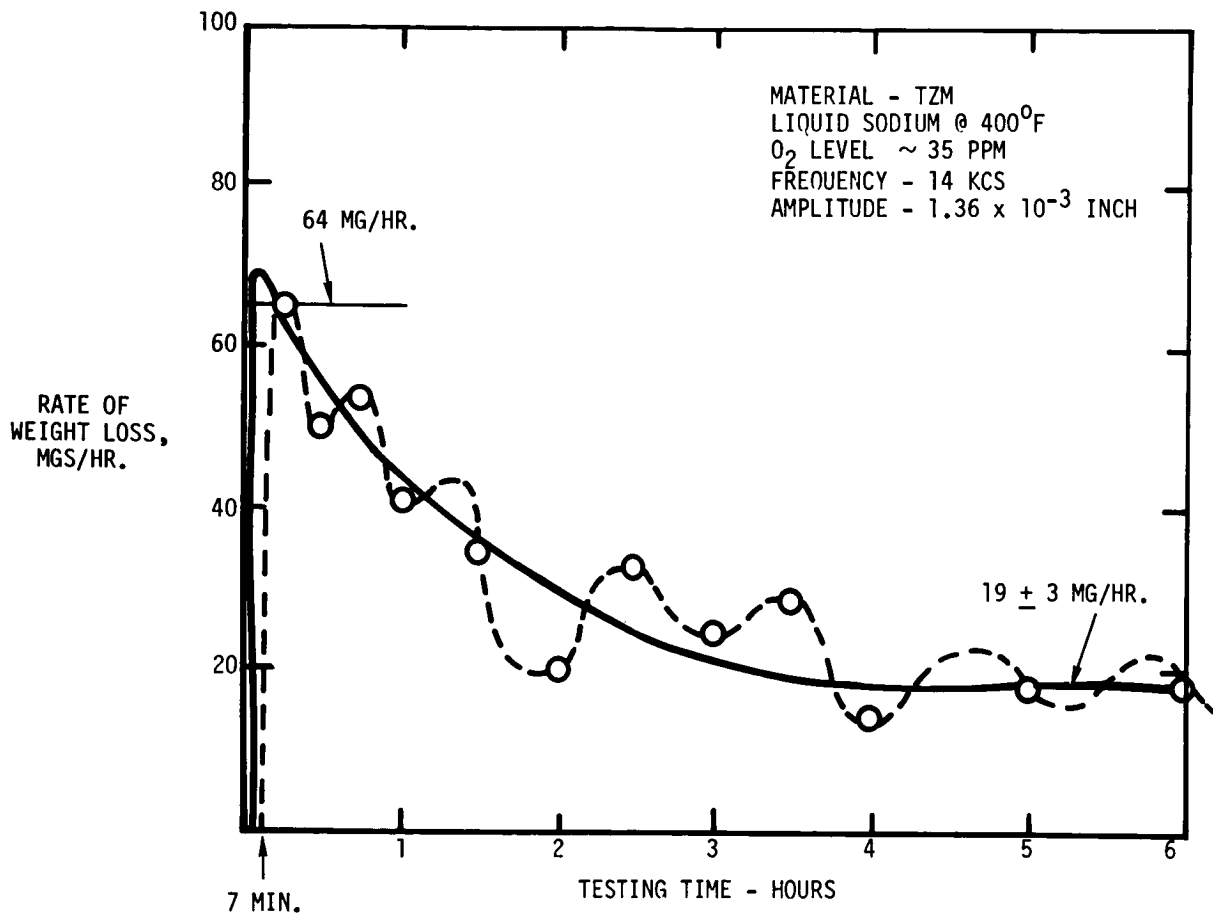


Fig. 10-10. Effect of testing time on rate of cavitation damage of TZM

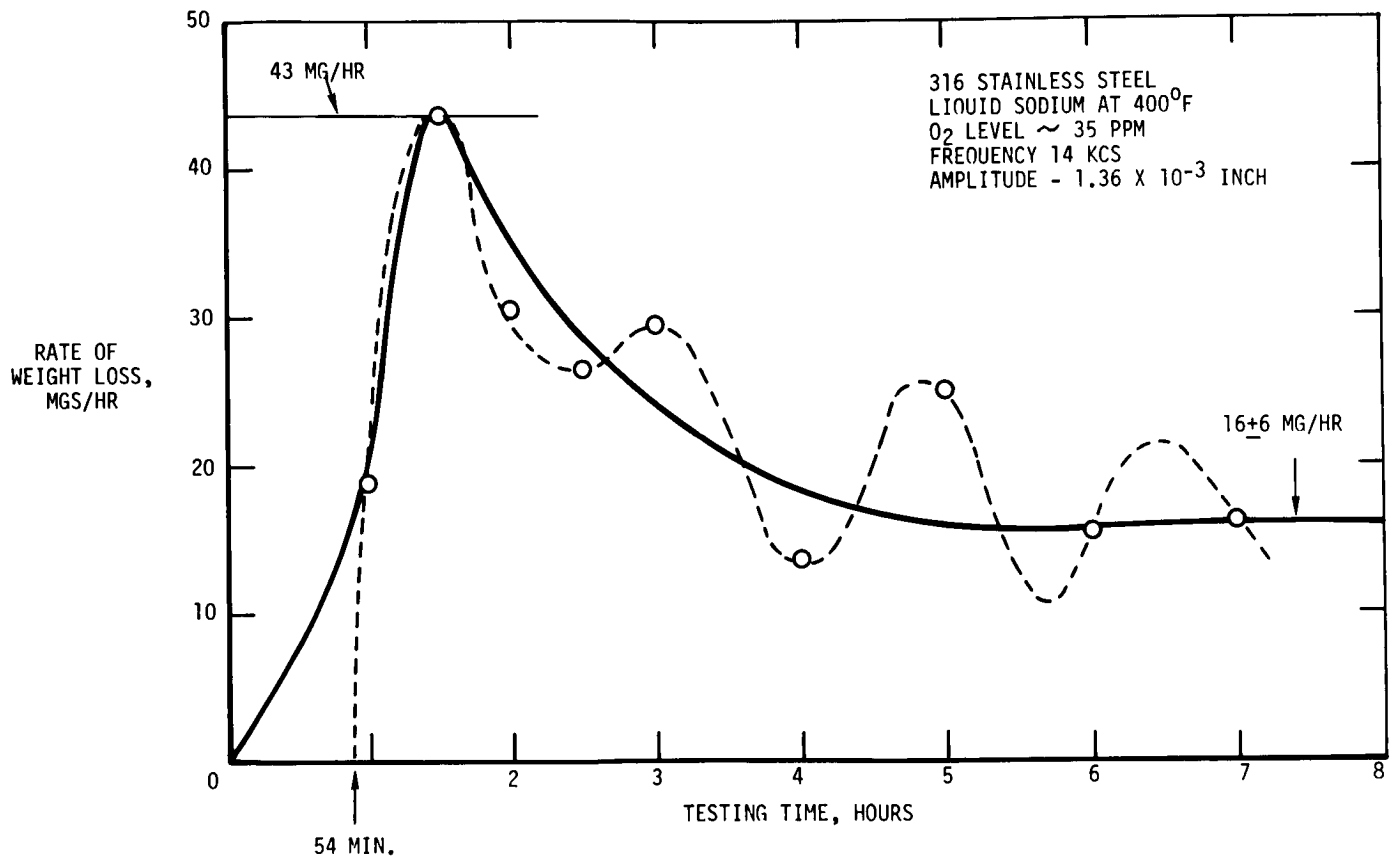


Fig. 10-11. Effect of testing time on rate of cavitation damage of 316 stainless steel

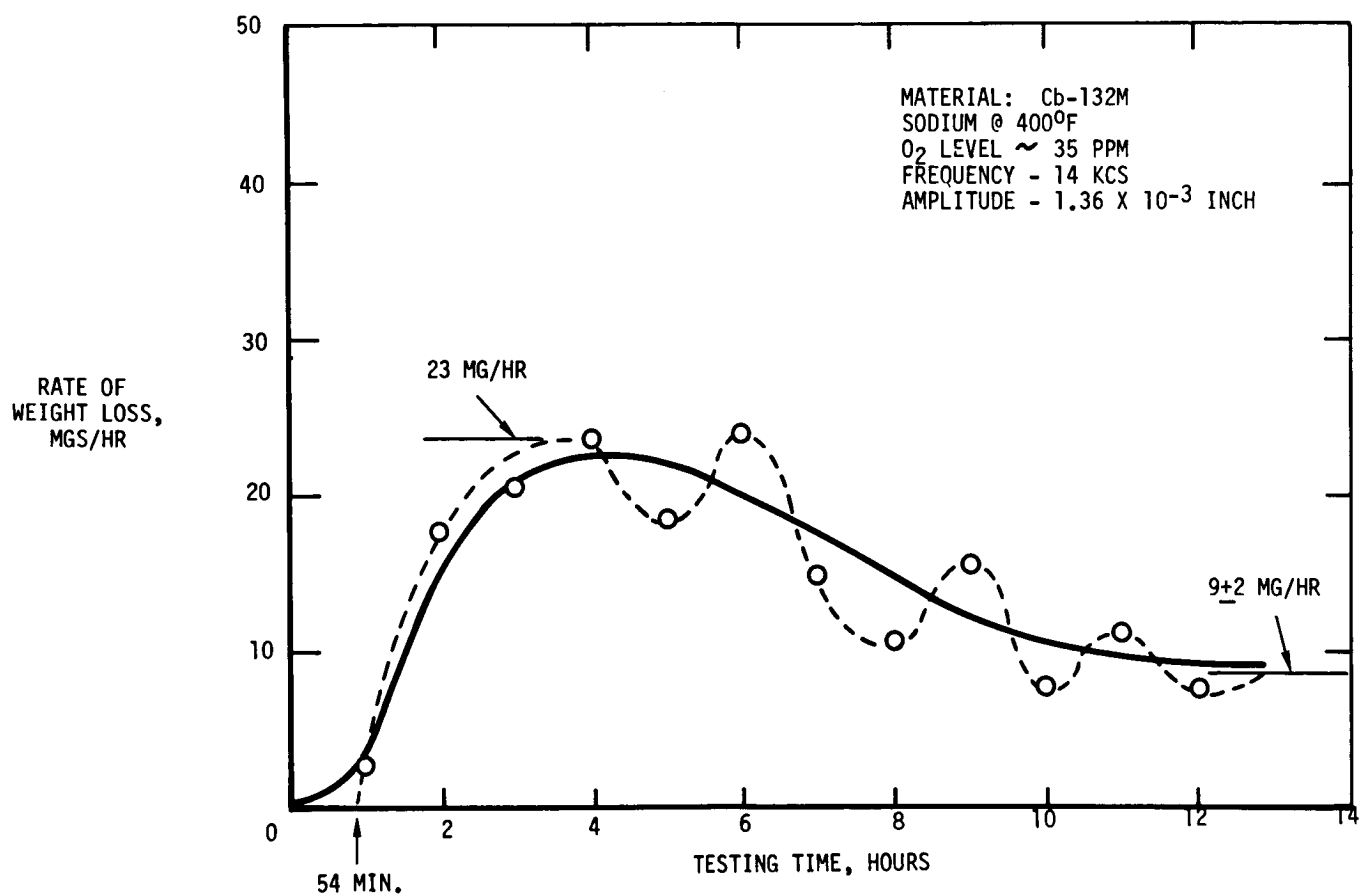


Fig. 10-12. Effect of testing time on rate of cavitation damage of Cb-132M

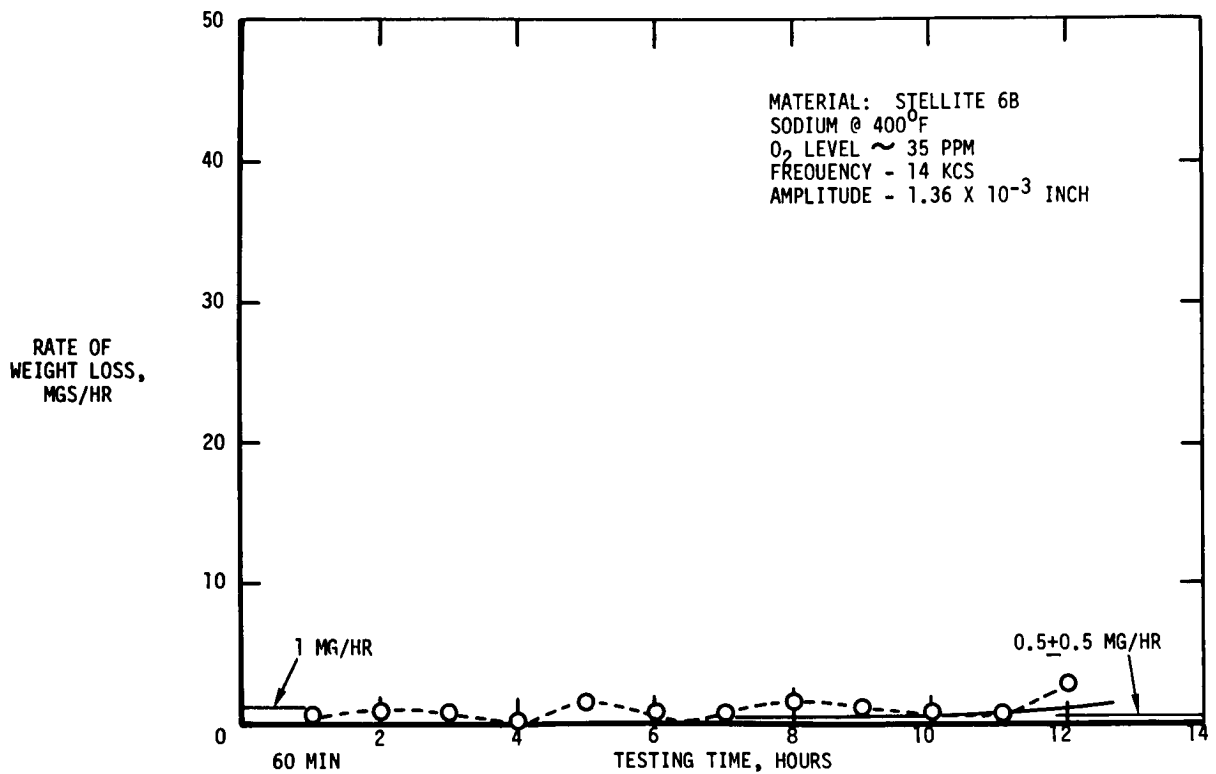


Fig. 10-13. Effect of testing time on rate of cavitation damage of Stellite 6B

11. SOME REMARKS ON THE WET VAPOR TURBINE

G. Gyarmathy
USAF
Wright-Patterson AFB
Dayton, Ohio

Besides the question marks clinging stubbornly to quantitative results of nucleation theory, another source of uncertainty in theoretical predictions regarding alkali metal vapor turbines comes from the lack of knowledge about the behavior of the vapor in the highly supersaturated state. Thereby, the location of the Wilson Point cannot be predicted accurately even if the nucleation theory were perfect (Fig. 11-1). The remedy is experiments, because they yield the location of the Wilson Point in terms of a pressure ratio rather than in terms of a supersaturation value (see Fig. 11-2).

In view of these pitfalls of theory, another method is to disregard these pitfalls, and try to apply theory (Ref. 11-1). The results are the Wilson lines for sodium and potassium as shown in Figs. 11-3 and 11-4, respectively. However, experimental evidence (indirect for sodium and direct for potassium) shows that the theory results in Wilson Points which lie too early, i. e., at too low equilibrium moisture contents. There is, however, some value in this approach; namely, it yields some interesting information about the influence of the expansion rate, on the location of the Wilson Lines, and on the number of fog droplets arising from the vapor. (The results on droplet number and droplet size are probably more reliable than the obtained location of the Wilson Point, since they are less significantly affected by the uncertainties of nucleation theory and of vapor behavior.)

The obtained representative (mean) fog droplet size is shown in Fig. 11-5 for sodium and in Fig. 11-6 for potassium. For mercury, no Wilson Point is obtained due to its anomalously high surface tension at the temperatures of practical interest.

After these preludes, an analysis of two-phase flow in metal vapor turbines was made. For these calculations, the supersaturated vapor properties were assumed on the basis of available information (enthalpy-entropy diagrams), and the dependence of the Wilson Point-super-cooling ΔT^* on the expansion rate \dot{P} was specified on the basis of an experimental point (which defines one pair of \dot{P} , ΔT^* values for one particular isentrope), and of theory (which gives the change of ΔT^* with \dot{P} and p_{SAT}). For the fog droplet number, the theoretical values were adopted. The experimental

onset point for sodium was estimated, since available experiments failed to produce condensation onset within the nozzle of the apparatus (Ref. 11-2). For potassium, the experimental point given in Ref. 11-3 was taken as the basis.

The outline of the calculation procedure is shown in Fig. 11-7. The equations used are, in essence, identical to those developed in Ref. 11-4.

The calculation was applied to the example of a four-stage wet-vapor turbine of roughly 200 kW output (Fig. 11-8) in which different working media (namely sodium, potassium, mercury, and steam) were assumed. The values of the rotor rpm were selected so that the interstage pressures remained the same for all working media (except for mercury, in which case the pressures were re-doubled to come closer to the range of practical interest).

The pertinent expansion lines are shown in Fig. 11-9. Some of the results are summarized in Figs. 11-10, 11-11, and 11-12.

Figure 11-10 shows the history of the supercooling ΔT along the turbine axis. For sodium, potassium, and steam, thermodynamic equilibrium is almost perfect downstream of the Wilson Point. The location of the Wilson Point, however, is gravely affected by differences in the assumptions regarding the behavior of the supersaturated vapor. (For sodium, the results are shown for two different, but conceivable sets of vapor property data.) For mercury, the supersaturation increases steadily since no fog formation occurs.

Figure 11-11 shows in its upper part the amount of total moisture and distribution between the fine form (fog) and the coarse forms (deposited, detached, rebounding, removed) along the turbine axis. The greatest part of the moisture is seen to remain in the finely dispersed form (fog). The amount of coarse moisture deposited (through surface condensation only) in the mercury case is comparable to the amount of coarse moisture formed by fog droplets deposition when self-condensing media are used. In the lower part of the figure, the history of the fog droplet size is plotted.

Figure 11-12 shows the magnitude of the efficiency losses due to two-phase flow effects, as compared to the case of an expansion in perfect thermodynamic equilibrium of a homogeneous medium, in percentage of the total enthalpy drop of the turbine. As shown, the losses are mainly caused by thermodynamic irreversibility, rather than by the undisciplined behavior of the coarse part of the moisture.

(But the latter is responsible for erosion effects.) The high supersaturation present in a mercury turbine is the cause of the very high loss associated with this case.

It should be noted that, with the exception of mercury, the results shown in Figs. 11-10 through 11-12 are accidental in a certain sense, namely, the size of the fog droplets. Therefore, the magnitude of the two-phase flow effects depend on the value of the expansion rate at which the Wilson Point was reached. The relative favorableness of the Wilson Point location encountered in any particular case can be characterized by comparing the value of \dot{P} at the Wilson Point to its maximum value occurring within the nozzle row in question. The pertinent \dot{P} values are marked under the y-curves of Fig. 11-11. It can be seen, for instance, that the potassium example represents the optimum possibility, because the Wilson Point lies at the maximum value of \dot{P} (which is, in that case, 8700 s^{-1}). Somewhat less ideal is the basic case for sodium, while the alternative sodium case and the steam case are even poorer. By adding inlet superheat, or changing the enthalpy drop of the first stages, the situation for each case may undergo, of course, significant changes.

DISCUSSION

The question was raised as to how Dr. Gyarmathy accounted for coarse moisture in the turbine. He stated that coarse moisture arises from the condensation droplets which are collected on the stator and rotor blades. On the rotor the droplets were centrifuged out, whereas on the stator, the droplets were stripped off and entrained by the stream. He assumed that 75% of the coarse droplets in the stream remain upon impact on the blades, whereas 25% rebound. Mr. Roszbach stated that potassium properties in the superheated region as provided by NRL can be extended into the supersaturated region and polytropic coefficients estimated quite accurately. He stated that they had done this on their potassium turbine. The question was raised as to whether Dr. Gyarmathy's model included condensation on the walls of the turbine, and he stated that it did.

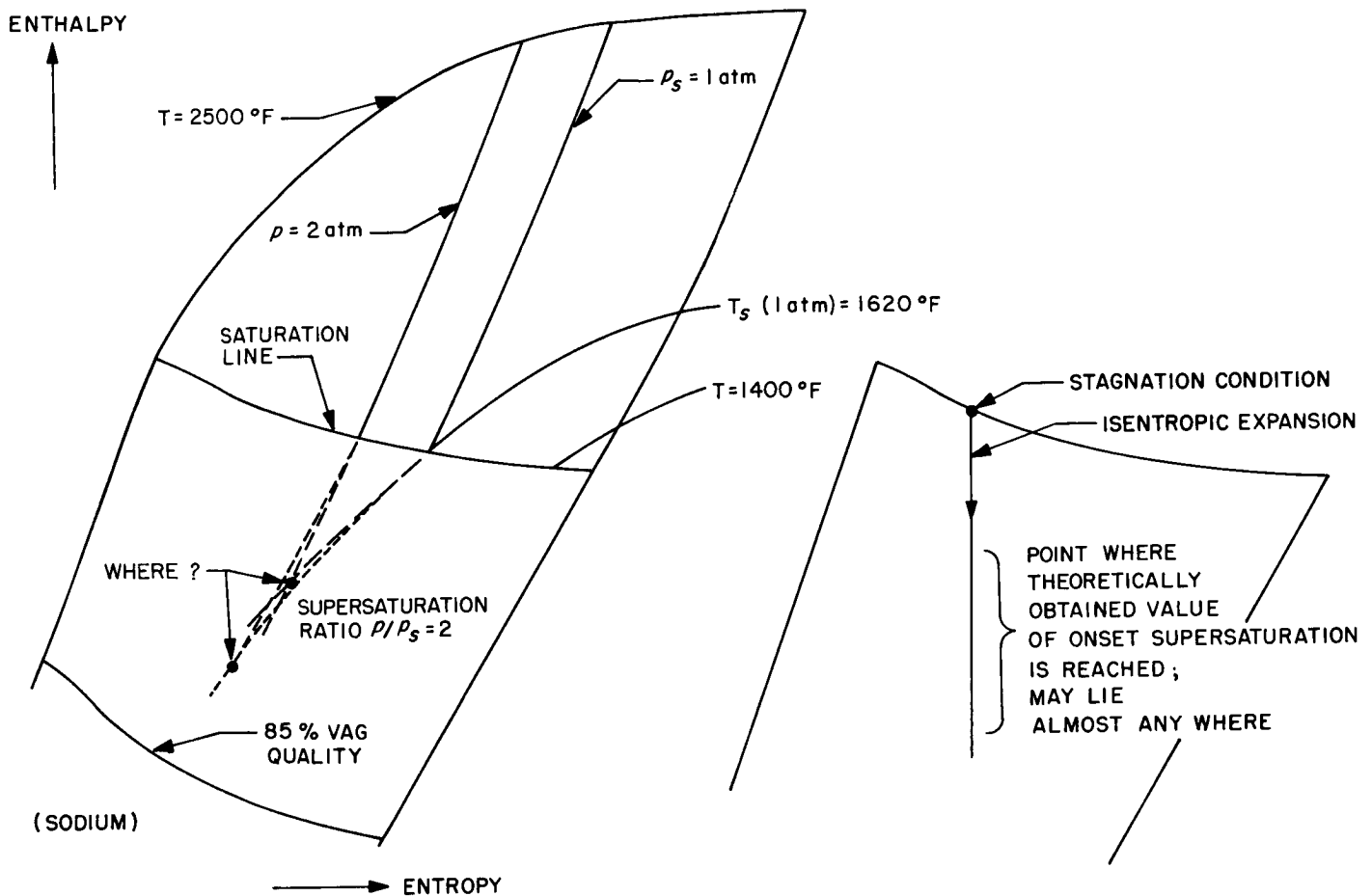


Fig. 11-1. Indeterminate data for Wilson Point location

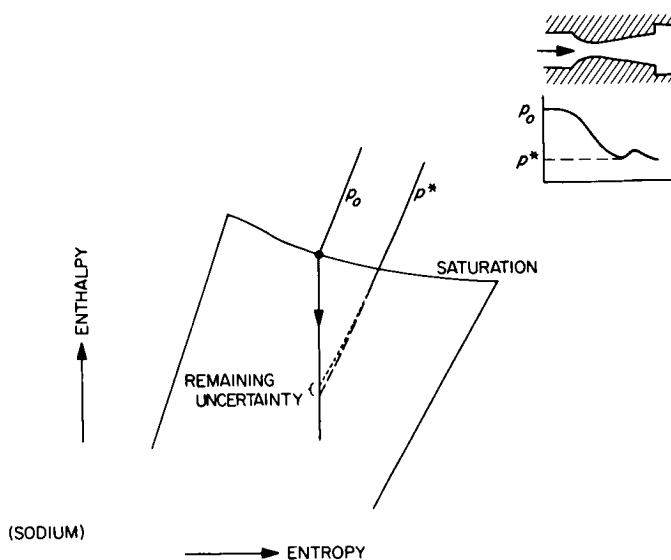


Fig. 11-2. Pressure ratio location of Wilson Point

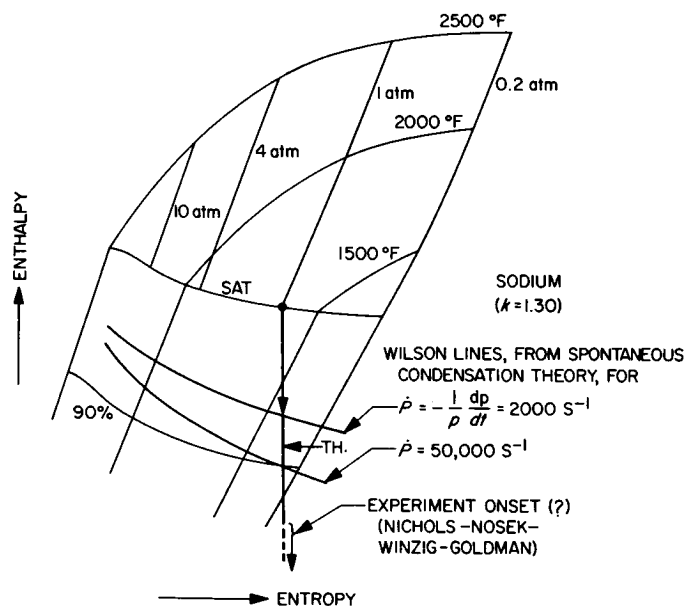


Fig. 11-3. Wilson lines for sodium

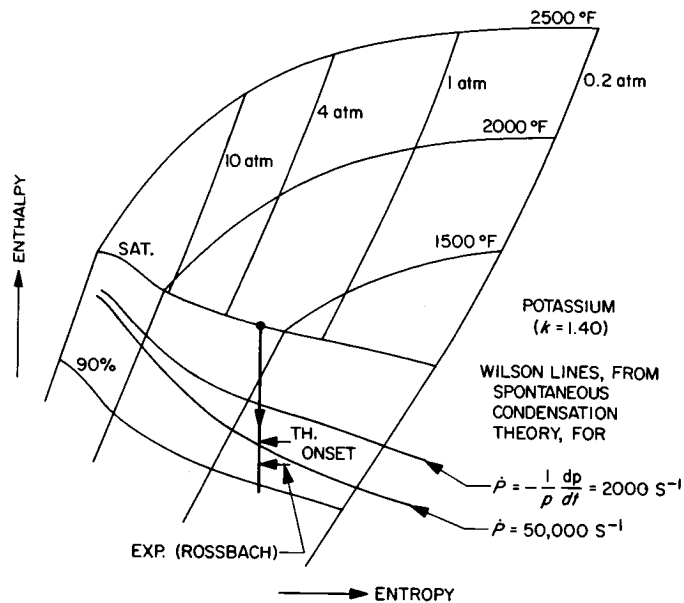


Fig. 11-4. Wilson lines for potassium

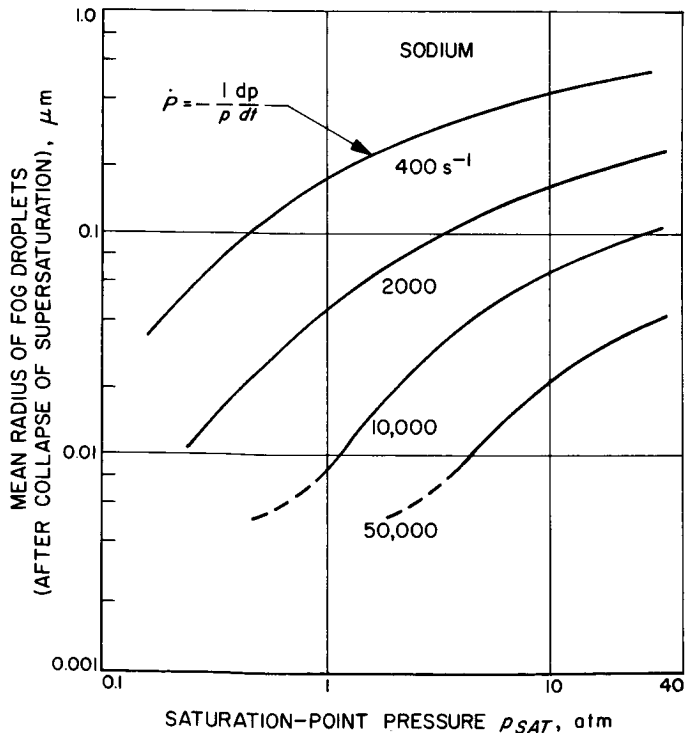


Fig. 11-5. Mean size of fog droplets for sodium

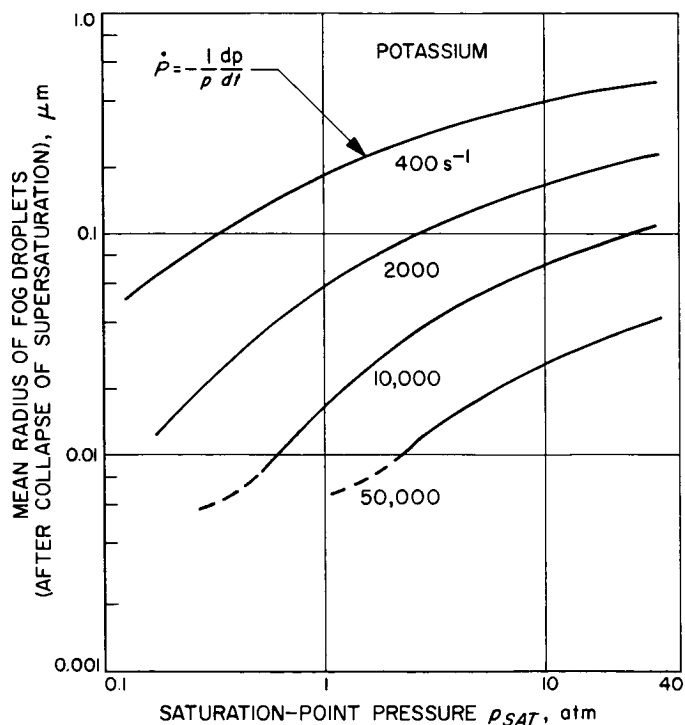


Fig. 11-6. Mean size of fog droplets for potassium

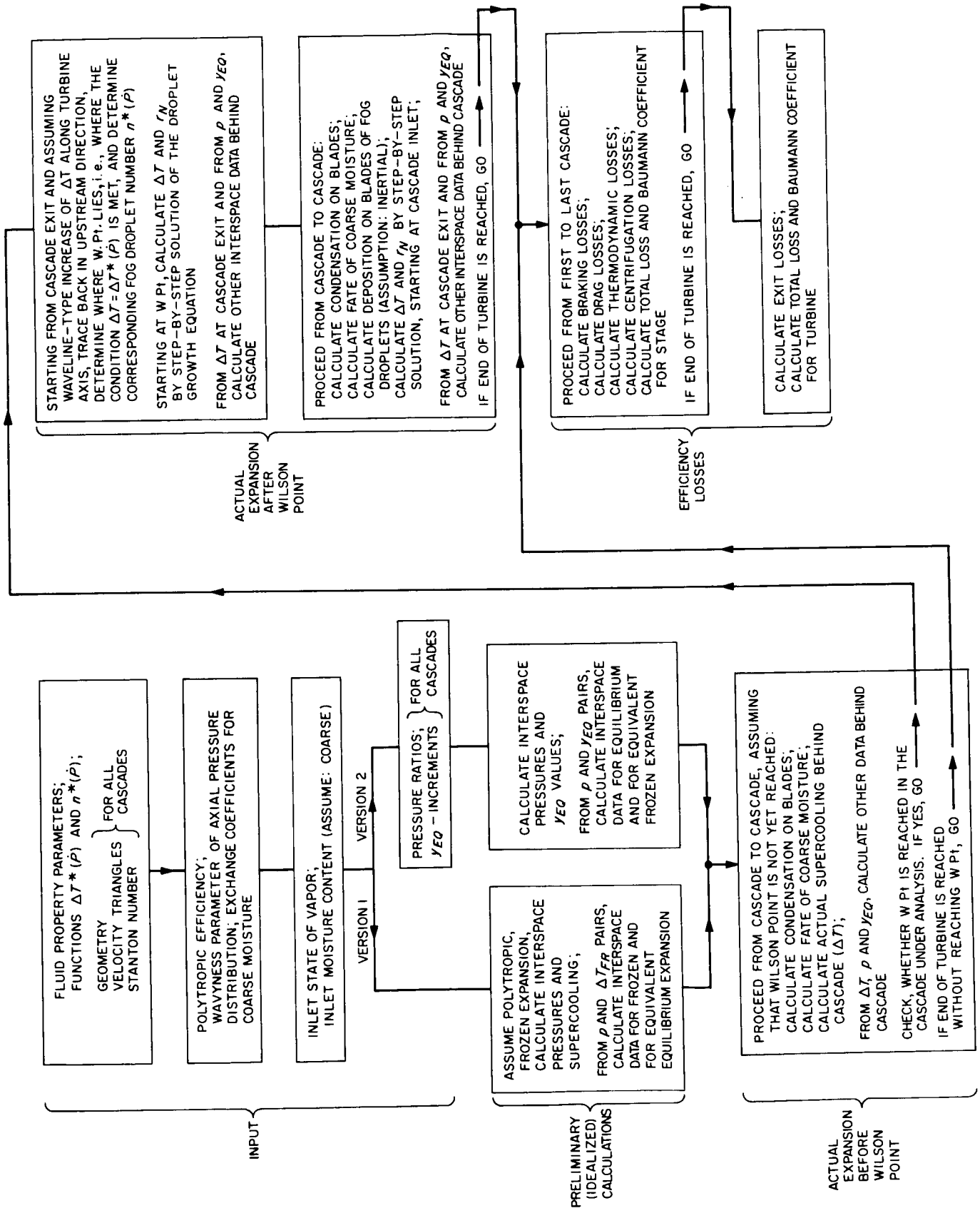


Fig. 11-7. Calculation procedure flow diagram

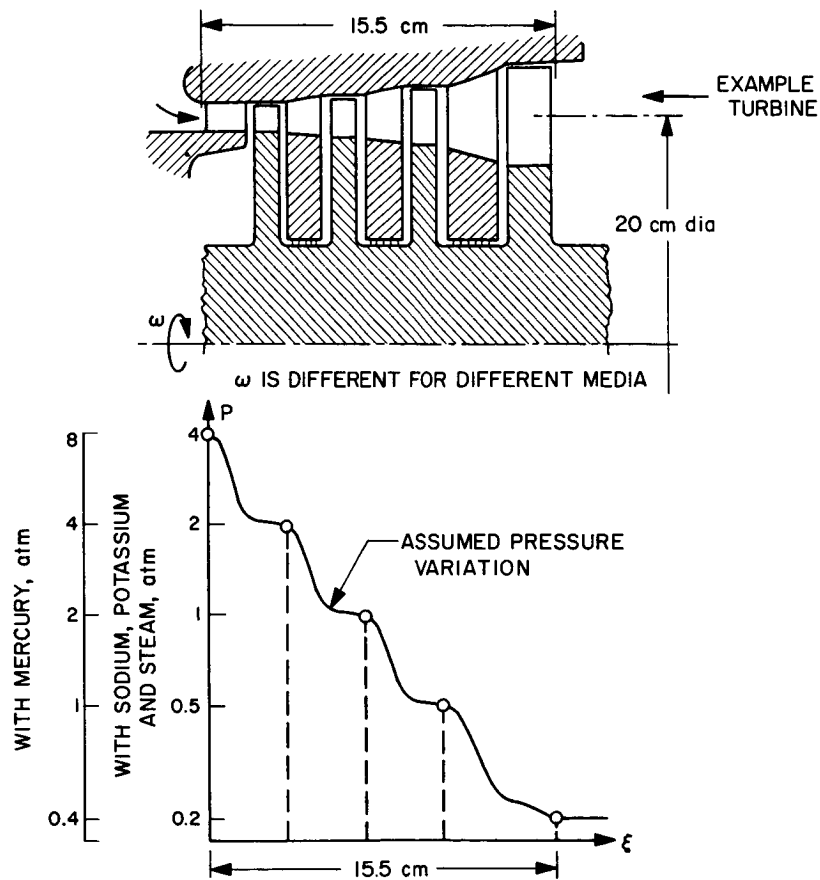


Fig. 11-8. Example application of four-stage wet-vapor turbine

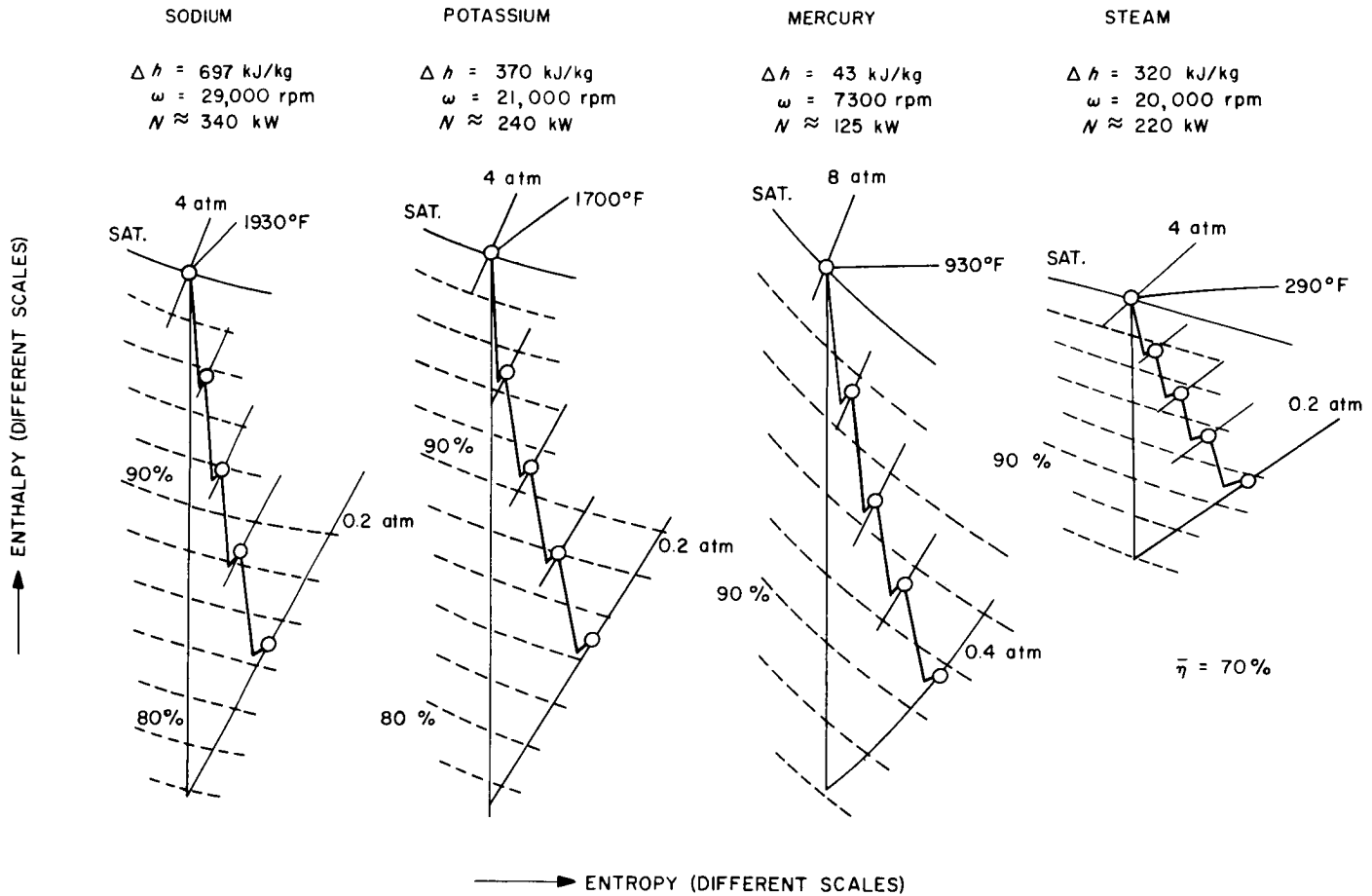


Fig. 11-9. Media expansion lines

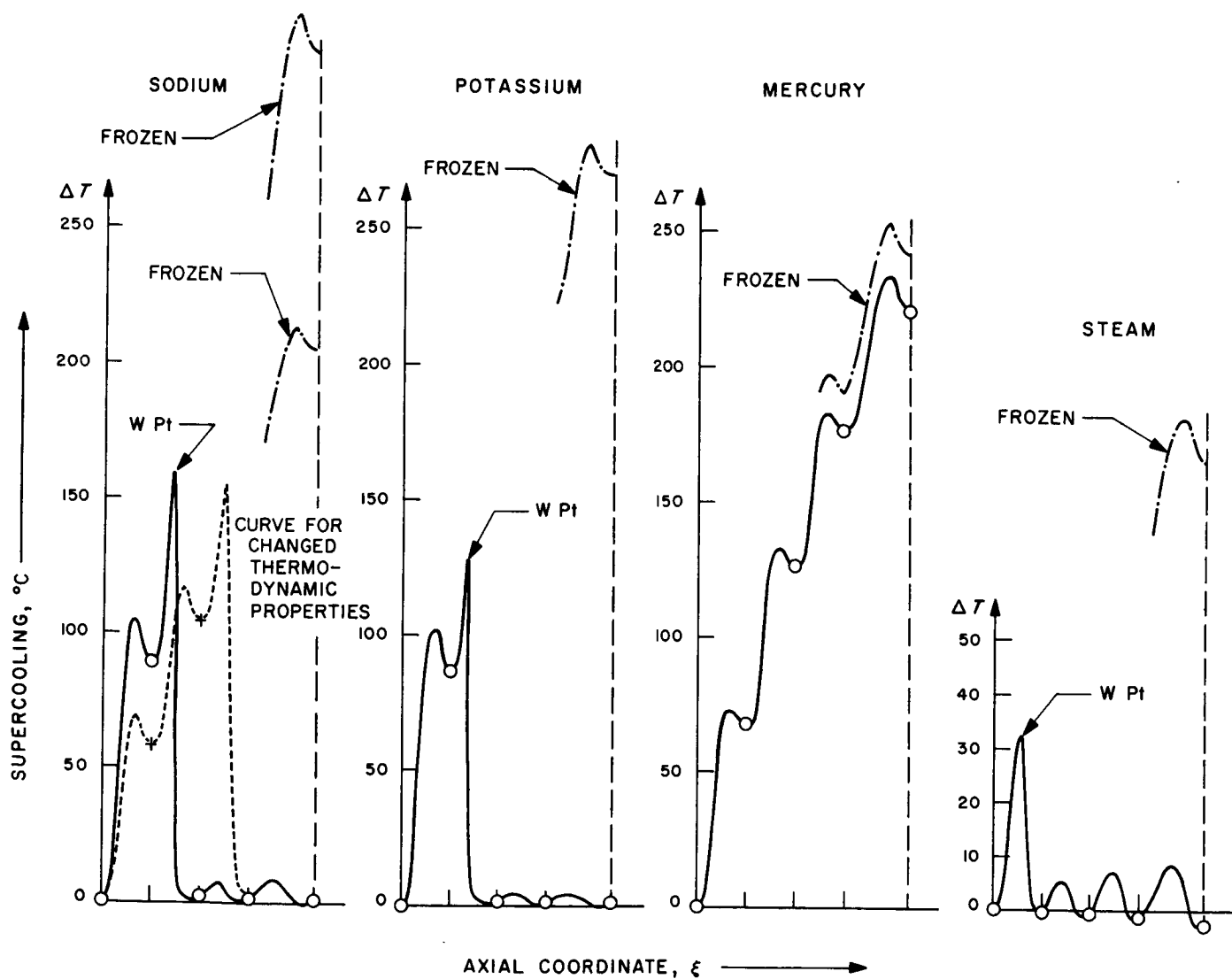


Fig. 11-10. Supercooling along turbine axis results

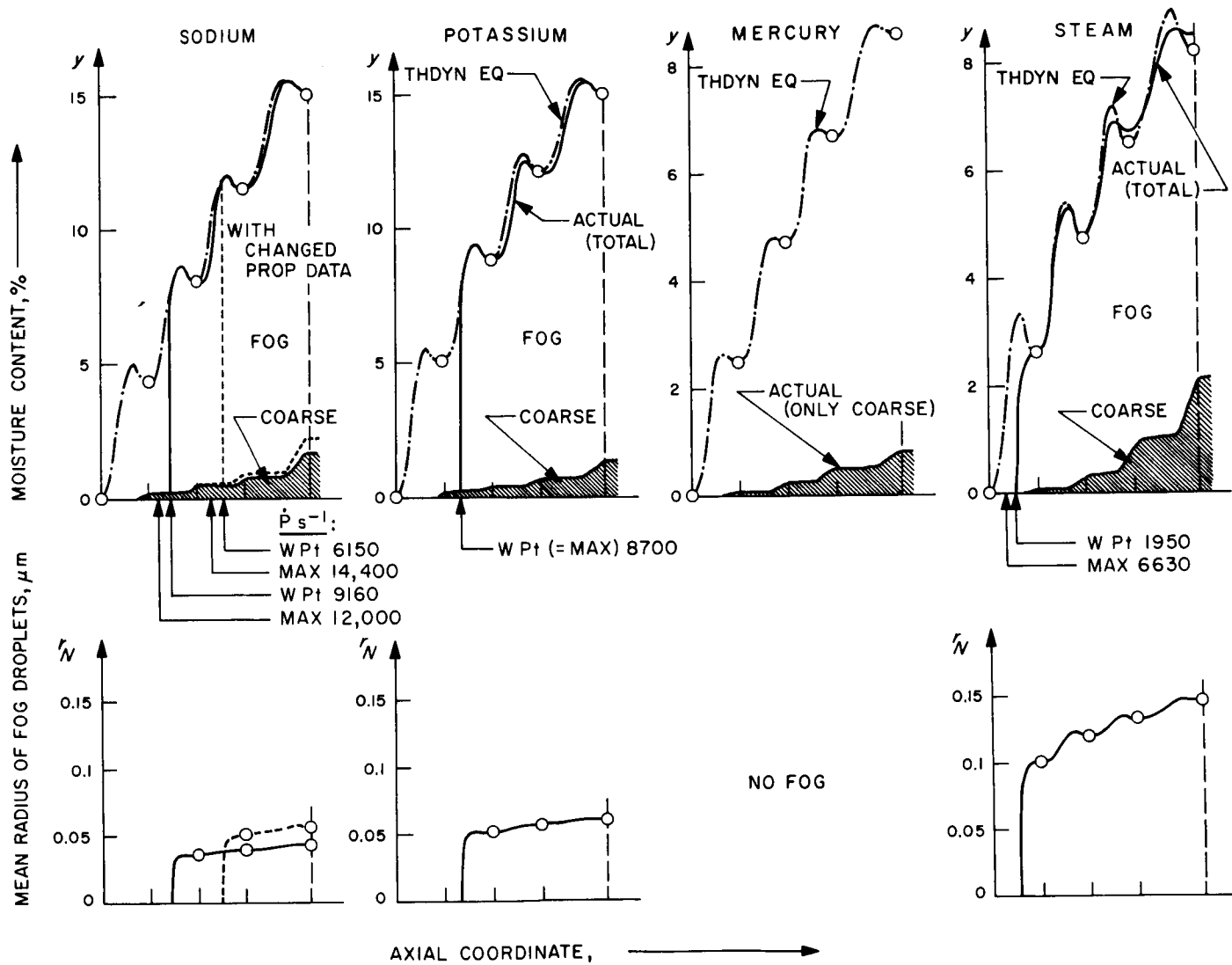


Fig. 11-11. Moisture content and fog droplet size results

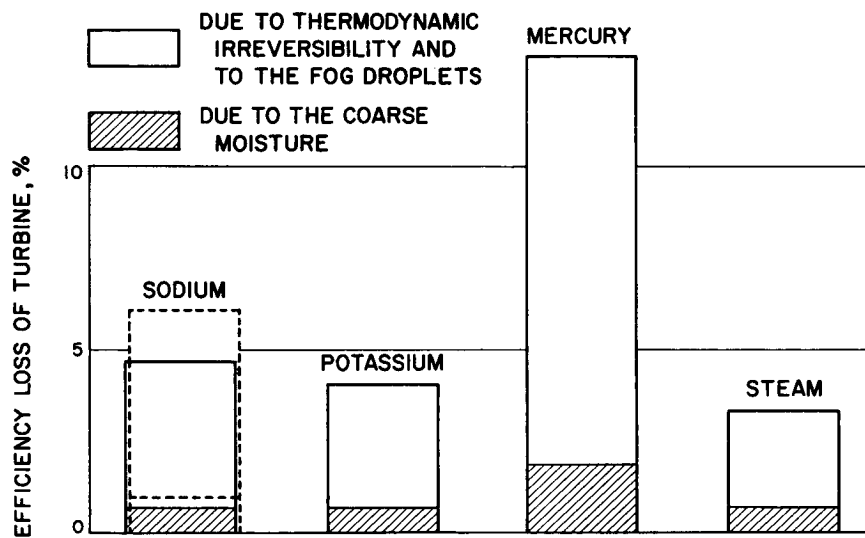


Fig. 11-12. Efficiency loss of turbine

REFERENCES

- 11-1. Gyarmathy, G., An Analytical Method to Calculate Spontaneous Condensation Processes. Ver. Deutsch, Ing. Forschungsheft Nr 508, Part 1, 1965.
Translation available, CECB Translation No. 4160.
- 11-2. Nichols, L. R., Experimental Determination of Sodium Vapor Expansion Characteristics With Inert-Gas-Injection Pressure-Measuring Technique, NASA TN D-2276. National Aeronautics and Space Administration, Washington, D. C., Apr. 1964.
- 11-3. Rossbach, R. J., "Critical Flow of Potassium Vapor Through Instrumented Converging-Diverging Nozzle," ASME Preprint 65-GTP-22, presented at the Gas Turbine Conference and Product Show, Washington, D. C., Feb. 28--Mar. 4, 1965.
- 11-4. Gyarmathy, G., Foundations of a Theory of the Wet Steam Turbine. Juris-Verlag, Zurich, 1962. Translation available as FTD-TT-63-785, Air Force System Command, Foreign Technology Division, Wright-Patterson AFB, Ohio, Aug. 1966.

PRECEDING
PAGE BLANK

12. EXPERIMENTAL INVESTIGATIONS OF INTERNAL FLOW IN TURBINES

D. G. Christie
Central Electricity Research Laboratory
Leatherhead, Surrey, England

This discussion reviews the turbine blade erosion work done by several groups in different departments of the research organization of the Central Electricity Generating Board. The work aspects include: laboratory evaluation of the erosion resistance of materials by D. Pearson at the Marchwood Engineering Laboratories; study of operating turbines, including cine photography of water flow on blades, by G. W. Hayward and P. Sculpher in the South Eastern Region Research Department; and at the Central Electricity Research Laboratories (CERL), K. H. Jolliffe has investigated the metallurgical aspects of the erosion, and a group under M. J. Moore has investigated the flow through blade cascades and the formation of drops causing erosion.

The paper describes work on the processes that cause water, entrained on blade and casing surfaces in the low pressure steam turbine, to shed as drops from fixed blades and cause erosion of moving blades. Observations, in operating turbines, of water flowing over the last-stage fixed blades give a practical insight into these processes, and laboratory studies on cascades under low pressure steam conditions provide data on the mechanism of drop formation and the sizes and velocities of the drops.

The eroded blade surfaces were examined, and the size and form of the erosion pits were related to the characteristics of the drops producing them.

Figure 12-1 shows the diagram of fixed and moving blades in a turbine and the velocity of entrained water drops which cause blade erosion. Large drops flow across the space between the fixed nozzle blades and moving blades at velocities very much lower than the stream velocity. The penetration of drops into the space between the moving blades depends upon the velocity of drops and moving blade row. Figure 12-2 shows an example of erosion encountered on steam turbine blades. The blade is from the last row of a 120-MW machine. The penetration of droplets into the space between the moving blades can be seen by the band that forms the end of the eroded region. The blade shown was stainless steel with no stellite shields. The tip velocity on this blade was 1400 ft/s.

A great deal of data on material removal was generated by a test rig at the Marchwood Laboratories. The test consists of a whirling arm that rotates two test specimens through a curtain of droplets. Impact velocities just over 1000 ft/s are attainable with the test rig. The shape of the erosion curve that occurs for most specimens consists of an incubation period, a period of rapid material removal, and then a falloff. The next three figures show the appearance of the surfaces at three different time periods of the erosion process. Figure 12-3 shows the surface during the incubation period. The forms of the pits in the surface are essentially surface depressions. This picture was taken by a scanning electron microscope. During the next stage, these pits begin losing material. As shown in Fig. 12-4, these pits became quite a bit deeper. Figure 12-5 shows the pit after quite a bit of material has been removed. The material shown is stainless steel.

To look into the formation and propagation of the droplets that produce erosion, another laboratory at CERL has been running tests featuring high-speed photography of moving droplets. Figure 12-6 shows the arrangement for taking pictures in a moving turbine with a periscope and pulsed light source. Most of the pictures were taken with lighting coming through the periscope. Figure 12-7 shows a picture of the periscope in the turbine. The method of lighting is very important because of the fog encountered in the turbine. The light source has to be arranged so that the beam intersects as little as possible the return beam to the camera. If the two beams cross to any extent, considerable scatter from the steam is obtained. Figure 12-8 shows the arrangement of the periscope in the turbine. Figure 12-9 shows the area of the blades photographed and shown in a film. The film showed streams of water and droplet detachment occurring in the turbine during operation.

To look at the actual stripping processes from the blades, a cascade steam tunnel was fabricated. Figure 12-10 shows a schematic of the steam tunnel. Figure 12-11 shows the test section with the cascade installed between the windows. These blades are identical to the geometry of the blades previously shown in the motion picture of the operating turbine. The work done in the steam tunnel has consisted mainly of photographic measurements combined with pitot measurements of the velocity fields. Water was initially supplied to the blades by upstream spraying through nozzles. However, this supply method led to reflection of the drops and to formation of a spray in the region of the stator blade. Water was subsequently introduced through the blades. The fact that a sizable quantity of water splashed from the

blade surface should be of great significance to examination of processes in a turbine. A film was shown of the stripping process in droplet flow from the blades of the cascade. The droplets stripped off as large as $1500\ \mu\text{m}$ and moved slowly in the wake until they were picked up by the main stream, accelerated and atomized.

For quantitative measurements, back lighting and a flash were used to obtain photographs of the droplet size and velocity. Figure 12-12 shows a sample photograph taken in the region before breakup was complete. The complicated shapes of the droplets suggest that their breakup cannot be related to any simple model, such as bag breakup or edge stripping. The size estimated from these photographs has been compared with other methods of measurement, and the agreement is within 10%. Figure 12-13 is another shot taken at a different condition. Both of these figures have a magnification of 26.4 X and an exposure time of $1/4\ \mu\text{s}$. Figure 12-14 shows the drop size distributions obtained from these photographs for three different conditions. This size distribution is that which is measured after breakup is complete. The three conditions are for low, intermediate, and high velocity at a given pressure. The low condition was Mach No. 0.55 (955 ft/s); intermediate condition was Mach No. 0.8 (1120 ft/s); and the high condition was Mach No. 1.2 (1520 ft/s). It is believed that the velocity effect which results is just due to the effect of the relative velocity of the stream and droplet on breakup. Figure 12-15 shows the droplet velocities as a function of distance from the trailing edge for drops of $150\text{-}\mu\text{m}$ diameter. The drop velocity is the velocity with respect to velocity of flow. All values of relative velocity appear to level off at values well below the main stream velocity. Figure 12-16 shows drop velocity as a function of droplet diameter for condition 2. In general the same type of trend is followed as was shown in the previous figure.

Wake traverses for condition 2 are shown in Fig. 12-17. The wake velocity gets to within 80 to 90% of the mainstream velocity within an inch or two from the blade. The wake from the blade is relatively narrow, indicating no separation. Figure 12-18 shows the wake in the supersonic condition. The wake leaving the blade is fairly broad due to the separation occurring under supersonic conditions. In addition, an oblique shock is generated, as shown in Fig. 12-18. For the subsonic cases the velocity used in the critical Weber number relation is that of the main stream, because droplets appear to find their way through the wake into the main stream where the final breakup occurs. For the supersonic, however, the velocity in the wake is used because of the broadening from the oblique shock.

The values for critical Weber numbers based on the velocities indicated are 19 for condition one, 24 for condition two, and 22 for condition three.

Figure 12-19 shows the form of damage encountered on the nose of the blade where the pits are about 100 μm . Figure 12-20 shows damage further in from the nose. Figure 12-21 shows damage even further in towards the region where the damage ceases. From the measurements of droplet size and velocity, the size of the pits can be correlated with the size of droplets that arrive in the different regions on the moving blade row. Figure 12-22 shows this correlation. This figure shows the measurements of the pit size from the photographs, and the droplet diameters that were estimated to penetrate at different axial locations on the moving blade. The pit size is significantly less than the droplet size.

DISCUSSION

Dr. Engel said that she noticed that the direction of pits seemed to correspond to the direction of the impact. Mr. Christie agreed with this. It was pointed out by Mr. Christie that an apparent anomaly exists because the direction of impact determines the alignment of the pits, but the weight loss equations correlate the data best with the normal impact component.

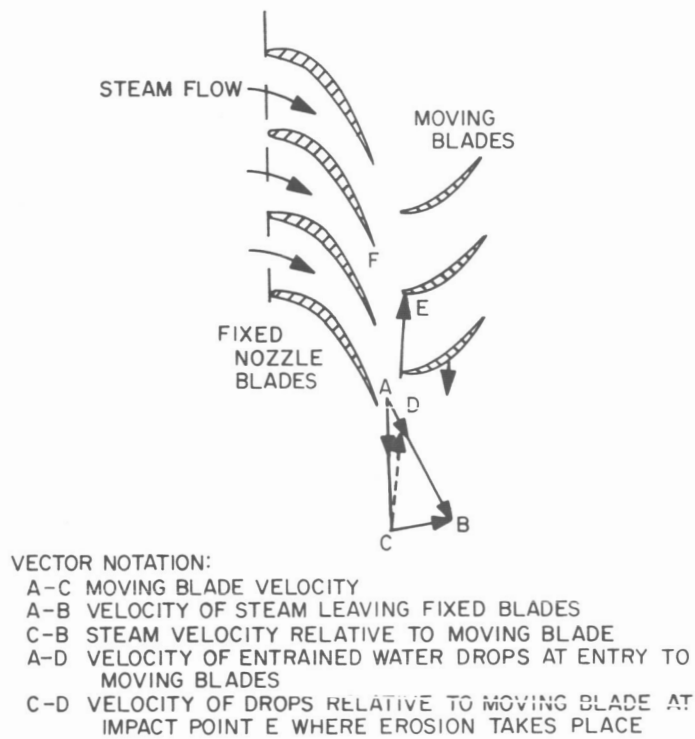


Fig. 12-1. Diagram of velocities, at entry to the moving blade, of steam and entrained water drops which cause blade erosion

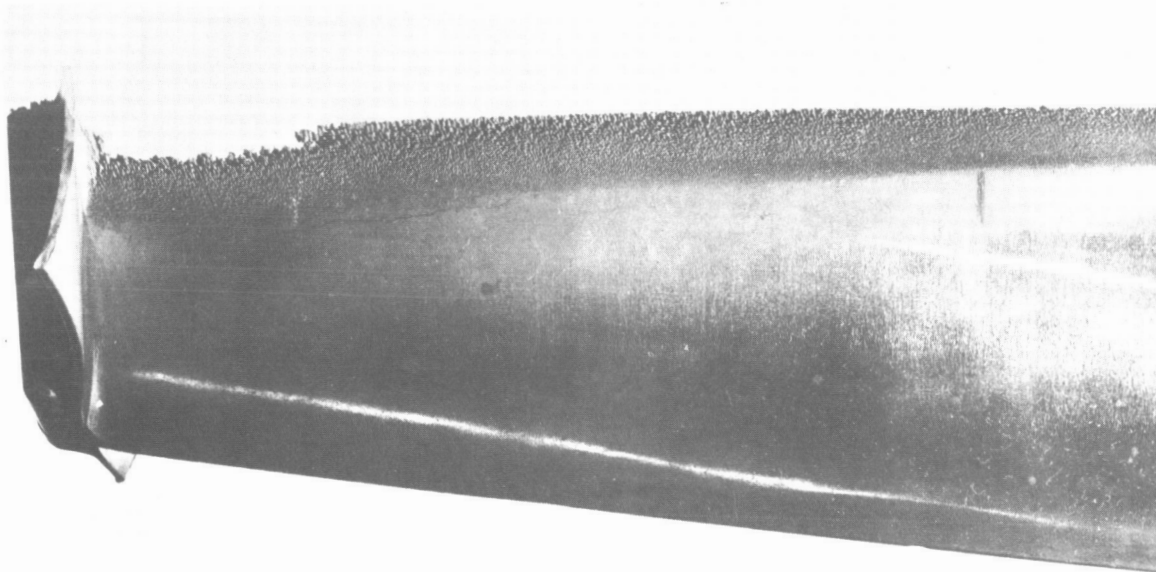


Fig. 12-2. Notching of moving blade at inlet edge by water (C in Fig. 12-9)

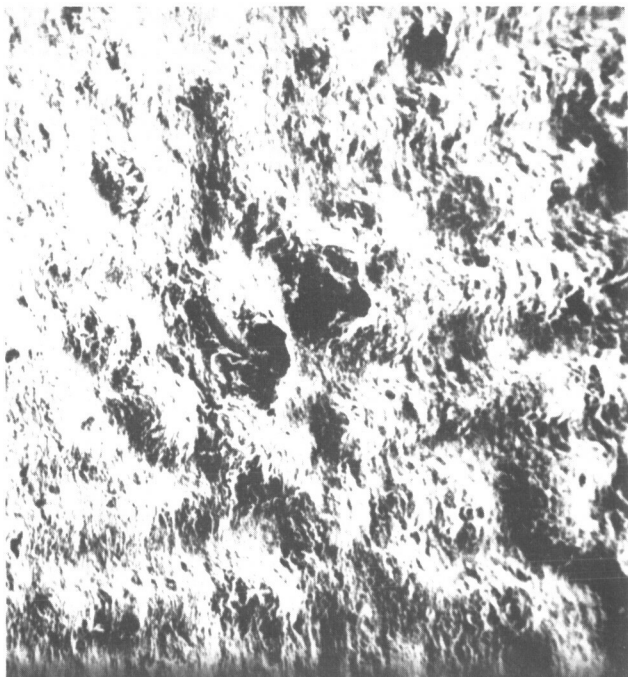


Fig. 12-3. Specimen surface during incubation period

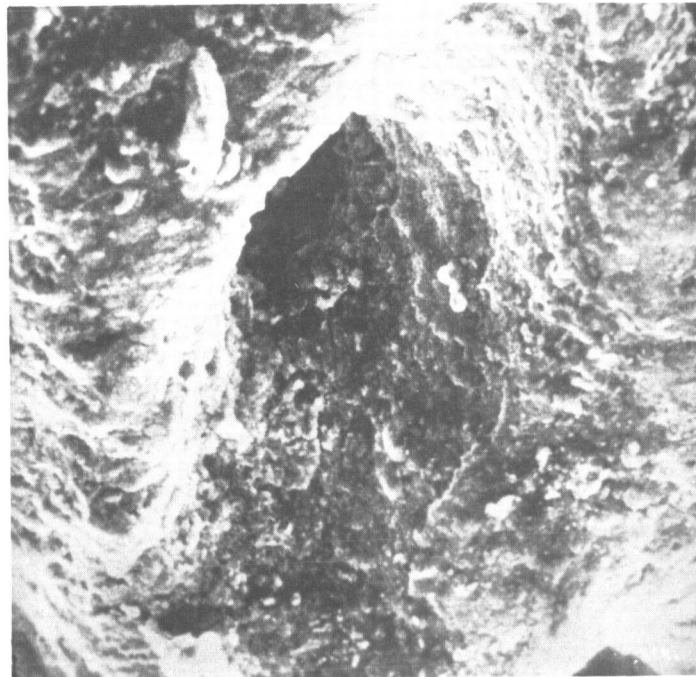


Fig. 12-5. Specimen surface, closeup of a pit

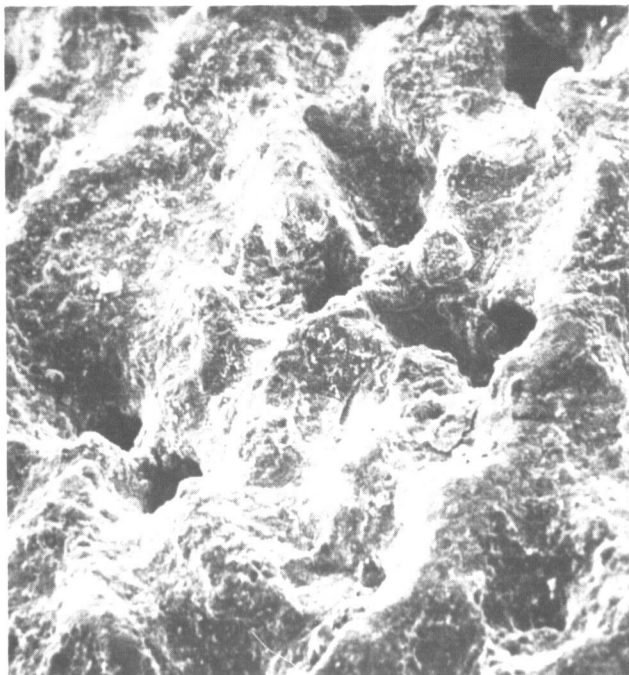


Fig. 12-4. Specimen surface with deeper pits

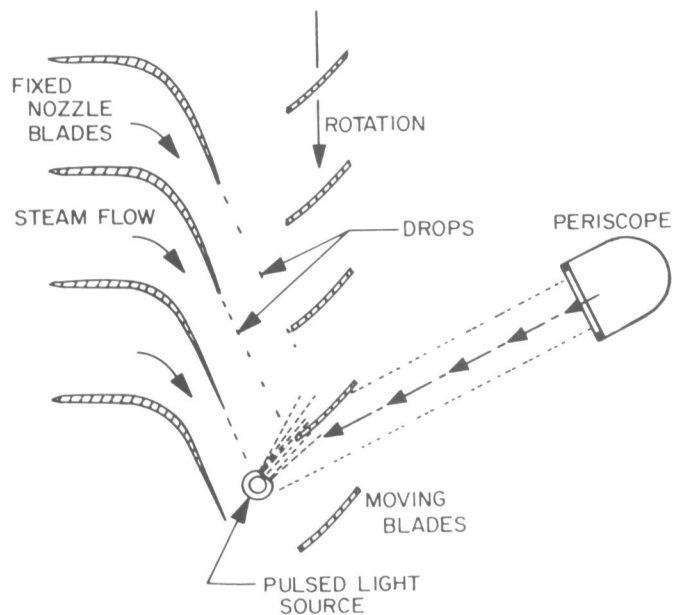


Fig. 12-6. Diagram of water drops at point of impact with moving blades

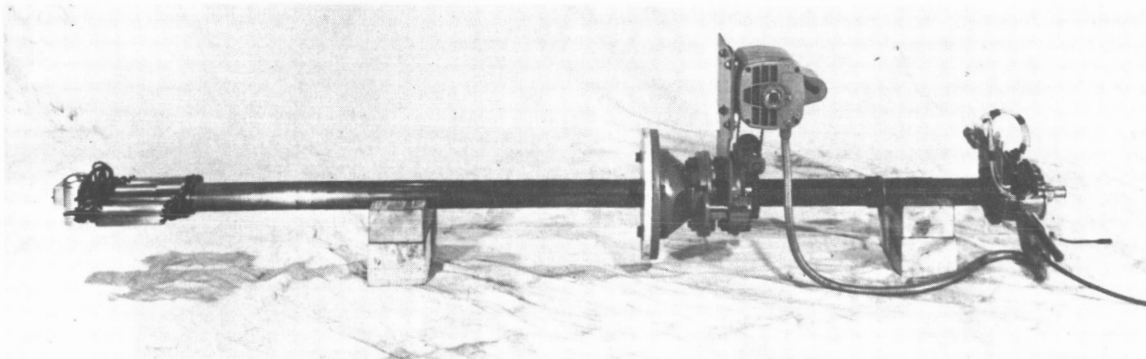
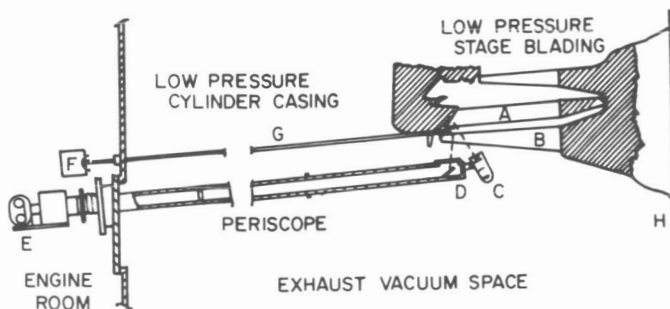
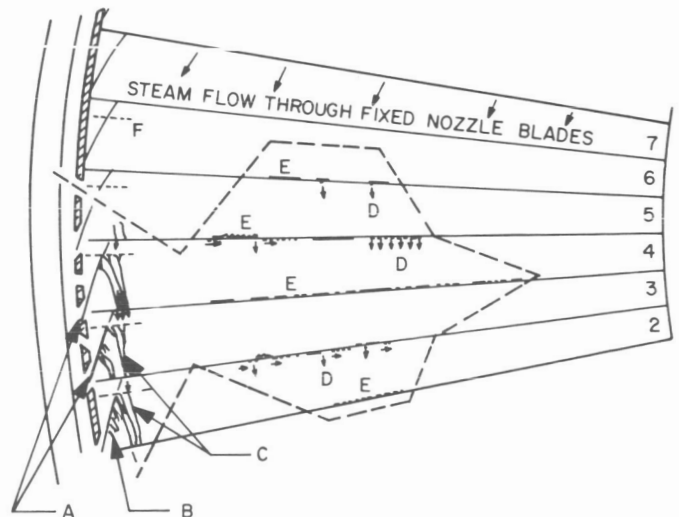


Fig. 12-7. Periscope used in the low pressure cylinder



- | | |
|---|---------------------------|
| A LAST LOW PRESSURE FIXED NOZZLE BLADES | D TILTING MIRROR |
| B ROTATING BLADES (TIP SPEED 1440 ft/s) | E CINÉ-CAMERA |
| C TUNGSTEN LIGHT SOURCE | F XENON FLASHLIGHT SOURCE |
| | G QUARTZ ROD LIGHT GUIDE |
| | H CENTRE-LINE OF TURBINE |

Fig. 12-8. Arrangement of periscope in the turbine



- A WATER STREAMS IN CORNER OF NOZZLE
 B FLOW INSTABILITY CAUSING BREAKAWAY OF WATER A
 C WATER CONCENTRATED BY SECONDARY FLOW IN NOZZLE
 D WATER DROPS SHEDDING AT PREFERRED POSITIONS
 (VERTICAL ARROWS)
 E AREAS OF FLOW SEPARATION CONTAINING WATER
 F UPSTREAM LIMIT OF VIEW DUE TO INCLINATION OF PERISCOPE.
 HORIZONTAL ARROWS INDICATE DIRECTION OF MOVEMENT OF WATER DROPS

Fig. 12-9. Sector of last low-pressure diaphragm showing sources of erosion producing water drops in downstream convex face and outlet edge of fixed nozzle blades 2 to 6

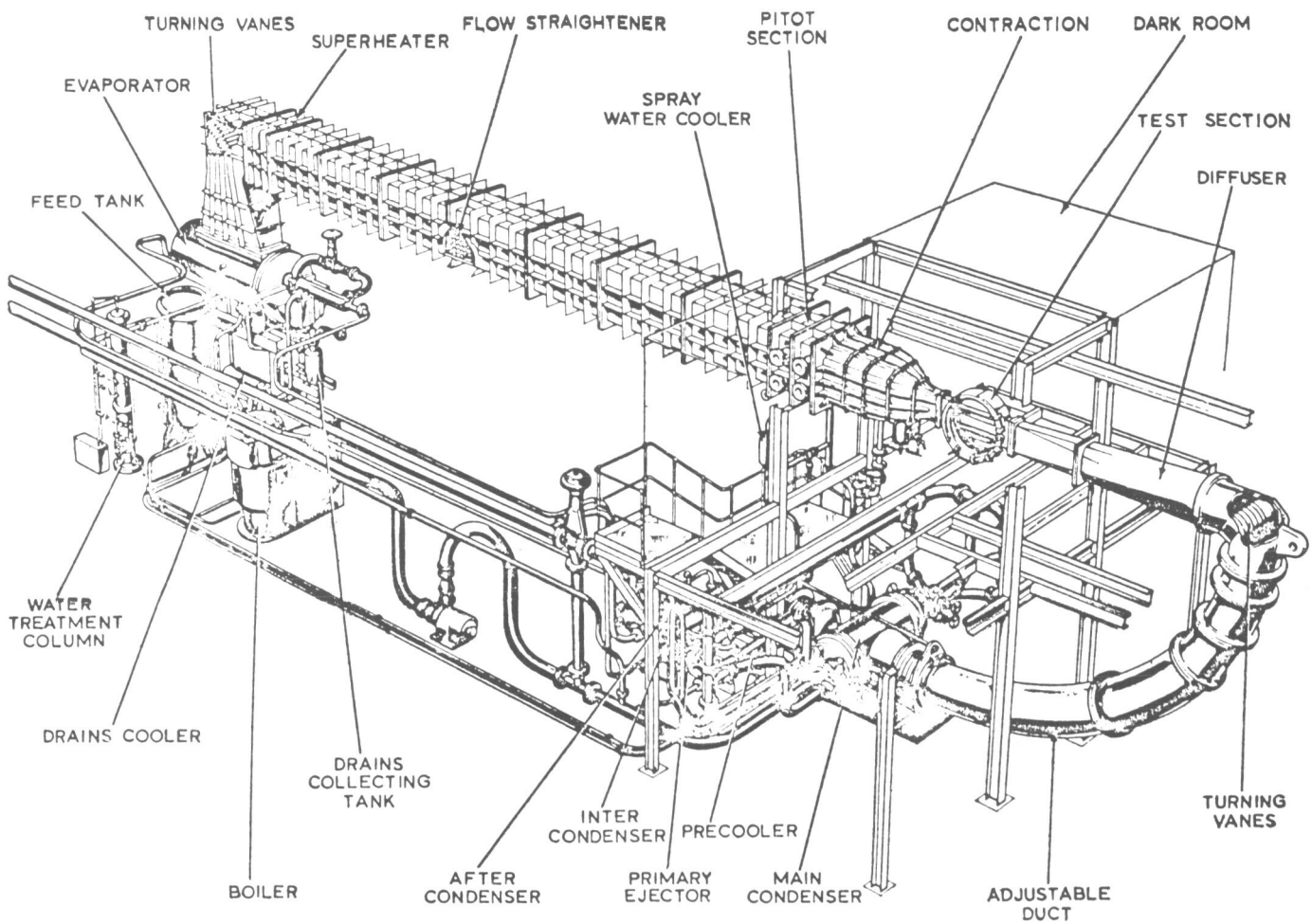


Fig. 12-10. Cascade steam tunnel

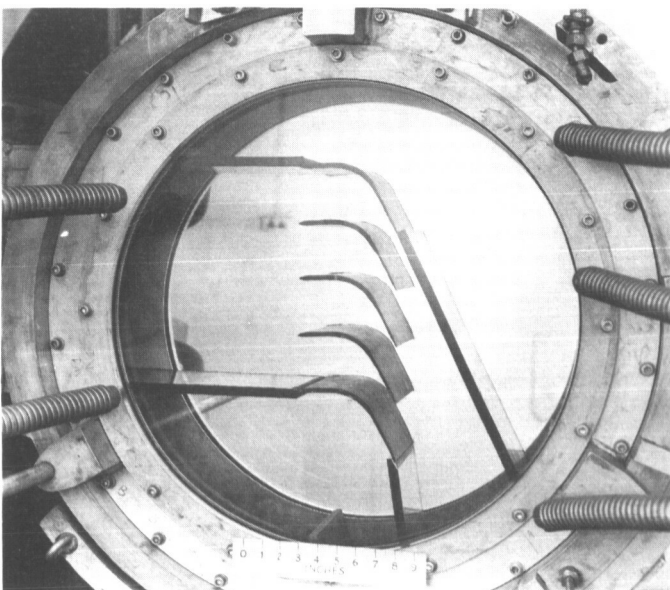


Fig. 12-11. Nozzle cascade in steam tunnel test section

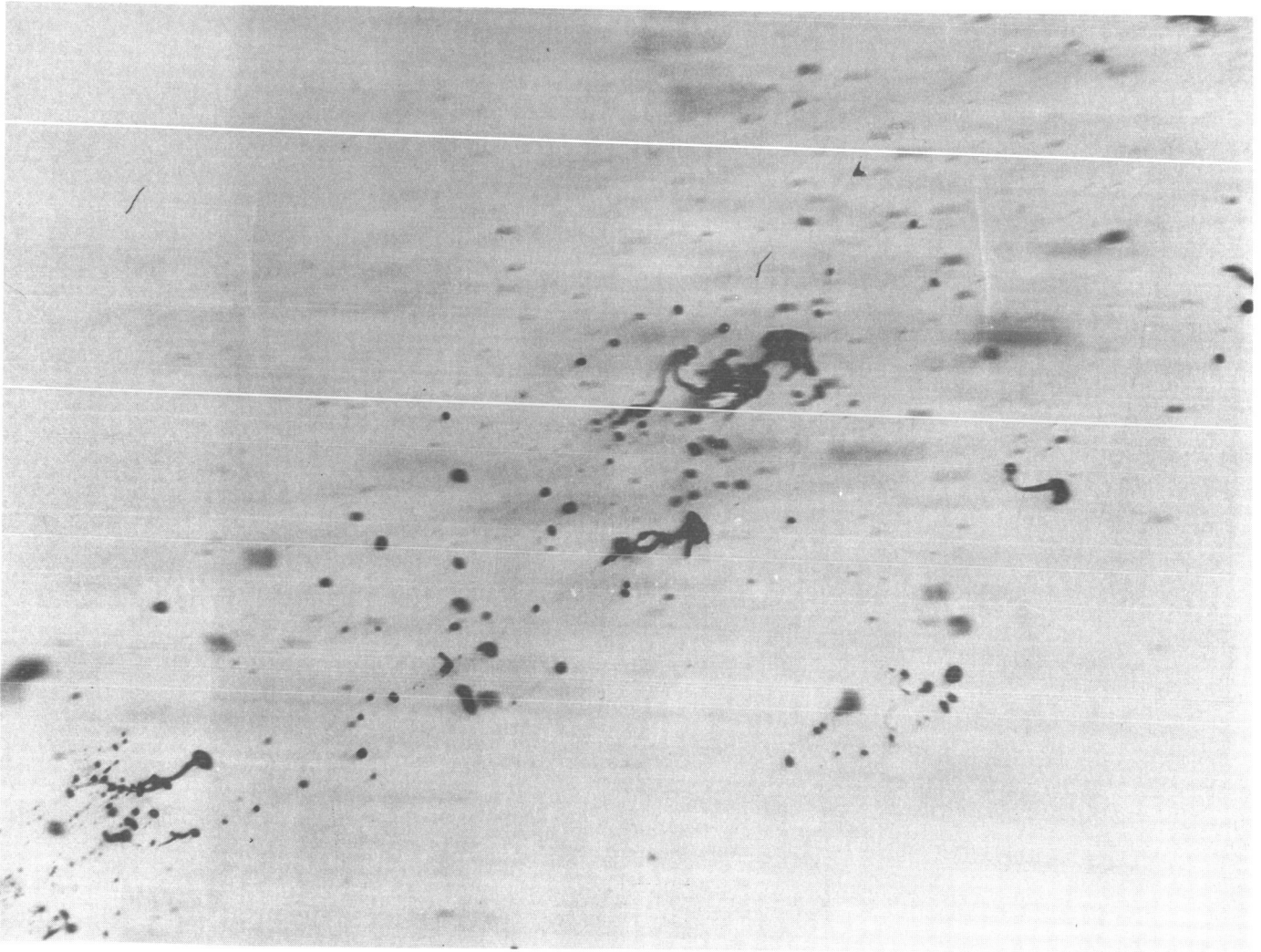


Fig. 12-12. Droplet size before breakup is complete

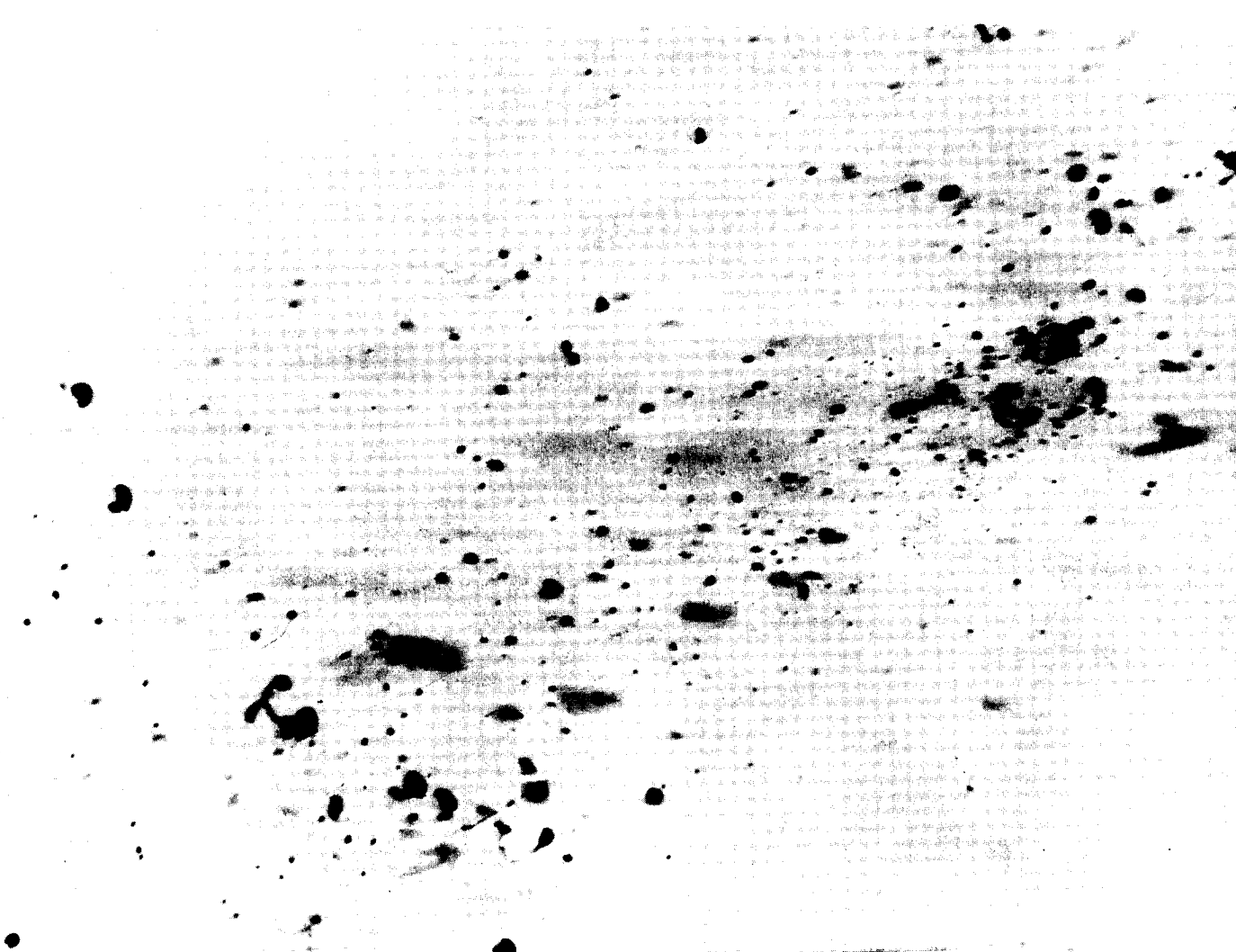


Fig. 12-13. Droplet size at a different test condition

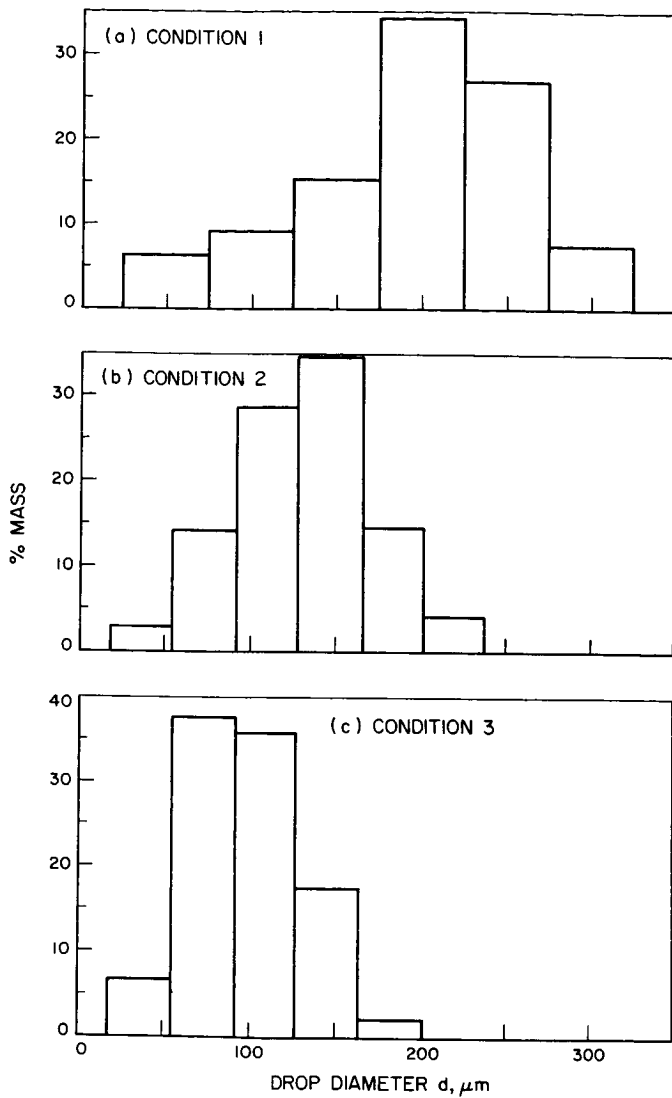


Fig. 12-14. Drop size distributions for three conditions

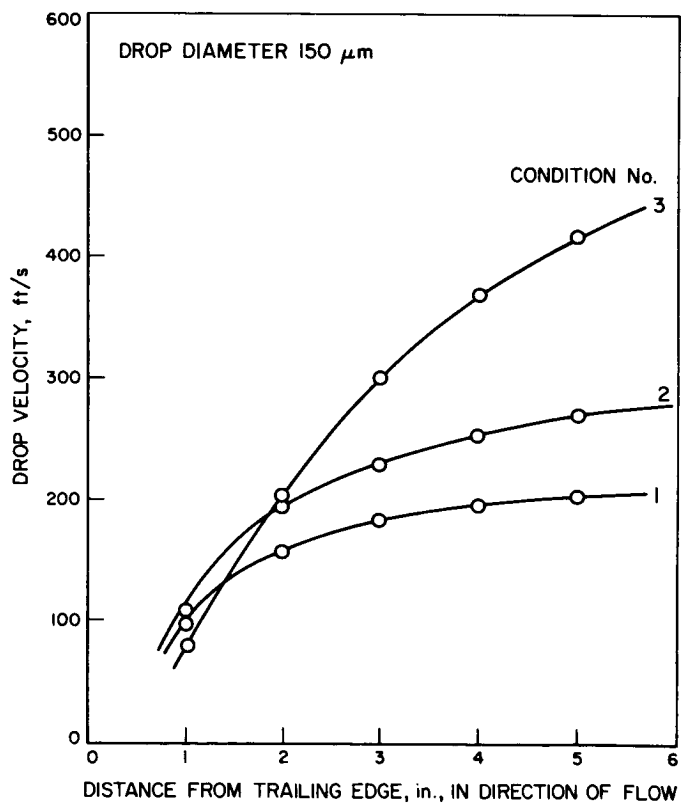


Fig. 12-15. Drop velocities for range of nozzle outlet conditions

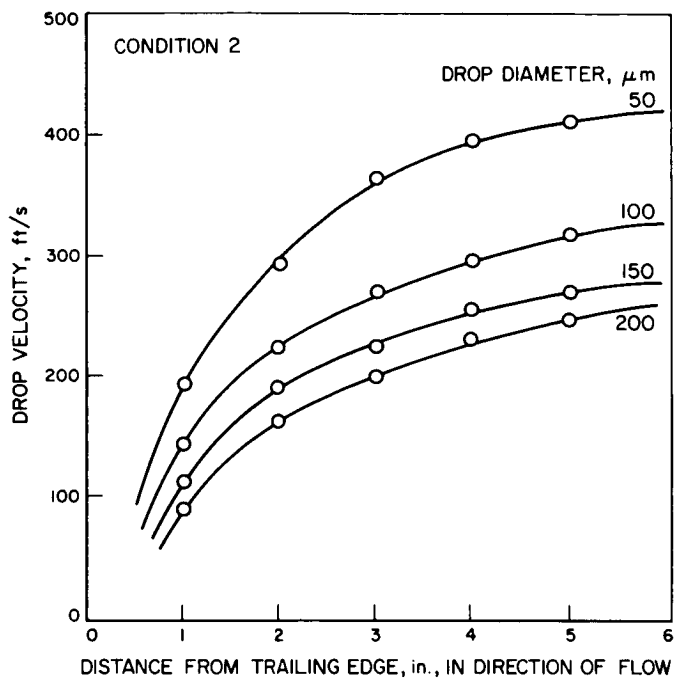


Fig. 12-16. Velocities of drops in the wake of a fixed blade

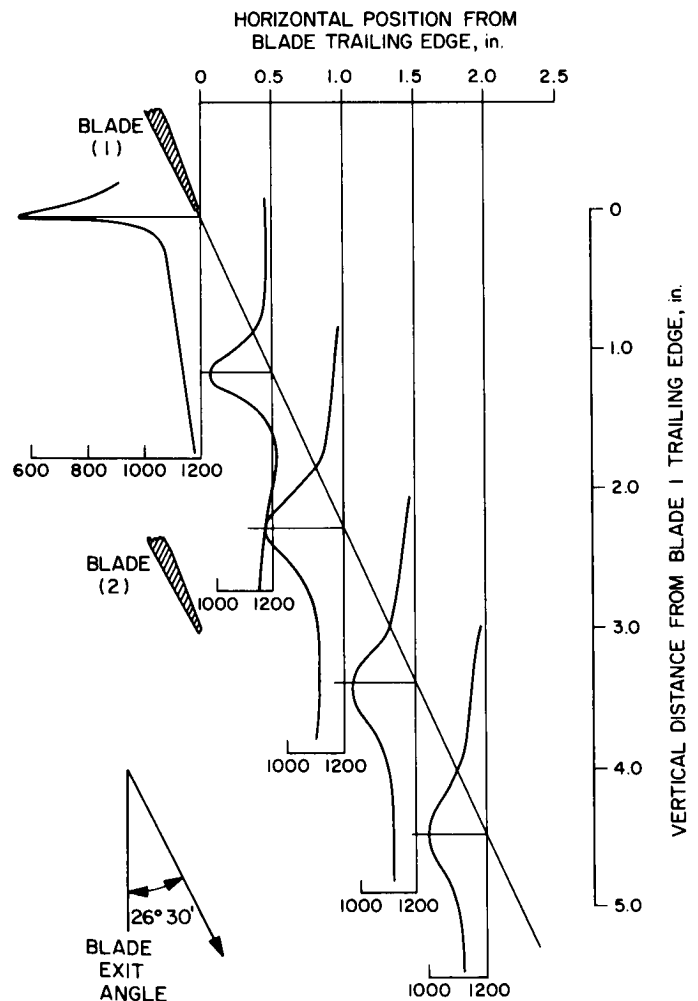


Fig. 12-17. Wake traverses for condition 2

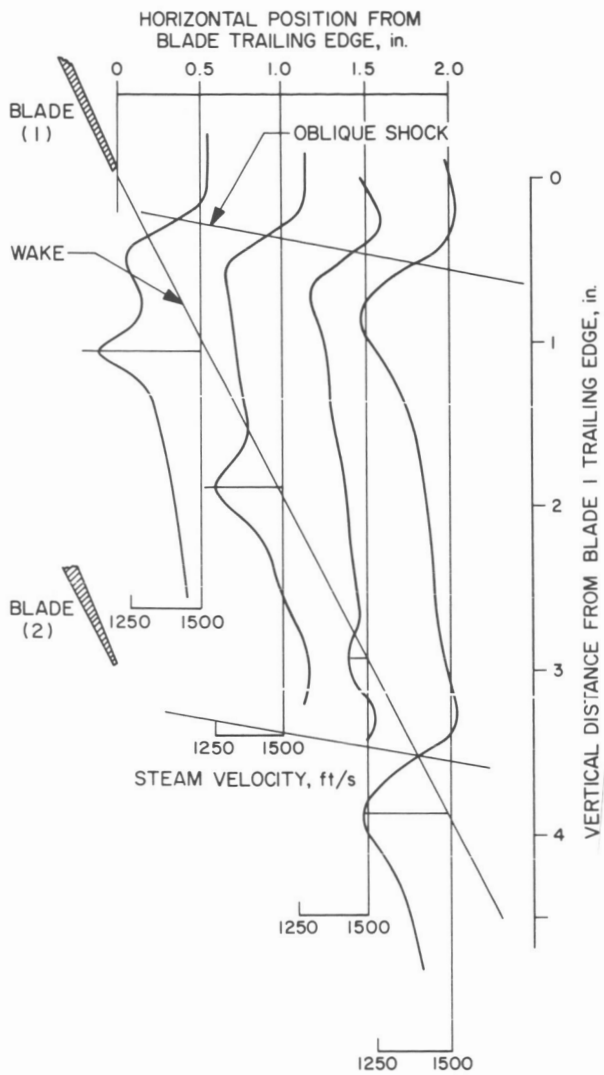


Fig. 12-18. Wake traverses for condition 3

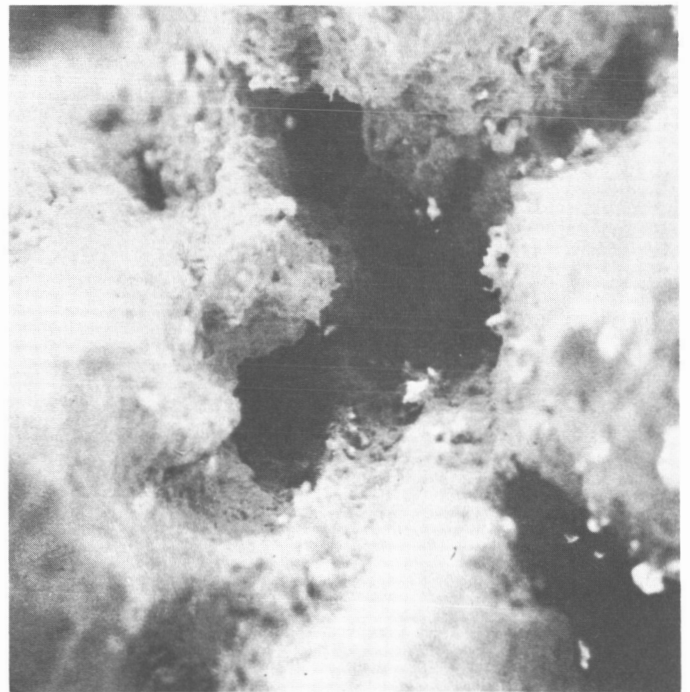


Fig. 12-19. Damage on nose of blade



Fig. 12-20. Damage further in from nose of blade

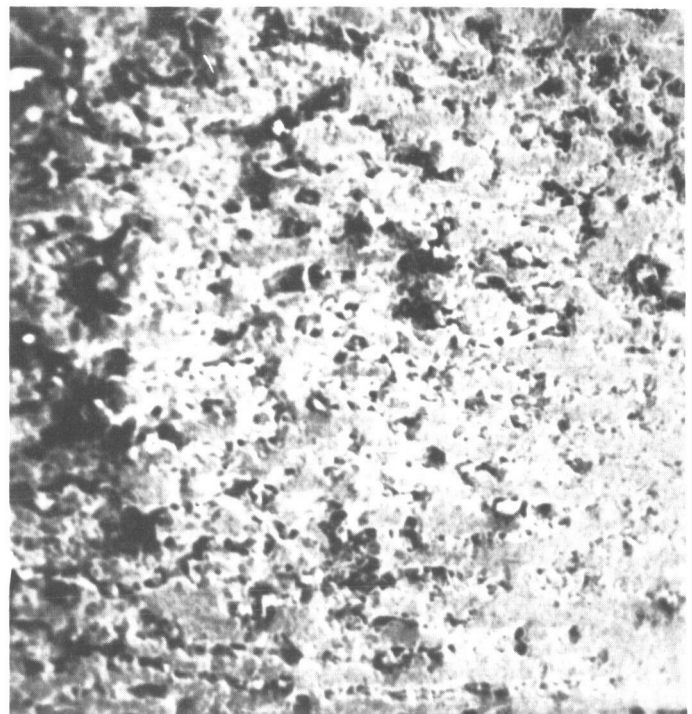


Fig. 12-21. Blade region near where damage ceases

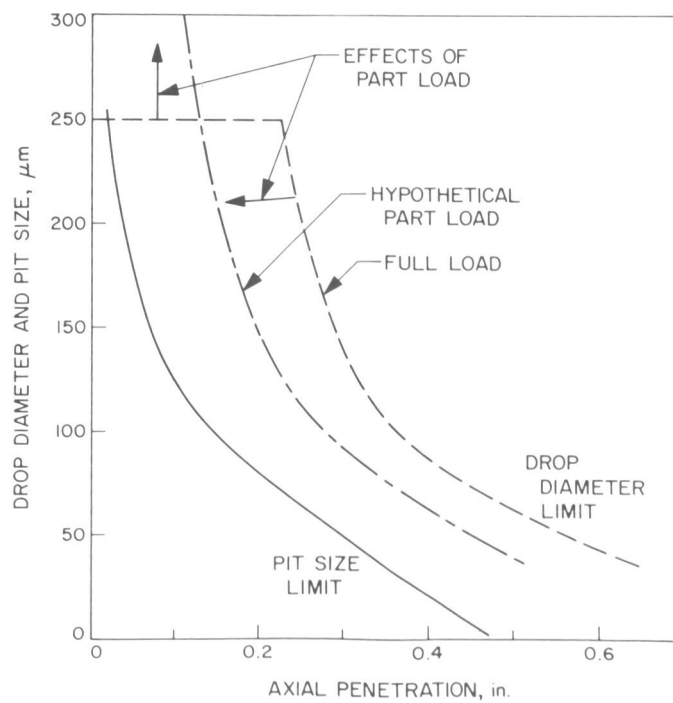


Fig. 12-22. Comparison of predicted drop penetration and measured pit size

13. LIQUID IMPACT AND MATERIAL REMOVAL PHENOMENA

J. H. Brunton
Cambridge University
Cambridge, England

SINGLE IMPACT

A simple extrusion technique was used to produce high-velocity jets of water. The principle of the method is shown in Fig. 13-1. Velocities up to 1200 m/s are easily achieved with this technique.

Figure 13-2 illustrates the different types of high-velocity water jets that can be produced. The core diameters are in the range 1--2 mm and the velocities are in the region of 700 m/s. For liquid-impact studies, the jets shown in frames 3 and 4 were most widely used.

Figure 13-3 illustrates a jet impact at 650 m/s. The time between frames is shown in the photograph. The figure illustrates the fact that the radial flow across the surface may be greater than the impact velocity. This effect is connected with the geometry of the front of the jet. The figure also illustrates the fact that the damage is completed shortly after the instant of impact. There is little further growth of fractures to be found in subsequent frames. This last feature is connected with the initial water hammer pressure decaying rapidly as a result of release waves moving in from the free surfaces of the jet. In this respect, a water drop impact is analogous to explosive loading of the surface; a sudden rise in pressure followed by an almost equally rapid fall. Figure 13-4 illustrates a load/time trace showing the short duration of the initial water hammer pressure. (The subsequent steady flow pressure of the jet is lower than the water hammer pressure and contributes little to the damage.)

The top left illustration of Fig. 13-5 shows a typical ring crack produced in a brittle material by drop impact; a section or a diameter of the ring is shown in the bottom left portion of the figure. The diameter of the ring is equal to the head diameter of the drop producing the ring. The center is undamaged since this region is in compression throughout. The ring crack and the outer circumferential cracks are due to tensile stress setup on impact. The main ring cracks chipped open, and the material was eroded from the outside of these fractures by the outward radial flow.

The original cracks form steps in the surface; these steps are eroded. A perfectly smooth surface seems to be unaffected by the outward flow even at these very high speeds.

The illustration in the top right of the figure shows the effect of a second impact (on the right) on a region already fractured by an earlier shot. The central damage in these figures lies beneath the surface. It is a region of complex fracture produced partly by the material beginning to flow plastically along trajectories of maximum shear stress and partly by fractures caused by tensile stresses tangential to the expanding front of the stress waves.

The illustration at the bottom right of Fig. 13-5 shows a multiple beam interferogram of the surface (each fringe is a surface contour). The scale is given by the spacing between fringes = 2730 \AA . The center is essentially flat; steps in the surface can be seen.

Figure 13-6 shows, in section, the fractures that occur in a 3.5-mm plate of polymethylmethacrylate. The greatest damage occurs near the lower surface of the plate (D) where the initial compression wave reflects as a wave of tension and causes scabbing fractures. The fractures near the upper surface (A and B) are the shear and tensile fractures previously described. This figure illustrates a very common effect in brittle materials; namely, that failure caused by reflection and interference of stress waves can be much greater than failure on the impact surface.

Figure 13-7 illustrates the damage produced in metals by water jet impact at 750 m/s. The figure on the left illustrates damage in stainless steel, and on the right in soft aluminum. The normal impact pressure produces the depression in the surface, and the radial flow causes the erosion around the rim of the depression. As with hard polymers, erosion by the outward flow was found to occur only at discontinuities in the surface, such as grain boundaries, slip lines, twins, inclusions, etc.

The single impact work shows that three general types of failure can occur:

- (1) Failure due to the rapid application of the impact load. In brittle materials, the tensile stresses induced by the loading give rise to ring cracks; in ductile material, the shear stresses cause flow and the formation of a depression.

- (2) Failure due to liquid flow across the surface. This type of failure causes material removal--true erosion at surface discontinuities. These failures may already exist in the surface, or be put in under the action of the normal impact load.
- (3) Damage arising from stress wave reflection and interference. This type is very important in brittle solids.

MULTIPLE IMPACT

Experiments were carried out using a wheel and jet system to produce erosion. Measurements of impact load and flow velocities show that water hammer effects and high-speed radial flow velocities arise in the same way as described in the single impact work. The new geometry (namely, a liquid cylinder struck from the side) gave rise to a different flow and fracture pattern, but this pattern could be interpreted in the same way as previously discussed. In brittle solids, instead of a ring fracture, two parallel lines of fracture (parallel to the jet axis) were produced. As before, the central region between the line fractures was undamaged (since this remained in compression throughout). In addition, the erosive forces, due to the outward flow, remain low in the central area of impact, since the flow velocities are low in this region. These features are illustrated in Figs. 13-8 and 13-9. In Fig. 13-8, the damage was produced by firing brittle methacrylate through a 1-mm diameter mercury jet from the side (the central undamaged zone is bounded by two faint lines), then by the parallel Hertzian fractures, and finally by erosion damage due to liquid flowing out across the cracked surface from the center. Figure 13-9 shows a similar distribution of fractures after several thousand impacts with a water jet at 68 m/s. Eventually these small fractures join up to produce deep surface pits on either side of a relatively undamaged central region.

The effects of altering impact variables, such as drop size, impact velocity, angle of impact, and surface roughness, were investigated. One interesting feature concerns the effect of the area of impact on erosion. Reducing the impact area by using successively narrower specimens increased time-to-fracture and effective erosion resistance by a large factor. This increase could be due to a reduction in duration of the initial water hammer pressure, and could explain the fact that small drops are less damaging than large drops. In any eroded surface, some small areas

seem, to stand out as peaks and erode much more slowly than materials in the depressions between the peaks. This aspect may again be an impact pressure duration effect.

In investigating the erosion of metals, a similar study of the impact variables was undertaken. A number of points emerge from this study. A general feature of erosion seems to be that deformation can occur at water hammer impact pressures that are much below the yield strength of the metal. What is observed is that, initially at these very low pressures, the surface yields locally to form small depressions a few microns across. Some of these depressions grow to form small pits and, at this stage, the grain boundaries generally show up. This stage is illustrated in Fig. 13-10 which shows the surface of a low carbon steel specimen after 50,000 impacts at 77 m/s (magnification 200 x). With further impacts, material erodes from the pits either by ductile fracture in soft low-strength metals, such as annealed copper and aluminum, or by propagation of primarily brittle cracks in harder alloys, such as steels. In steels, corrosion and fatigue failures are evident at the roots of the surface pits; fractures of this kind are shown in Fig. 13-11. In this case, the surface had received approximately 10^6 impacts at 90 m/s (magnification 900 x).

It might be argued that local yielding at very low average pressures could be due to cavitation in the flow or impact. Experiments with a liquid shock tube (Fig. 13-12) have proved that a plain liquid shock repeatedly impinging on a specimen will, in the absence of cavitation, produce depressions (the first stage of erosion) identical with those produced in the wheel and jet apparatus. Part A of Fig. 13-13 shows depressions produced by the wheel and jet, and part B illustrates depressions produced in the shock tube. This result indicated that depressions are a material phenomena and occur in regions where the yield strength is very much below average. The depressions develop slowly but at different rates, suggesting that some shapes may be more effective in their stress concentrating effect and in overcoming the resistance developed by work hardening.

The shock tube apparatus produced the surprising result that sharp-fronted shocks were more effective in producing deformation than slowly rising stress pulses even though the latter were of greater absolute magnitude.

Another point suggested by the present investigation is the importance of surface profile on erosion. Scanning electron microscope studies of eroded blade

materials have shown that the peaks which correspond more or less with the original levels of the surface are deformed plastically; whereas, the sides and bottoms of the depressions between the peaks fracture in a brittle manner. These effects are illustrated in Figs. 13-14 and 13-15, at magnifications of 100x and 500x, respectively. These figures show part of an eroded stellite shield taken from a steam turbine blade. It is an intriguing problem to explain how the very deep depressions form and how erosion continues at the bottom of these depressions that are well below the impact surface. It seems most likely that the repeated passage of shock waves from the impact fatigues the walls and, particularly, the converging ends of the cavities.

The behavior of cobalt and its alloys seems to be anomalous among the ductile metals. All the metals and alloys examined began to erode by forming depressions and, then later, by the depressions developing into pits. An example is given in Fig. 13-16 which shows depressions formed after a few thousand impacts in stainless steel. Figure 13-17 illustrates the appearance of pure cobalt after the same treatment. Depressions are not formed; instead a roughening and tilting occurs on the surface by the formation of slip and twin shears. The investigation suggests that the distribution of soft spots in cobalt and its alloys (the stellites for example) is very different than that in most other metals. This effect may be associated with its unusually faulted crystal structure and high rate of hardening. Figure 13-18 illustrates the high erosion resistance of pure cobalt in spite of its relatively low strength; this result is even more marked in some of the stellite alloys.

Considerable evidence now exists to suggest that fatigue plays an important role in the erosion of high-strength metals and alloys. In Figs. 13-19 and 13-20, erosion curves are compared with S-N fatigue curves to show that a similarity exists between the two. The upper curve in each figure is a standard S-N fatigue curve for that material. The lower curves plot impact velocity (as a measure of maximum impact load) against time to reach measurable weight loss, or in the low curve to increase erosion by a standard amount. It is interesting to note that where the S-N curve predicts a fatigue limit the erosion curve levels out. This result is somewhat surprising, particularly so when it is considered that conditions favor corrosion fatigue.

Examination of the fracture surfaces in the scanning microscope show these surfaces to be striated. This fact can be taken as strong evidence that propagation of the fractures occurred by a fatigue process involving cyclic loading.

ACKNOWLEDGMENT

Much of the recent work on multiple impact erosion in metals described in this report has been carried out by Mr. G. P. Thomas of The Physics and Chemistry of Solids Laboratory, Cambridge. This work will be published in full in the near future. Part of the work described was supported by a grant from the Central Electricity Generating Board.

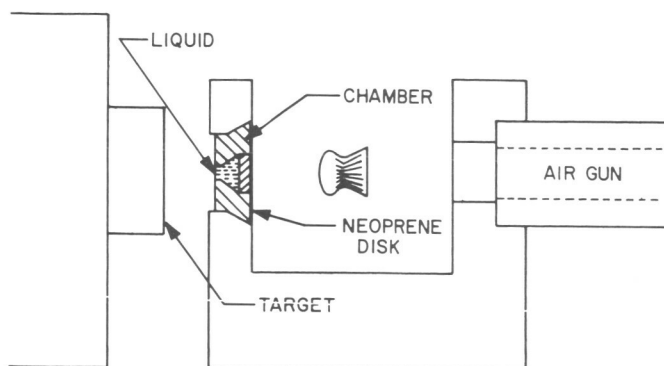


Fig. 13-1. Diagram of method for producing a high-velocity liquid jet

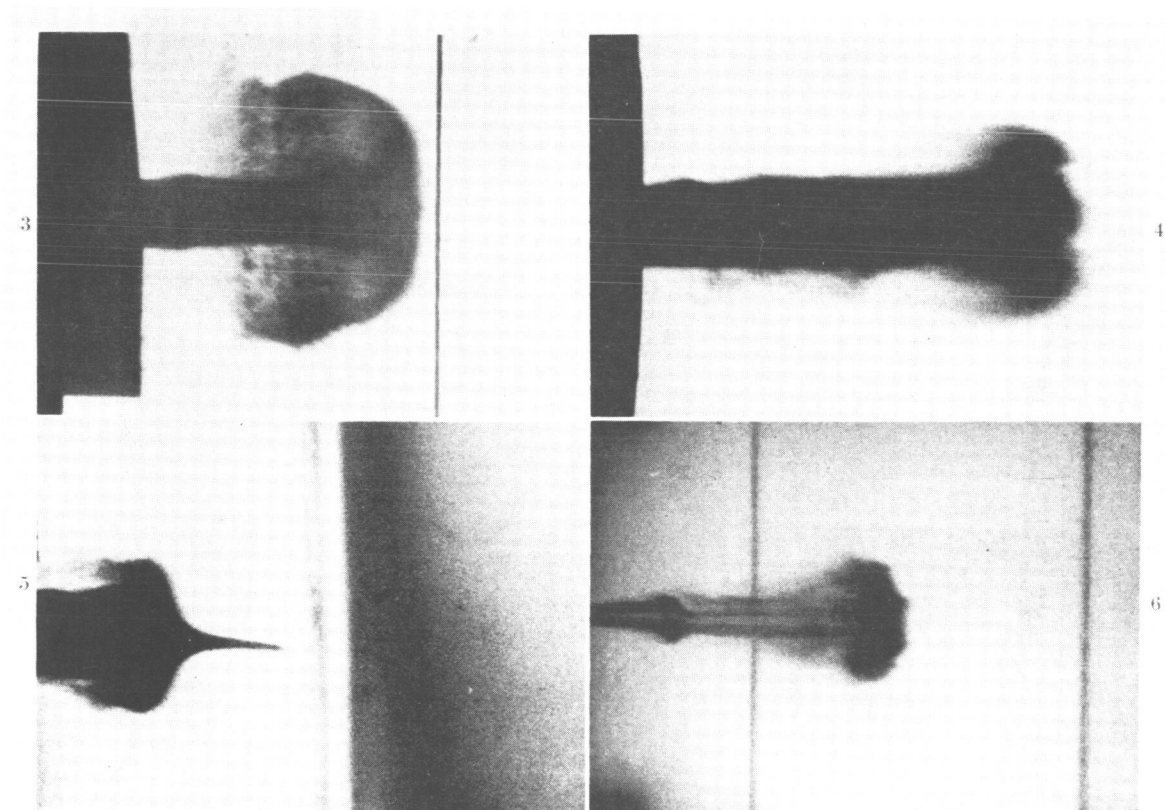


Fig. 13-2. Types of high-velocity water jets

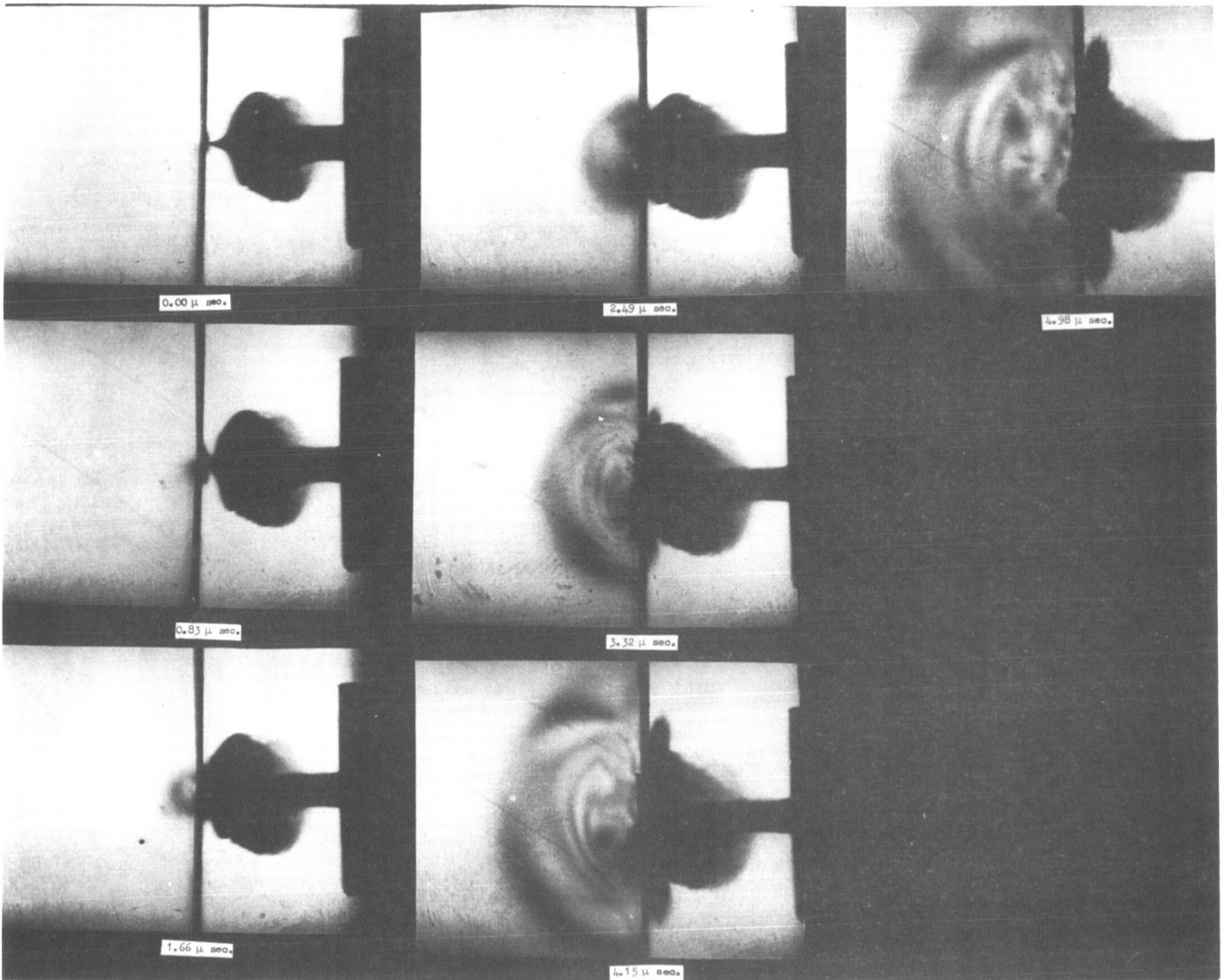


Fig. 13-3. Sequence of water jet impact

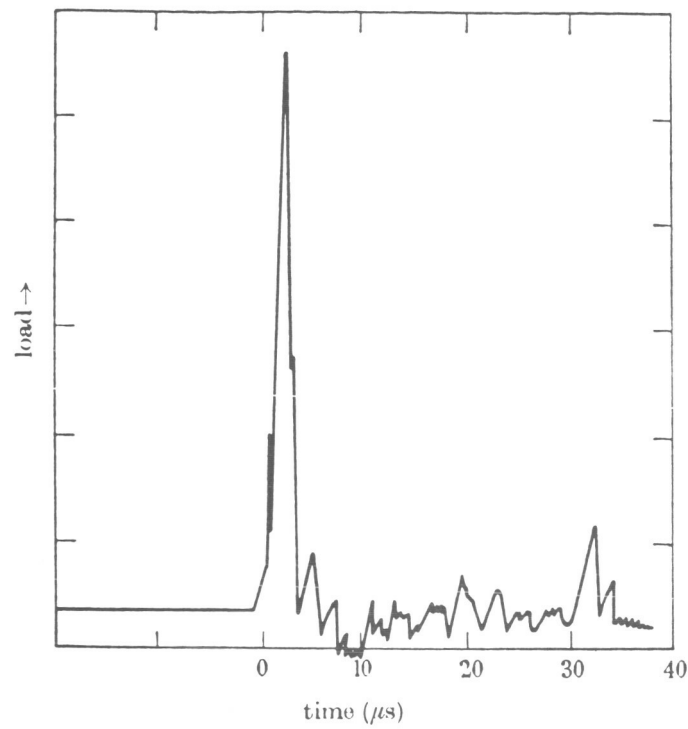


Fig. 13-4. Load vs time trace

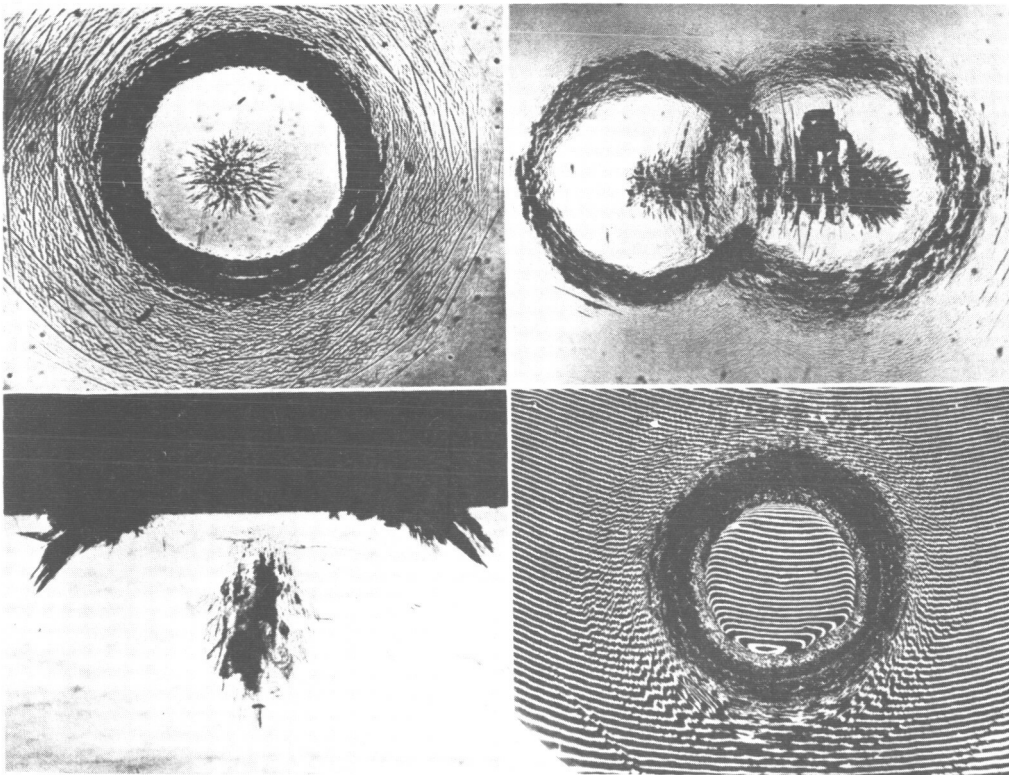


Fig. 13-5. Drop impact damage to brittle material

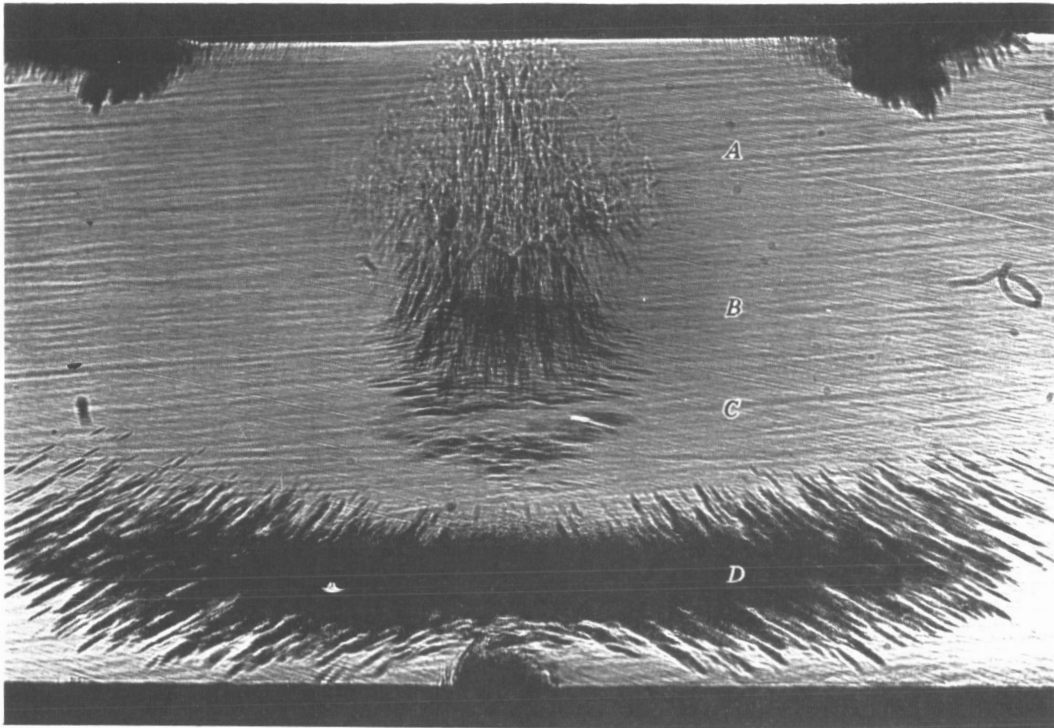


Fig. 13-6. Plate fracture, sectional view

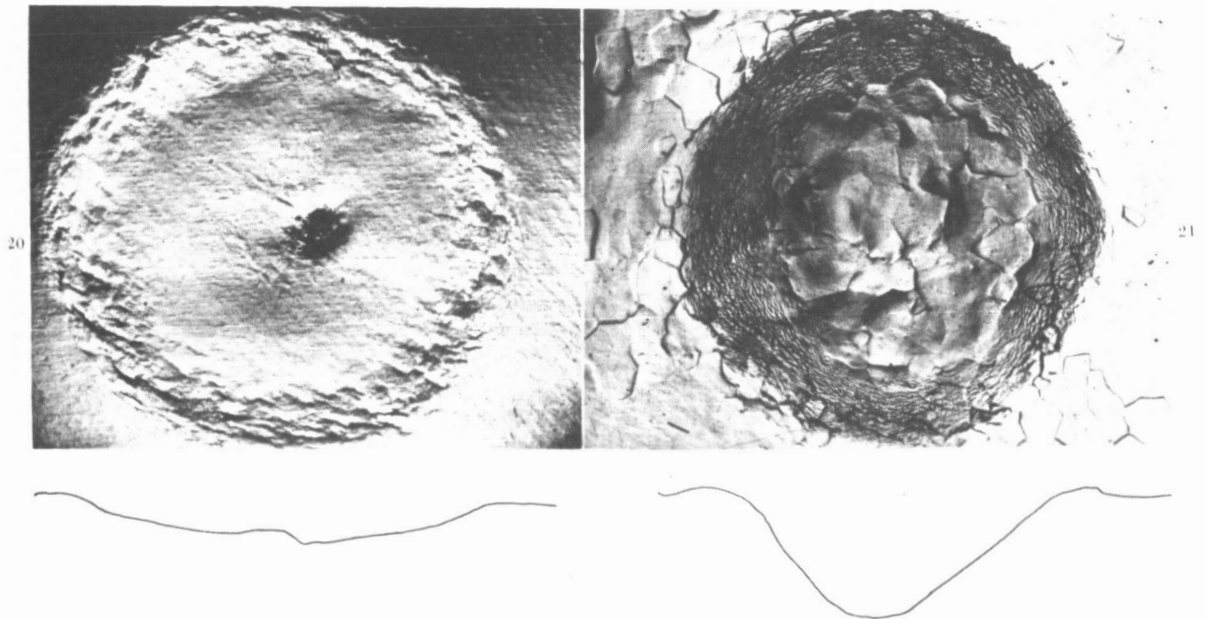


Fig. 13-7. Water jet impact damage to metals

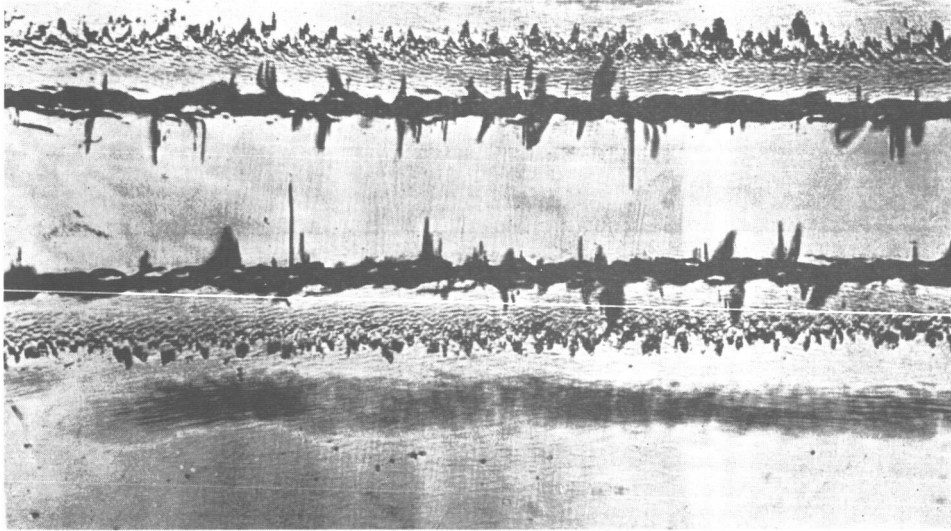


Fig. 13-8. Multiple impact damage

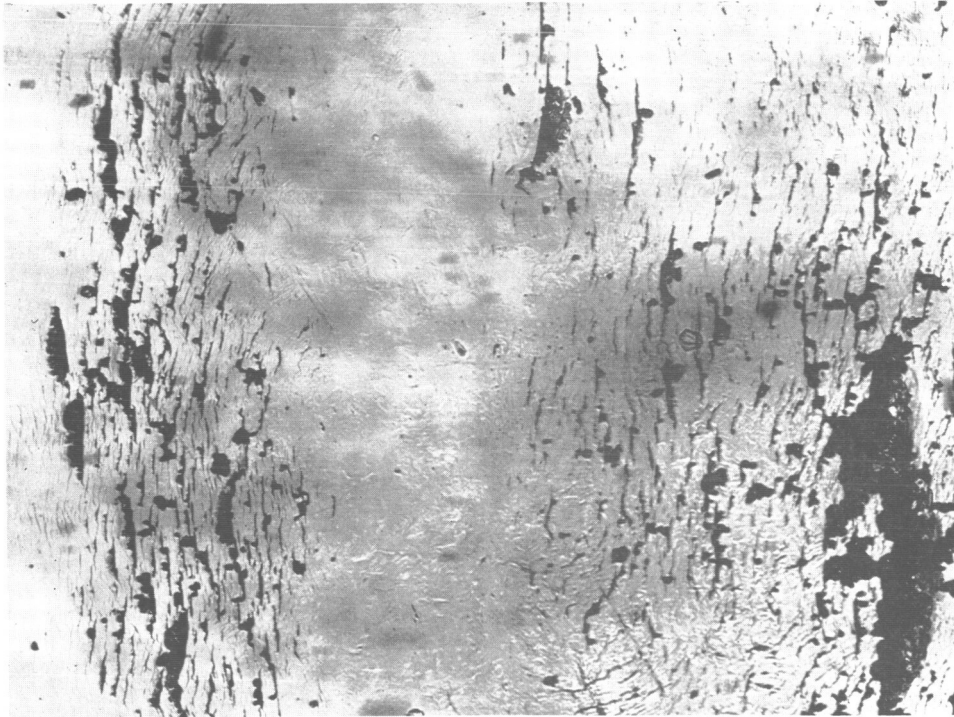


Fig. 13-9. Damage after several thousand impacts

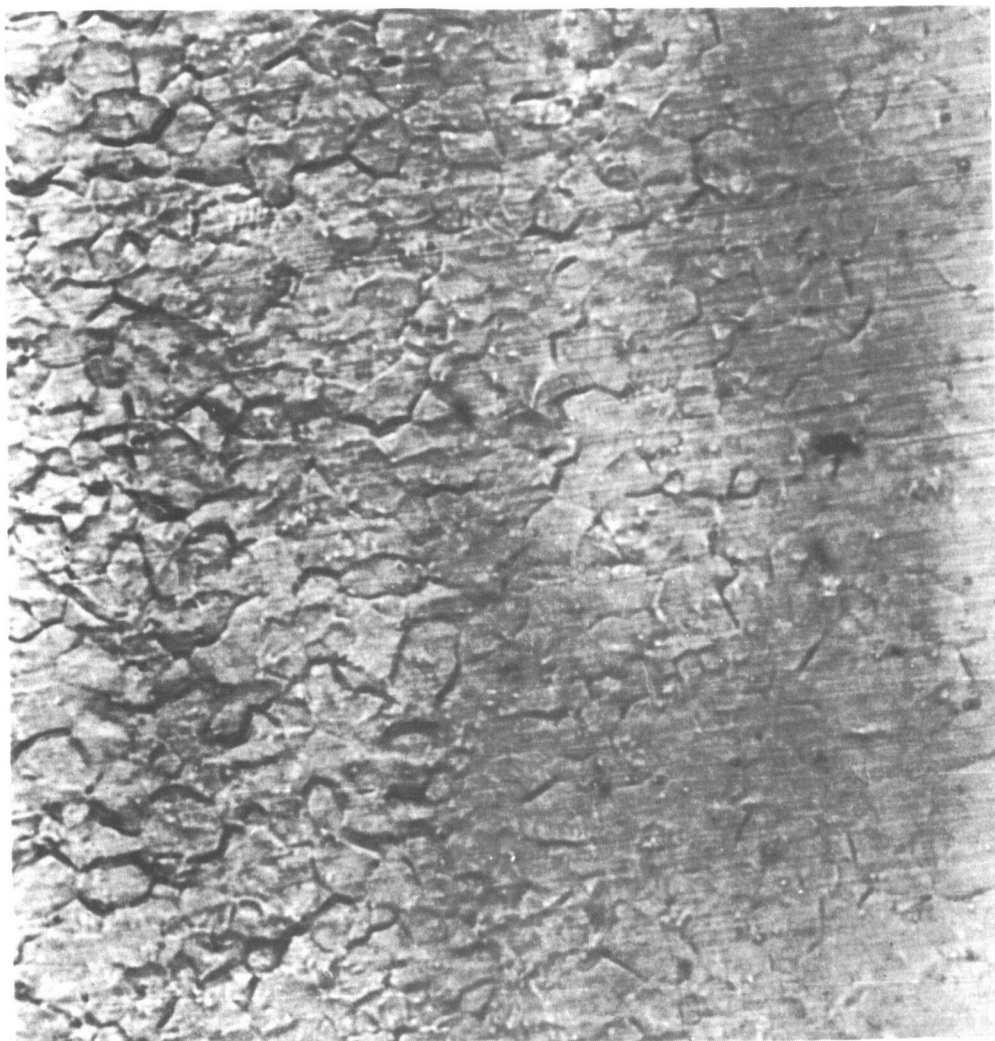


Fig. 13-10. Damage to low carbon steel specimen

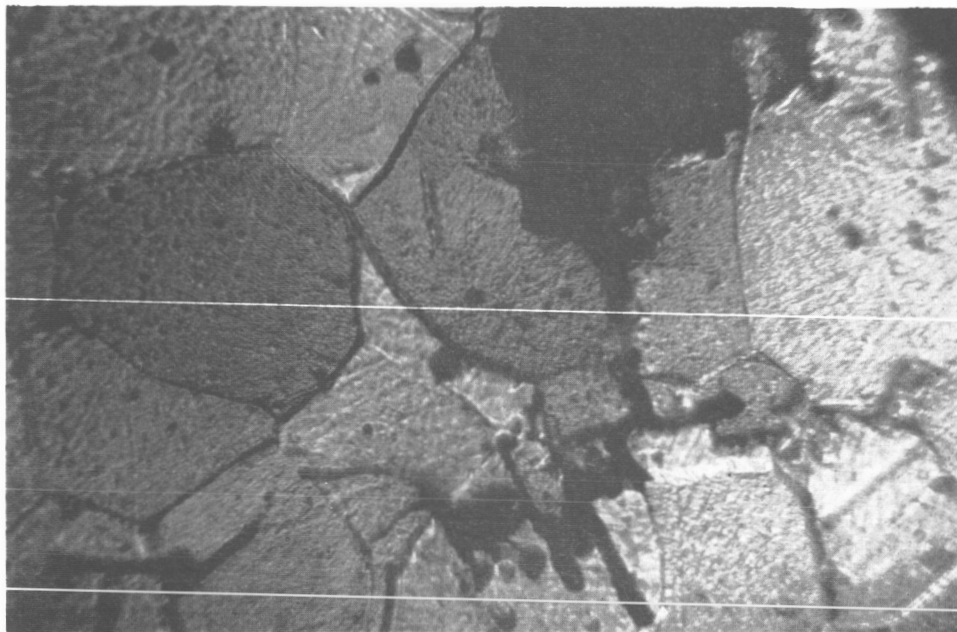


Fig. 13-11. Corrosion and fatigue failure fractures in steel

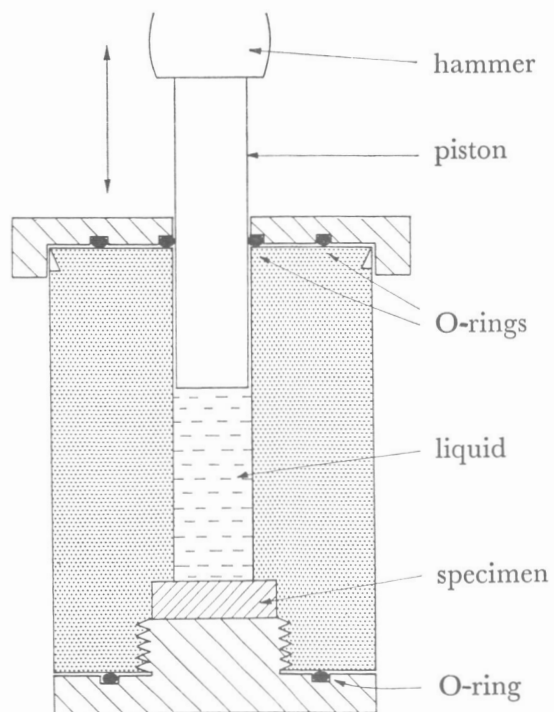
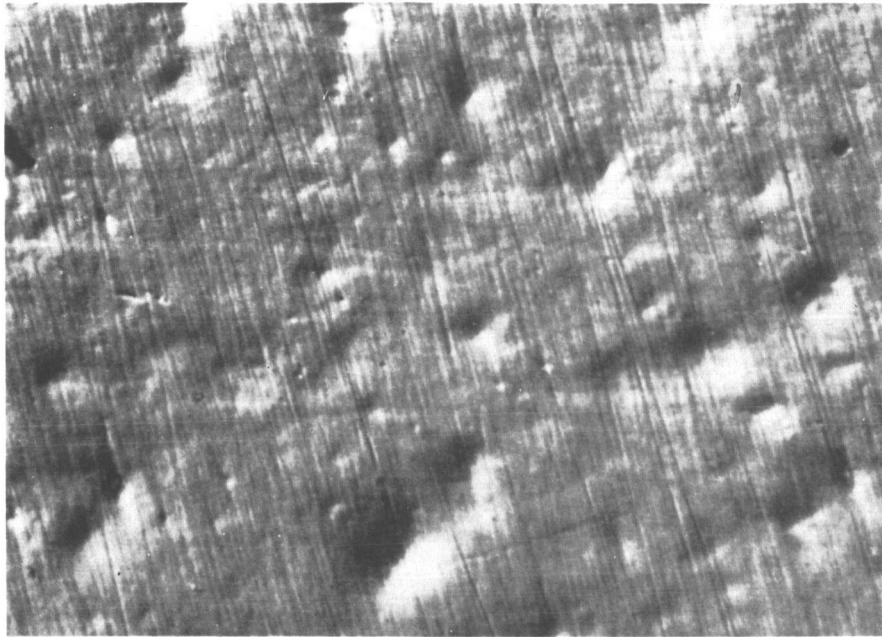


Fig. 13-12. Liquid shock tube diagram



(a)



(b)

Fig. 13-13. Specimen depressions produced by shock tube and wheel/jet

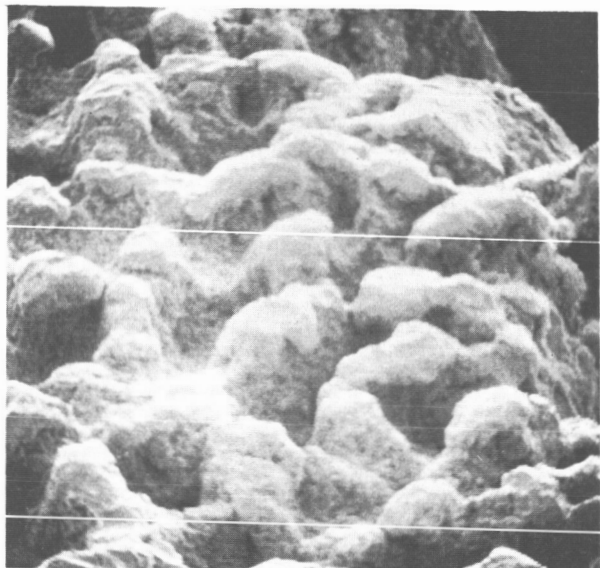


Fig. 13-14. Eroded stellite shield, magnification 100 x



Fig. 13-15. Eroded stellite shield, magnification 500 x

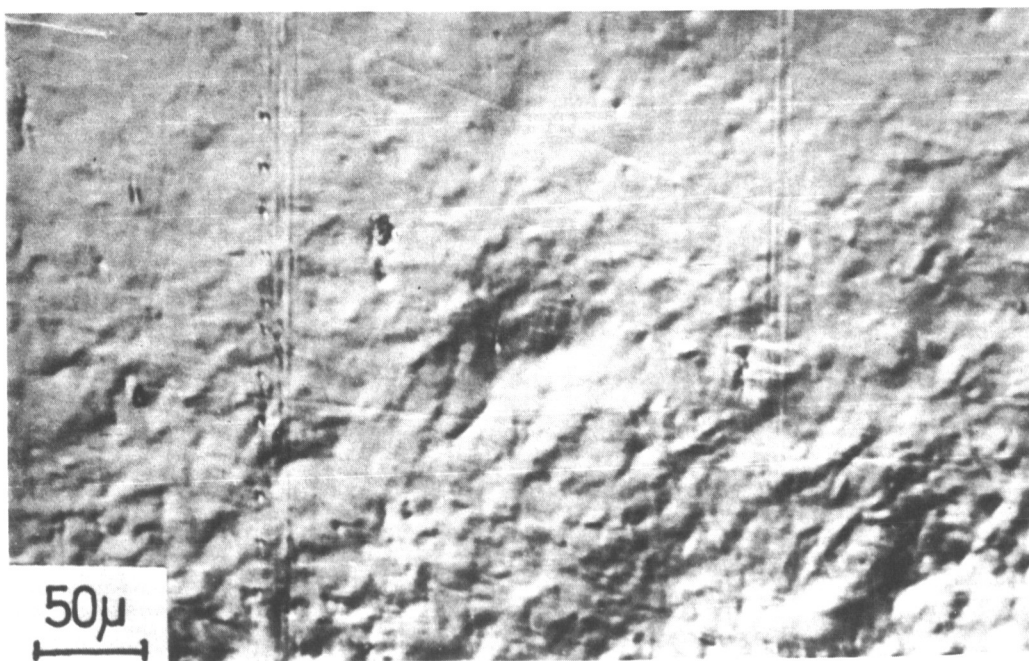
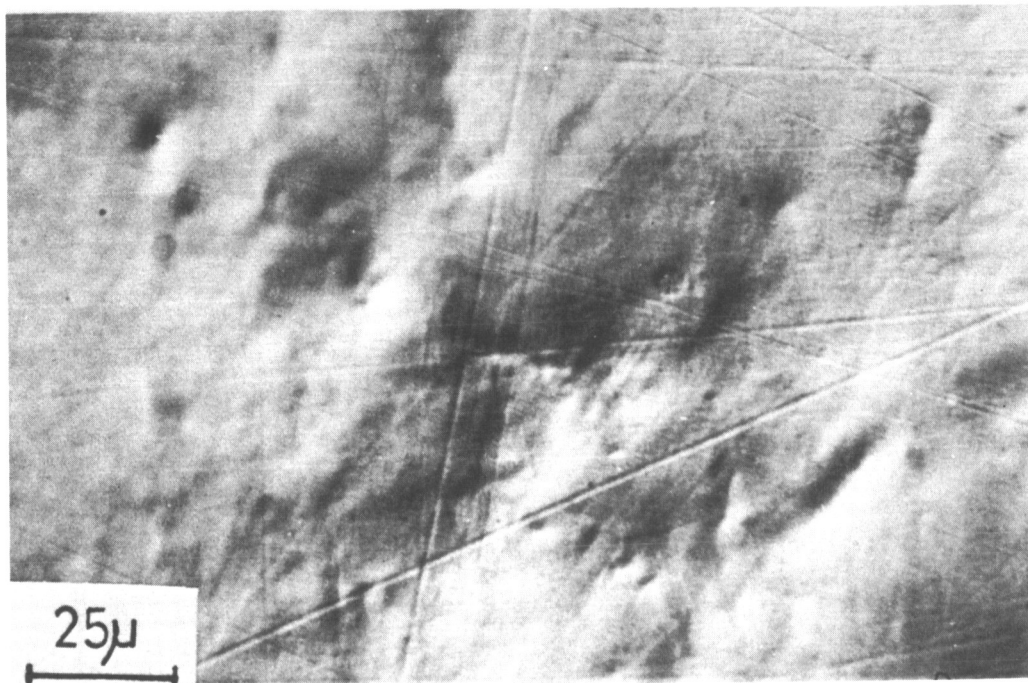


Fig. 13-16. Depressions in stainless steel

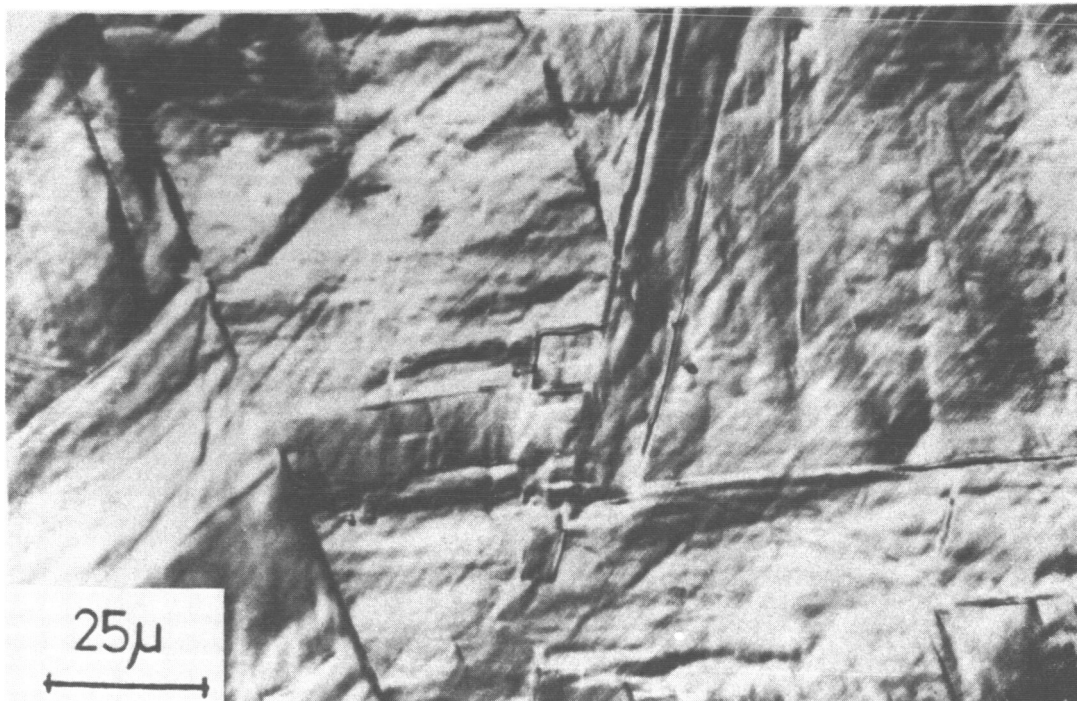
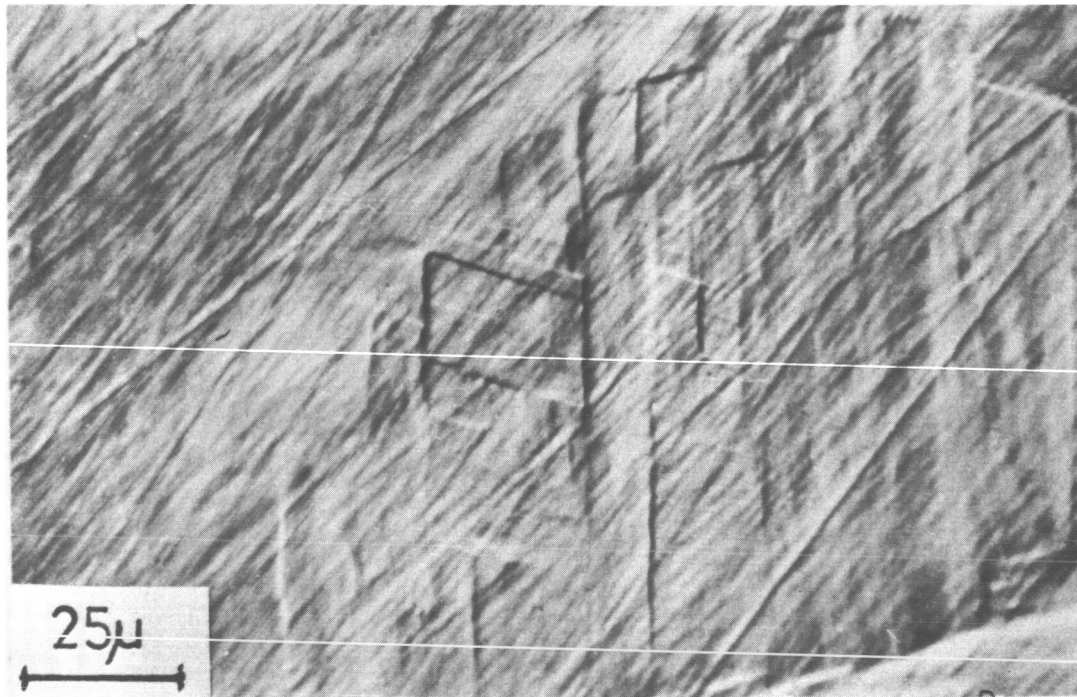


Fig. 13-17. Damage to cobalt

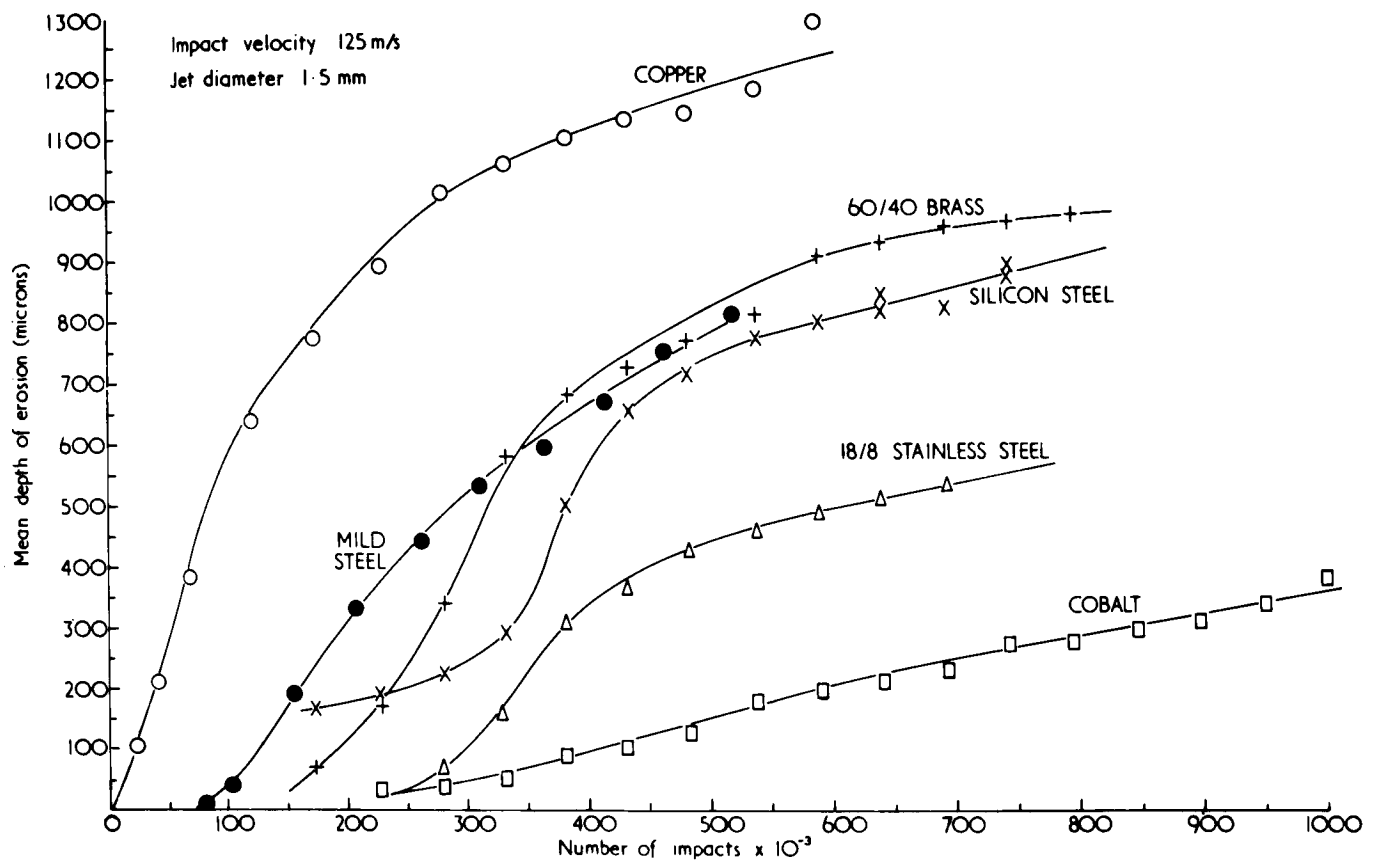


Fig. 13-18. Erosion vs impact in metals

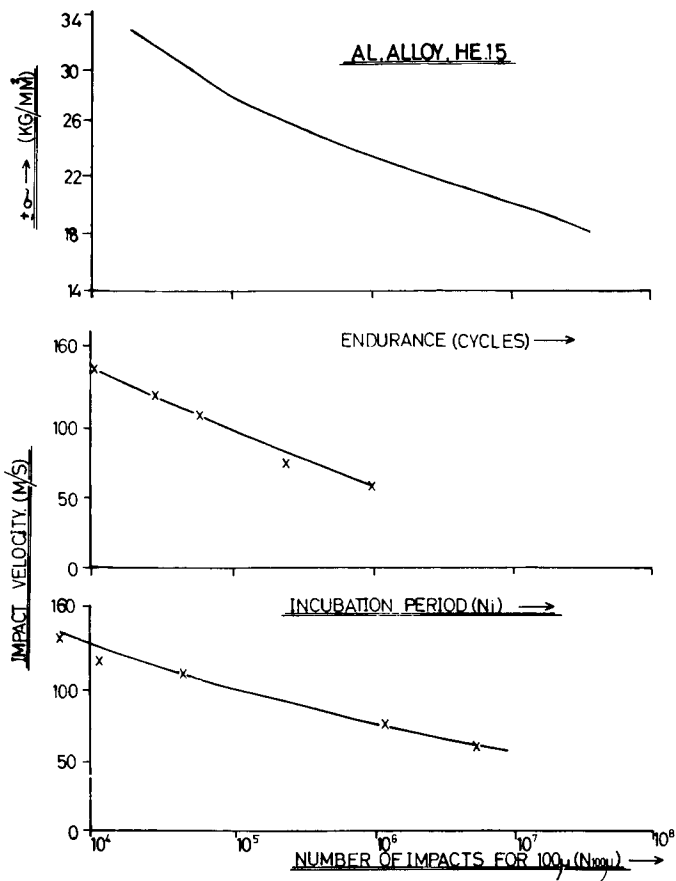


Fig. 13-19. Erosion and S-N fatigue curves for Al alloy HE 15

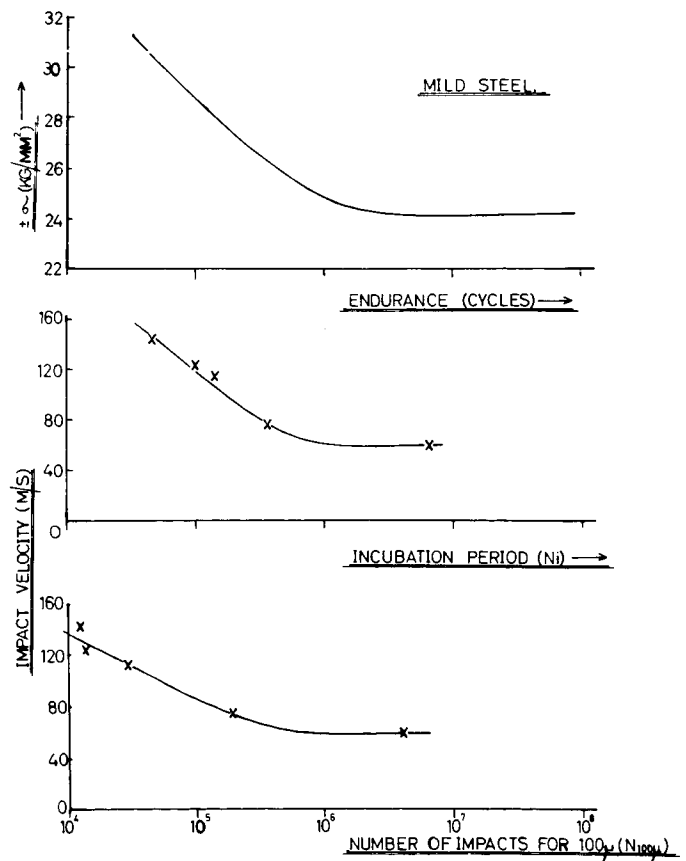


Fig. 13-20. Erosion and S-N fatigue curves for mild steel

14. THEORY OF EROSION

A. Thiruvengadam
Hydronautics, Inc.
Laurel, Maryland

Recent research on cavitation erosion has led to the definition of intensity of erosion as the power absorbed by unit area of the eroded material (Fig. 14-1). Based on this definition, a nomogram was constructed to help designers select proper materials (Fig. 14-2). Such a simple approach to erosion problems is limited by the fact that the rate of erosion is time dependent (Figs. 14-3 and 14-4). Such effects are being recognized in other types of erosion, such as turbine erosion and rain erosion (Fig. 14-5).

It is necessary to understand and predict these time effects quantitatively if we want to extrapolate laboratory data to field systems. The following is a theory with such an objective.

When these time effects were first recognized, the relationship between the intensity of erosion and the test time was divided into four zones as shown in Fig. 14-6. It was postulated that the accumulation zone was the result of an increased energy absorption rate due to changes in the material, while the attenuation zone was due to the attenuation of the shock of collision as the depth of erosion increased. Making use of these two postulates and the definition of the intensity of erosion, a differential equation of erosion is derived (Fig. 14-7). This equation is normalized with respect to the time at which the intensity is a maximum (Fig. 14-8) and a general solution is obtained. Assuming that $n = 2$ (since the shock intensity attenuates as the reciprocal of r^2) and that the efficiency is associated with Weibull-type fatigue distributions, the relative intensity is calculated as a function of the relative time (Fig. 14-9). The data presented in Fig. 14-3 are compared with the theoretical prediction corresponding to the normal distribution (Fig. 14-10). With this elementary theory, it is possible to explain most of the experimental observations made so far on this effect.

However, the above theory can be generalized with the assumptions that the intensity of collapse (or collision), the depth of erosion, and the material fracture are all statistical phenomena with known distributions (Fig. 14-11). It can be shown that the generalized equation of erosion is again the same type of differential equation with a new function ϕ_4 which is the resultant distribution of these three distributions.

It is suggested that the function ϕ_4 is the actual erosion distribution and that the time effects observed in the experiments represent this function quantitatively.

ACKNOWLEDGMENT

This research was supported by the office of Naval Research, Department of the Navy, Contract No. Nonr-3755(00) - (FBM) NR 062-293.

$$E_a = \Delta V \cdot S_e$$

$$P_a = \frac{\Delta V \cdot S_e}{t}$$

$$\text{Intensity} = \frac{\text{POWER ABSORBED}}{\text{AREA OF EROSION}}$$

$$I = \frac{\Delta V \cdot S_e}{A_e \cdot t} = \frac{i S_e}{t}$$

i - AVERAGE DEPTH OF EROSION

S_e = EROSION STRENGTH OF MATERIAL

t = DURATION OF EROSION

Fig. 14-1. Intensity of cavitation damage

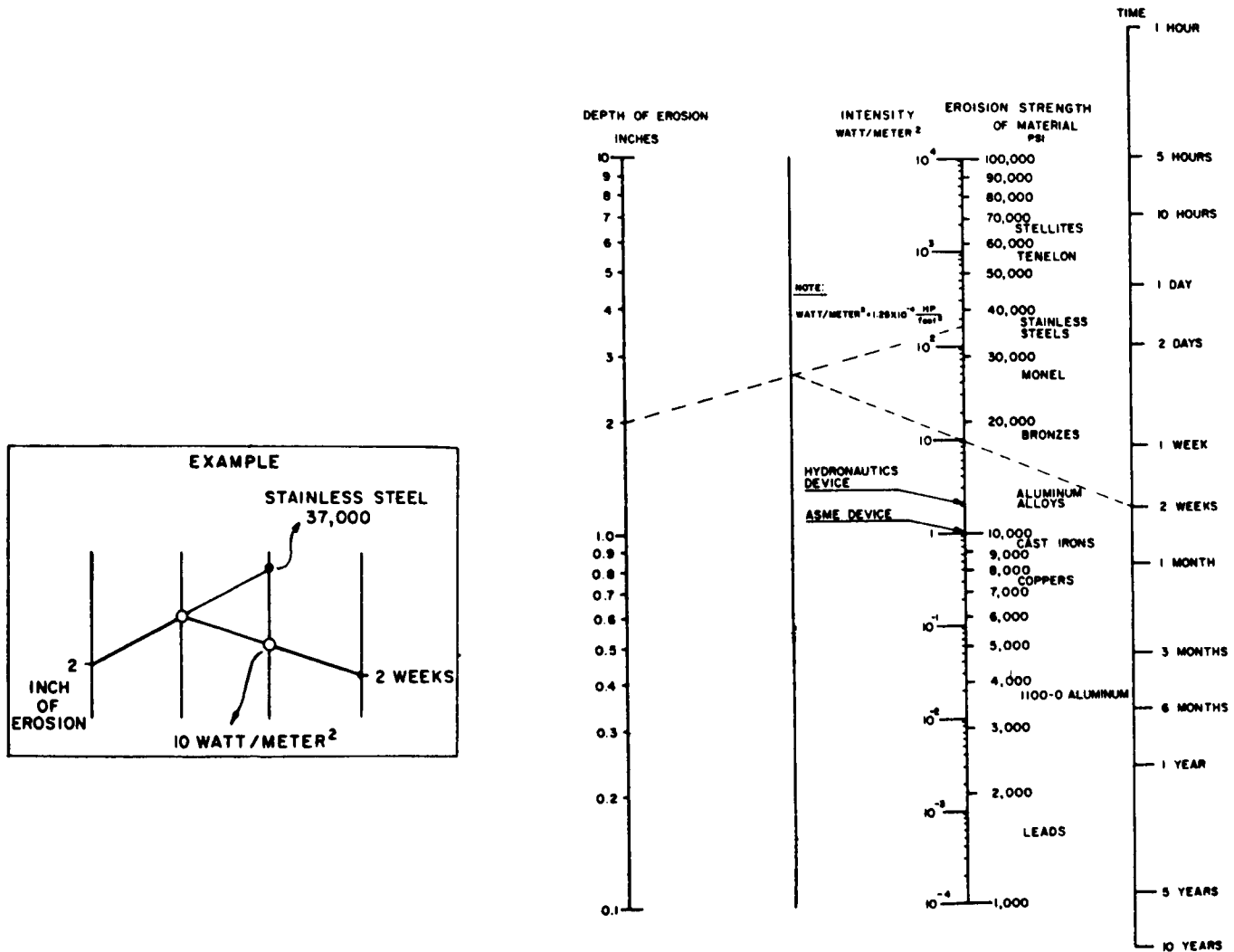


Fig. 14-2. Erosion intensity estimator

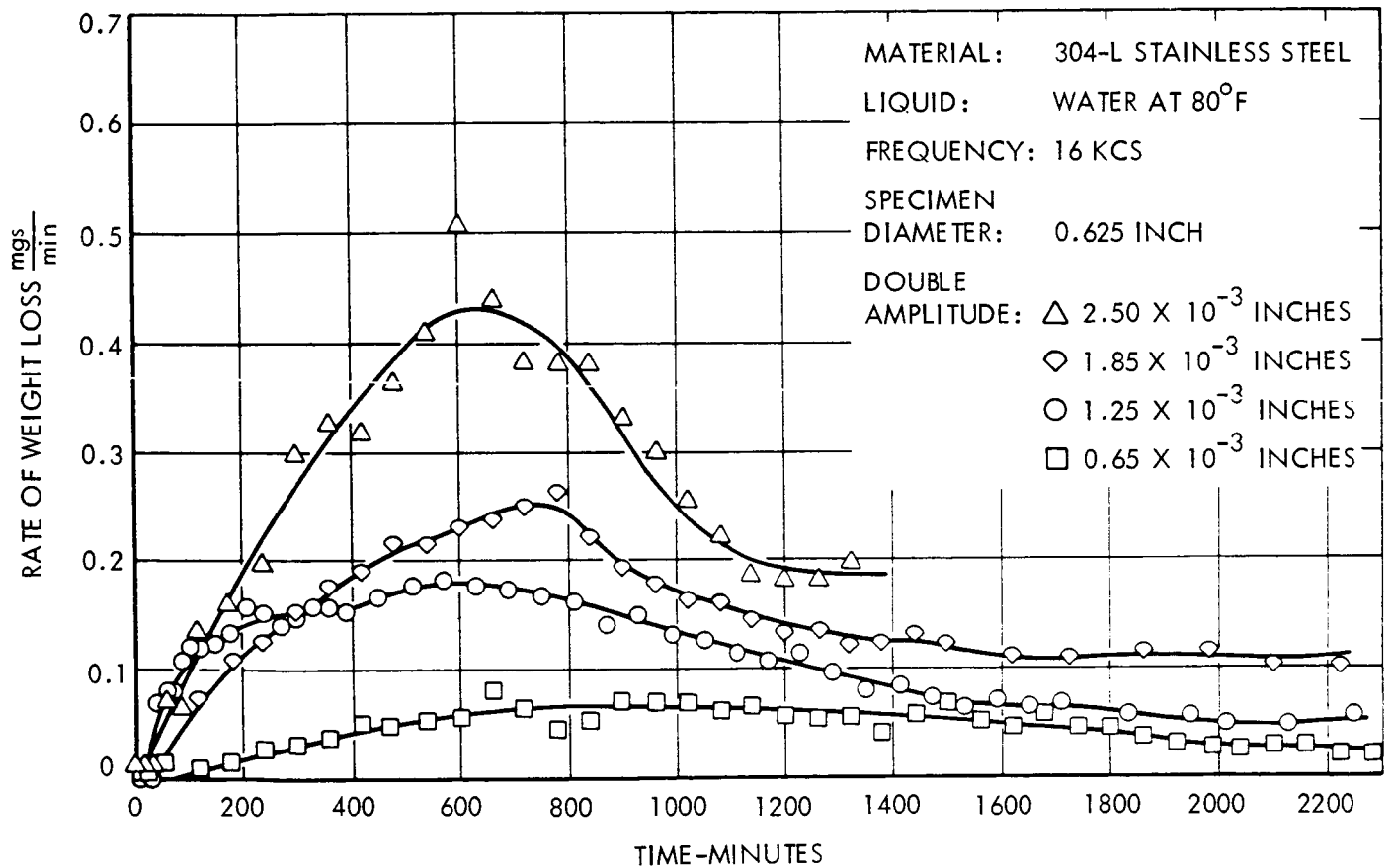


Fig. 14-3. Effect of time on cavitation damage rate for various amplitudes

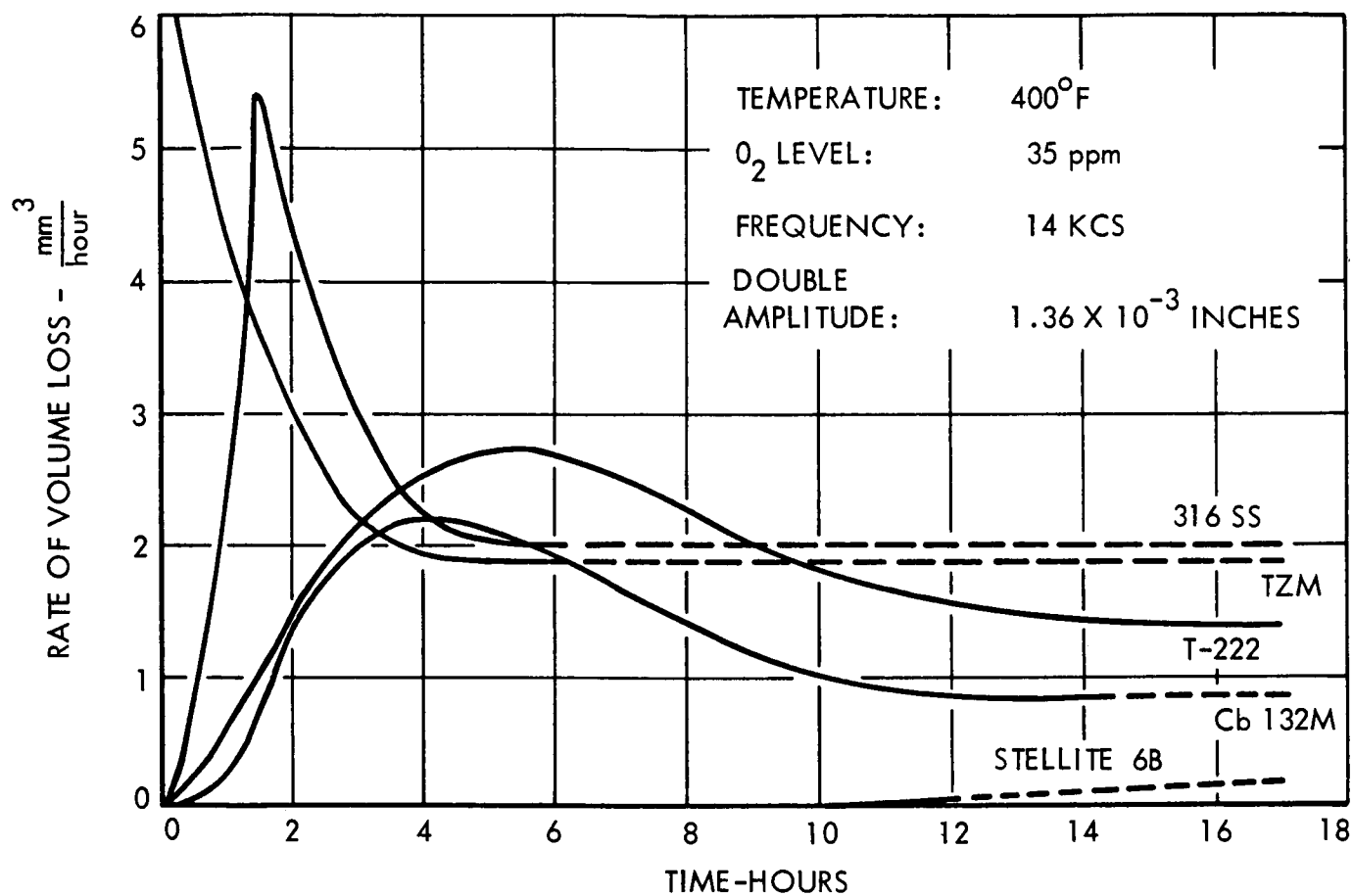


Fig. 14-4. Relative cavitation damage resistance of five metals tested in 400°F sodium

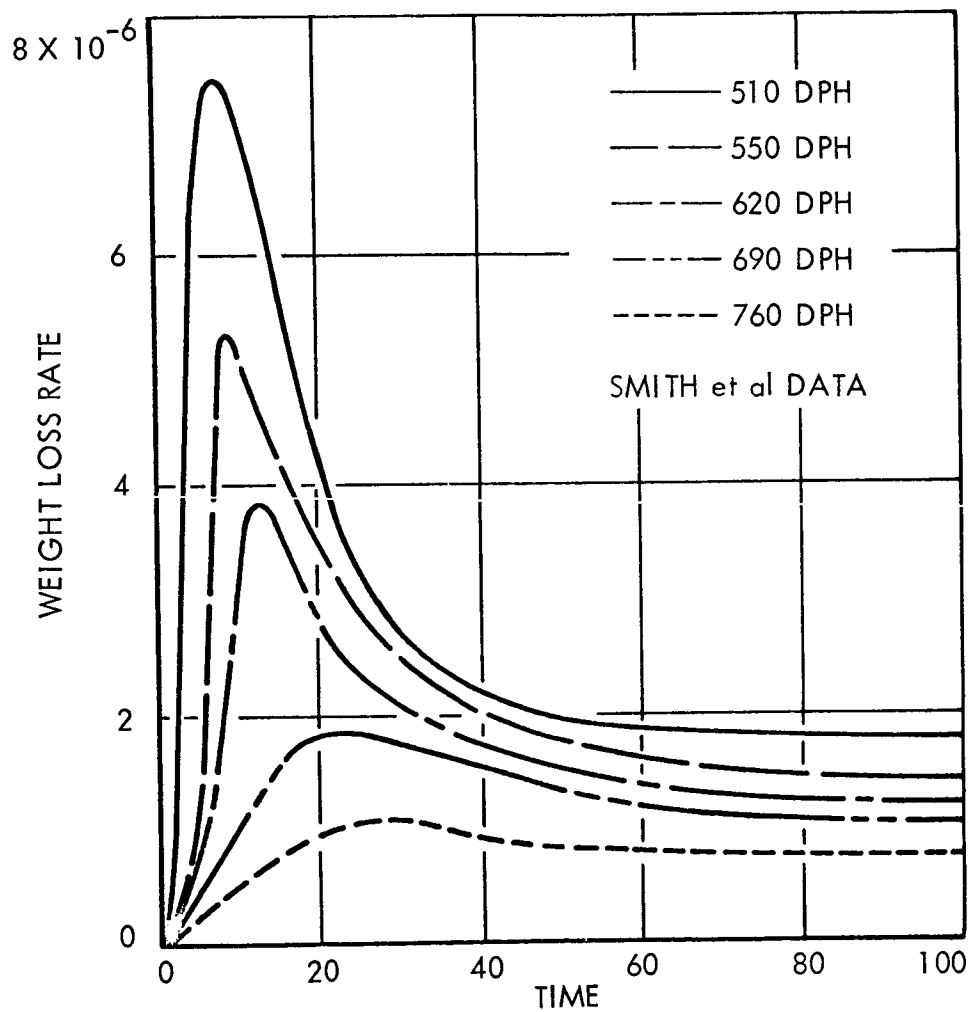


Fig. 14-5. Effect of time on liquid impact erosion on materials with various hardness

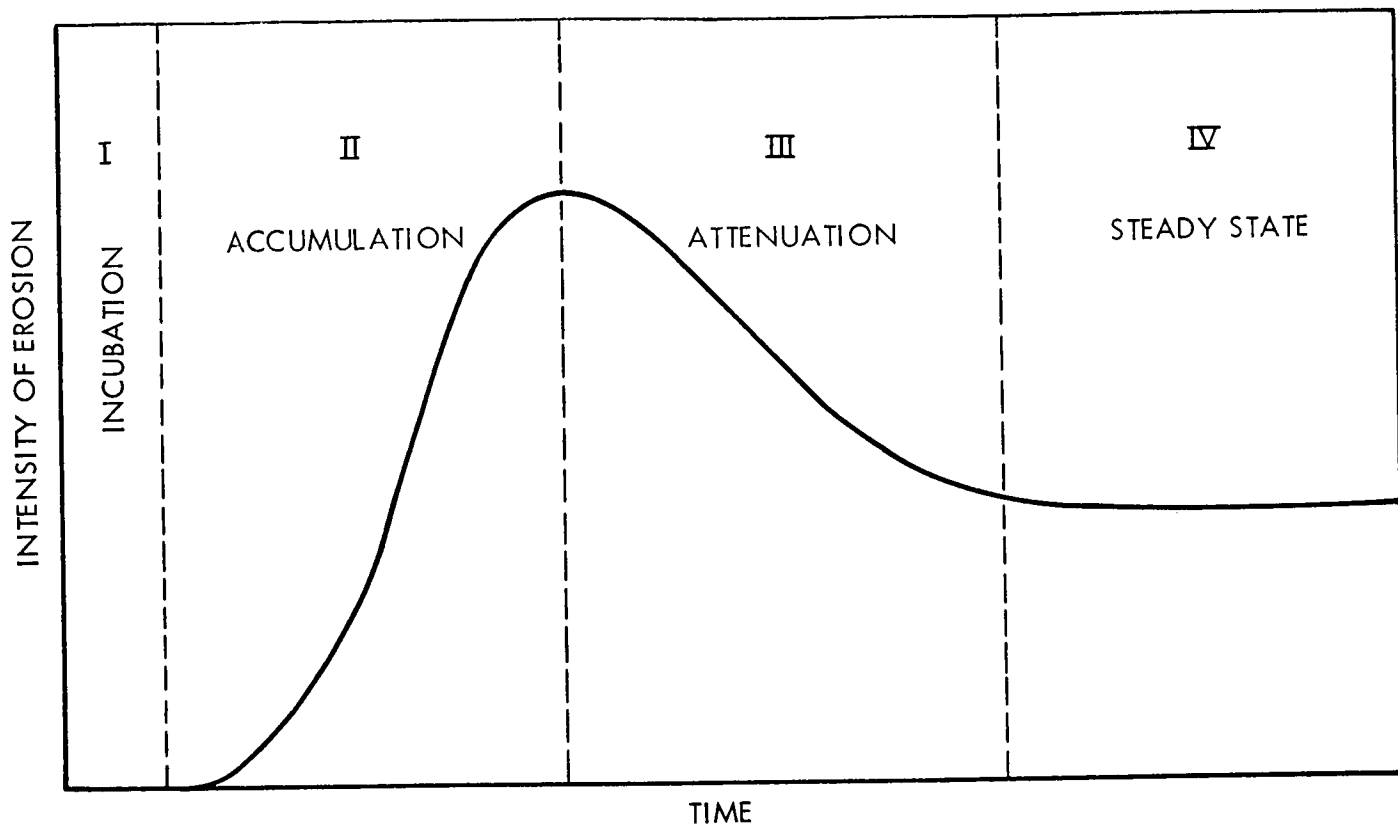


Fig. 14-6. Effect of time on intensity of erosion

ASSUMPTIONS:

$$1. \text{ INTENSITY OF IMPACT } I_i = \frac{A^n I_c}{r^n}$$

$$2. \text{ INTENSITY OF DAMAGE } I_d = \eta I_i$$

$$\text{DEFINITION: } I_d = S_e \frac{dr}{dt}$$

DIFFERENTIAL EQUATION OF EROSION:

$$\frac{dI_d}{dt} + k \frac{I_d^{\frac{2n+1}{n}}}{\eta^{\frac{1}{n}}} - \frac{I_d}{\eta} \frac{d\eta}{dt} = 0$$

WHERE

$$k = \frac{-n}{(AI_c)^{1/n} S_e}$$

AND

- I_c = INTENSITY OF COLLISION OR
COLLAPSE
 r = FILM THICKNESS OR DISTANCE
OF COLLAPSE
 A = CONSTANT WITH LENGTH
DIMENSION
 n = CONSTANT
 η = EFFICIENCY OF EROSION
 t = TIME
 S_e = EROSION STRENGTH

Fig. 14-7. Elementary theory

$$\text{AT } t=t_1; I_d = I_{\max}; \eta = \eta_1; \frac{dI_d}{dt} = 0; \tau = \frac{t}{t_1}; \bar{I} = \frac{I_d}{I_{\max}}; \bar{\eta} = \frac{\eta}{\eta_1}; \bar{k} = \frac{d\eta}{d\tau} \bigg|_{\tau=1}$$

$$\frac{d\bar{I}}{d\tau} + \bar{k} \frac{\bar{I}}{\bar{\eta}} \frac{\frac{2n+1}{n}}{1/n} - \frac{\bar{I}}{\bar{\eta}} \frac{d\bar{\eta}}{d\tau} = 0$$

GENERAL SOLUTION

$$\bar{I} = \frac{\bar{\eta}}{\left[1 + \bar{k} \frac{n+1}{n} \int_1^{\tau} \bar{\eta} d\tau \right]^{\frac{n}{n+1}}}$$

WHEN $n=2$

$$\bar{I} = \frac{\bar{\eta}}{\left[1 + \frac{3}{2} \bar{k} \int_1^{\tau} \bar{\eta} d\tau \right]^{2/3}}$$

WEIBULL DISTRIBUTION

$$\eta = 1 - \text{EXP} [-\tau^a]$$

GUMBEL DISTRIBUTION

$$\eta = \text{EXP} [-\text{EXP}(-\alpha\tau)]$$

Fig. 14-8. Normalized equation of erosion

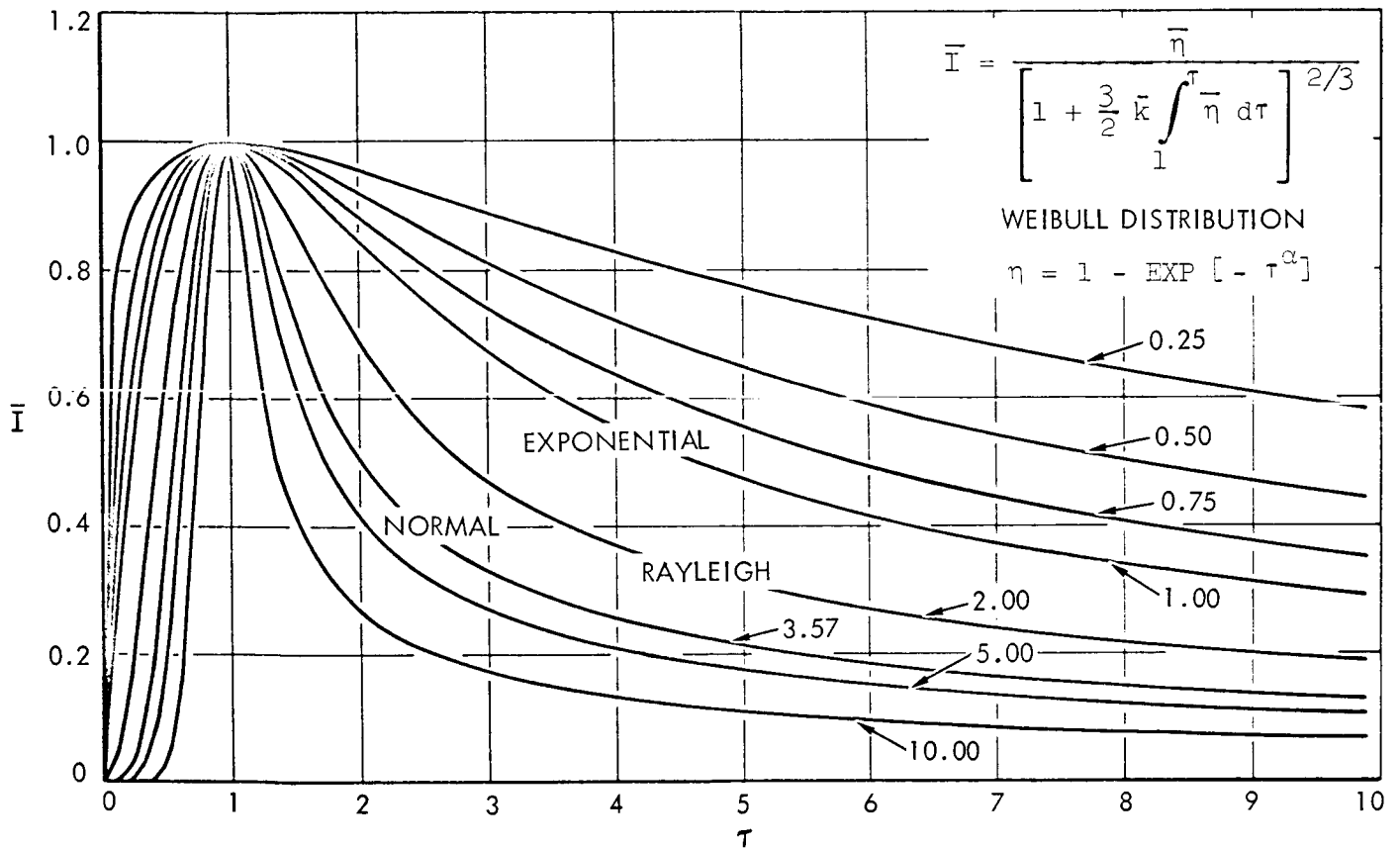


Fig. 14-9. Theoretical prediction of effect of time on intensity of erosion

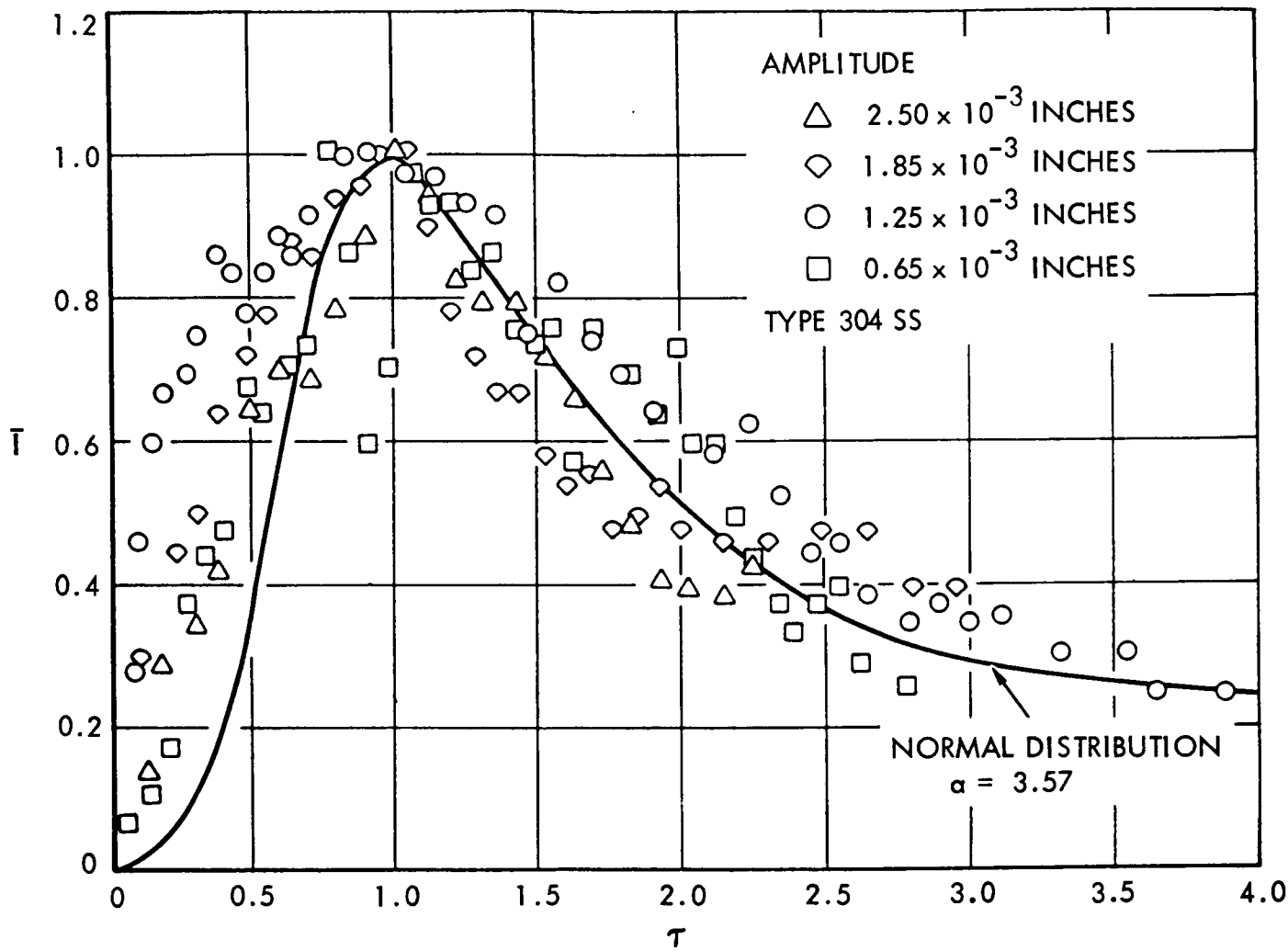


Fig. 14-10. Comparison of theory and experiments

$$\left. \begin{aligned} I_c &= \Phi_1(t) \\ r &= \Phi_2(t) \\ \eta &= \Phi_3(t) \end{aligned} \right\} \begin{array}{l} \text{PROBABILITY DISTRIBUTIONS} \\ \text{CONTROLLING THE STATISTICAL EVENTS} \end{array}$$

ORIGINAL ASSUMPTIONS

$$1. \quad I_1 = \frac{A^2 I_c}{r^2} \frac{\varphi_1}{\varphi_2^2} \qquad 2. \quad I_d = \eta I_1 \varphi_3 = \frac{\eta A^2 I_c}{r^2} \frac{\varphi_1 \varphi_3}{\varphi_2^2} = \frac{\eta A^2 I_c}{r^2} \varphi_4$$

$$\text{WHERE } \varphi_4 = \frac{\varphi_1 \varphi_3}{\varphi_2^2}$$

EQUATION OF EROSION

$$\frac{dI_d}{dt} + k \frac{I_d^{\frac{5}{2}}}{\varphi_4^{\frac{1}{2}}} - \frac{I_d}{\varphi_4} \frac{d\varphi_4}{dt} = 0$$

Fig. 14-11. General theory of erosion